An experimental and numerical study of forced convection in ventilated chambers.

Vazquez Numez, Bernardo

AN EXPERIMENTAL AND NUMERICAL STUDY OF FORCED CONVECTION IN VENTILATED CHAMBERS

BERNARDO VAZQUEZ NUNEZ

A thesis submited for the degree of
Doctor of Philosophy
to the Faculty of Engineering
University of London

Department of Mechanical Engineering
King's College London

July 1997

ABSTRACT

The thesis describes a combined experimental and numerical investigation of the three-dimensional flow processes in ventilated chambers. Four different geometrical configurations of square cross-section jets discharging into a rectangular chamber were studied. The configurations were selected to simulate four characteristic flow patterns encountered in the ventilation of rooms; these correspond to rooms with high wall, low wall, ceiling and floor ventilation inlets.

For the experimental part of the study laser-sheet flow visualization observations and laser-Doppler anemometry measurements were made to describe the flow characteristic qualitatively and quantitatively, respectively. Detailed measurements of the three mean velocity components and of the corresponding turbulence levels were made. A range of flow Reynolds numbers were investigated to determine the effect of the flow rate and flow regime on the ventilation patterns.

For the numerical part of the work a Computational Fluids Dynamics method was used to predict the mean flow and turbulence fields. The time-average equations for the conservation of mass, momentum and enthalpy were solved in finite-volume form. For the turbulent flow calculations, both the standard and low Reynolds number version of the κ–ε turbulent model were employed. The numerical predictions were assessed by comparison with the measurements. The calculations were in good qualitative and quantitative agreement with the experimental data and showed that most of the features of the flow were accurately predicted.

The effects of inlet configuration, flow rate and flow regime on the mean flow and turbulence characteristics were analysed in detail, In particular, the effects of the inlet jet throw, spread and drop on the ventilation patterns were quantified.

After the predictions had been assessed through comparison with LDA data, the CFD models were used to predict the effect of non-isothermal flows and contaminants dispersion in as well as the effect of inlet jet angle on large scale chambers. The implications of the results for the ventilation of buildings are assessed and recommendations for the improvement of related CFD predictions of the flow are made.

To My Parents

who always were there for me

To the memory of my mother Ma Teresa.

who always knew more of me than I could possible imagine.

To

S *us adorables cabellos rizados y encantadora sonrisa*

U *n verso que lleno mi vida de alegria, pasion y amistad*

E *s un poema de quien profundamente te ama.*

ACKNOWLEDGEMENTS

I would like to thanks all the people that in so many different ways, helped and supported me during my years of study at King's College London.

First of all I would like to sincerely thank my supervisor, Dr. Mihalis Yianneskis, for his guidance, encouragement and friendship during all these years.

I also want to thanks my friend and colleague Dr. Ricardo Gomiciaga with whom I have had innumerable discussions and who has shared with me the ups and downs. To Dr. Kalok Lee who advised and helped me in the difficult times.

To David Elgar who built the experimental test sections and had consistently talked about an interesting and amazing subjects.

To my colleagues in the Mechanical Engineering department, thanks for your help and friendship, to Kung NG, Dr. Maumodi, David Foster, Dr. Fu, Kieran Rutherford, also Ms Soon Lin.

To my friends at King's College, with whom I exchanged ideas, experiences and customs, and treated me as one more in the family, to Mar, Jose', Paolo, Vic, Lucinda, Alex, Simon, and Saul.

To Ms Carmen Huerta who kept me on her e-mail list, and coped with my calls for help when necessary. To all my friends and colleagues at LES.

To John Meagher who kindly helped me on the final lap, and for all his invaluable pieces of advice.

To my sister Rebeca who always kept in touch, my brothers Renato and Roberto, to who have understood my absence and their supported me.

To all my friends.

And Finally my most special thanks to Sue, my sunshine and support, for all the late nights and long weekends, her patience and invaluable help and advice on the revision of the whole document, because you believe in me.

To the CONACYT for the grant to support my PhD project.

TABLE OF CONTENTS

CHAPTER 4

MEASUREMENT AND PREDICTION OF THREE-DIMENSIONAL ISOTHERMAL FLOWS IN A CHAMBER VENTILATED BY A HIGH-WALL JET. 74

CHAPTER 5

CHAPTER 6

LIST OF FIGURES

NOMENCLATURE

A	Area (m^2)
a_i	Coefficient of finite difference equation
A_j	Coefficient in finite-volume equation (TDMA)
Ar	Archimedes number ($Ar = gh\beta\Delta T/u_o^2 = Gr/Re^2$)
b	Width of inlet (m)
$C_1, C_2, C_3, C_D, C_\mu$	Constants of turbulence model
b_x, b_y	Dimensions of control volume (m)
D_e, D_w, D_s .....etc	Diffusion term (kg/s)
d_e, d_w, d_s ..... etc	Coefficient in pressure correction term
F_e, F_w, F_s .....etc	Convection coefficients (kg/s)
F	Body force (N)
f_1, f_2, f_3, f_μ	Functions for LRN turbulence model
G_B	Buoyancy production
G_k	Generation rate of turbulence energy
Gr	Grashoff number ($Gr = gh^3\beta\Delta T/\nu^2$)
g	Gravitational acceleration (m/s^2)
h	Inlet height (m)
H	Chamber height (m)
κ	Kinetic energy of turbulence (m^2/s^2)
L	Chamber length (m)
P	Pressure (Pa)
Pe	Peclet number
Q	Mass flow rate (kg/s)
Re	Reynolds number ($Re = \rho lu/\mu$)
r.m.s or rms	Root-mean square
S	Source term
t	Time (s)
T	Temperature (°C or °K)
TI	Turbulence intensity (%)
u,v,w	Instantaneous velocity components in x,y and z directions respectively (m/s)
U,V,W	Mean velocity components (m/s)
u',v',w'	Velocity fluctuations (m/s)
x	Distance from origin from in the x direction (m)
x, y, z	Coordinate directions in Cartesian system (m)
x_o	Distance to virtual origin (m)
y	Normal distance from surface (m)
y+	Dimensionless wall distance ($U_r y_p \rho/\mu$)

Greek symbols

β	Coefficient of thermal expansion (1/K)
Γ	Diffusion coefficient (m^2/s)
δ	Wall jet width, area, boundary thickness (m or m^2)
δ_{ij}	Kronecker delta
ε	Dissipation rate (m^2/s^3)
κ	Von Karman's constant ($\kappa = 0.4187$)
λ	
μ	Dynamic viscosity for air at 20 °C ($\mu = 1.817x10^5$) (kg/m s)
μ_{eff}	Effective dynamic viscosity ($\mu_{eff} = \mu+\mu_t$)
μ_t	Turbulent eddy viscosity (kg/m s)
ρ	Density for dry air at 20 °C ($\rho = 1.204$) (kg/m^3)
σ_l	Laminar Prandtl number ($\sigma_l=\nu/\mu=0.713$)
σ_t	Turbulent Prandlt number ($\sigma_t=\nu_t/\Gamma_t=1.0$)
σ_κ	Turbulent Prandlt number of turbulent kinetic energy ($\sigma_\kappa = \nu_t/\Gamma_\kappa=1.0$)
σ_ε	Turbulent Prandlt number of energy dissipation ($\sigma_\varepsilon = \nu_t/\Gamma_\varepsilon=1.3$)
ι	Shear stress (Pa)
ι_w	Wall stress tensor (Pa)
Φ	Generalized variable
ϕ‘	Time averaged value of Φ
ν	Kinematic viscosity (m^2/s)

Subscripts

eff	Effective value
e, w, n, s, h, l	Control volume faces
E, W, N, S, H, L	Central node and its neghbours
i, j, k	Cartesian indicators of direction
l	Laminar
max	Maximmun value
o	Inlet, supply
P	Centre point in control volume
ref	Reference
rms	Root mean square
t	Turbulent

Abbreviations

FDM	Finite difference method
FEM	Finite element method
FVM	Finite volume method
LRN	Low Reynolds Number
RSM	Reynolds stress model
SIMPLE	Semi implicit method for pressure linked equations
SIMPLER	Semi implicit method for pressure linked equations revised
TDMA	Tridiagonal matrix algorithm

CHAPTER 1

INTRODUCTION

1.1 Preamble

One of the main objectives of building design is to provide the occupants with the appropriate thermal comfort conditions, under which they may carry on their indoor activities. The thermal comfort conditions of the occupants inside a building are influenced directly by the air speed, humidity, and temperature gradients produced by the convective processes within the building. Therefore, the prediction of the air flow patterns and the temperature distribution within the building is very important if appropriate comfort conditions are to be allowed for during the design stage. A detailed study of the convection phenomena in building ventilation is therefore required, in order to aid understanding of the effect and interaction of design variables such as ventilation inlet and outlet location, magnitude and direction of ventilating flow supply, etc. on the flow patterns (velocity distribution), turbulence levels, heat transfer, and temperature fields (temperature distribution).

The need to calculate the velocity and temperature fields accurately as well as the understanding of the influence of different boundary conditions on these fields is very important. Only with this knowledge, can one optimise the air conditioning equipment, the location of heating elements and/or ventilation openings, etc. In so doing one can achieve appropriate comfort conditions during the design stage. Although the primary objective in such work is the provision of appropriate thermal comfort conditions within a building, another important consideration is the minimisation of the energy

expended to heat or cool the building. For this reason appropriate strategies for saving energy must be established. Energy saving in building design is directly related to the reduction of the amount of air supply required to heat or cool a room.

1.2 Air flow characteristics in a ventilated room

A reduction of the supplied air may however have undesirable effects such as an increase of the concentration of indoor pollutants. In addition, larger temperature gradients may be generated, resulting in a non-uniform temperature distribution throughout the occupied zone. This may result in a considerable stratification inside a room, with higher temperatures near the ceiling (see, for example, Proceedings of IMechE, *Seminar* "Computational Fluid Dynamics-tool or toy?", (1991)). The main factors affecting the thermal comfort conditions are the air supply velocity and the positions of the air inlets and outlets, which determine the overall flow pattern in the room. The temperature gradients produced by heat sources such as the occupants, machinery, windows, etc., are also of great importance. Therefore, it is very significant to predict the different flow patterns and temperature distribution accurately, in order to evaluate and optimise design decisions. It is also desirable to be able to predict the effects of air inlet and outlet locations and inlet flow rate on the overall flow pattern. Different types of jet will produce different ventilation patterns, which in turn will affect on the heat transfer coefficients of the various surfaces inside a room.

The investigation of the air flow behaviour within an occupied space can be achieved by means of three approaches: analytical, numerical (by solving the governing flow equations) and experimental. Due to the complexity of the governing equations, analytical solutions are often not

possible. The conservation equations can be solved only for some very simple geometries. For buildings, analytical solutions are only known for some elements of the building structure under special boundary conditions, such as vertical walls, heat transfer through walls, etc. The understanding of convection flows has therefore been restricted.

Notwithstanding the complexity of the governing equations used in calculations of convective problems, the understanding of convective flows has improved in the last ten years through the use of numerical solutions of the conservation equations, which has been achieved with CFD models. CFD codes can be used by the designer as a prediction tool when accurate estimates are required for the assessment of thermal comfort and air movement and for the calculation of convection heat transfer coefficients. A well-designed air distribution system can reduce the ventilation rate necessary for removing air contaminants and moisture, and in this way reduce building energy consumption (Zhang (1991)). In comparison, the accuracy of zero or one-dimensional thermal models commonly used to simulate the dynamic energy performance of a building is very poor. These models provide only space-averaged values for the air velocities and temperatures required for the assessment of the safety and comfort conditions of the ventilated environment (Bradshaw et al (1990)).

The experimental approaches make use of either small scale models or full scale prototypes. Small scale models make it possible to extrapolate experimental results to different geometrical configurations without the necessity and expenditure of building full scale prototypes. Although small scale models are far cheaper to build, scaling problems are encountered when the temperature measurements are extrapolated to the full scale room. Small scale experiments are thus normally restricted to isothermal problems. Small scale models may only be used where there is a

knowledge of proper scaling methods, so that the data can be extrapolated to full scale rooms.

With the experimental approach other problems may be encountered. These are related to the small magnitude of the velocities and temperatures measured inside occupied buildings. Velocity and temperature data are normally obtained with intrusive techniques, using a probe immersed into the air flow (hot-wire anemometers and/or thermocouples), or by means of a non-intrusive techniques such as laser-Doppler anemometry (LDA). Accurate non-intrusive techniques for temperature measurements however are not as developed as LDA. A non-intrusive technique presents advantages because the air flow will not be disturbed. Moreover with LDA, the range of velocities that can be measured is greater then that with hot-wire anemometry (Cheesewright and King (1985)).

1.3 Literature review

Throughout the last 25 years a large number of studies relevant to the convective heat transfer processes inside buildings have been reported. Buildings and small scale models of various shapes and sizes have been investigated and the results of these studies are compared, where appropriate, with those obtained for the chambers under study in Chapters IV to VII in this thesis.

The studies reviewed below are either experimental or numerical, or a combination of both. In the remainder of this section, a brief introduction of the ventilation studies in buildings reported in the last 25 years is followed by a detailed review of important aspects of studies particularly related to the research work performed for this thesis, which includes three dimensional wall jets, similarity studies, and contaminant dispersion.

One of the first investigations of the air flow and heat transfer in ventilated buildings was that of Nielsen (1974). He applied a numerical method for the solution of the air flow in a two-dimensional auditorium, with a rectangular cross section. He based his studies on a previous work by Gosman (1969), where the flow equations were solved in terms of the stream function and the vorticity. The velocity profiles calculated numerically were compared with the experimental data, and reasonable agreement was reported. Although in this study Nielsen did not consider the buoyancy term, this term was included in later work (Nielsen, 1978). Nielsen's calculations and experiments made use of two non-dimensional numbers; the Reynolds number (Re = 3600) and the Archimedes number ($Ar = 4x10^{-5}$-$6x10^{-5}$). Other similar numerical studies were carried out by Hertager and Magnussen (1977), Timmons et al (1980) and Etheridge and Nolan (1979). They found that the near-wall zone that includes the boundary layer, was not adequately modelled. This was attributed partly to the size of the mesh used in that zone and partly to limitations of the models.

Full-scale chambers (see for example, Chen et al (1991), Bauman et al (1983), Gadgil (1980)) have been used for experimental studies under well-controlled conditions. Some full scale room studies have been concern with the measurement of air flow velocities (Melikov et al (1989) and Sandberg (1989)). Measurements obtained from these studies have shown good agreement with numerical predictions, although the latter were performed only for the occupied part of the room. Large factory buildings have been modelled by Jones and O'Sullivan (1985): the aim of this work was to model flows in buildings heated by warm air systems. In addition, radiant heating systems were considered. Non-regular geometries were modelled using body-fitted coordinates and the results were

compared with in-situ measurements. Chen et al (1991) and Timmons et al (1980) found that when mechanical air conditioning systems are used the flow patterns depend strongly on the size, shape and location of the air inlets and outlets. Bauman et al (1983) studied the transition from laminar to turbulent flow, while Gadgil (1980) observed that laminar flow was maintained for Rayleigh numbers up to 6.75×10^5.

Studies of building ventilation have included those related with the subject of ventilation when a fire is present, and some early work was reported by Markatos and Pericleous (1984), who used a finite volume method in two-dimensions and solved the equations of conservation of mass, momentum and energy, as well as the two equations for turbulence energy and its dissipation rate, using the κ–ε turbulence model. The flow configuration studied was that of natural convection in a square cavity. The cavity had two differentially heated walls, and two adiabatic horizontal surfaces corresponding to the floor and ceiling. The results showed good agreement with experimental data for laminar as well as turbulent convection. Markatos et al (1982) solved the two-dimensional steady state flow equations for the prediction of the spread of fire in a room. A three-dimensional version of the model was developed by Markatos et al (1984), who also included extra terms to the κ and ε equations to predict a highly buoyant flow. Steady state and transient flows were studied and the compressibility of the fluid was also modelled. The aim of the study was to model the fire development within a shopping mall and to predict smoke concentration levels. Only partial validation of the predictions was carried out mainly due to the lack of experimental data.

A number of other studies have predicted air velocity distributions using the κ–ε turbulence model (Nielsen et al (1978, 1979), Gosman et al (1980), Murakami et al (1987), Choi (1987), Chen and van der Kooi (1987)). The

numerical models were tested on small-scale rooms, where the flows were highly turbulent except for the boundary layer region. However, there are zones inside the room were low turbulence levels are expected (close to lateral walls, floor and ceiling). For such low turbulence regions the standard $\kappa-\varepsilon$ turbulence model is not considered to achieve good results (Chen (1991), Zhang (1991)). A variation called the low-Re $\kappa-\varepsilon$ model has been used as an alternative by Chen et al (1990).

More recently, (Hoffman and Galea (1993 a, b) extended CFD modelling, using the Eulerian-Eulerian approach, to the modelling of fire events in which two phases are involved. The aim of this work was to predict fire-sprinkler interaction. The results obtained have been compared with experimental data and shown qualitatively good agreement. The study showed the necessity of employing parallel computers to reduce the CPU time used for the simulation, and the urgent need for more detailed experimental data in this field.

The International Energy Agency created the Annex 20 program that includes the experimental and numerical results obtained from a full scale test case by various researchers using different numerical codes. The codes were all used to calculate the flow in the same experimental test rig. Although general qualitative agreement between the different sets of predictions and measurements was reported (Whittle and Clancy (1991)), experimental data obtained by different researchers varied by 40-65% and numerical predictions by 45-95%. The differences for the experimental results were attributed to differences between test rigs (such as thermal symmetry, supply air temperature, steady flow and diffuser velocity profiles). On the other hand the numerical variations were attributed to the specification of initial conditions (such as velocity profiles, kinetic energy of turbulence and its dissipation rate), the turbulence model, and numerical

diffusion. McGuirk and Whittle (1991) suggested the use of a numerical bench-mark test case, to be used for the assessment of different CFD codes under specified boundary conditions for building design calculations.

In 1991 another Annex 20 team adopted Nielsen's original auditorium geometry as a benchmark test case for different numerical models (Nielsen (1990)). The results showed agreement with experimental data for the jet (close to the ceiling surface) and the recirculation (occupied zone) regions, but they failed to predict small recirculations in the zone close to the top of the end wall which was observed with flow visualisation and measured with LDA by Restivo (1979). They also reported differences in the numerical results when the buoyancy term in the energy equation was included (Heikkinen (1991), Chen (1991), Said (1991) and Vogl and Renz (1991)) .

The main element in any ventilation pattern is the turbulent wall jet formed immediately downstream of the inlet, and for this reason studies concerned with such jets are reviewed below. A turbulent wall jet is formed when an air stream is discharged into confined space, through an inlet parallel to a confining wall. The cross-sectional area of the jet increases in proportion to the distance from the inlet. Turbulent wall jets have been extensively studied in two (Schwarz and Cosart (1961)), and three-dimensional (McGuirk and Rodi (1977)) forms. Analytical (Hammond (1982)), numerical (Restivo (1979)), and experimental (Polushkin (1977), Restivo (1979), Andrade and Restivo (1982)) studies have been reported. Some relevant observations can be found in the ASHRAE Handbook (1981), Jackmans (1973) and Chen and Rodi (1980).

The characteristics of turbulent wall jets have been reported in various studies (Nielsen (1974), Restivo (1979), Murakami and Kato (1989),

Zhang (1991)). However there is still a lack of data and understanding of how the geometrical dimensions of the confined space and the Reynolds number will affect the wall jet. Poz (1994) studied the planar turbulent jet in small scale enclosures of various sizes. The average velocity, turbulent velocity pulsations, turbulent kinetic energy and Reynolds stresses of the planar turbulent jet and the reversed flow pattern formed by the jet were measured. Poz found that the height of the models affected directly the values of the turbulent parameters. His work has helped to obtain a more precise assessment of numerical methods used for the modelling of room air distribution systems. He also found out that over the return section the flow covering the occupied zone was anisotropic, i.e.:

$$w' \neq u' \neq v'$$

where u', v', w', are the turbulence levels in the three coordinate directions.

A three-dimensional wall jet is formed when the air flow is produced by a rectangular opening of aspect ratio $b/h < 40$. The jet presents three main regions:

1.- A first zone from the inlet opening to the location where the boundary layer meets the two shear layers from the upper free boundary. This zone is known as the core zone.

2.- A second zone, which starts where the core zone ends and extends to the point where the two shear layers from the two free sides meet. This zone is called the characteristic decay region.

3.- The radial type decay region which extends to the point where the maximum velocity, U_{max}, decays approximately as $(x/h)^{-1}$ where x is the distance from the inlet and h the inlet height.

When b/h > 40 the wall jet is known as a slander jet. Three-dimensional jets have been studied experimentally for aspect ratios, of 10 (Viets and Sforza (1966)), 20, and 40 (Sforza and Herbst (1967)): For aspect ratios of 20 and 40, the exponent of the velocity decay is similar to that of a plane wall jet (-0.5). When the aspect ratio is equal to 10, the exponent is found to be -0.16. The results of these studies showed that for these two types of jet (three-dimensional and plane wall jet) the velocity distributions are similar in the characteristic and radial type decay regions. The only similarity found with the slander jet was the shape of the velocity distribution for the characteristic decay region in the three-dimensional wall jet. The following expression is used to represent the jet decay of a three-dimensional wall jet (Rajaratnam (1976):

$$\frac{U_m}{U_o} = 8.325\left(\frac{x}{\sqrt{A_e}}\right)^{-1}$$

where U_m, U_o, x, and A_e are the maximum velocity, initial velocity, length, and inlet cross section area respectively. The potential core length, L_c can be described by:

$$L_C = 8.235\sqrt{A_e}$$

When an air stream enters a chamber, different air zones can be distinguished inside the room (Chen et al (1969)). The first zone is close to the air inlet and its extends to the location where the air velocity has reached a certain threshold value (approximately 1.8 m/s). The flow in the second zone is still under the influence of the incoming air but the air velocity in this zone is below 0.8 m/s. Zones where the air remains nearly

stagnant represent a third zone (with air velocities below 0.08 m/s). A general air motion zone is created by the recycling air stream entraining into the incoming air jet (the first and second zones).

Two other aspects of jet flow are also of importance: the entrainment of surrounding air and the spread angle of the jet. The first is important to the overall motion of the flow and it affects the incoming air flow before it reaches the occupied zone (ASHRAE Handbook (1981)). The second is a measure of how much the jet has spread in the occupied space. Spread angles are usually found to be between 20 and 24 degrees. For a wall jet the angle of spread is around half of that found on a free jet (Hellickson et al (1973)).

The stability of the jet flow inside a ventilated chamber is also important and has been studied for isothermal and non-isothermal three-dimensional wall jets. Two non-dimensional numbers have been used to study these types of jet and how they influence the overall flow pattern in a ventilated chamber. The first is the Reynolds number (Re), which represents the ratio of inertia forces to viscous forces. Timmons (1984a, 1984b) and Restivo (1979) found that the flow pattern inside a ventilated chamber will become stable when Re is greater than a threshold value ($\cong$ 5000). The second is the Archimedes number (Ar), which has been used (Baturin (1972), Moog (1981), Christianson et al (1988)) to determine the stability of non-isothermal flows. Ar represents the ratio of buoyancy forces to inertia forces. Both Ar and Re are used in similarity studies, as discussed below.

Based on dynamic similarity considerations, results obtained from small-scale models can be extrapolated to full-scale chambers. Small-scale models are less expensive and more convenient experimentally than full-scale experiments. The use of small scale models allows the researcher to

increase the number and type of experimental tests to be carried out in a particular room. However there are limitations which depend on the scaling method used to extrapolate the results, qualitatively as well as quantitatively, to full-scale rooms. Due to the complexity of the air flow inside a room, partial similarity is frequently used, with which some parameters are altered while the most important ones remain unaltered.

The majority of the small scale studies have utilised water as the working fluid (Moog (1981), Anderson and Mehos (1988), Whittle and Clancy (1991)). The calculations underpredicted the air velocity by 30%, and overpredicted the room turbulence velocity scale (defined as the standard deviation of the velocity fluctuations) by 120%. Air has also been used as the working fluid in small-scale studies, but limitations exist due to the difficulty encountered in the scaling of the temperature fields. Many studies have been limited to isothermal flow (Restivo (1979)) and models of scale 1:9 (Murakami and Kato (1989)). A novel scaling technique using a refrigerant as the working fluid has been developed in MIT by Glicksman et al (1996) with promising results. Linden et al (1990) and Copper (1995) have been studying the fluid mechanics of natural ventilation using water with salt solutions of different densities as the working fluid, utilising refractive index changes and associating them with temperature fields to visualise natural convection currents. Linden et al's (1990) experimental results have been compared with those obtained in full scale buildings and the agreement has been very good.

As mentioned earlier, the studies of Timmons et al (1980), (1984a), Nielsen (1978), and Restivo (1979) to mention but a few, have shown that the type of flow found inside a ventilated chamber is influenced by the size and position of the air inlets. They also found that when the inlet velocity and inlet height were greater than a certain threshold value, a rotary type of

flow (mixed ventilation) is generated inside the chamber. The maximum eddy size of this rotary flow will depend on the position of the inlet and the room dimensions (Timmons (1984a), Deurloo et al (1988)). When the jet travels close to the ceiling wall it remains attached to the ceiling until it reaches the opposite wall, a phenomenon known as the Coanda effect (Restivo (1979), Timmons et al (1980)). In addition the jet stream moving along the floor has a component that moves upward, towards the incoming air stream near the ceiling (Ogilvie et al (1988), Restivo (1979), Timmons (1980)). The velocities in the recirculation zone depended to a great extend on the momentum of the inlet velocity.

One of the practical problems encountered in experimental studies of ventilated chambers is the provision of suitable flow tracers for visualisation experiments and for this reason a short review of the different techniques used to visualise the flows is given below. Flow visualisation has been is used to obtain qualitative information of the flow patterns in ventilated chambers. Flow visualisation methods can be used to characterise the global flow field, in contrast to single-point methods of measurement (LDA, hot wire anemometry, etc.). Several methods have been used for flow visualisation (Freymuth (1993)) and some of them have been extended to obtain quantitative information on the air flow. Flow visualisation techniques take advantage of the light scattered by small particles introduced into the air flow, and/or changes in the index of refraction in fluids with different densities. The particles used as flow followers are required to have small inertia and follow the flow faithfully.

The methods of introducing particles in an air flow for flow visualisation tests include the suspension of small vaporised oil particles (Restivo (1979), atomised water droplets (Kennedy (1987), small particles of fine magnesium carbonate powder (Murakami et al (1985)) and heated

metaldehyde (Nielsen (1974)). For water flows, ink, or fluids of different densities (Linden et al (1990)) can be used as tracers. Under turbulent flow conditions however, rapid dispersion of the introduced particles occurs however and the range of the flow visualisation tests of e.g. Nielsen and Restivo was limited to about Re = 500 due to strong mixing. One of the most attractive tracers is the water fog used by Kennedy (1987) to visualise air flows in laboratory experiments, as the particles produced are non-toxic and non-irritant, in contrast to the substances used by Nielsen (1974), Restivo (1979), and Murakami and Kato (1989). Neutrally buoyant balloons have also been used, with a video recording and computer-based image analysis (Alexander (1994)). Flow visualisation tests have been also reported by Freymuth (1993), Merzkirch (1989), Yang (1989) and Awbi (1991).

1.4 Contaminant dispersion

Determination of contaminant dispersal in occupied spaces is very important, as the contaminant could disperse very quickly in a room, particularly if the room has mixed ventilation. In a mixed ventilation system a jet is used to supply the air flow to a room, and a large rate of entrainment and circulatory motion can be found. The contaminants in an occupied room need to be removed and the concentration level has to be reduced to a threshold limit value specified by the standards and regulations of different countries. The levels of concentration can either be measured of predicted. For the former different experimental techniques have been used in large scale rooms (Nielsen (1981), Murakami et al (1983), Davison and Olson (1987)), and small-scale rooms (Kurabuchi and Kusuda (1987), Yamanaka and Narasaki (1992)). These studies have been limited by lack of appropriate scaling rules for the contaminant equations. Some studies have been concern with novel ventilation systems ("Spiral

Vortex", Nagasawa et al (1990), mixed ventilation (Nielsen (1981), Roulet and Cretton (1992)), and displacement ventilation (Nickel (1990), Roulet and Cretton (1992)). The perceived air quality has been assessed by human subjects and compared with numerical simulations (Bluyssen and Lemaire (1992)). The results indicated that the perceived air quality can be affected by temperature variations, the occupants' positions and adsorption effects. Some other studies have been concerned with the ability of the building layout to withstand sudden outdoor air contamination (Siren (1993)). These studies used models to calculate the infiltration air flows, the contaminant transport inside the room and the temperature decay of the building.

An important distinction should be made at this stage by differentiating air change efficiency and ventilation efficiency. The former is a measure of how effectively the air present in a room is replaced by fresh air supplied by the air conditioning system. The latter is a measure of how quickly a contaminant is removed from an occupied room (Sutcliffe (1990), Sandberg and Sjoberg (1983), Skaret and Mathisen (1983)). The term ventilation effectiveness (Pozin (1993)) is frequently used instead of ventilation efficiency. Experimentally the measurement of local mean age of air at various locations is used to verify the efficiency of the ventilation system (Roulet and Cretton (1992)).

Numerical predictions are performed by adding a transport equation for concentration to the set of equations that represent the problem under study. The equation can then be solved in time-averaged or time-dependent forms after a converged solution has been achieved for the other transport equations (i.e. of mass, momentum, energy). Some studies have included the buoyancy term (Murakami et al (1983), Nickel (1990), Nielsen (1990)), while other studies have dealt with isothermical flows (Nielsen

(1981), Kurabuchi and Kusuda (1987)). There have been studies of two (Nielsen (1981, 1990), Davison and Olson (1987)), and of three dimensional flows (Murakami et al (1983), Kurabuchi and Kusuda (1987), David and Olson (1987), Nickel (1990), Subrata et al (1993)). Some of these studies have concentrated their efforts on the contaminant distribution and how it is affected by different inlet sizes and their location (Nielsen (1981), Nickel (1990)), and/or the effect of the contaminant source location on the contaminant dispersal (Nielsen (1981), Subrata et al (1993)). A smaller inlet was found to increase the ventilation efficiency (Nielsen (1981), Murakami et al (1983)), and the location of the inlet was found to modify the flow pattern inside the room, affecting the ventilation efficiency (Nielsen (1981)). Draughts are found to be the main outcome of an increased air flow supply rate to the room (Nielsen (1981)), and these draughts are expected to result in a reduction of thermal comfort. Ventilation efficiency was found to be strongly dependent on room air movement and contaminant source location. Nielsen (1991) reported high contaminant concentrations in relatively stagnant zones within the occupied room. The location of the return opening is far more important for contaminant dispersion than for the air velocity distribution in the room. Nielsen (1991) has suggested locating contaminants in high velocity zones.

It has been found that low turbulence levels will result from low air flow rates. This has been observed (Nielsen (1991), Skovgaard (1991)) in a room ventilated by a side wall inlet. These low turbulence levels influence the ventilation effectiveness, and clearly turbulence models that can handle the problem adequately must be identified. So far the predicted contaminant concentration, tends to be greater than the contaminant quantities measured (Murakami et al (1983), Nielsen (1990)).

Detailed reviews of the relevant literature are given in Awbi (1991). An overview of the application of CFD to building air flows is provided in Whittle (1986).

1.5 Summary of literature review

The numerical studies reported have been concerned with both two- and three-dimensional laminar and turbulent flows. The κ–ε model has been used most extensively in the prediction of three-dimensional turbulent flows (Chen (1992)), but concern remains about the use of this or others turbulence models in the predictions of turbulent flows (Bradshaw et al (1990)). The reported results did not predicted accurately the flow in the zone close to the wall (boundary layer). This is thought to be principally due to the size of the mesh used. Some methods have been proposed and tested to solve this problem (Chen et. al (1991), Said (1993)). Although CFD codes have proved to be a powerful tool in the area of building design, their application to room ventilation problems to date shows that they have to be used with care if accurate and/or representative results are to be obtained from the related predictions.

Experimental studies on the other hand can be found for laminar and turbulent flow in buildings with both mechanical air conditioning and natural ventilation. Some of the research reported has been concerned with the determination of the heat transfer coefficients on vertical walls inside the buildings. A major part of the research effort was aimed at to establishing the flow patterns inside rooms, by using flow visualisation techniques (limited by strong mixing to Re = 500 (Restivo (1979), Murakami and Kato (1989)), hot wire anemometry and LDA measurements. For flow visualisation oil droplets have mainly been used,

with only one example of water-based droplets. Water fog clearly presents advantages over oil due to is availability and non-toxicity.

The experimental data reported to date show a pronounced lack of boundary condition measurements that are urgently needed for CFD calculations. Detailed measurements of initial conditions such as inlet mean velocity profiles and turbulence parameters (especially κ), are necessary to assess numerical models accurately. Flow patterns in room geometries where rotary flow is present, seem to be independent of Reynolds number for Re values over 3800 (Timmons et al (1980), Restivo (1979)). The turbulence was found out to be anisotropic over the return section (Poz (1984)). Discrepancies are presented between numerical studies in terms of small recirculation zones which have been observed in experiments, but are not reproduced by the predictions.

The above survey of the published literature has indicated that although a large number of studies have been reported, there has not been to date a concerted effort to study the different types of ventilation patterns produced by different inlet locations. In addition, detailed assessment of CFD predictions of ventilation flows is lacking and in particular inlet condition data are not available in the literature. Assessment of an appropriate model of turbulence for the CFD predictions is also desirable. Finally it may be concluded that, small-scale studies can be utilised for adequate characterisation of the mean flow turbulence distributions, but large-scale studies are necessary to assess the temperature, heat transfer and contaminant dispersion characteristics of the flows.

1.6 Objectives of present work

The main objective of the work reported in this thesis is to study the airflow inside four configurations of square cross-section jets discharging into a rectangular small scale chamber, which are representative of the four main types of air supply to ventilated rooms: high wall, low wall, ceiling and floor inlets. For this purpose, the study will be concerned with:

1. The design and development of four experimental small-scale rigs for studying room air distribution with different air supply locations.

2. Experiments which will be used to acquire accurate flow data and thus estimate more accurately boundary conditions for CFD predictions of the flows, as well as assess the results obtained from the predictions. The experiments will utilise flow visualisation techniques for a qualitative and LDA for a quantitative description of the flows in view of the difficulties associated with large-scale tests, all experiments shall be carried out in small-scale chambers and under isothermal conditions.

3. CFD predictions of the flows in both small- and full-scale chambers will be to predict the mean flow and turbulence fields, by solving the conservation equations in their finite volume forms. Two turbulence models will be employed, the standard $\kappa-\varepsilon$ and low Reynolds number $\kappa-\varepsilon$ models. The fact that in previous studies the three-dimensional nature of the flows has not been studied fully, provides the motivation for another objective of the present work: the assessment of the three-dimensional mean flow and turbulence characteristics inside the different chambers studied. The work will also be concerned with the comparison of the predicted and measured turbulence kinetic energy levels, which has hitherto received relatively little attention.

4. The numerical part of the study will be concerned at first with the small-scale isothermal predictions which will be compared with the experimental results. Once the accuracy of the predictions has been assessed by the above comparisons, the CFD models will be used to predict non-isothermal flows and contaminants dispersion in large sealed chambers.

5. The results of this work could thus provide an improved understanding of the flows which could be then used to develop methods for estimating the effect of the airflow, temperature and contaminant distributions on the comfort of the occupants and the energy consumption of buildings.

1.7 Outline of thesis

The contents of the remainder of this thesis are as follows: Chapter 2 is concerned with the experimental set up and the description of the different experimental techniques used (flow visualisation, laser Doppler anemometry, etc.). In Chapter 3 mathematical and numerical fundamental considerations and formulations of the models are outlined together with a the detailed description of the turbulent models used. In Chapter 4 the measurements and predictions for a chamber ventilated for a high-wall jet are presented and discussed, while in Chapter 5 similar results and discussion are given for a low-wall jet. Chapter 6 presents the measurement and predictions for a chamber ventilated by vertical jets from ceiling and floor inlets. Chapter 7 presents a study of the effect of inlet angle, contaminant dispersion and Archimedes number on the mean flow and turbulence structure inside a ventilated chamber. Chapter 8, the final chapter, contains the conclusions and recommendations for future work.

CHAPTER 2

FLOW CONFIGURATION AND EXPERIMENTAL TECHNIQUES

2.1 Introduction

In this chapter the experimental configurations studied and the flow visualisation and Laser-Doppler Anemometry (LDA) techniques employed for the characterisation of the flows are described. In the following section, the geometry and flow conditions of the four ventilated chambers employed in the present work are described. Subsequently, the experimental techniques used to obtain first qualitative (flow visualisation) and then quantitative (LDA) information on the flows are discussed in sections 2.3 and 2.4 respectively.

2.2 Test section

The experiments were carried out in four small-scale models of ventilated rooms. The size and configuration of each of the four test sections is shown in Figures 2.1 (a)-(d), which show only one half of each configuration, as they were all symmetric about the x = 50 mm plane. The four chambers studied were identical except for the location of the inlet and outlet.

In the following text, the terms lateral, end and side walls(s) are employed to refer to the z = 0 mm, z = 300 mm, x = 0 mm, walls respectively, while the terms ceiling and floor refer, of course, to the y = 0 mm and y = 100 mm of the chambers.

Chamber 1 incorporates a high-wall inlet on the lateral wall, and a low-wall outlet in the opposite side. The geometry of chamber 2 represents the opposite case i.e. a low wall inlet and a high-wall outlet on the lateral and end walls respectively. Chamber 3 incorporates a ceiling inlet that produces a vertical down-flowing wall air jet; the outlet it is located on the upper part of the end wall. Chamber 4 represents an opposite configuration a vertical up-flowing wall air jet produce by an inlet located on the floor surface, and outlet located in the lower part of the end wall. The internal dimensions of the chambers are: height (H) = 100 mm, length (L)= 300 mm and width (W)= 100 mm.

The inlets and outlets were w = 30 mm wide and h = 10 mm high, and ow = 45 mm wide and oh = 15 mm high, respectively, for all cases studied. The test sections were manufactured from transparent acrylic plastic (Perspex) of 5 mm thickness so that flow visualisation and LDA optical techniques could be used. A honeycomb section was placed in the ducting upstream of each inlet to laminarise the flow and produce a velocity profile akin to plug flow at the inlet plane of the chamber. Air was supplied to the test sections by a compressed air supply.

2.3 Laser-sheet flow visualisation technique

Flow visualisation experiments were performed for a range of air flow rates in the four chambers studied. Figure 2.2 shows a schematic diagram of the experimental arrangement used for this purpose. The air flow was seeded with atomised water droplets. The compressed air was passed through a pressure gauge and flow meter. The air stream was subsequently divided in two parts, one flowing through a bank of water atomisers of 500 ml capacity (Dart-Respiration Model 5207) and the second part through a by-pass pipe. The atomisers were capable of producing a very fine mist of

water droplets of 3 to 5 μm diameter. The mist cloud (seeded air) was then fed to a settling chamber, were the particles from the different atomisers were mixed and large particles were eliminated through settling. A small jet pump was used to mix the air from the by-pass pipe and the seeded air. The jet pump produced a syphoning effect, dragging the seeded air from the settling chamber. This arrangement was designed to allow the amount of droplets entering into the test section to be controlled.

During the flow visualisation test, individual planes in a test section were illuminated by a sheet of laser light. The water droplets scattered the laser light and indicated the path followed by the air flow inside the cavity. A 2 Watt Argon-Ion Laser operating at a wavelength of 546.1 nm was used as the light source. The laser light passed through a small convex lens to focus the laser beam and then through a cylindrical lens to produce the sheet of light. A series of mirrors was used to redirect the sheet of light through the different planes in the test sections (Figure 2.3). The streaklines produce by the droplets and the resulting flow pattern was recorded with a video camera.

2.4 Laser Doppler anemometry

Laser-Doppler Anemometry is a non-intrusive technique which has been used widely to measure mean flow and turbulence characteristics for a large number of diverse applications. LDA offers a number of advantages over probe-based methods such as the hot-wire anemometry technique. For example, the flow direction can be determined without ambiguity, no calibration is needed, measurements of the velocity components are independent of pressure and temperature gradients inside the test section, and with LDA high spatial and temporal resolution can be achieved. However application of LDA for flow measurements can only be made if

particles are present in the flow to scatter light from the interference fringe volume and optical access to the flow field is required. In addition, velocity information can only be obtained if there is a particle crossing the measurement volume and hence a continuous record of the velocity variations with time cannot be obtained.

The principle of the LDA technique rests on the ability to measure the variations in the intensity of the laser light scattered by moving particles crossing thought a fringe pattern. This fringe pattern (Figure 2.4) is formed when two laser beams of equal intensity are crossed. The particles crossing the dark and light fringes of the intersection volume produce a modulation of the scattered light intensity. The resulting signal from each particle crossing is known as a Doppler burst. The light scattered by the moving particles is collected by a photomultiplier detector. The voltage from the photomultiplier is then processed and analysed by a signal processing unit. The frequency of the modulation of the scattered light is proportional to the component of the velocity of the particle perpendicular to the bisector of the angle between the 2 laser beams. The ambiguity in the velocity direction inherent in LDA is resolved by imposing a known frequency difference (shift) between the two laser beams, which is then added or subtracted from the Doppler frequency depending on the direction of the flow.

The fringe spacing (λ^*), the distance between a pair of light or dark bands in the interference fringe volume, is given by the ratio of the angle of the intersecting beams θ and the wavelength of the laser light λ:

$$\lambda^* = \frac{\lambda}{2\sin\left(\frac{\theta}{2}\right)} \tag{2.1}$$

When the moving particles cross the measurement volume (fringe pattern) with a velocity component U in the direction perpendicular to the bisector of the laser beam angle, the frequency of the variation of the intensity of the light scattered by the particle, F_D, is proportional to the velocity V and the laser light wavelength (λ):

$$\mathbf{F_D = \frac{2V \sin\left(\frac{\theta}{2}\right)}{\lambda}} \qquad (2.2)$$

Several factors control the amount of light scattered by a particle, for example the size, shape and refractive index of the particle and the direction of observation. The scattered light always has a low frequency intensity variation (pedestal) in addition to the modulation frequency of the Doppler burst.

As mentioned earlier the velocity direction ambiguity can be resolved by imposing a different optical frequency on the two laser beams, for example by means of a rotating diffracting grating. If F_S is the supplied frequency shift, equation (2.1) can be written as:

$$\mathbf{V = \frac{\lambda \left(F_D \pm F_s\right)}{2 \sin\left(\frac{\theta}{2}\right)}} \qquad (2.3)$$

The frequency shift is given by:

$$\mathbf{F_s = \frac{2mnN_g}{60}} \qquad (2.4)$$

Where m is the order of the diffracted beams, n is the number of etched radial lines on the grating and N_g is the grating speed in rpm.

The optical components and considerations particularly relevant to the present study are described in the following section. An extensive description of the principles and practice of the LDA technique is beyond the scope of this chapter but can be found in Durst et. al (1976), and Drain (1980).

2.4.1 Optical arrangement

The laser-Doppler anemometer comprised a 10 mW Helium-Neon laser, a rotating diffraction grating, and a photomultiplier (model EMI 9817B) fitted with a zoom lens, and associated lenses and optics. All the parts and the arrangement of the optical system used are shown schematically in Figure 2.5. The system operated in the forward scattered mode.

The grating was mounted on a small sliding table in an arrangement which enables the place of the beams to be rotated for the measurement of different velocity components. The diffraction grating disk 21600 radial lines engraved and the grating was rotated at speeds of up to 5000 rpm by means of an electric motor. The first order beams were used to form the measurement volume. The characteristics of the LDA system used are tabulated below.

Focal length of lens L_1	(mm)	120
Focal length of lens L_2	(mm)	500
Focal length of lens L_3	(mm)	300
Frequency shift f_s	(MHz)	1-3.5
Half angle between laser beam θ/2 (in air)	(°)	2.1
Measurement volume diameter b_x	(μm)	77.9
Measurement volume length b_y	(mm)	1.0
Number of fringes N_l		13.5
Frequency/velocity conversion factor	(m/s/MHz)	4.0

Where:

The diameter of the control volume b_x is given by:

$$b_x = \frac{b_0}{\cos\left(\frac{\theta}{2}\right)},$$

The length of the measurement, b_y, is given by:

$$b_y = \frac{b_0}{\sin\left(\frac{\theta}{2}\right)},$$

where θ is the intersection angle of the beams and b_0 is the laser beam diameter.

b_0 and N_1 are given by:

$$b_0 = \frac{4lf_1f_3}{\pi b_0 f_2},$$

and

$$N_1 = \left(\frac{2b_0}{\lambda}\right)\tan\left(\frac{\theta}{2}\right)$$

The photomultiplier collected the light scattered by particles with a zoom lens of 80-200 mm focal length.

The optical arrangement was mounted on a optical bench that could be traversed in three orthogonal directions. The test section was then aligned with respect to the optical arrangement.

2.4.2 Signal processing system

A frequency counter system was used to process the signals obtained from the photomultiplier. The signal quality was constantly monitored on an oscilloscope. The Doppler burst were first amplified and band pass filtered, to remove low frequency pedestal and high frequency noise.

A 3-channel frequency counter (Thermofluids Section 'Model 3' Phase-Doppler Counter (Hardalupas and Laker (1993)) was used for signal processing. Only one of the three available channels was used for the LDA measurements reported in this thesis. The counter made one measurement for every validated Doppler burst detected.

The frequency/velocity data collected was then transferred to a computer, fitted with an interface card (National Instruments AT-DIO-32F). The software processing system displayed and updated results of mean and r.m.s. velocities and included data displaying and plotting utilities. For most measurement locations the ensemble-averaged mean and r.m.s.

velocity values presented below were obtained from 2048 individual velocity realisations.

2.4.3 Validation of results and experimental errors

Several sources of error may be present when the LDA technique is employed. The accuracy and precision of the measurements can be affected principally by:

Location of the control volume

The determination of the location at the measurement volume depends on the accuracy of the traversing mechanisms and the accuracy of the procedure with which the operator places the control volume at a reference point. The accuracies of the traversing table were ±0.05 mm in the X and Y directions and ±0.25 mm in the Z direction.

Seeding

The working fluid needs to be seeded with particles that must follow the flow faithfully, because the LDA measured the instantaneous velocities of these seeded particles. The air was seeded with atomised water particles with diameters below 3 μm (Steventon and Wilson (1979)). Due to the interaction of gravity and drag forces the particles will present a slip velocity, given by:

$$U_T = \left(\frac{4\, d_p\, (\rho_p - \rho)\, g}{3\, \rho\, C_D} \right)^{0.5} \qquad (2.3)$$

where d_p is the mean diameter of the particles in m, ρ_p is the density of the particle in kg/m^3, ρ is the density of the fluid in kg/m^3, g is the acceleration due to gravity in m/s^2 and C_D is the drag coefficient. Using C_D = 10 and 0.44 for laminar and turbulent flows around the particles respectively (Nouri et al 1987b), U_T is respectively 0.032 mm/s and 0.152 mm/s. This slip velocity can be considered negligible and the velocity fidelity of the particles can be considered excellent.

Frequency shift variations

Another possible source of error (Melange (1977)) is a variation of the speed of the diffraction grating used to produce the required frequency shift between the two beams. The fluctuation of the rotational speed of the grating disk was monitored in regular intervals during the tests through the use of a optical tachometer and was found to be less than 1%.

Velocity bias effect

The velocity bias effect can result in the mean velocity estimated from individual realisations being higher than the mean, because the rate of particle arrivals to the control volume can be in direct proportion to the particle velocity. No universally-suitable methods to cancel this type of error have been proposed to date (see Hoesel and Rodi (1977), Durao and Whitelaw (1974), Drain (1980)). No corrections were applied to the data presented in this thesis for velocity bias as the turbulence intensity in most parts of the flows studied was sufficiently high so that bias effects were relatively not significant.

Velocity gradient broadening

Velocity gradient broadening takes place when the control volume is located in positions where the velocity gradients are steep,. Particles moving through different parts of the control volume will have different velocities. These variations of mean velocities may result in errors in the velocity estimates. The errors can be caused by: gradients in mean velocity (σ_G), velocity fluctuations within a measurement volume (σ_F) (being of the same magnitude as σ_G), the finite time taken by the particles to cross the measurement volume (σ_T) and the finite instrument bandwidth (σ_I). Brownian motion and laser linewidth (Durst et al (1976)) may also have an effect. Considering the last two effects negligible (Melling (1997)) the total mean square contribution of the broadening errors, $(\sigma_b)^2$, is given by:

$$(\sigma_b)^2=(\sigma_G)^2+(\sigma_F)^2+(\sigma_T)^2+(\sigma_I)^2 \qquad (2.6)$$

and the measured mean square of fluctuations $(\sigma_D)^2$ is the sum of the actual flow $(\sigma_V)^2$ and the broadening contributions $(\sigma_b)^2$:

$$(\sigma_D)^2=(\sigma_V)^2+(\sigma_b)^2 \qquad (2.7)$$

Particles crossing different parts of the measurement volume will present different velocities, if measurements are made across a velocity gradient this may result in broadening and skewing of the Doppler frequency spectrum, causing errors in both the mean and r.m.s. velocities. These errors can be estimated as follows:

$$\overline{U}_m = \overline{U}_a + \left(\frac{\sigma_{mv}^2}{2}\right)\left(\frac{\partial^2\overline{U}}{\partial r^2}\right)_a \qquad (2.8)$$

and

$$\left(\frac{\mathbf{u}'}{\overline{\mathbf{U}}}\right)_m = \left| \overline{\mathbf{U}}_a + \left(\frac{\sigma_{mv}^{\ 2}}{2}\right)\left(\frac{\partial \overline{\mathbf{U}}}{\partial \mathbf{r}}\right)_a \right| \qquad (2.9)$$

where $\overline{\mathbf{U}}_m$ is the measured mean velocity, $\left(\frac{\mathbf{u}'}{\overline{\mathbf{U}}}\right)_m$ is the measured turbulent intensity, $\overline{\mathbf{U}}_a$ is the true velocity corresponding to a point measurement, and $\sigma_{mv}^{\ 2}$ is the standard deviation of the measurement volume dimension along its long axis.

The error in the velocities will be small if the velocity gradient is nearly linear along the measurement volume, whereas if the mean velocity gradient is steep and non-linear, it will cause a large error in turbulent intensity, particularly if the mean velocity is small or there is a reversed flow. To minimise velocity broadening effects, a small control volume was used.

Statistical errors

Statistical errors in the determination of the measured mean and r.m.s. velocities may arise if an insufficient number of samples is used to calculate the corresponding ensemble average. These errors can be assessed in the manner suggested by Yanta (1973). For a sample size of 2048 a turbulence intensity of 5% (i.e. near the inlet) and a confidence level of 95%, the statistical errors in the determination of the mean and r.m.s. velocities are around 1.5% and 3% respectively.

Finally estimations of the total (overall) error of LDA systems practically identical to the one used in the present study have been carried out by both Cheung (1989) and Suen (1992). They found the overall errors to be 1-5%

for the mean and 5-10% for the r.m.s. velocities respectively. The uncertainties introduced by the different source of errors mentioned are small enough to have a insignificant impact on the measurements of mean velocity and turbulence obtained in the present work.

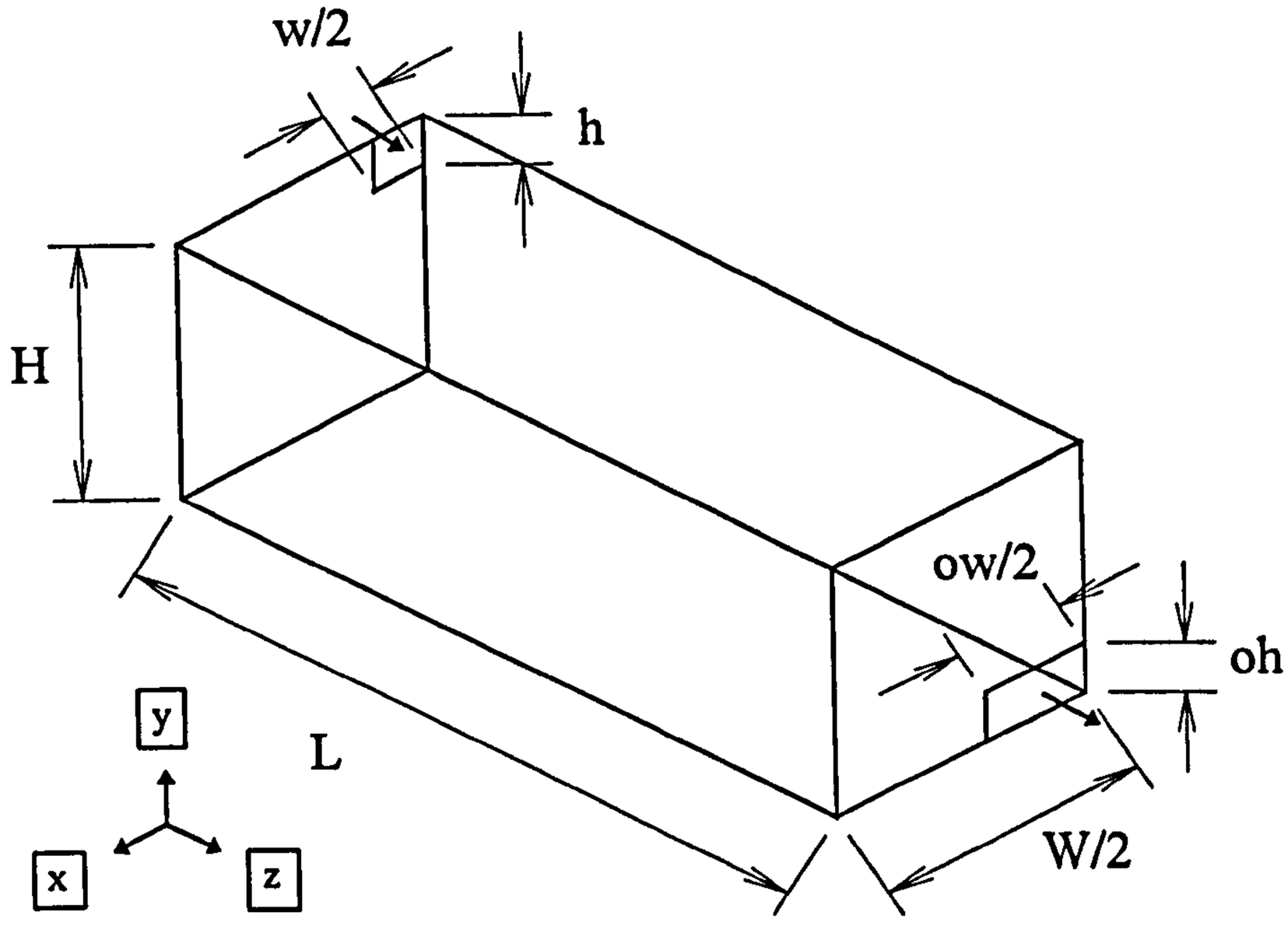

Figure 2.1.(a) Three dimensional view of one-half of the experimental test section-Chamber 1.

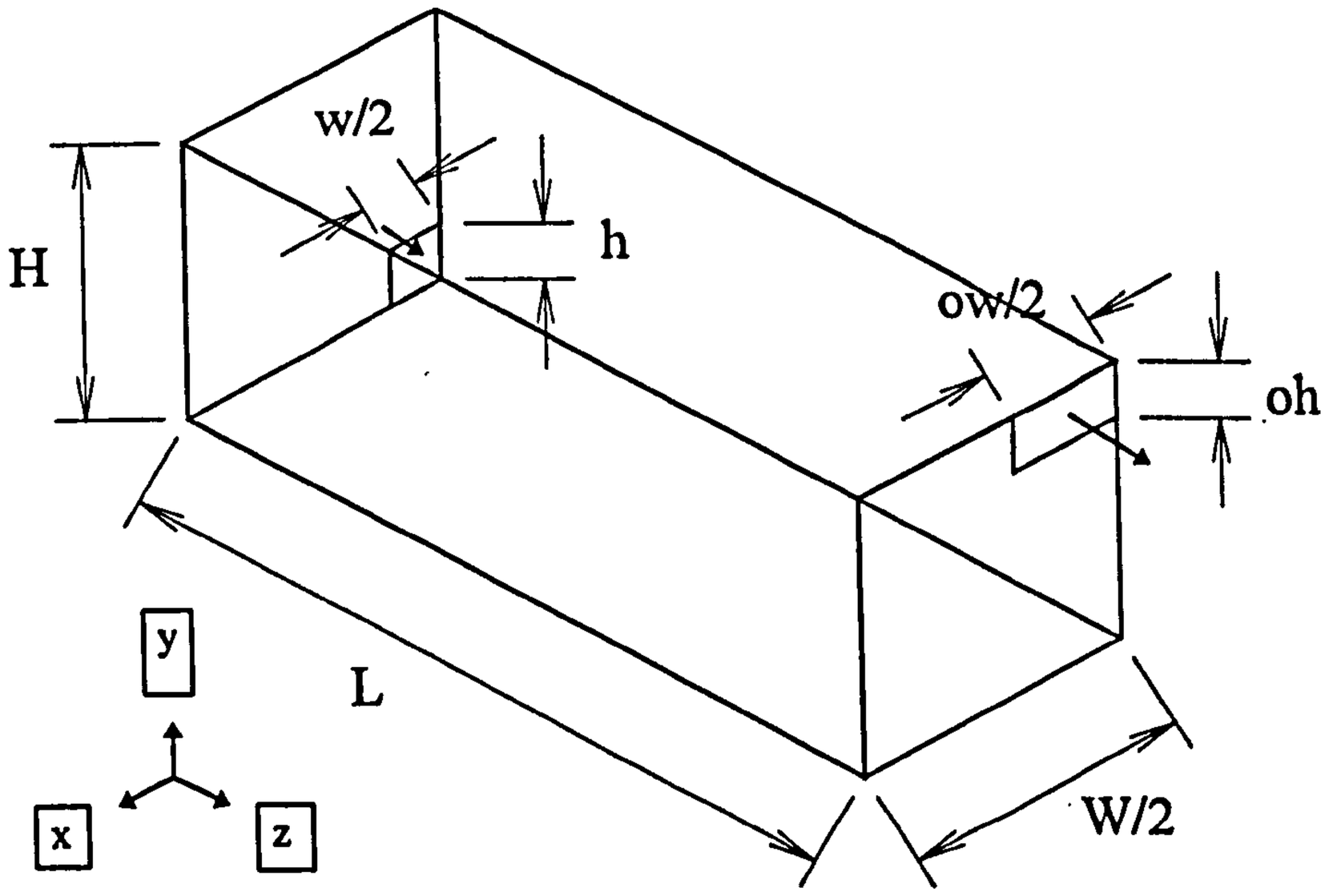

Figure 2.1.(b) Three dimensional view of one-half of the experimental test section-Chamber 2.

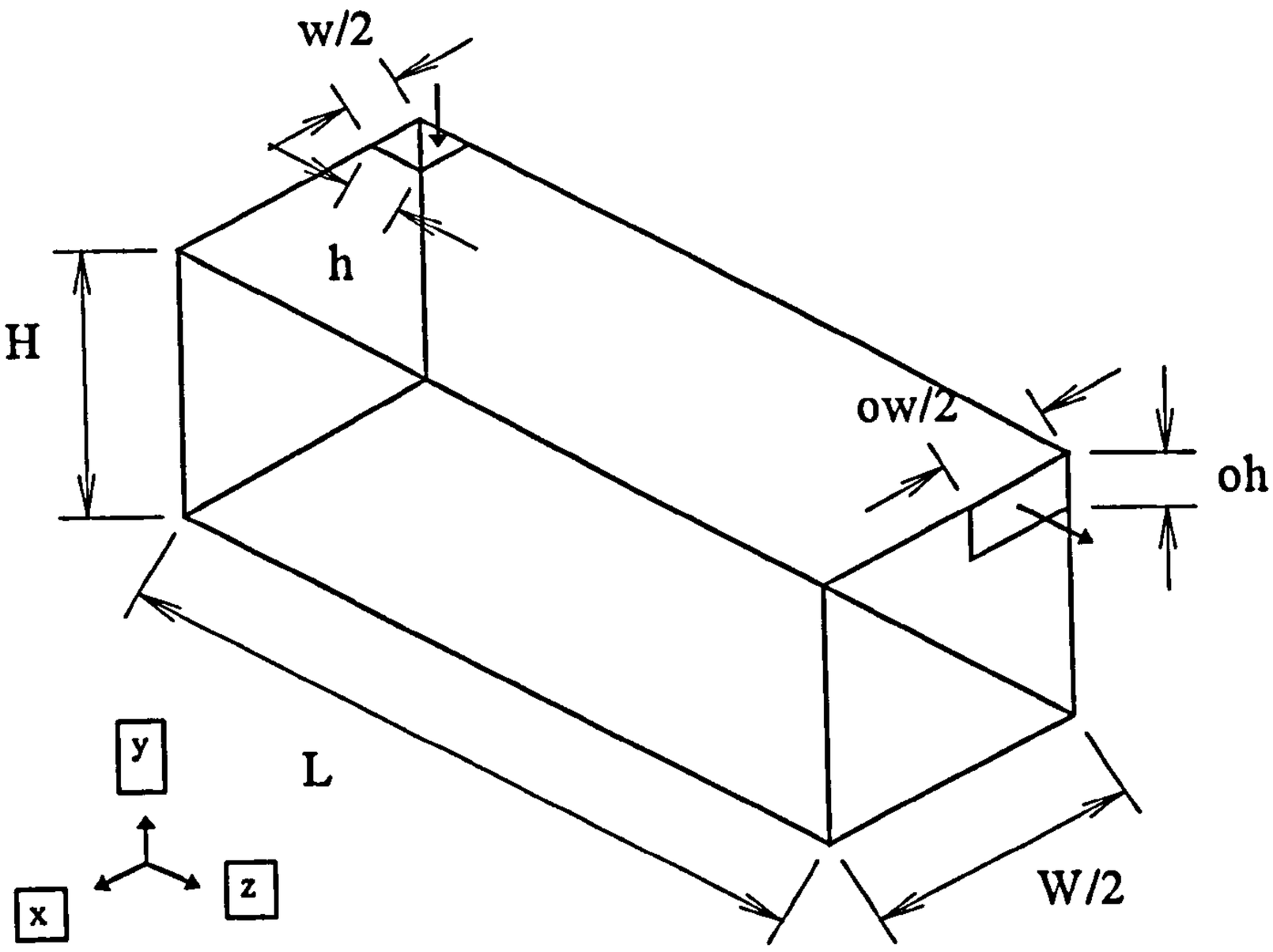

Figure 2.1.(c) Three dimensional view of one-half of the experimental test section-Chamber 3.

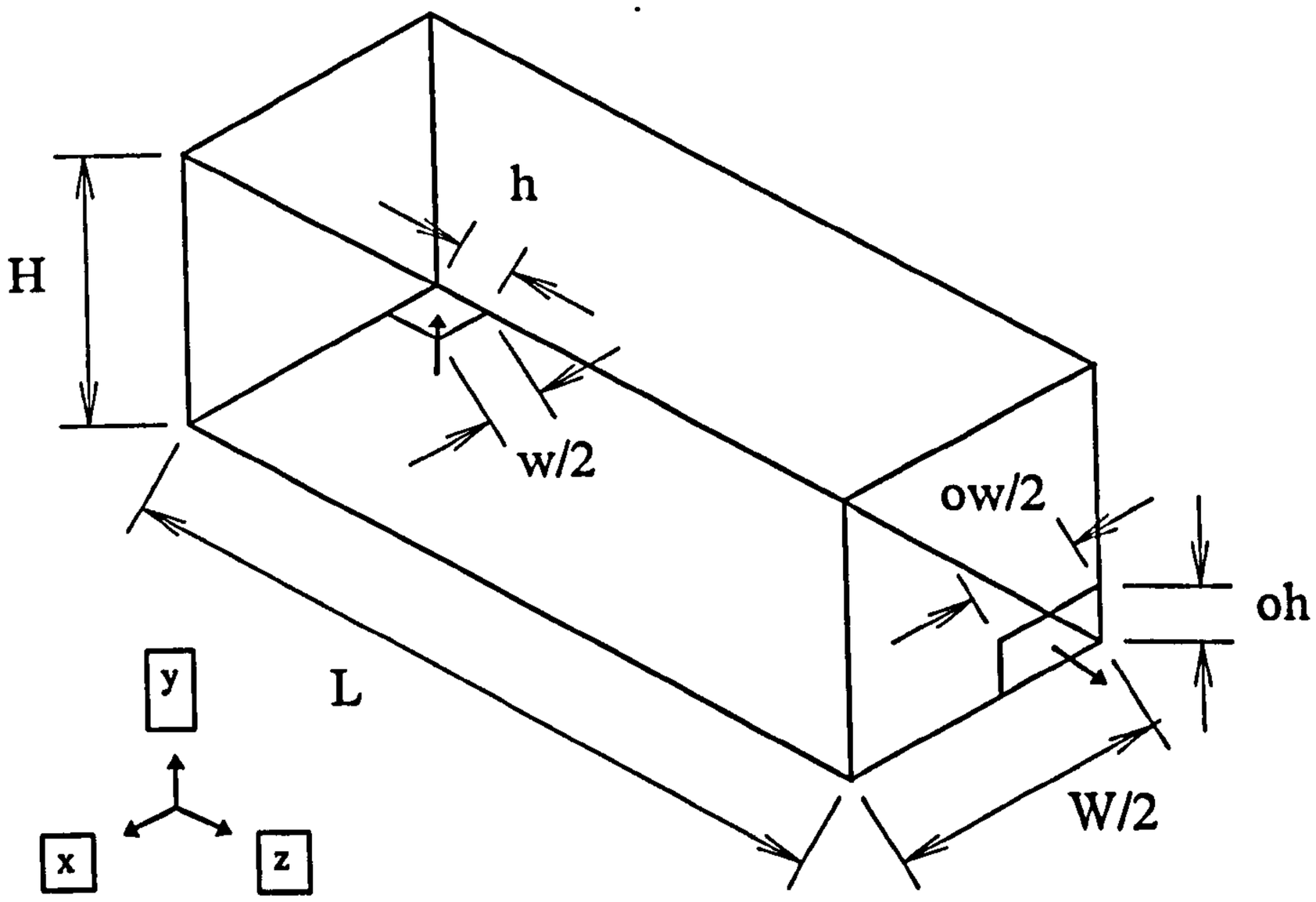

Figure 2.1.(d) Three dimensional view of one-half of the experimental test section-Chamber 4.

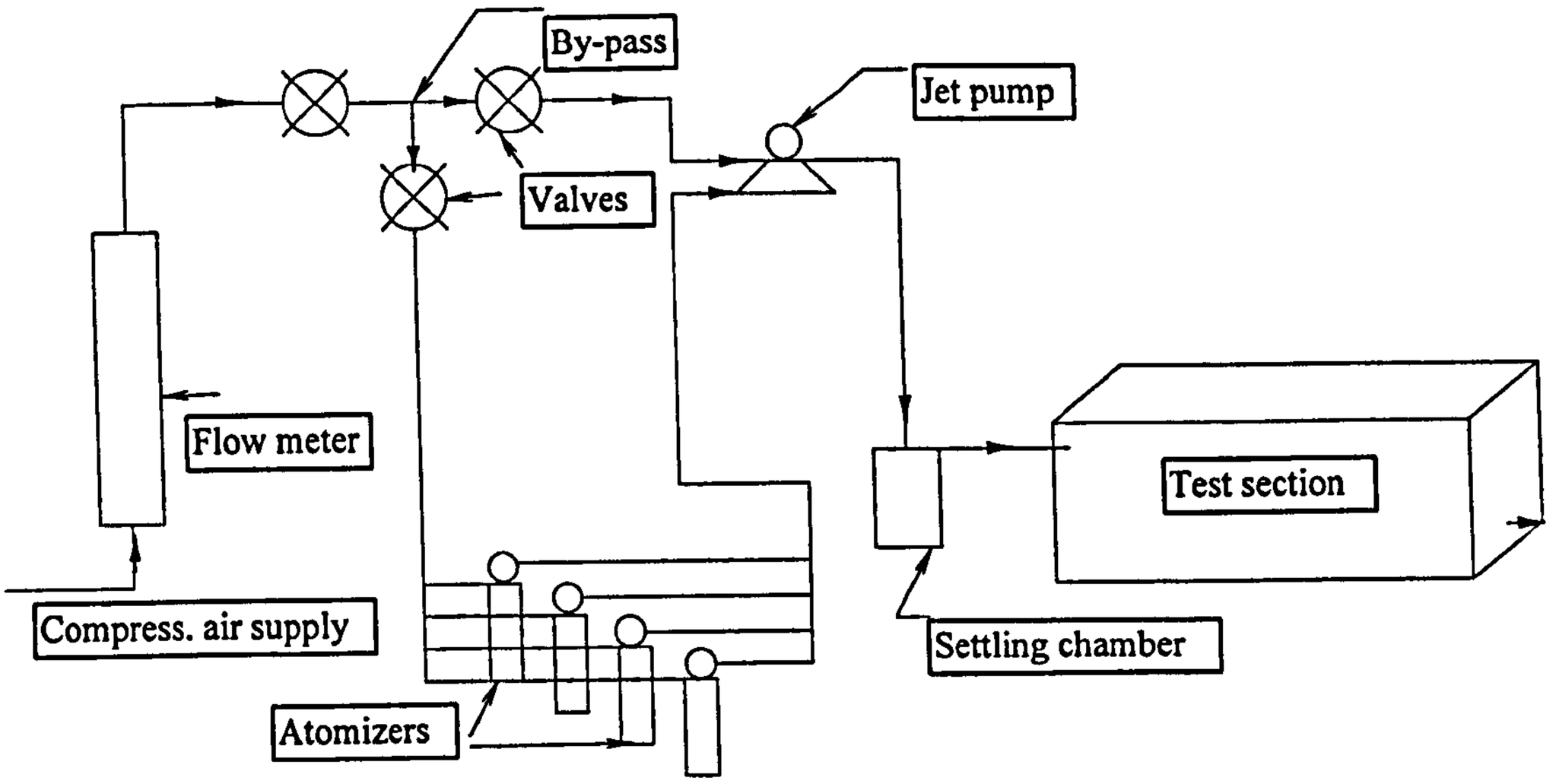

Figure 2.2 Schematic diagram of flow rig.

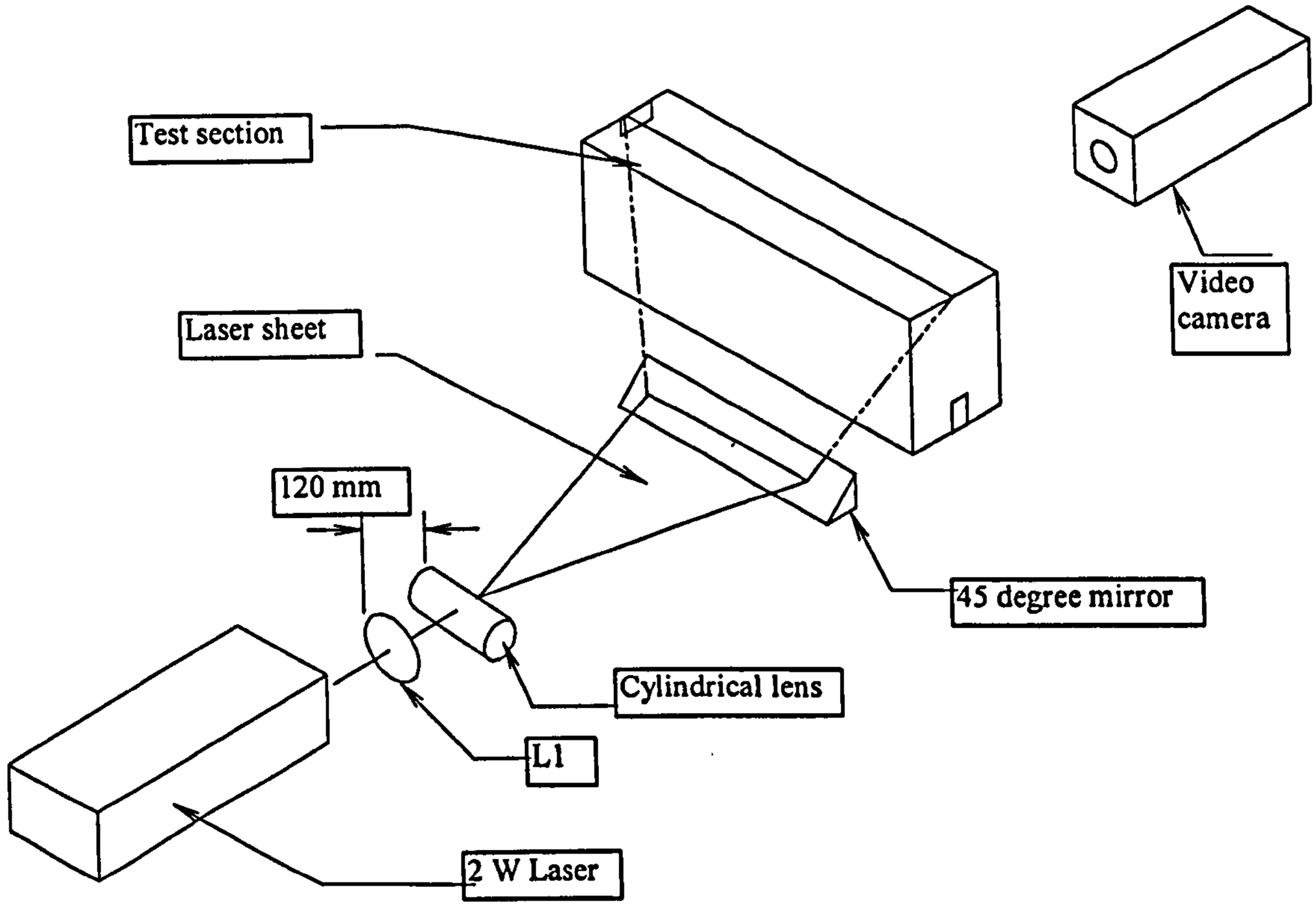

Figure 2.3 Optical arrangement for laser-sheet flow visualisation.

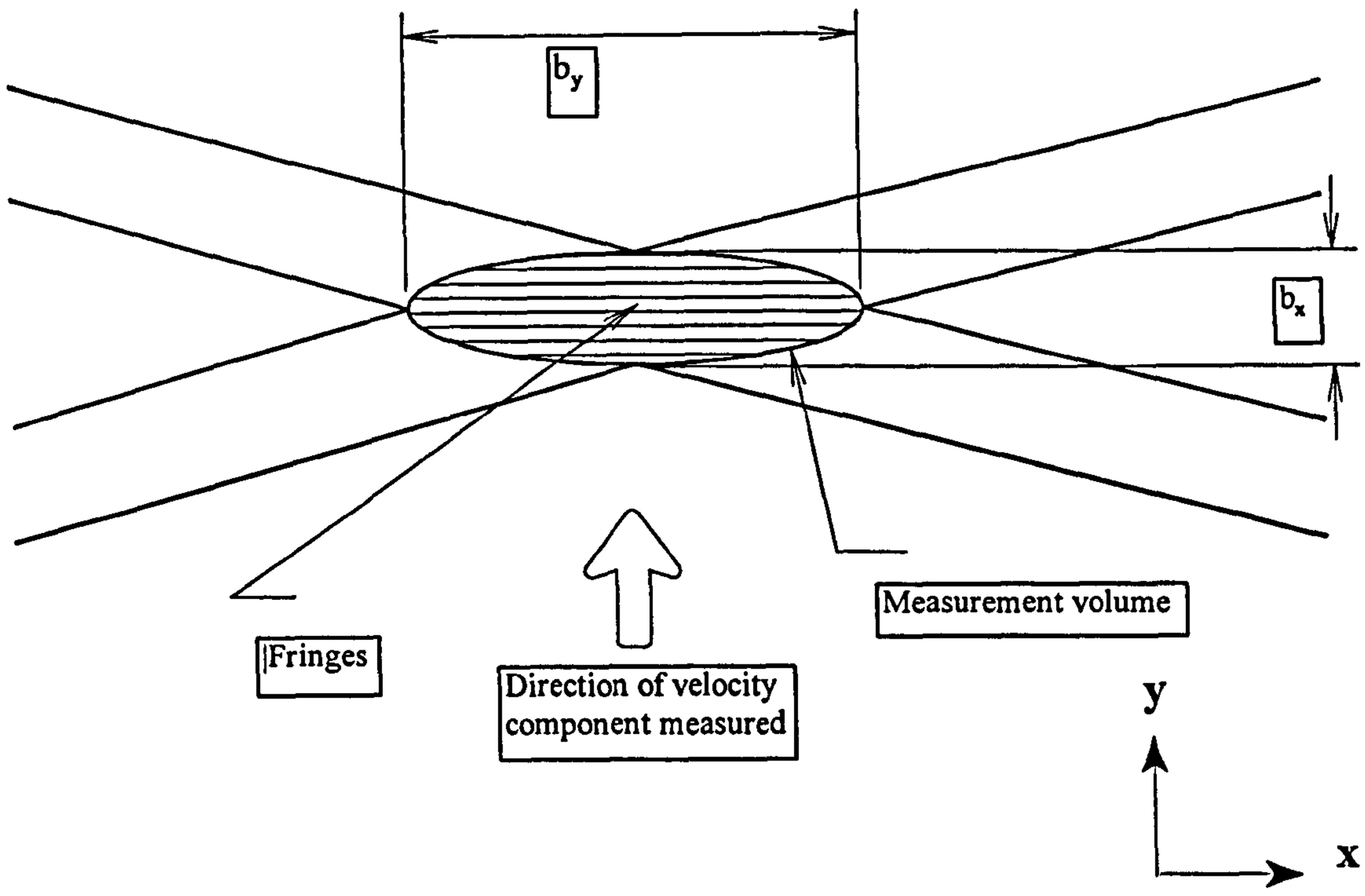

Figure 2.4 Schematic diagram of interference fringe pattern/measurement volume at the intersection of the two laser beams.

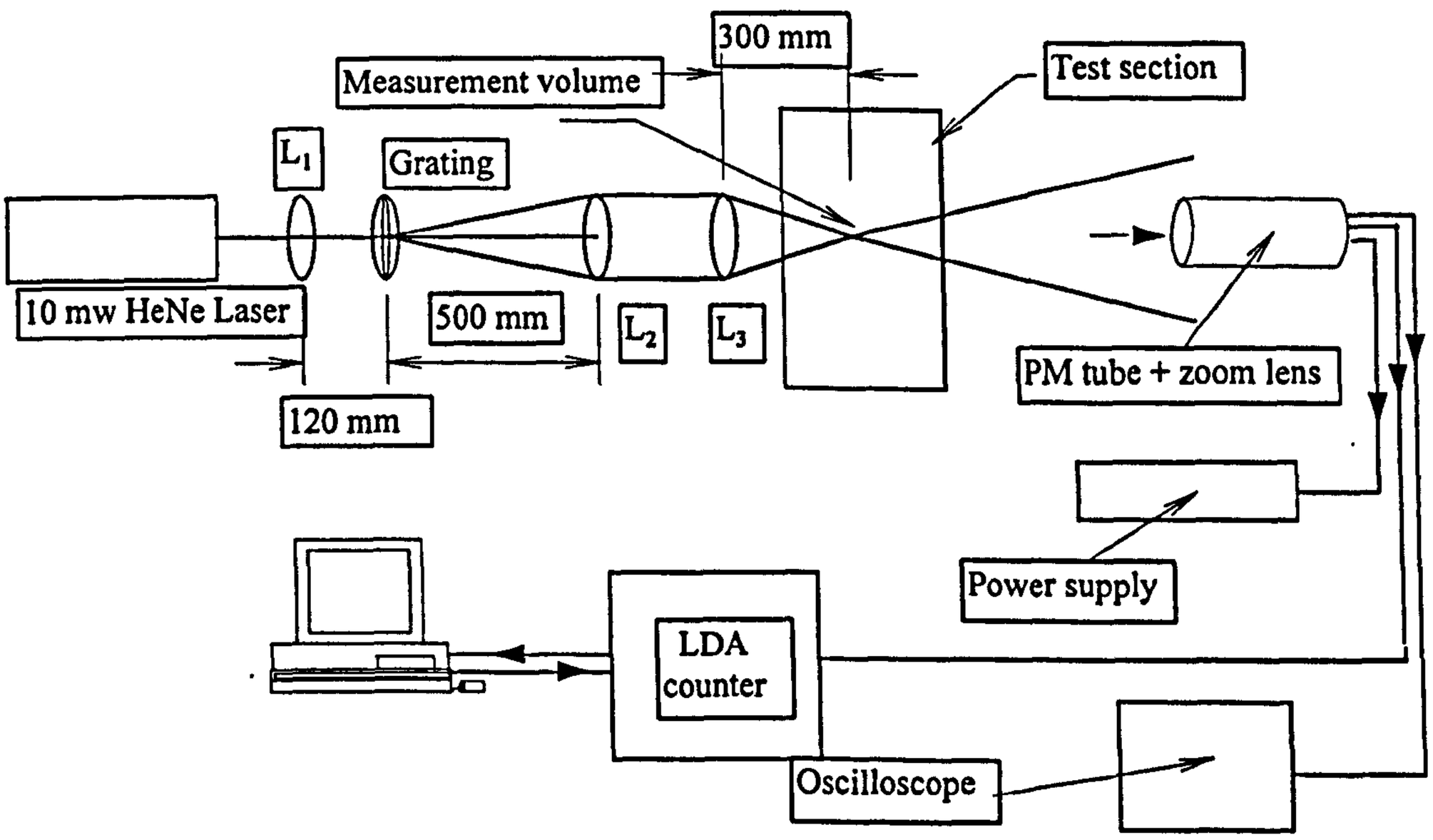

Figure 2.5 Schematic diagram of LDA optical and signal processing systems

CHAPTER 3

THE NUMERICAL METHOD AND THE TURBULENCE MODEL

3.1 Introduction

In this chapter the numerical method, the turbulence models, and the CFD code used are described. The differential equations of conservation of mass, momentum, energy and concentration, as well as the equations of the kinetic energy of turbulence and its rate of dissipation are first transformed, by integration, into a set of algebraic equations, by means of a discretisation method. The algebraic equations are then solved with the CFD code.

Due to the turbulent nature of the air flow in the room a brief description of the turbulence phenomena is included. The air flow inside a room, can considered to be a mixed flow type, with both laminar and turbulent flow present within the occupied space. Calculation of laminar flow is more simple than that of turbulent flow. While the laminar flow can be described exactly in terms of the governing partial differential equations (of the physical quantities (mass, momentum, energy, concentration of species, etc.), the turbulent flow can not be described exactly due to the fluctuations of the same physical quantities, and the interaction between them. Turbulent flow is characterised by random, almost chaotic, fluctuation. The turbulence inside the chambers originated mainly from the shear of the mean flow (if the Reynolds number is sufficiently high). Turbulent flows are still not well understood and can not be described exactly, as most of the physical properties and quantities are fluctuating and constantly interacting (such as velocity, enthalpy, pressure, density, species

concentration, etc.). Mathematically the conservation laws that describe the phenomena, constitute a large set of differential equations, that cannot be solved analytically.

It can be said that the turbulence can be seen as a fluid flow formed by a large quantity of disordered eddies of different sizes. These eddies are stretched by the preferential direction of the mean flow and randomly by interaction with neighbour eddies, causing the breaking of large eddies into smaller ones. Smaller eddies are representatives of high frequencies and large eddies of low frequencies.

The larger the Reynolds number the more significant the amount of small eddies. This means a wider spectrum of frequencies. Therefore for high Reynolds numbers the difference between the low frequency (large eddies) and high frequency (small eddies) is large. The turbulence motion can be described by mean of a three level procedure (Kovasznay (1970)), called the mean motion, a large eddy motion and a small eddy motion. The large eddies need to be properly simulated, because they have a direct interaction with the mean flow and they are primarily responsible for the momentum and heat transport.

During simulation, the size of the numerical grid is normally smaller than the size of the large eddies. The small eddies on the other hand are thought of as an essentially isotropic turbulence carried along by the mean motion and the large eddies.

There are two main methods employed for the prediction of turbulence, the turbulent transport models and the large-eddy simulation. The turbulent transport models treat the dynamic quantities as some sort of statistical average turbulent fields and simulate only the gross features of the

turbulent flow, and are named so because attempts are made to model directly the terms governing the transport of momentum, heat, concentration, etc. Large-eddy simulation attempts to solve the large eddy motion by numerically solving a filtered set of equations governing the three-dimensional time-dependent motion. The sizes of the eddies are chosen so that they can be simulated with the available size of present-day computers. Turbulent transport approximations are then used for the small eddies and the small eddy motion can be modelled independently of the flow geometry. Although the method is very successful, the computational time required to obtain a solution is still very large for practical applications. Although two numerical approaches have been mentioned, turbulence transport models seem to be more suitable in modelling the air flow inside a room, because large-eddy simulation would require prohibitively long computer run times to describe the complex three-dimensional fluid flow and heat transfer processes in a room. In the following sections a brief description of the flow equations, of the two most commonly used turbulence models and of the discretisation schemes is given.

3.2 Mathematical description

The mathematical model described in this chapter is based on the governing equations for fluids dynamics and the former of the two approaches of turbulence modelling.

3.2.1 The flow equations

The equations that describe the fluid movement in a room are the continuity equation, the momentum equation, the energy equation and the concentration equation. Calculations were performed in this work for both

forced and natural convection in ventilated chambers under both steady and transient conditions. All the properties were assumed to be constant and the Boussinesq approximation was used for the air flow calculation in the room. Boussinesq (1877) suggested that the turbulent stresses are proportional to the mean velocity gradients By using this approximation (Gray and Giorgini (1980)) the density is kept constant in all terms except for the body force term.

If U, V and W are the velocity components in the x, y, and z directions respectively, ρ the density and t the time and the air in the chamber is treated as an ideal gas, the differential equations can be written as:

Continuity:

$$\frac{\partial \rho}{\partial t}+\frac{\partial}{\partial x_i}(\rho U_i)=0 \qquad (3.1)$$

Momentum equation:

$$\frac{\partial U_i}{\partial t}+\frac{\partial U_i U_j}{\partial x_j}=-\frac{1}{\rho}\frac{\partial P}{\partial x_j}+\frac{\partial}{\partial x_j}\left[\frac{\mu}{\rho}\left(\frac{\partial U_i}{\partial x_j}+\frac{\partial U_j}{\partial x_i}\right)\right]+\rho F_i \qquad (3.2)$$

Energy equation:

$$\frac{\partial \rho H}{\partial t}+\frac{\partial}{\partial x_j}(\rho U_j H)=\frac{\partial}{\partial x_j}\left(\frac{\lambda}{C_p}\frac{\partial H}{\partial x_j}\right)+S_H \qquad (3.3)$$

Concentration equation:

$$\frac{\partial \rho C}{\partial t}+\frac{\partial}{\partial x_j}(\rho U_j C)=\frac{\partial}{\partial x_j}\left(\rho D\frac{\partial C}{\partial x_j}\right)+S_C \qquad (3.4)$$

In equations (3.3) and (3.4) P is the static pressure, μ is the viscosity of the fluid, ρF_i is the body force term, D is the diffusion coefficient, S_C and S_H are source terms and λ and C_p are the heat conductivity and specific heat of air respectively.

The above equations are non-linear and non-homogeneous, and they are strongly coupled. For this reason it is impossible to solve the set of equations (unless a very simple flow is considered). One way to solve the problem and to study the turbulent aspects of the flow, is to look at the time averaged flow field, by decomposing the dependent variables in the conservation equations, into their mean and fluctuating components and to subsequently average each equation afterwards. The velocity will be treated as a statistical variable and regarded as having a normal distribution. The use of time averaged equations, from the statistical point of view, allows the description of the macroscopic behaviour of turbulent motion.

If the instantaneous quantities in the equation are replaced by the sum of their mean and fluctuating components, the mean conservation equations for turbulent flow will be obtained. If the following terms are defined:

$$\mathbf{U_i = \bar{u}_i + u'_i;} \quad \mathbf{P = \bar{p} + p';} \quad \rho = \bar{\rho} + \rho'; \quad \mathbf{H = \bar{H} + H';}$$
$$\mathbf{C = \bar{C} + C'} \tag{3.5}$$

Where overbars denote mean quantities and primes denote the corresponding fluctuations.

Averaging (3.5)

$\bar{u}_i' = 0; \quad \bar{p}' = 0; \quad \bar{\rho}' = 0; \quad \bar{H}' = 0;$

$\bar{C}' = 0$

If we substitute equation (3.5) in the continuity equation (3.1), the time averaged equation of conservation of mass is

$$\frac{\partial}{\partial x_i}\left(\rho\left(\overline{u_i + u_i'}\right)\right) = 0$$

averaging

$$\frac{\partial}{\partial x_i}\left(\rho u_i\right) = 0 \tag{3.6}$$

In the same manner, substituting equation (3.5) into equations (3.2), (3.3), (3.4) will give

Momentum equation:

$$\frac{\partial \rho u_i}{\partial t} + \frac{\partial\left(\rho u_i u_j\right)}{\partial x_j} = -\frac{\partial \bar{p}}{\partial x_j} + \frac{\partial}{\partial x_j}\left[\mu\left(\frac{\partial u_i}{\partial x_j} + \frac{\partial u_j}{\partial x_i}\right) - \rho\overline{u_i' u_j'}\right] + \rho F_i \tag{3.7}$$

Energy equation:

$$\frac{\partial \rho H}{\partial t} + \frac{\partial}{\partial x_j}\left(\rho u_j H\right) = \frac{\partial}{\partial x_j}\left(\frac{\lambda}{C_p}\frac{\partial H}{\partial x_j} - \left(\overline{\rho H u_j}\right)\right) + S_H \tag{3.8}$$

Concentration equation:

$$\frac{\partial \rho C}{\partial t} + \frac{\partial}{\partial x_j}\left(\rho u_j C\right) = \frac{\partial}{\partial x_j}\left(\frac{\lambda}{C_p}\frac{\partial C}{\partial x_j} - \left(\overline{\rho C u_j}\right)\right) + S_c \tag{3.9}$$

The additional terms appearing in equations (3.7), (3.8), and (3.9) $\overline{\rho u_i u_j}$ and $\overline{\rho H_i u_j}$, $\overline{\rho C_i u_j}$ are called the Reynolds stresses and the turbulent fluxes respectively, while the equations themselves are called the Reynolds equations.

In order to solve the above set of equations an additional equation needs to be solved. Boussinesq (1877) suggested the replacement of the Reynolds stress by an expression containing the turbulent eddy viscosity (μ_t). Several methods have been formulated for the determination of μ_t.

The number of turbulent models available has increased with the growing use of computational techniques for numerical predictions. From all the methods available only two are mentioned in the following sections: the Reynolds stress model and the $\kappa-\varepsilon$ model (including the low Reynolds number $\kappa-\varepsilon$ variant) lines below as they are the most widely used today.

3.2.2 The Reynolds stress model

For complex (recirculating) flows turbulence models may describe inadequately the local state of turbulence, specifically where there is boundary layer separation or reattachment. In this cases the Boussinesq suggestion may fail, the shear stress may vanish where the mean velocity is non-zero and vice versa. The turbulent stress is not directly related to the mean velocity gradients:

$$-\rho\overline{u'_i u'_j} \neq \mu_t\left(\frac{\partial \bar{u}_i}{\partial x_j}+\frac{\partial \bar{u}_j}{\partial x_i}\right)-\frac{2}{3}\delta_{ij}\rho k \qquad (3.10)$$

The set of equations presented in the previous section can describe the turbulent motion, but cannot be solved, because the appearance of the velocity fluctuations makes the set incomplete. In order to solve these equations this deficiency has to be overcome by modelling the stresses. The Reynolds stress models implicitly the transport equations for each one of the Reynolds stresses $-\rho\overline{u'_i u'_j}$.

3.2.3 The κ–ε and low Reynolds number κ–ε models

An exact transport equation can be derived for the turbulent kinetic energy and its dissipation rate from the Navier-Stokes equations (3.1 to 3.4). This new equation increases the number of unknown correlations of the velocity fluctuations. A modelled form, depending on the mean velocity field only, is necessary for the κ and ε equations.

The next step is to find a means to calculate the κ and ε equations. From the Navier-Stokes equations it is possible to derive an exact transport equation for the kinetic energy of turbulence and its dissipation rate so that both are dependent only on the mean velocity field.

If isotropic turbulence is assumed we can write (Boussinesq (1877),

$$-\rho\overline{u'_i u'_j} = \mu_t\left(\frac{\partial \bar{u}_i}{\partial x_j}+\frac{\partial \bar{u}_j}{\partial x_i}\right)-\frac{2}{3}\delta_{ij}\rho k$$

The last term including the Kronecker delta is necessary to fulfil the standard definition of turbulent kinetic energy.

Using the Boussinesq approximation on (3.7) will result in:

$$\frac{\partial}{\partial x_i}(\rho u_i u_j) = -\frac{\partial P}{\partial x_i} + \left[\mu + \mu_t\left[\frac{\partial u_i}{\partial x_j} + \frac{\partial u_j}{\partial x_i}\right]\right] - \frac{2}{3}\rho\delta_{ij}\frac{\partial k}{\partial x_i} + \rho F_i \qquad (3.11)$$

The effective viscosity is defined as

$$\mu_{eff} = \mu + \mu_t \qquad (3.11.a)$$

From (Rodi (1980)), μ_t, can be expressed as:

$$\mu_t = \rho C_\mu \frac{\kappa^2}{\varepsilon} \qquad (3.11.b)$$

and κ and ε as

$$\kappa = \frac{1}{2}\left(\overline{u^2} + \overline{v^2} + \overline{w^2}\right)$$

$$\varepsilon = \frac{\mu_t}{\rho}\left[\overline{\frac{\partial u_i}{\partial x_j}\frac{\partial u_i}{\partial x_j}}\right] \qquad (3.11.c, d)$$

In this way the intensity of the velocity fluctuations is the kinetic energy of turbulence and the mean vorticity times the molecular viscosity arising from them will be described by its dissipation rate. The above assumptions are valid when high Reynolds number flows are considered, where local isotropy in the small scale fluctuation predominates, so the κ and ε equation for the high Reynolds model are as follows (Rodi (1980)):

$$\frac{\partial}{\partial x_i}(\rho u_i \kappa) = -\frac{\partial}{\partial x_i}\left[\frac{\mu_t}{\sigma_\kappa}\frac{\partial \kappa}{\partial x_i}\right] + \left[\mu_t\frac{\partial u_i}{\partial x_j}\left[\frac{\partial u_i}{\partial x_j} + \frac{\partial u_j}{\partial x_i}\right]\right] - C_D\rho\varepsilon \qquad (3.12)$$

$$\frac{\partial}{\partial x_i}(\rho u_i \varepsilon) = -\frac{\partial}{\partial x_i}\left[\frac{\mu_t}{\sigma_\varepsilon}\frac{\partial \varepsilon}{\partial x_i}\right] + \left[C_1\mu_t\frac{\varepsilon}{\kappa}\frac{\partial U_i}{\partial x_j}\left[\frac{\partial U_i}{\partial x_j} + \frac{\partial U_j}{\partial x_i}\right]\right] - C_2\rho\frac{\varepsilon}{\kappa}\varepsilon \qquad (3.13)$$

Where (Launder et al. (1974)):

$$C_\mu = 0.09, \quad C_1 = 1.44, \quad C_2 = 1.92, \quad \sigma_\kappa = 1.0, \quad \sigma_\varepsilon = 1.3, \quad C_D = 1.0$$

The velocity has to be calculated outside the boundary region and the above C values are used in the momentum and turbulence equations. The above approach is valid only when the fluid is fully turbulent and it is located far away from zones in which the fluid flow is affected by viscous effects (boundary layer). If the velocities of the flow need to be calculated close to the wall zones the use of the κ–ε turbulent model is difficult to implement. For these near-wall regions a new different approach is used, the so called κ–ε low Reynolds number turbulence model (LRN). This model takes into consideration the viscous effects. Several forms of such methods can be found in the related literature (see e.g. Patel et al (1985)). Patel et al. (1985) reviewed the existing low Reynolds number models and concluded that there is a lack of a physical basis in the modifications of the basic high Reynolds number models. The different methods were compared for different flows and it was not clear which of the models could be used with confidence. They concluded that the models of Launder and Sharma (1974), Chien (1982) and Lam and Bremhorst (1981) which are based on the κ–ε model, and of Wilcox and Rubesin (1980), performed considerably better than the other models reviewed. However even these methods needed further revisions in order to be used for the calculation of near wall and low Reynolds number flows.

For the present numerical calculations a version of the low Reynolds method proposed by Lam and Bremhorst (1981) is used for the transport equations of kinetic energy and the dissipation rate of turbulence:

$$\frac{D\kappa}{Dt} = \frac{\partial}{\partial x_j}\left[\left(\frac{\nu_t}{\sigma_t} + \nu_t\right)\frac{\partial \kappa}{\partial x_j}\right] + \nu_t\left(\frac{\partial u_i}{\partial x_j} + \frac{\partial u_j}{\partial x_i}\right)\frac{\partial u_i}{\partial x_j} - \varepsilon \qquad (3.14)$$

$$\frac{D\varepsilon}{Dt} = \frac{\partial}{\partial x_j}\left[\left(\frac{\nu_t}{\sigma_t} + \nu_t\right)\frac{\partial \varepsilon}{\partial x_j}\right] + C_1 f_1 \nu_t \frac{\varepsilon}{\kappa}\left(\frac{\partial u_i}{\partial x_j} + \frac{\partial u_j}{\partial x_i}\right)\frac{\partial u_i}{\partial x_j} - C_2 f_2 \frac{\varepsilon^2}{\kappa} \qquad (3.15)$$

The eddy viscosity is used to determine the time-averaged flow field as follows:

$$\mu_t = \nu_t C_\mu f_\mu \kappa^2 / \varepsilon \qquad (3.16)$$

where

$$\sigma_\kappa = 1.0, \quad \sigma_\varepsilon = 1.3, \quad C_1 = 1.44, \quad C_2 = 1.92, \quad C_\mu = 0.09$$

The above equations represent the general form of those given by Launder and Spalding (1974), where the functions f_1, f_2 and f_μ are assumed to be equal to one (Chen 1990). This assumption cannot be valid within a laminar sublayer or in low Reynolds number flows, for which the functions f_1, f_2 and f_μ are given by the following equations (Chen 1990),

$$f_\mu = \left(1 - e^{-A_\mu R_\mu}\right)^2 \left[1 + \frac{A_t}{R_t}\right]$$

$$f_1 = 1 + \left[\frac{A_{c1}}{f_\mu}\right]^3 \qquad (3.16.1)$$

$$f_2 = 1 - e^{-R_t^2}$$

where R_κ and R_t are the turbulence Reynolds numbers, and $A_\mu = 0.0165$, $A_t = 20.5$ and $A_{c1} = 0.05$.

It can be seen that the low Reynolds turbulent κ–ε model is similar to the standard κ–ε one. Only small differences can be found in the values used for the constants. If the flow is fully turbulent both methods will show identical results (Skovgaard (1991)).

3.3 Discretisation of the differential equations

Each one of the equations governing the forced and natural convection phenomena inside the ventilated chamber, namely the conservation equations for mass, momentum, energy can be represented by the general form:

$$\frac{\partial}{\partial x_i}(\rho \mathbf{U}_i \Phi) = \left[\Gamma_\Phi \frac{\partial \Phi}{\partial x_i}\right] + \mathbf{S}_\Phi \qquad (3.17)$$

Where the dependent variable Φ may be any of the following: Velocity component U, V, W (in the x, y, z directions respectively), enthalpy H or concentration C. Two additional equations are solved for the turbulence energy κ and the rate of dissipation of κ, ε. The coefficients Γ_Φ and S_Φ corresponding to each of these dependent variables as well as the empirical coefficients appearing in the turbulence model are tabulated below.

Source terms in the transport equations.

Equation	ϕ	Γ_ϕ	S_Φ
Continuity	1	0	0
i-direction momentum	u_i	μ_{eff}	$-\frac{\partial P}{\partial x_i}+\frac{\partial}{\partial x_j}\left[\mu_{eff}\left[\frac{\partial u_i}{\partial x_j}+\frac{\partial u_j}{\partial x_i}\right]\right]+\rho\beta g\phi$
Thermal energy	H	μ_{eff}/σ_H	s_H
Turbulence energy	κ	μ_{eff}/σ_κ	$G-\rho\varepsilon+G_B$
Turbulence dissipation	ε	$\mu_{eff}/\sigma_\varepsilon$	$\left[\varepsilon\left(C_1 f_1 G-C_2 f_2 \rho\varepsilon\right)/\kappa\right]+C_3\frac{\varepsilon}{\kappa}G_B$
Concentration	C	μ_{eff}/σ_c	s_C

where:

$$G=\mu_t\left(\frac{\partial u_i}{\partial x_j}+\frac{\partial u_j}{\partial x_i}\right)\frac{\partial u_i}{\partial x_j}$$

The buoyancy source or production term in the κ and ε transport equations is given by:

$$G_B=\frac{\beta}{C_P}g_i\frac{\mu_t}{\sigma_{H,t}}\frac{\partial\theta}{\partial x_i}$$

where θ is the excess temperature ($T-T_r$) and

T_r is the reference temperature,

The turbulence model constants are:

Constant name	standard κ–ε model	low Reynolds κ–ε model
C_μ	0.09	0.09
C_1	1.44	1.44
C_2	1.92	1.92
C_3	-	
σ_κ	1.3	1.3
σ_ε	1.0	1.0
f_μ	1.0	$\mathbf{f_\mu = \left(1-e^{-A_\mu R_\mu}\right)^2\left[1+\frac{A_t}{R_t}\right]}$
f_1	1.0	$\mathbf{f_1 = 1+\left[\frac{A_{c1}}{f_\mu}\right]^3}$
f_2	1.0	$\mathbf{f_2 = 1-e^{-R_t^2}}$

The equations shown above describe fluid flow under isothermal and incompressible conditions. The set of equations is non-homogeneous, non-linear and strongly coupled. Due to this reason an analytical solution is too difficult to achieve, and the only option is the use of numerical solution techniques to solve the set of equations.

Due to the elliptic nature of the governing equations, the localised perturbations influence the whole solution domain. This means that in order to obtain a unique solution that will depend continuously on the boundary conditions, a set of boundary conditions must be provided at all boundaries for all dependent variables. In an elliptic flow a solution for all variables is obtained simultaneously; this differs from a parabolic solution

where it is possible to obtain a local solution for a point adjacent to a boundary by a series of expansions.

The finite volume method (FVM) was used for the solution of the governing equations (Patankar (1980)). The method works by replacing the continuous values of the variables contained in the exact solution of the differential equation by discrete values. There are other two methods that can be compared with FVM. These are the finite difference method (FDM), and the finite element method (FEM). One of the advantage of FVM is that it allows a direct physical interpretation of the variables and together with the overall integration of the governing equations make the method more appropriated to cover the objectives of this thesis.

A series of steps is followed to achieve the numerical solution of the governing equations. The solution includes only the relevant steps necessary to achieve a solution for the problem being studied in this work. A more extensive description of the finite volume technique can be found in Patankar (1980) and Launder and Spalding (1974).

A discretisation grid is used. Over each point of the grid the different variables will be calculated see (Figure 3.1). The grid can be uniform or non-uniform and the selection will be based on the type of problem to be solved, for example, by allowing small spacing in zones where steep gradients are expected.

The domain is separated into a finite number of cells (volumes). In each cell all variables are represented by means of values located over the grid in the mesh of computational cells. By means of integration of the governing general equations a set of algebraic equations is then obtained.

This set of equations is then solved by applying appropriate boundary conditions.

The letter P represents the node at the centre of the cell and, N, S, E, W, H and L are the centres of the neighbouring cells (termed the North, South, East, West, High and Low cells respectively). The letters n, s, e and w denote the location of the interfaces between adjacent cells. For simplicity, the control volume boundaries of all the grid cells used in this thesis were located half-way between the grid nodes.

All scalar variables (e.g. temperature and pressure) are stored at the grid nodes in the centres of the control volumes while the velocity components are stored at staggered locations coinciding with the boundaries of the control volume. The use of the staggered grid ensures that the velocities lay between the pressures that induce them and are directly available for calculating the convective fluxes of scalar flow variables. The staggered grid and the velocity components are shown in Figure 3.2.

The general equation is then integrated over a control volume (cell) in the solution domain:

$$\int_v \frac{\partial}{\partial x_i}(\rho \mathbf{U}_i \Phi)\mathbf{dV} = \int_v \frac{\partial}{\partial x_i}\left[\Gamma_\Phi \frac{\partial \Phi}{\partial x_i}\right]\mathbf{dV} + \int_v \mathbf{S}_\Phi \mathbf{dV} \qquad (3.18)$$

Convection term | Diffusion term | Source term

In the following sections the discretisation of the general equation is presented for each one of the terms that form it. For simplicity, only two dimensions will be considered. Although three dimensions were used in all

of the calculations, the discretisation, method applies for both two and three-dimensional analysis.

3.3.1 Discretisation of the convective term

The convection term on the general equation (3.18) is integrated with respect to x, y and t over the staggered control volume (Figure 3.2):

$$\int_t^{t'}\int_s^n\int_w^e \left[\frac{\partial(\rho u\phi)}{\partial x}+\frac{\partial(\rho v\phi)}{\partial y}\right] dx\, dy\, dt \tag{3.19}$$

Using the central differencing scheme (discussed below), a linear variation is assumed between the grid nodes. At the interface the value of ϕ is:

$$\begin{aligned} \phi_e &= \frac{1}{2}(\phi_E-\phi_p) \quad \phi_w = \frac{1}{2}(\phi_p-\phi_W) \\ \phi_n &= \frac{1}{2}(\phi_N-\phi_p) \quad \phi_s = \frac{1}{2}(\phi_p-\phi_S) \end{aligned} \tag{3.20}$$

Substituting (3.20) into equation (3.19) after integration

$$\begin{aligned} &\frac{\rho u_e}{2}\Delta Y\int_t^{t'}(\phi_E+\phi_p)\,dt - \frac{\rho u_w}{2}\Delta Y\int_t^{t'}(\phi_p+\phi_W)\,dt + \\ &\frac{\rho u_n}{2}\Delta Y\int_t^{t'}(\phi_N+\phi_p)\,dt - \frac{\rho u_s}{2}\Delta X\int_t^{t'}(\phi_p+\phi_s)\,dt = 0 \end{aligned} \tag{3.21}$$

Equation (3.21) represents the integration of the control volume for the convective term. The solution of the time integral is explained in section 3.3.5.

3.3.2 Discretisation of the diffusion term

If only two dimensions are considered the diffusion term can be written as

$$\Gamma\left[\frac{\partial^2\phi}{\partial x^2}+\frac{\partial^2\phi}{\partial y^2}\right]=0 \qquad (3.22)$$

If $\Gamma=\kappa/C_p$ and multiplying (3.22) by C_p, the equation becomes

$$\kappa\left[\frac{\partial^2\phi}{\partial x^2}+\frac{\partial^2\phi}{\partial y^2}\right]=0 \qquad (3.23)$$

If κ is constant and integrating (3.23) with respect to x, y, t over the control volume of Figure 3.1, the diffusion term becomes:

$$\int_t^{t'}\int_s^n\int_w^e\left[\frac{\partial^2\phi}{\partial x^2}+\frac{\partial^2\phi}{\partial y^2}\right]dx\,dy\,dt=0 \qquad (3.24)$$

where $t' = t + \Delta t$

If we integrate over the control volume $\frac{\partial\phi_i}{\partial x_i}=\frac{\Delta\phi_i}{\delta x_i}$:

$$k\int_t^{t'}\left(\frac{(\Delta\phi)_e}{\delta X_e}\Delta Y-\frac{(\Delta\phi)_w}{\delta X_w}\Delta Y+\frac{(\Delta\phi)_n}{\delta X_n}\Delta X-\frac{(\Delta\phi)_s}{\delta X_s}\Delta X\right)dt=0 \qquad (3.25)$$

where:

$$
\begin{aligned}
(\Delta\phi)_e &= \phi_E - \phi_p \\
(\Delta\phi)_w &= \phi_p - \phi_W \\
(\Delta\phi)_n &= \phi_N - \phi_p \\
(\Delta\phi)_s &= \phi_p - \phi_S
\end{aligned}
\tag{3.26}
$$

Combining (3.26) and (3.25) the diffusion term becomes

$$
\begin{aligned}
&\frac{k_e}{\delta X_e}\Delta Y\int_t^{t'}\left(\phi_E-\phi_p\right)dt - \quad \frac{k_w}{\delta X_w}\Delta Y\int_t^{t'}\left(\phi_p-\phi_W\right)dt + \\
&\frac{k_n}{\delta X_n}\Delta Y\int_t^{t'}\left(\phi_N-\phi_p\right)dt - \quad \frac{k_s}{\delta X_s}\Delta Y\int_t^{t'}\left(\phi_p-\phi_S\right)dt = 0
\end{aligned}
\tag{3.27}
$$

3.3.3 Discretisation of the transient term.

Following the same procedure as for the integration of the diffusion term, the transient term in the general equation can be integrated over a control volume (Figure 3.1). Dividing by C_p, the transient terms will be expressed as follows:

$$
\rho_0\int_t^{t'}\int_s^n\int_w^e\left[\frac{\partial\phi}{\partial t}\right]dx\,dy\,dt = 0 \tag{3.28}
$$

$$
\rho_0\,\Delta X\,\Delta Y\int_t^{t'}\frac{\partial\phi}{\partial t}dt = 0
$$

$$
\rho_0\,\Delta X\,\Delta Y\left(\phi'-\phi^0\right) = 0
$$

where ϕ^0 represents the variable at the centre of the control volume (P) at time t and, ϕ' the same variable at time $t + \Delta t$. Therefore all ϕ' s can be substituted by $\phi^0 = \phi^0{}_p$ and $\phi^0 = \phi'_p$ so that:

$$\rho_0 \, \Delta X \, \Delta Y \left(\phi_p^{'} - \phi_p^{0} \right) = 0 \tag{3.29}$$

3.3.4 Discretisation of the source term

The source term is considered to have a linear variation between adjacent nodes:

$$S_\phi = C_x \left(V_x - \phi_p \right) + C_y \left(V_y - \phi_p \right) \tag{3.30}$$

where C_x and C_y are the coefficients in the x and y directions, and

V_x and V_y are the values in the x and y directions.

In order to set the boundary conditions or the internal sources on the transport equation, the above values and coefficients are used. This will be discussed below.

The source term then is substituted from equation (3.30) and integrating over the control volume (Figure 3.1) over x, y and t:

$$\int_t^{t'} \int_s^n \int_w^e \left[C_x \left(V_x - \phi_p \right) + C_y \left(V_y - \phi_p \right) \right] dx \, dy \, dt = 0 \tag{3.31}$$

$$C_x \, V_x \, \Delta Y \, \Delta t + C_y V_y \, \Delta X \, \Delta t - C_x \, \Delta Y \int_t^{t'} \phi_p \, dt - C_y \, \Delta X \int_t^{t'} \phi_p \, dt = 0 \tag{3.32}$$

$$\int_V S_\Phi dV = \int_V \left(S_p \Phi_p + S_c \right) dV = \left(S_p \Phi_p + S_c \right) \Delta x \, \Delta y \, \Delta z \tag{3.33}$$

3.3.5 Solution of the time integrals.

This section is concern with the solution of the time integrals that must satisfy the overall discretisation method and the differential equations. The following equation is used to solve the time integrals:

$$\int_t^t \phi_p \, dt = \left[f\phi_p^{'} + (1-f)\phi_p^0 \right] \Delta t \qquad (3.34)$$

Where f varies between 0 and 1 and its value must be chosen so that the coefficients of the algebraic equations (see following section 3.4) are always positive. If negative coefficients are found, physically unrealistic results could result. By adopting the fully-implicit scheme, negative coefficients are avoided. This scheme uses a value of f equal to unity in equation (3.34), satisfying simplicity and physically realistic behaviour. By substituting (3.34) into (3.27) the diffusion term becomes:

$$\begin{aligned}
&\frac{k_e}{\delta X_e} \Delta Y \, \Delta t \left[\left(f\phi_E^{'} + (1+f)\phi_E^0 \right) - \left(f\phi_p^{'} + (1+f)\phi_p^0 \right) \right] - \\
&\frac{k_w}{\delta X_w} \Delta Y \, \Delta t \left[\left(f\phi_p^{'} + (1+f)\phi_p^0 \right) - \left(f\phi_W^{'} + (1+f)\phi_W^0 \right) \right] + \\
&\frac{k_n}{\delta Y_n} \Delta X \, \Delta t \left[\left(f\phi_N^{'} + (1+f)\phi_N^0 \right) - \left(f\phi_p^{'} + (1+f)\phi_p^0 \right) \right] - \\
&\frac{k_s}{\delta Y_s} \Delta X \, \Delta t \left[\left(f\phi_p^{'} + (1+f)\phi_p^0 \right) - \left(f\phi_S^{'} + (1+f)\phi_S^0 \right) \right] = 0
\end{aligned} \qquad (3.35)$$

By using f = 1 (full-implicit scheme),

$$\frac{k_e}{\delta X_e}\Delta Y\ \Delta t\left(\phi'_E-\phi'_p\right)-\frac{k_w}{\delta X_w}\Delta Y\ \Delta t\left(\phi'_p-\phi'_W\right)+$$
$$\frac{k_n}{\delta Y_n}\Delta X\ \Delta t\left(\phi'_N-\phi'_p\right)-\frac{k_s}{\delta Y_s}\Delta X\ \Delta t\left(\phi'_p-\phi'_S\right) \qquad (3.36)$$

Following the same procedure for equation (3.21) and (3.33) for the convective and source term, we obtain respectively:

Convection term:

$$\frac{\rho u_e}{2}\Delta Y\ \Delta t\left(\phi'_E-\phi'_p\right)-\frac{\rho u_w}{2}\Delta Y\ \Delta t\left(\phi'_p-\phi'_W\right)+$$
$$\frac{\rho v_N}{2}\Delta X\ \Delta t\left(\phi'_N-\phi'_p\right)-\frac{\rho v_S}{2}\Delta X\ \Delta t\left(\phi'_p-\phi'_S\right) \qquad (3.37)$$

Source term:

$$C_x V_x\ \Delta Y\ \Delta t+C_y V_y\ \Delta X\ \Delta t-C_x\ \Delta Y\ \Delta t\left(\phi'_p\right)-C_y\ \Delta X\ \Delta t\left(\phi'_p\right)=0 \qquad (3.38)$$

Equations (3.29), (3.36), (3.37) and (3.38) are the discretized terms for the general differential equation (3.18). Regrouping these terms into the general equation, and including the new variables listed below, the general equation can be rewritten as:

$$\phi'_i = \phi_i$$
$$\frac{k}{C_p} = \Gamma_i$$
$$\frac{\Gamma_i}{\delta X_i} = D_i$$
$$(\rho u)_i = F_i$$

where i = n, s, e, w, p

$$\phi_p\left[\begin{array}{l}\left(\frac{F_e}{2}+D_e\right)\Delta Y-\left(\frac{F_w}{2}+D_w\right)\Delta Y+\left(\frac{F_n}{2}+D_n\right)\Delta X+\left(\frac{F_s}{2}+D_s\right)\Delta X \\ +C_x\,\Delta Y+C_y\,\Delta X+\dfrac{\rho_0\,\Delta X\,\Delta Y}{\Delta t}\end{array}\right]=$$

$$\left(-\frac{F_e}{2}+D_e\right)\Delta Y\,\phi_E+\left(\frac{F_w}{2}+D_w\right)\Delta Y\,\phi_W+\left(-\frac{F_n}{2}+D_n\right)\Delta X\,\phi_N+$$

$$\left(\frac{F_s}{2}+D_s\right)\Delta X\,\phi_S+C_xV_x\,\Delta Y+C_yV_y\,\Delta X+\frac{\rho_0\,\Delta X\,\Delta Y}{\Delta t}\,\phi_p^0$$

The coefficients are defined as follows:

$$a_E=\left(-\frac{F_e}{2}+D_e\right)\Delta Y \qquad a_N=\left(-\frac{F_n}{2}+D_n\right)\Delta X$$

$$a_W=\left(\frac{F_w}{2}+D_w\right)\Delta Y \qquad a_S=\left(\frac{F_s}{2}+D_s\right)\Delta X$$

$$a_p^0=\frac{\rho_0\,\Delta X\,\Delta Y}{\Delta t} \qquad b=C_xV_x\,\Delta Y+C_yV_y\,\Delta X+a_p^0\,\phi_p^0$$

$$a_p=\left(\frac{F_e}{2}+D_e\right)\Delta Y-\left(\frac{F_w}{2}+D_w\right)\Delta Y+\left(\frac{F_n}{2}+D_n\right)\Delta X+\left(\frac{F_s}{2}+D_s\right)\Delta X$$

$$+C_x\,\Delta Y+C_y\,\Delta X+\frac{\rho_0\,\Delta X\,\Delta Y}{\Delta t}$$

The equation can then be rewritten in the following form

$$a_p\phi_p=a_E\phi_E+a_W\phi_W+a_N\phi_N+a_S\phi_S+b \qquad (3.39)$$

This equation represents the discretized equation for two dimensions. In similar fashion, for three dimensions (3.39) can be written as

$$a_p\phi_p=a_E\phi_E+a_W\phi_W+a_N\phi_N+a_S\phi_S+a_H\phi_H+a_L\phi_L+b \qquad (3.40)$$

Where the a's represent the coefficients and the source term.

3.4 Differencing schemes

During the process of discretisation several assumptions were made in order to obtain the set of algebraic equations. These assumptions need to be assessed in order to validate their accuracy. This section deals mainly with two of those assumptions; the integration of the velocity field over a staggered grid and the linear variation assumed between adjacent nodes.

When a linear variation is assumed, the solution is approximated to that of the real fluid flow behaviour. In order to assess the true behaviour an analytical solution must be used. Due to the complexity of the problem analytical solutions are difficult, if not impossible, to obtain. A way around this problem is the use of a one dimensional case that is easy to compare with an exact analytical solution. Following this line, the convective and diffusive terms are taken from the general equation, which can be written as follows,

$$\frac{\mathbf{d}}{\mathbf{dx}}(\rho \mathbf{u}\phi) = \frac{\mathbf{d}}{\mathbf{dx}}\left(\Gamma \frac{\mathbf{d}\phi}{\mathbf{dx}}\right) \tag{3.41}$$

If the variable x is in the range $0 \leq \mathbf{x} \leq \mathbf{L}$ and Γ and (ρu) have constant values, the boundary conditions are:

$$\phi = \phi_0 \quad \text{at} \quad x = 0$$
$$\phi = \phi_L \quad \text{at} \quad x = L \tag{3.42}$$

$$\frac{\phi - \phi_0}{\phi_L - \phi_0} = \frac{\exp(Pe\, x / L) - 1}{\exp(Pe) - 1}$$

The above equation represents the analytical solution for the differential equation (3.41). The variable ϕ is a function of the Peclet number (Pe) which is defined as

$$Pe = \frac{\rho u L}{\Gamma} \tag{3.43}$$

The Peclet number represents the ratio of the influence of convection over that of diffusion.

Four distinct differencing schemes have been compared with the analytical solution (Patankar (1980)). Their characteristics and integration methods are described in the following sections. The dependent variable ϕ_p is used to assess the different methods, assuming a linear variation of this variable between adjacent nodes.

3.4.1 Central differencing scheme

In the central differencing scheme the value of ϕ at the interface of the control volumes takes the form of equation (3.20) by assuming a linear variation between grid nodes. This scheme was used in section 3.3.4 to obtain equation (3.21) and is not repeated here. When the Peclet number (Pe) is less than two the scheme yields accurate results (Patankar (1980)).

3.4.2 Upwind Scheme

With this scheme, the procedure used in the central differencing scheme is applied when the |Pe| < 2, for the formulation of the diffusion term. The formulation of the convection term is then calculated assuming that the value of ϕ at the grid node is equal to the variable ϕ at the interface on the 'upstream' (upwind) side of the face; for instance:

$$\begin{aligned} \phi_e &= \phi_P \quad \text{if} \quad F_e \rangle 0 \\ \phi_e &= \phi_E \quad \text{if} \quad F_e \langle 0 \end{aligned} \qquad (3.44)$$

For all Peclet numbers the upwind scheme gives realistic and stable behaviour. This scheme is preferred over the central differencing scheme in terms of accuracy for |Pe| > 2, but it has been shown to be slightly inferior for smaller values of Pe.

3.4.3 Hybrid scheme

A combination of the upwind and the central differencing methods is the hybrid scheme. For the range $-2 \leq \mathbf{Pe} \leq 2$ the central differencing scheme is employed, and for other Pe values the upwind method is used, assuming that the diffusion is zero outside this range ($-2 \leq \mathbf{Pe} \leq 2$). The coefficients are expressed in non-dimensional form (e.g. as a_E/D_e) as functions of the Peclet number

$$\frac{a_E}{D_e} = -P_e \qquad \text{if} \quad Pe_e \langle -2$$

$$\frac{a_E}{D_e} = 1 - \frac{Pe_e}{2} \qquad \text{if} \quad -2 \le Pe_e \le 2 \tag{3.45}$$

$$\frac{a_E}{D_e} = 0 \qquad \text{if} \quad Pe_e \rangle 2$$

This method offers a close approximation to the exact solution and the advantages of the two previous schemes (central differencing and upwind schemes) for the corresponding Peclet number ranges.

3.4.4 Power-law scheme

This scheme is represented by four different Peclet number ranges. This method offers a better approximation to the analytical (exact) solution (Patankar (1980)).

$$\frac{a_E}{D_e} = -P_e \qquad \text{if} \quad Pe_e \rangle -10$$

$$\frac{a_E}{D_e} = \left(1 + 0.1Pe_e\right)^5 - Pe_e \qquad \text{if} \quad -10 \le Pe_e \le 0$$

$$\frac{a_E}{D_e} = \left(1 + 0.1Pe_e\right)^5 \qquad \text{if} \quad 0 \le Pe_e \le 10 \tag{3.46}$$

$$\frac{a_E}{D_e} = 0 \qquad \text{if} \quad Pe_e V$$

The improved accuracy of this method is balanced by the higher computational cost.

All schemes shown above provide physically realistic solutions. The central differencing scheme however can produce results that do not obey the constraints of the boundary conditions. The scheme adopted in this work was the hybrid scheme as it provides a reasonable balance between accuracy and economy of calculation.

3.5 Solution procedure for the pressure field

The momentum and continuity equations are linked, in that pressure appears in all the momentum equations, and the velocities appear in both equations.

For the solution of the pressure field the algorithm adopted is the one called SIMPLEST which is a variation of the SIMPLE algorithm (Spalding (1980)). The main steps in the algorithm are:

(1) Initialise pressure field with guessed values.

(2) Solve the momentum equations using this pressure field. Obtain velocities which satisfy the conservation of momentum, but not continuity.

(3) Estimate the continuity errors for each cell: inflow - outflow.

(4) Solve the pressure correction equation. The coefficients are d(velocity)/d(p), and the sources are the continuity errors.

(5) Adjust the pressure and velocity fields. Obtain velocities which satisfy continuity, but not momentum.

(6) Go back to step 2, and repeat with the new pressure field. Repeat until continuity and momentum errors are acceptably small.

3.6 Boundary conditions

A set of boundary conditions must be provided to complete the mathematical solution of the problem. The boundary conditions depend entirely on the type of problem to be solved, and they will be given in detail in Chapter 4. The way in which these conditions are incorporated into the volume-domain equations is discussed in this section.

Four different types of boundary conditions can be identified in the present problem: prescribed value, symmetry plane, wall, outlet. In general the boundary conditions are represented as linearised sources for cells adjacent to boundaries. The value of the variable in the computational cell remains unchanged during the solution of the equations. This is achieved by using the source term in the discretisation equation. The conditions can be a constant value or a constant flux at the flow boundaries for any velocity or scalar value. At the symmetry plane all gradients normal to the surface are equal to zero and the velocity normal to the surface is zero. For the walls the boundary conditions can be specified as a constant value of temperature on the wall, or as a constant heat flux through the wall and can also have the form of a linear or non-linear function specified at the wall. For any of these cases the procedure to introduce the boundary conditions into the general discretised equation is described below:

Equation (3.40) can be expressed as

$$\mathbf{a}_p\phi_p = \sum_{i=E\_L} \mathbf{a}_i\phi_i \tag{3.47}$$

or

$$\phi_p = \frac{\sum_{i=E\_L} \mathbf{a}_i\phi_i + \mathbf{CVT}_{Vol.}}{\sum \mathbf{a}_i + \mathbf{CT}_{Vol.}} \tag{3.48}$$

where C is a coefficient, V a variable and T a physical quantity such as volume. When C is a large number and the variable $V = \phi_{BC}$ (where ϕ_{BC} is the value at the boundary condition), then $\phi_P \approx \phi_{BC}$, giving a constant value ϕ_{BC} at the boundary. For a constant flux, C is very small and the product $C\phi_{BC}$ is set to be equal to the required flux. When a linear or non-linear function is required at the boundary, the product $C\phi_{BC}$ or the value ϕ_{BC} is calculated separately and introduced in the same manner as explained above.

The boundary conditions at the wall will be modified depending on which variation of the turbulence model is being used. This means that the no-slip boundary condition applied to the wall will be different for the standard κ–ε turbulent model and the low Reynolds number κ–ε turbulent model. The main reason for this is because the standard turbulence model method is valid only for fully turbulent flow and it cannot be used for the near wall region.

For the outlet all gradients in the outflow plane are set to zero. The velocity perpendicular to the outflow plane is set to fulfil the overall continuity of mass.

3.7 Solution of the algebraic equations

After the integration of the governing equations over the finite volume has been carried out, a set of algebraic equations is obtained once the solution has been linearised and the appropriate boundary conditions have been applied. The algebraic equations can be written as:

$$\mathbf{a_P \phi_P = \sum_i a_i \phi_i + S_C} \tag{3.49}$$

One way to solve this set of equations is to assemble all the discretised algebraic coefficient equations on a matrix form and then to be solve the resulting set, which could be a time-consuming method. Another way to solve the system of equations is through the use of an iterative method. The method used is the Tridiagonal-Matrix Algorithm (TDMA). To apply the TDMA method to the entire matrix field, a chosen line in the x direction is swept, solving the equations along that line. The method proceeds line by line until the whole field is solved. The value in the cell being solved is calculated, while values in the other cells are assumed. The grid is swept as many times as necessary until a converged solution is obtained.

3.8 Convergence criterion.

The solution of the algebraic equations is monitored iteration after iteration until the values do not change, when the solution is considered to have converged. The change in the residual values is then restricted by a certain criterion for the convergence of the iterative procedure. The residuals can be estimated by means of the equation:

$$\mathbf{R}_{\phi} = \mathbf{a}_{p}\phi_{p} - \sum \mathbf{a}_{i}\phi_{i} + \mathbf{b} \qquad (3.50)$$

The solution that produces sufficiently small residuals for all the variables solved in the field is regarded as a converged solution. The physical meaning of R_ϕ depends on the equation to be solved. In the momentum equation R_ϕ represents an imbalance in the conservation of momentum, and for the continuity equation it represents an imbalance in the mass conservation. The criterion applied is:

$$\sum_{\text{Flowfield}} \left|\mathbf{R}_{\phi}\right| \leq \psi \mathbf{R}_{\phi,\text{ref.}} \qquad (3.51)$$

where ψ is a convergence number, and $\mathbf{R}_{\phi,\text{ref.}}$ is a reference value specified relative to an appropriate property in the flow. A converged solution is achieved when the residuals $\sum \mathbf{R}_{\phi}$ for all the variables satisfy equation (3.51).

3.9 The computer program and its structure

The computer program used for the CFD predictions was Phoenics, which is an acronym for Parabolic Hyperbolic or Elliptic Numerical Integration Code Series. This code is capable of solving fluid-flow, heat and mass transfer problems from one-dimensional single-phase and steady, to three-dimensional multiphase and transient. More information about the binary code and its structure can be found in Gunton et al (1983).

The main steps followed by the solving algorithm used by Phoenics are:

(1) Solve slab number one (the first line of control volumes in the x direction). In this first step it is assumed that all the values of the boundary

conditions, initial conditions, geometry and physical properties are defined so that the flow field in a plane can be calculated.

(2) Solve the scalar variable equations using an iterative method to solve the algebraic equations for each variable. This is carried out with the TDMA method in an iterative way.

(3) Solve the velocity variable equations. The velocities are calculated using a staggered grid and the hybrid scheme.

(4) Solve the pressure correction equation. A set of equations for the pressure is calculated.

(5) Check if the momentum and continuity equations have been satisfied and if not repeat from step 2.

(6) In this way every slab is visited until the last slab is calculated. Thereafter the calculation starts all over again from slab number one until the criteria of convergence is satisfied.

Phoenics was employed to predict the air flow under steady and transient conditions inside a ventilated chamber. All the results were considered fully converged when the residual values were smaller than 10^{-6}. Grid sensitivity was also tested and the results are described in chapters 4 to 7. The predicted results, the CPU times used and the sizes of the meshes employed for the different flow calculations are all described in Chapters 4 to 7.

3.10 Concluding remarks

The general form of the transport differential equations, the procedure used to integrate them and the turbulence models employed have been described. The integration was carried out using the finite-volume method to transform the partial differential equations into several algebraic equations which are then solved by means of a linear equation method, the TDMA. The methods used to define the boundary and initial conditions as well as the convergence criteria and some other features of the method were described. The structure of the Phoenics code and the iterative procedure used in the code to solve the algebraic equations were also outlined.

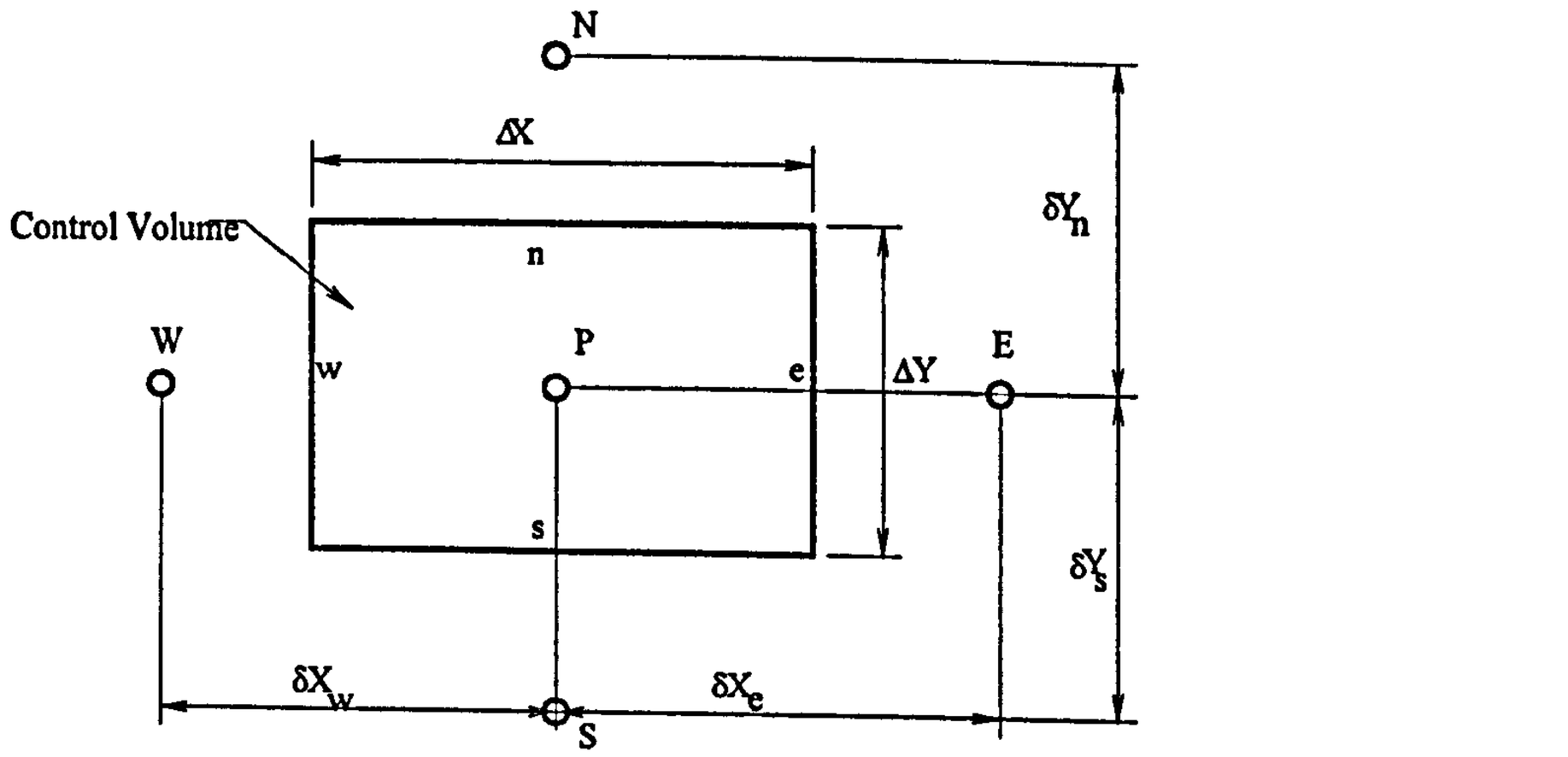

Figure 3.1 Control volume cell with grid information.

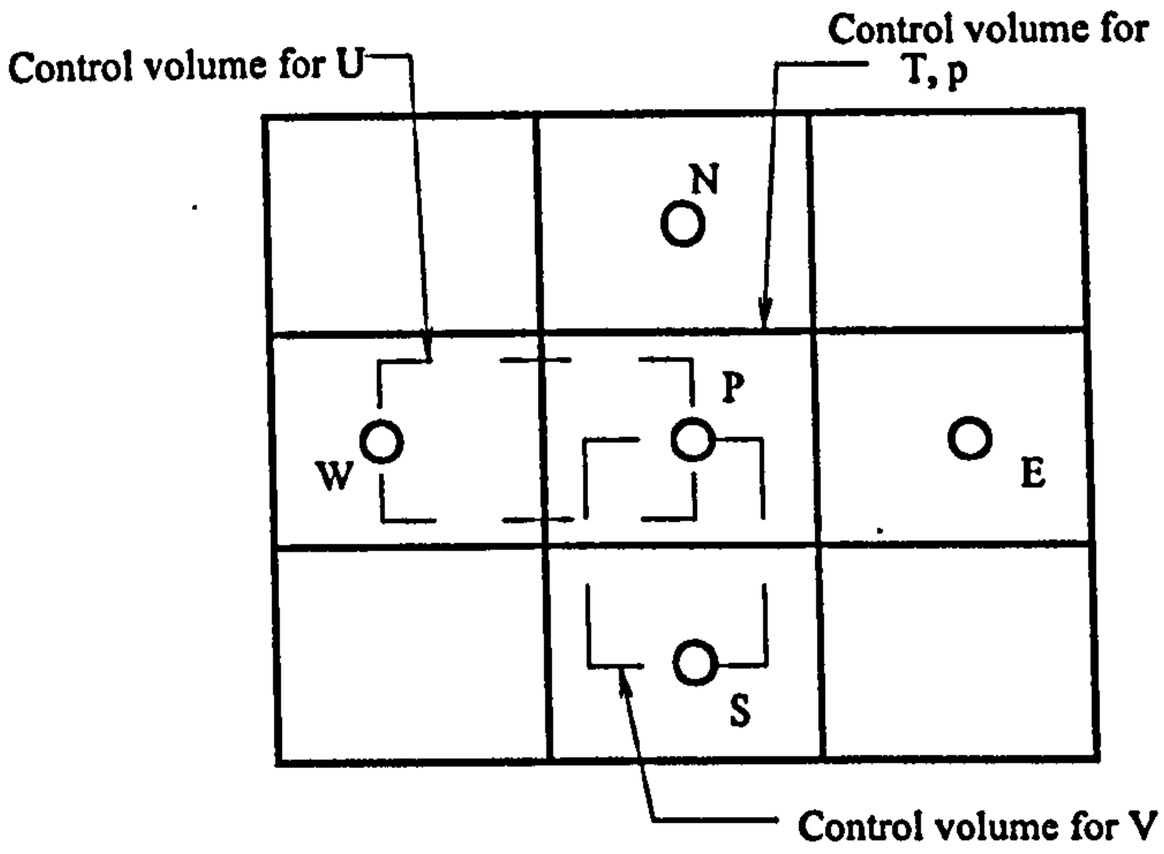

Figure 3.2 Control volume staggered cell.

CHAPTER 4

MEASUREMENT AND PREDICTION OF THREE-DIMENSIONAL ISOTHERMAL FLOWS IN A CHAMBER VENTILATED BY A HIGH-WALL JET.

4.1 Introduction

Computational Fluids Dynamics predictions, LDA measurements and flow visualisation of three-dimensional jet flows issuing into a chamber from a high-wall inlet are the subject of this chapter. Four different geometrical configurations of a square cross-section jet discharging into a rectangular chamber were studied. The first, comprising a three-dimensional horizontal high-wall jet, is presented here; chapters 5, 6 and 7 deal with the three remaining geometrical configurations. The first case corresponds to the flow through a side-wall mounted diffuser located close to the ceiling of a room. The air flow discharging into the rectangular chamber through this type of inlet forms a three-dimensional wall jet. Several aspects of the flow were studied through numerical simulations and experiments. The numerical results were obtained following the procedure described in Chapter 3 and comprise predictions of three-dimensional isothermal flows for several flow rates. The predictions were assessed by comparison with the measured mean velocity components and the corresponding turbulence levels. The effect of flow rate or, equivalently, flow Reynolds number (Re) on the mean flow and turbulence characteristics was studied in detail. In particular the variations of the inlet jet throw, spread and drop with Re were quantified.

4.2 Experimental and computational details

4.2.1 Flow configuration and LDA measurement locations

The geometrical configuration is shown in Figure 4.1. The characteristics of the chamber have been described in detail in Chapter 2. The symmetry of the flow patterns across the whole chamber was established through LDA measurements on either side of the plane of symmetry; the results showed that the flow was symmetrical to within the precision of the measurements. Subsequently, six locations were selected where LDA measurements of the three components of the mean velocity, u, v and w, and the corresponding r.m.s. levels, u', v' and w', were made: z/L = 0.5, 1.0 1.5, 2.0, and 2.5 in the x/H = 0.0 plane and z/L = 1.5 in the x/H = 0.4 plane.

4.2.2 Computational details

The CFD code described in Chapter 3 was used to obtain the predictions presented in this chapter for isothermal flow conditions. At the inlet plane, the following initial boundary conditions were set: (i) turbulence intensity equal to 4%; (ii) the w component of the velocity was determined from the incoming air flow rate corresponding to each Reynolds number predicted; and (iii) the u and v velocity components and the pressure were set to zero. At the outlet plane all gradients were set to zero. The flow was assumed, as shown by the LDA results, to be symmetrical and all the gradients were set to zero across the symmetry plane, where a slip condition was used. As a result, only half of the domain was simulated.

The numerical mesh used for the calculation is shown in Figure 4.2. Grid independence tests were carried out with mesh sizes (in the x, y, and z

directions respectively) of 10x20x20, 10x30x30, 18x36x30 and 18x37x36 volumes. An irregular mesh of 18x36x30 volumes was found to provide a good compromise between accuracy and acceptable computer time cost. The mesh independence tests showed that the results with 18x36x30 and 18x37x36 volumes were practically identical. A characteristic comparison is shown in Figure 4.3. It can be seen clearly that although there are differences between the results obtained with the two coarser grids, the two finer grids produce essentially identical results. This was also the case across the whole flow field. This mesh was used for the results presented in this chapter and the corresponding low-wall jet results presented in Chapter 5. Isothermal conditions were assumed throughout. The numerical solutions comprised 3000 iterations which took approximately 1.3 hours of CPU time on a VAX 4100 machine.

4.3 Flow visualisation

A qualitative description of flow patterns was obtained through flow visualisation using the technique described in Chapter 2. Flow visualisation was possible for Re values up to 2000, as for Re > 2000 there was strong mixing inside the cavity and the water mist used as flow tracer diffused very rapidly. It should be noted that previous flow visualisation investigations within a similar cavity performed by Restivo (1979) were restricted to Re < 500 for similar reasons.

Characteristic results are shown in Figure 4.4 for a Re = 1500. The Figure shows a sequence of four images recorded during the flow visualisation tests. The images were recorded at intervals of one second and indicate the instantaneous flow patterns under steady state conditions. The air stream entering the cavity remains attached to the ceiling surface until it reaches the end wall, where it is deflected downwards forming a small

recirculation zone on the corner of the upper and the end wall. This region cannot be distinguished in the reproduced images due to its small size, but was clearly evident during the tests. The main jet air stream is deflected downwards, forming a descending stream along the end wall which is directed toward the exit. In the vicinity of the outlet the jet is divided in two parts, one of which exits the cavity, while the other forms a large recirculation zone in the chamber. The irregular shape of the jet edge along the top of the chamber indicates entrainment of fluid from/to the recirculation region. The differences that can be observed between the four images are due to the turbulent nature of the flow: observations of the flow patterns over long periods of time (20 to 30 minutes) showed that the flow was steady. The visualisation showed that the flow pattern formed inside the cavity is highly three-dimensional.

The flow visualisation experiments indicated that the flow remained laminar for Reynolds numbers up to 600. For Re's above this value, oscillations of the flow were observed, indicating transition to turbulent flow. Although it was not possible to record the flow patterns for Re > 2000, it could be observed in the experiments that the flow was fully turbulent for Re > 4800.

4.4 Predicted mean flow patterns

Computational CFD predictions were performed for several flow rates which are tabulated in Table 4.1. The predictions were made using the standard $\kappa-\varepsilon$ turbulent model for all the Reynolds numbers listed in Table 4.1. For Re = 6000, predictions were also made with a modified "low-Re" $\kappa-\varepsilon$ turbulence model in order to compare the two models.

The computational results are presented below in the form of velocity vector distributions, mean velocity and r.m.s. profiles, as well as contours of the kinetic energy of turbulence. For economy of presentation, the results for Re = 600, 3600, and 8400 are described relatively briefly, while the results for Re = 6000 will be described in greater detail.

Reynolds number	Inlet velocity (m/s)	Outlet velocity (m/s)	Flow rate (m^3/s)
600	0.92	0.41	0.277E-03
3600	5.55	2.46	1.66E-03
6000	9.25	4.10	2.770E-03
6000 low-Re $\kappa-\varepsilon$ model	9.25	4.10	2.770E-03
8400	12.95	5.74	3.880E-03

Table 4.1

4.4.1 Predictions with the standard $\kappa-\varepsilon$ turbulence model, Re = 600

As mentioned earlier, the flow visualisation indicated laminar flow for Re > 600. Predictions were however made for Re = 600 with the $\kappa-\varepsilon$ model, i.e. assuming fully-turbulent flow. Predictions made assuming laminar flow at Re = 600, without employing the turbulence model, yielded essentially identical results to those presented below. It must be noted that there is no consensus in the published literature regarding the Re values at which the flows become turbulent (Restivo (1979), Nielsen (1972), Mohammad (1986), Setrakian (1988), Skovgaard (1991)). Therefore, it was decided to treat the Re = 600 flow as turbulent, primarily to ascertain the effect of flow rate/Reynolds number on the mean flow and turbulence energy in the chamber.

The three-dimensional velocity vector distribution for Re = 600 is presented in Figure 4.5. This three-dimensional representation shows the main features of the flow pattern predicted for this particular Reynolds number through the presentation of the vectors in the x/W = 0.0, y/H = 0.0 and z/L = 0.0 planes. The air flow stream can be seen entering the cavity and moving towards the opposite wall. The jet remains attached to the ceiling until it has reached the end wall. Once it has reached the end wall, the air stream is deflected downwards flowing along the end wall where it is divided. One part of the stream exits through the cavity outlet, while the other part forms a large recirculation zone. Steep velocity gradients can be observed along the jet trajectory; these gradients are considerably smaller in the recirculation zone.

Other than the jet region, there are two main flow features. First, the large recirculation region occupying around 25% of the area of the symmetry plane, which has its centre at z = 261 mm and y = 56 mm in this plane. Second a small vortex is formed in the corner of the top and end walls, as also evidenced in the flow visualisation tests. This vortex is around 21 mm long and 4 mm high in the symmetry plane.

The predicted flow pattern exhibits all the flow features observed in the flow visualisation. The predicted and observed length of the large recirculation zone are very similar (approximately 0.25 m). The size and location of the small recirculation in the upper/end wall corner and the trajectory of the air jet are also very similar in experiment and simulation.

4.4.2 Predictions with the standard κ–ε turbulence model, Re = 3600

The velocity vector distribution for Re =3600 is shown in Figure 4.6. The velocities show similar features to those for Re = 600, such as the large recirculation region and the small recirculation zone near the upper/end wall corner. Due to the higher flow rate for this Re, the velocity magnitudes are larger. The air stream remains clearly attached to ceiling surface possibly due to the Coanda[1] effect. The magnitude of the vectors in the recirculating flow (occupied zone) has also increased. The recirculation zone has been displaced toward the centre of the symmetry plane and its centre (z = 260 mm, y = 70 mm) is located at around 3/4 of the cavity length from the inlet. The centre of this recirculation in the symmetry plane is now at z = 261.40 mm and y = 50 mm; the centre has been displaced towards the bottom of the chamber by only 5 mm compared to the Re = 600 case.

The small corner recirculation is reduced in size as the increased momentum of the inlet jet at this Re results in higher velocities and thinner boundary layers along the ceiling of the chamber. Comparison of Figures 4.5 and 4.6 shows that the shape of the boundary layers is significantly altered as Re is increased. For Re = 600 the boundary layer profile indicated by the vectors is nearly parabolic, as might be expected for this essentially laminar flow. This is in contrast to the steeper near-ceiling gradients present with Re = 3600.

---

1 "The proximity of a surface to one side of the supply inlet restricts the fluid entrainment to that side. This causes a pressure difference across the jet which curves it towards the surface, further reducing the entrainment to that side of the jet." (Awbi (1991)). The curvature of the jet increases and remains attached to the surfaces. This effect can be seen in Figure 4.29b, that compares velocity profiles for different Re numbers at z = 200 mm, when the air jet has traveled ¾ of the cavity length.

4.4.3 Predictions with the standard κ–ε turbulence model, Re = 6000

The predicted velocity vectors and κ contours at Re = 6000 are presented in Figures 4.7- 4.12 and several aspects of the development of the incoming jet flow are analysed.

The velocity magnitudes are higher as the flow rate is twice that for Re = 3600. Again as a consequence of the Coanda effect, the incoming air jet remains attached to the ceiling until it has reached the opposite wall, where a small recirculation zone is again formed. This recirculation can be seen in Figures 4.7 and 4.8 but is more evident in Figure 4.10.

In Figure 4.8 the vectors at the z/L = 3.0, y/H = 1.0 and x/W = 0.5 planes show the air flow patterns at the cells closest to the lateral wall, the end wall and the ceiling. It can be seen that the jet remains attached to the ceiling and very little spread sideways can be observed. The air flow along the lateral wall indicates the presence of a recirculation zone as in the symmetry plane (Figure 4.7) but the magnitudes of the reverse velocities in the x/W = 0.5 plane are around 50% of those in the symmetry plane. Figure 4.9 shows the vectors in different vertical planes along the cavity length. The spread and throw of the jet along its trajectory through the cavity can be seen more clearly in this Figure. The air stream spreads from the half-width symmetry plane 15 mm at z = 50 mm and 30 mm at z = 150 mm. Along the end wall, the jet spreads diagonally. Again, the three-dimensionality of the air flow inside the cavity is evident in Figure 4.9. The jet horizontal spread of the jet does not exceed 30 mm. The velocity of the incoming air stream decays with distance from the jet, from 9.35 m/s to around 5.0 m/s, near the end wall.

Figure 4.10 shows the vectors in the symmetry plane (x/W = 0.0) and Figure 4.11 in the plane x/W = 0.4. The flow pattern in Figure 4.10 shows the recirculation zone formed on the upper end wall corner. This zone is 20 mm long and 5 mm high at this Re, an increase of around 5% in length and decrease of 20% in height compared to Re = 600. When the vector distribution of Figure 4.10 is compared with that in Figure 4.11, it can be observed that the magnitude of the vectors has decreased significantly at the x/W = 0.4 plane: although both the jet and the recirculating flow are still in evidence in the latter plane, the velocity magnitudes in these regions do not exceed 2.66 m/s and 2.97 m/s respectively. The corresponding values in the symmetry plane and near the centre of the chamber are around 9.35 m/s and 3.99 m/s respectively.

Figure 4.12 shows the contours of the kinetic energy of turbulence along the symmetry plane. The kinetic energy values decrease as the jet flow moves along its trajectory. The highest values of κ are found along the jet trajectory. The κ contours follow closely the pattern of the velocity distribution. Along the floor and in the recirculation zone the κ values are considerably smaller (0 - 0.9 m^2/s^2) than those predicted for the jet core (3.0 - 4.3 m^2/s^2) The predicted κ values were found to be uniformly low (below 1.2 m^2/s^2) across 75% of the cavity cross-section.

4.4.4 Predictions with the low-Re κ–ε turbulence model, Re = 6000

Further predictions were carried out for Re = 6000, using a different numerical approximation for the zone close to the walls, known as the low- Re κ–ε turbulence model. The purpose of this test was to assess the suitability of this model in comparison to the standard κ–ε turbulence model. The results are shown in Figures 4.13 to 4.15. It can be seen that there are no appreciable differences between these results and those

obtained for this Re using the standard κ–ε model. However the CPU time required for the calculations increased by 25% compared with the standard κ–ε model calculations, due to the additional equations that had to be solved. Figure 4.13 shows a three-dimensional velocity vector distribution while Figure 4.14 shows the vectors in the symmetry plane. When these results are compared with the predictions presented in Figures 4.10 and 4.11 respectively, it can be seen that the small recirculation region on the upper/end wall corner predicted with the standard κ–ε turbulence model is larger by approximately 1.0 mm in length and height. Another difference is found in the velocity magnitudes on the reverse flow, close to the bottom wall below the inlet: in this region, velocities are higher by around 80% with the low-Re κ–ε turbulence model.

Contours of the kinetic energy of turbulence at the plane of symmetry are shown in Figure 4.15. The overall distribution is similar to the one predicted by the standard κ–ε model. The turbulent kinetic energy is predicted to be around 20% lower than with the standard κ–ε model (Figure 4.12). For example, a maximum of 3.5 $m^2/s^2$is predicted for the low-Re κ–ε turbulence model compared with a maximum of 4.3 m^2/s^2 predicted by the standard κ–ε model.

4.4.5 Predictions with the standard κ–ε turbulence model, Re = 8400

In this section calculations obtained for Re = 8400 using the standard κ–ε turbulence model are presented. The three-dimensional velocity distribution and the main features of the flow pattern predicted can be seen in Figures 4.16 to 4.19. Figure 4.16 shows the velocity vector distribution in the plane of symmetry and near the floor and the inlet wall. Figure 4.17 shows the velocity vector distribution along the ceiling, lateral and bottom walls and Figure 4.18 the vectors in the symmetry plane. The centre of the

main recirculation region is now at z = 271 mm and y = 45 mm, i.e. it is found nearer the bottom part of the chamber and closer to the end wall compared to lower Re's. The length and the height of the jet are also modified. The small recirculation zone near the upper/end wall corner is predicted to be shorter compared with that for Re = 6000 using the standard κ–ε model. This is attributed to the increase of the flow rate and consequently of the momentum of the jet, manifested by the increase of the values of the mean velocities The width of the region is similar (within 1 mm) to that predicted for Re = 6000. In the recirculation zone the mean velocities are around 30% larger than those predicted for Re = 6000.

Except for the expected increase in velocity magnitudes and the small changes in sizes of the recirculations, the solution shows practically the same flow pattern to that for Re = 6000. This suggests that the air flow patterns become essentially independent of the Reynolds number for Re > 6000, while between Re = 3600 and 6000, the shape of the jet profile is modified as well as the centre of the large recirculation zone as mentioned above. Previous investigations in a cavity with similar aspect ratio, have observed this through both experiments (Restivo (1979)) and predictions (Lemair (1992)).

Contours of the kinetic energy of turbulence at the plane of symmetry can be seen in Figure 4.19. The contours are similar to those predicted for Re = 6000, but their magnitudes are nearly 100% higher in the jet core. In conclusion, both the mean flow and turbulence energy predictions show that the flows at different Re's are similar. The sizes and centres of the recirculations vary slightly with Re, but the variations are very small and the flow pattern might be considered to be independent of Re for Re > 6000.

4.5 Comparison of predictions and experimental data

4.5.1 Comparisons at Re = 6000

The numerical calculation results presented in the previous sections are compared below with the experimental data obtained using the LDA technique described in Chapter 2. Numerical and experimental mean velocity profiles in the plane of symmetry for Re = 6000 are compared in Figure 4.20. It can be observed that the velocities in the recirculation region are predicted well in the z = 150, 200 and 250 mm profiles. It can be seen as well that the numerical method predicts well the mean velocity distributions in the incoming air jet core along the ceiling: the LDA and CFD results in this region are nearly identical at z = 50, 100, 150 and 200 mm.

Considering that in the predictions plug-flow inlet velocity profiles were specified at the inlet, agreement with the LDA data is excellent. This result indicates that it may not always be necessary to use experimental data at the CFD inlet boundary. This is further confirmed by comparison of the measured and predicted jet spread, which is also well predicted in the x-direction, as discussed later in this chapter.

The mean velocity values in the recirculation zone were underpredicted by 10% at z = 250 mm and overpredicted by 20 and 30% at z = 50 and 100 mm respectively. However, the general agreement between experimental data and predictions is qualitatively excellent across most of the cavity and quantitatively very good across nearly two thirds of the plane shown.

In Figure 4.21 measured and predicted profiles of the κ are compared. The κ is underpredicted by the numerical method across most of the profile

shown. The experimental kinetic turbulence energy was obtained through the r.m.s. values measured at z = 200 mm for the 3 velocity components; the u', v' and w' profiles are shown in Figure 4.22. It can be observed in Figure 4.22 that in the jet core and near the floor area the flow is strongly anisotropic while close to the centre, for 0.02m < y < 0.06m, it is nearly isotropic. This behaviour could explain the differences found in Figure 4.21. These differences may be attributed to the implicit assumption of local isotropy made in the formulation of the standard $\kappa-\varepsilon$ turbulence model; this will be discussed later in more detail. A representation of the turbulence levels as $\frac{\sqrt{k}}{1.1}$ was suggested by Nielsen (1991) when experimental values of one or more turbulence levels are not available. A comparison of the measured u' levels with the predicted $\frac{\sqrt{k}}{1.1}$ values is shown in Figure 4.23. This plot shows, as well as Figure 4.21, that the numerical method underpredicts the κ values. Similar observations have been made by Heikkinen (1991) and Chen (1991) for two-dimensional test predictions of flows in ventilated chambers.

Another possible reason for the underprediction of κ is the presence of mean velocity fluctuations due to instabilities (flapping) of the jet emerging from the inlet. Although such flapping could not be observed at Re = 6000 in the visualisation test, it has been observed in many jet flows (Chen et al (1994), Naradajah (1992)). Ensemble-average LDA measurements interpret such mean velocity variations as an increase in the r.m.s. values and therefore predicted values of κ will be lower as the variations are not accounted in the modelling. Time-resolved LDA measurements can be utilised to remove this variation and calculate the true levels of turbulence using, Fast Fourier Transform (FFT) and filtering techniques (see, for example, Balabani and Yianneskis (1996)). As suitable signal processing equipment was not available for the experiments

presented in this thesis, such measurements could not be obtained. It would be interesting though to determine whether such mean flow variations are present in this flow and to quantify them in future work. This will be discussed further in Chapter 8.

4.5.2 Comparisons at Re = 8400

The numerical calculations for Re = 8400 are compared in this section with the experimental data obtained. Figure 4.24 shows a comparison of the numerical and experimental mean velocities in the plane of symmetry. It can be observed that the predicted recirculation velocities are again higher at z = 50 and 10 mm, but are well predicted at z = 150 and 200 mm, as was the case with the predictions obtained for Re = 6000. The mean velocities along the incoming air jet core along the ceiling have been in general well predicted as for Re = 6000 and qualitative and quantitative agreement is good across most of the plane.

Experimental and numerical comparisons of the kinetic turbulent energy are shown in Figure 4.25, while the r.m.s. values measured at z = 200 mm for the 3 velocity components are again shown separately in Figure 4.26. The kinetic turbulent energy has again been underpredicted by the numerical method. As before, these differences can be attributed to the flow anisotropy shown in the experimental results of Figure 4.26 and the local assumption of isotropy implicit in the turbulence model used. A comparison of turbulence levels calculated from the predictions using Nielsen's (1991) proposed expression for the representation of the turbulence levels and the measured u' levels is shown in Figure 4.27. This confirms again that the numerical method consistently underpredicts the κ values.

4.6 Discussion

4.6.1 Flow and turbulence structure

The experimental and numerical results presented in the previous section confirmed the presence of a highly three-dimensional flow in the cavity, which is produced by the interaction of the incoming high momentum air jet with the geometry of the cavity, and the presence of the Coanda effect for high Reynolds numbers. The main features of the flow are the large recirculation zone centred around 3/4 of the length of the cavity from the inlet and a small recirculation zone at the upper/end wall corner, which were predicted by the numerical method and observed through flow visualisation. This particular behaviour can be observed in all the cases studied in previous sections, and confirm previous experimental and numerical investigation in a cavity with a similar aspect ratio by Restivo (1979). The maximum velocities have been found along the incoming core jet and the maximum velocities in the recirculation zone are located at around two thirds of the cavity length from the inlet. The results shown here corroborate the progressive decay of the jet velocity. In Figure 4.28 the non-dimensional velocity profiles of the measured data are compared with the measurements of Sforza and Herbst (1967) for the decay of a three dimensional wall jet with w/h = 40, and of Verhoff (1963) for a two-dimensional jet. The velocity u and distance from the ceiling have been normalised with the maximum velocity in the jet (u_{max}), and the height ($Y_{1/2}$), respectively.

The measured variations of u/ u_{max} at z= 100 and 200 mm in the present flow are similar to those of the earlier investigations and indicate that the incoming jet is akin to a wall jet, in agreement with the findings of Nielsen (1972) and Restivo (1979). The peak in the velocity profile in the present

flow is located however at y/ $Y_{1/2}$ = 0.50 compared with 0.25 in the wall jet flows.

The experimental results showed that in some regions inside the cavity the flow is anisotropic and in some isotropic. The experimental results were compared with their predicted counterparts and the comparison showed clearly that the numerical method underpredicted the κ values; this is probably due to the implicit assumption of local isotropy made in the turbulence model formulation. Although only one value of κ was used as the initial condition, Skovgaard (1991) has reported that the effect of the κ values specified at the inlet is negligible. A Reynolds stress model capable of accounting for anisotropy might improve predictions of the levels of κ. However, the possibility of the presence of mean flow variations which would result in an overestimation of the turbulence levels should be further investigated, as mentioned earlier.

4.6.2 Effect of Reynolds number

The experimental and numerical results presented in the previous section confirmed that the air flow patterns for this particular geometry become independent of the Reynolds number, for Re > 6000, for this type of inlet configuration. Above Re = 6000, an increase of the Reynolds number results in an increase of the magnitude of the velocity vectors and of the κ values but the flow structure remain qualitatively similar. The Coanda effect on the incoming jet becomes clearly apparent when the Re is increased over 2400, while for Re = 600 this effect is not manifested.

The variations of the jet half width (jet spread) with axial distance in the symmetry plane is shown in Figure 4.29 for three different Re`s. It can be observed that $Y_{1/2}$ increases with axial distance as the flow develops

further. The rate of spread decrease with increasing Re. Polynomial fits were applied to the curves of this Figure. The results show that the polynomials for Re 6000 and 8400 are very similar, supporting the observation[2] that the air flow becomes independent of the Reynolds number.

The velocity magnitudes over the cavity length in the jet and in the recirculation zones increase by 30 to 40% with an increase in Re from 6000 to 8400. The small recirculation zone in the upper/end wall corner reduced in size by 20 to 30% with an increase of the Re from 6000 to 8400.

4.6.3 Assessment of the effect of the turbulence model used

The predictions of the mean flow were found to be in very good agreement with the experimental data, although the levels of turbulence were underpredicted by more than 30% in some parts of the chamber. Because of the two different turbulence models used, further analysis of certain aspects of the predicted mean velocities and turbulent parameters is called for. Predictions of the decay of the maximum velocity (drop and throw), the maximum velocity in the recirculation zone (occupied zone), and the of jet spread (or growth of the jet width), can be seen in Figures 4.30 to 4.37.

Figure 4.30 shows the decay of the maximum velocity in the jet at y= (H-h)/2 predicted for Re = 6000, while in Figure 4.31 the variation of the reverse velocity near the floor surface at y = h/2 is shown. Due to the different wall functions used, the curve predicted by the low Re model in

---

2 Further experimental and numerical tests were carried out at Re number 3500, 4000, 5000 and 5500. The results of these tests are not shown here due to lack of space. Figure 4.29b shows how the velocity profiles for Re = 6000 and 8400 are almost equal.

Figure 4.30 indicates that a thinner layer is formed along the ceiling compared to the solution with the standard κ–ε turbulence model. Larger differences between the predictions in the turbulence models appear to be present between the occupied zone flow region (Figure 4.31), at y = h/2, i.e. at z = 150 mm and the inlet wall, where the standard κ–ε turbulence model predicted larger velocities as can be seen in Figure 4.31.

Figure 4.32 shows the measured and predicted axial velocity decay against the rectangular wall jet decay results of Viets and Sforza (1966) for w/h = 10. The measured velocity decay is slightly overpredicted by the calculations. This has also been observed by Heikkinen (1991) and Skovgaard (1991) for a two-dimensional wall jet. The data of Viets and Sforza (1966) indicate a more rapid decay of u/u_o for $z/H \geq 0.5$ than the current flow, this might be expected to stem from the differences in the flow geometries.

Both methods predicted the small recirculation zone formed when the jet is deflected downwards near the end wall, as described in detail in previous sections. This small recirculation zone has not been predicted by previous investigations of flows in two-dimensional cavities (Chen (1991), Heikkinen (1991), Skovgaard (1991), Lemair (1992)). It has been reported that the low-Re κ–ε turbulence model performance is improved if the y+ range is between 5 to 30 (Skovgaard (1991), Chen (1991)); in the case of the present predictions y+ does indeed fall in this range.

Figures 4.33 and 4.34 show the velocity variations in the z/L = 100 mm and z/L = 200 mm respectively in horizontal planes at locations near the ceiling (y = (H-h)/2) and floor (y = h/2) surfaces. It can be suggested that a faster decay of the measured velocities corresponds to a faster growth in

the jet width at y = (H-h) /2 (the jet core zone). Differences in the predictions obtained with the two models are larger at z = 100 mm, while in Figure 4.34 at y = h/2 the air stream shows very similar velocity magnitudes predicted by both turbulent models along the horizontal plane.

The predicted mean velocity decay at y = (H-h)/2 and x/W = 0.0 is shown in Figure 4.35, while the mean velocity in the occupied zone at y = (H-h)/2 is shown in Figure 4.36, both for Re = 8400. Practically the same behaviour as observed in Figures 4.30 and 4.31 for Re = 6000 can be seen. Figure 4.37 shows the horizontal spread of the jet at z/L = 100 mm and at z/L = 200 mm respectively for Re = 8400 at two locations: y = (H-h)/2 (ceiling surface) and y = h/2 (floor surface), for the jet core and the reverse flow. The behaviour is again quite similar to that observed for Re = 6000. Results at z = 200 mm are not included for economy of presentation; they showed a similar trend of those observed for Re = 6000. Similarly, the jet growth (spread) for Re = 8400 is not shown as it exhibited very similar behaviour to that for Re = 6000 in Figure 4.32.

The distribution of the velocities in the occupied zone is more uniform than that in the jet core. Heikkinen (1991) found that the kinetic turbulent energy was also predicted to be lower than the measurements near the ceiling, while agreement at locations near the floor was poor. It was reported that differences can be larger near the floor due to numerical diffusion (Heikkinen (1991)). Chen (1991) suggested that such differences are due to an underestimation of the v` and w` levels, in agreement with the present finding that κ's (and its constituent r.m.s. levels) is underestimated.

4.7 Concluding remarks

1. Flow visualisation of the flow patterns inside the cavity with a horizontal jet issuing from a high-wall inlet for Re up to 2400, showed the presence of a highly three-dimensional jet. By utilising a water droplet aerosol it was possible to visualise the flows at Re's considerably higher than those achieved in earlier investigations (Restivo (1979)). These flow visualisation tests showed a large zone of recirculation occupying 25 to 30% of the chamber. A smaller recirculation zone was observed on the upper end wall corner.

2. CFD predictions of the flow were made and assessed against the experimental results, both flow visualisation recordings and LDA measurements. The predicted incoming air stream formed a wall-type jet, due principally to the Coanda effect. The maximum velocities were found in the jet core zone. In the recirculation zone the highest velocities are located around 3/4 of the cavity length from the inlet.

3. The kinetic energy of turbulence was highest in the vicinity of the incoming jet. Elsewhere, the κ values decrease in the recirculation zone, and remain low over the remainder of the cavity. It was found that the numerical methods used predict well the velocities in the air jet core, but underpredict them in some parts of the recirculating zone. The kinetic energy of turbulence was underpredicted by both turbulence models. However, the agreement between experimental and predicted mean velocities is qualitatively and quantitatively excellent over many parts of the flow with both models.

4. Differences between the two numerical models used are not significant, apart from the CPU time used for each method to obtain a converged

solution. Values of the kinetic energy of turbulence predicted by the low Re model were lower than those obtained using the standard κ–ε model. The standard κ–ε model seems to be more adequate for the purposes of this calculation, using less computational time and predicting more accurately both the mean flow and in particular the recirculation zones found near the upper end wall corner and the lower rear wall corner and the turbulence levels.

5. The experimental and numerical results presented in this chapter indicate that the air flow patterns for this particular geometry become independent of the Reynolds number for Re > 6000.

6. An increase of the Re from 3600 to 6000 produce an increase of the magnitude of the velocity vectors and the κ values, by around 60%, while for Re from 6000 to 8400, they increase around 40%, both for the jet core and the return flow zone.

7. The incoming jet shows many similarities with two- and three-dimensional wall jet flows and indicate that data obtained from such flows could be used for a qualitative assessment of CFD predictions of the jet region in the present flow.

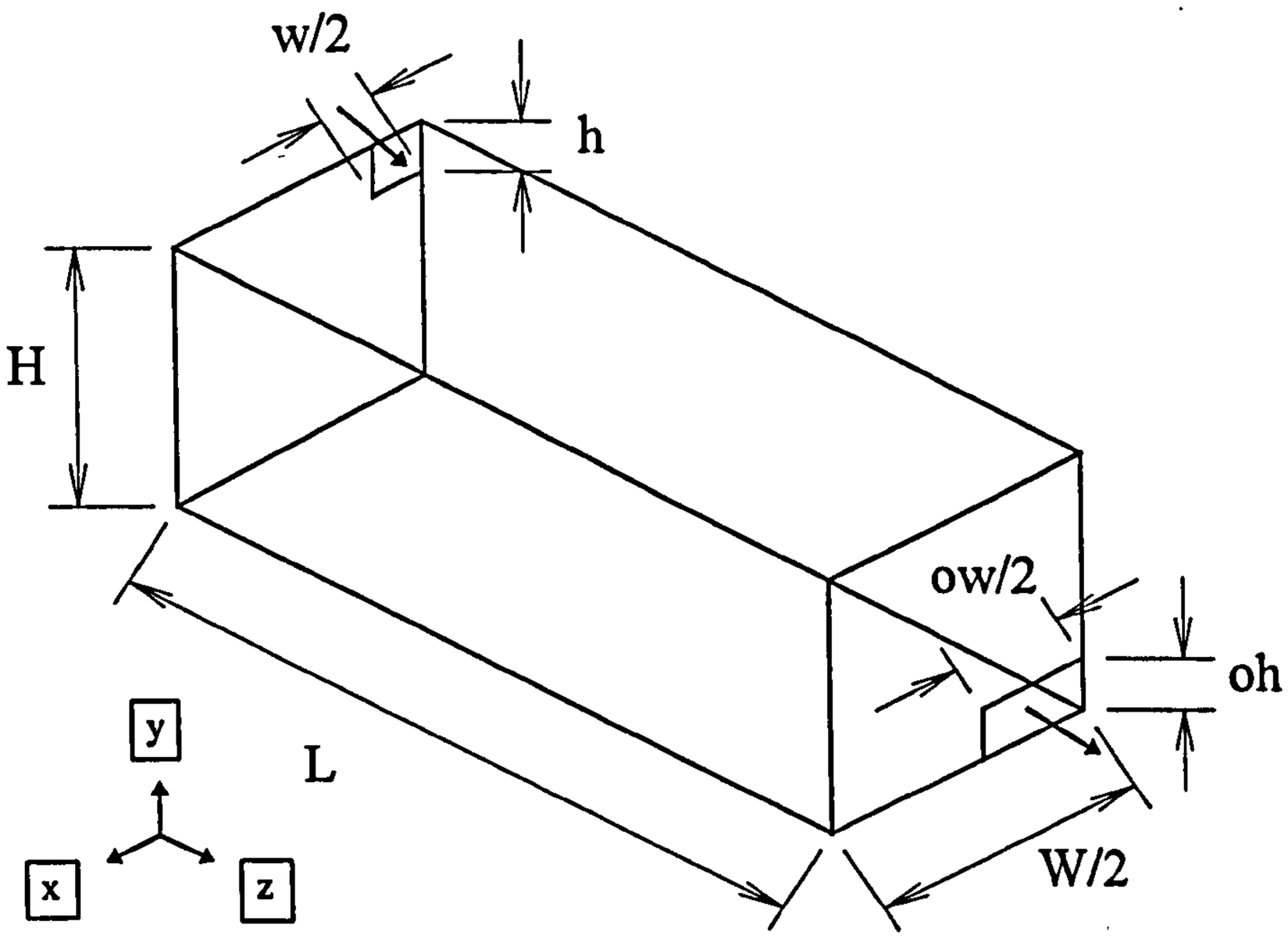

Figure 4.1 Flow configuration: schematic diagram of one-half of test section, chamber 1.

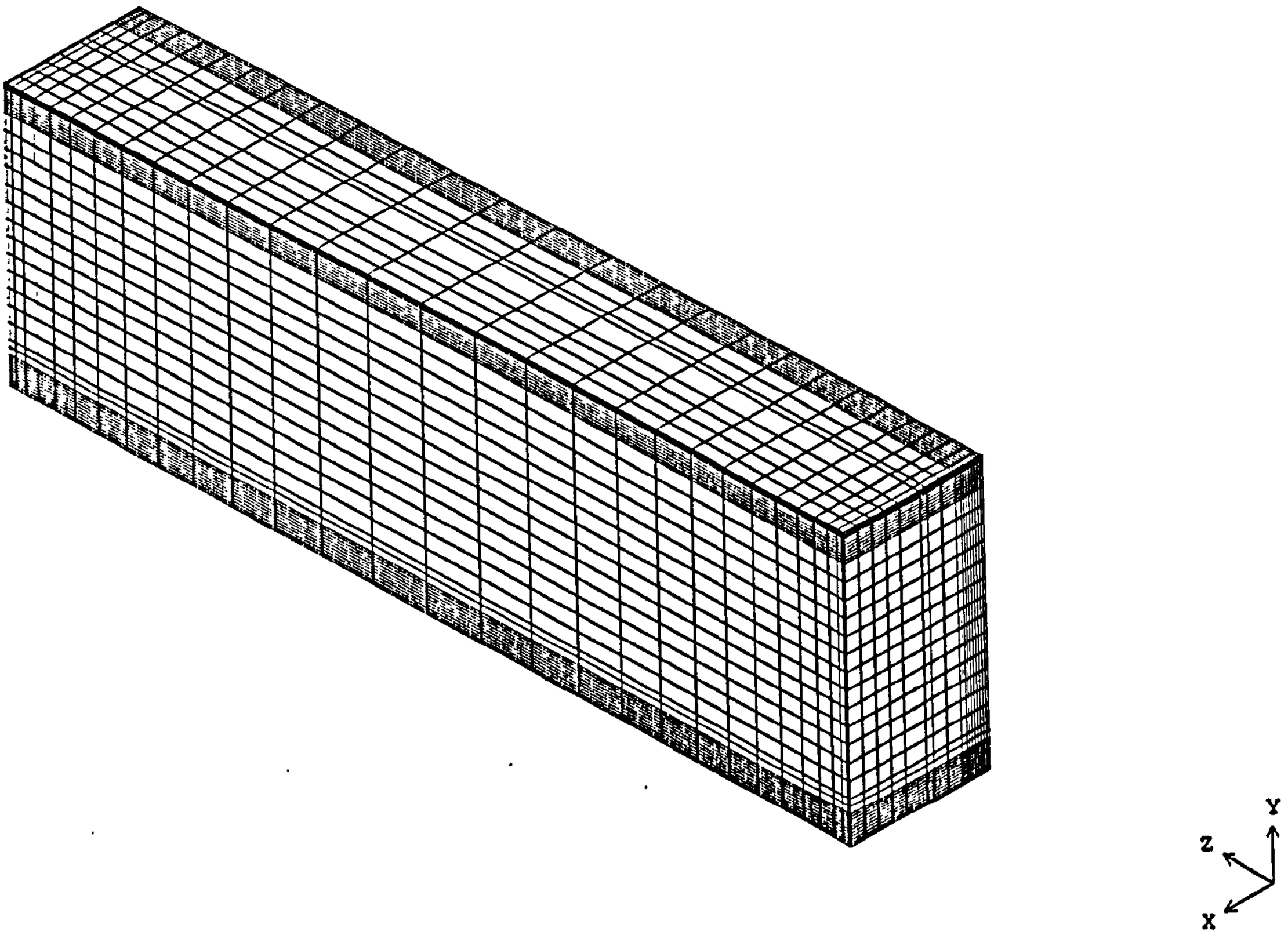

Figure 4.2 Numerical mesh.

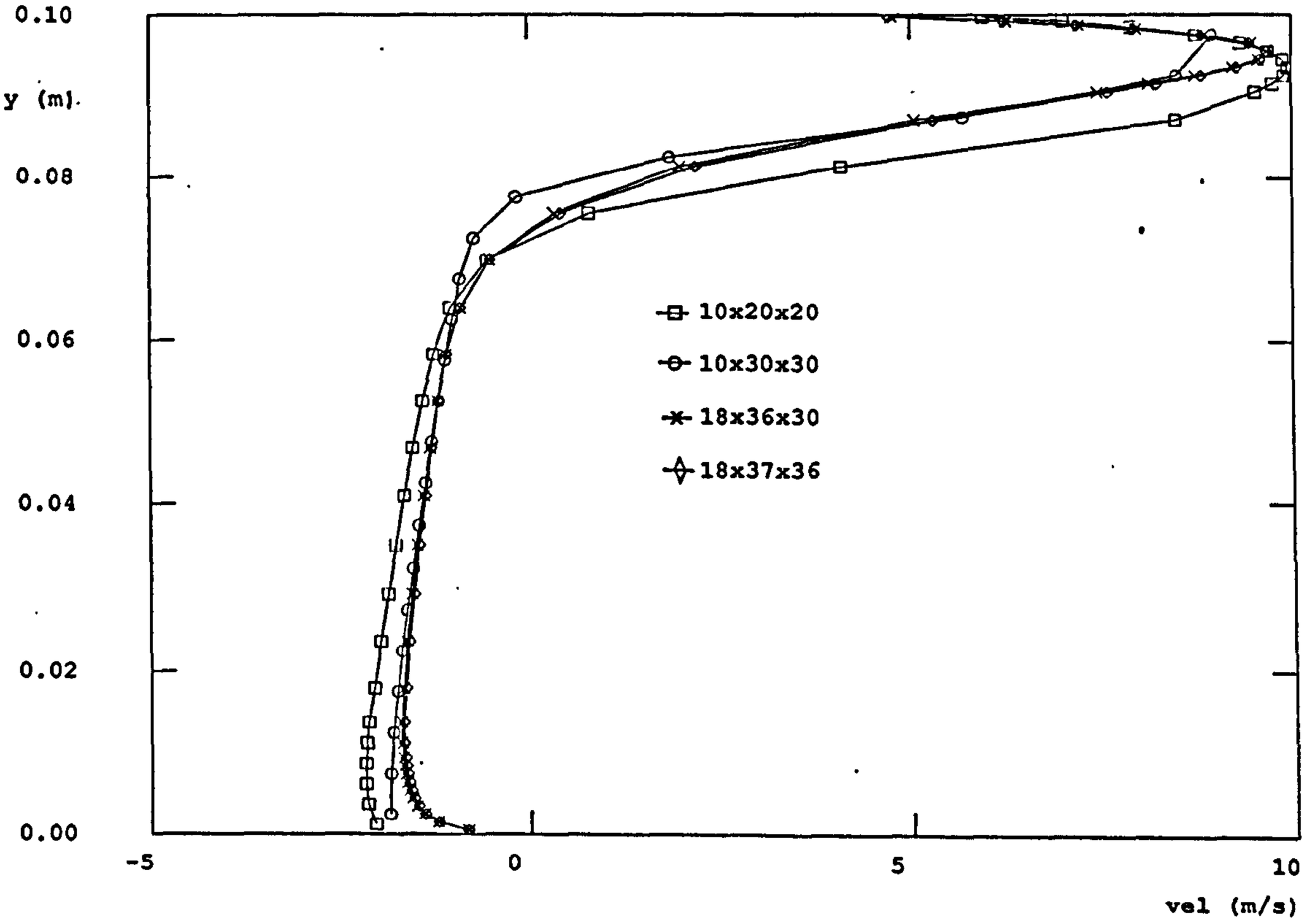

Figure 4.3 Comparison of u velocity profiles at z = 1.0, predicted with four different grid sizes; Re = 6000.

Figure 4.4 Flow visualization test at Re = 1,500.

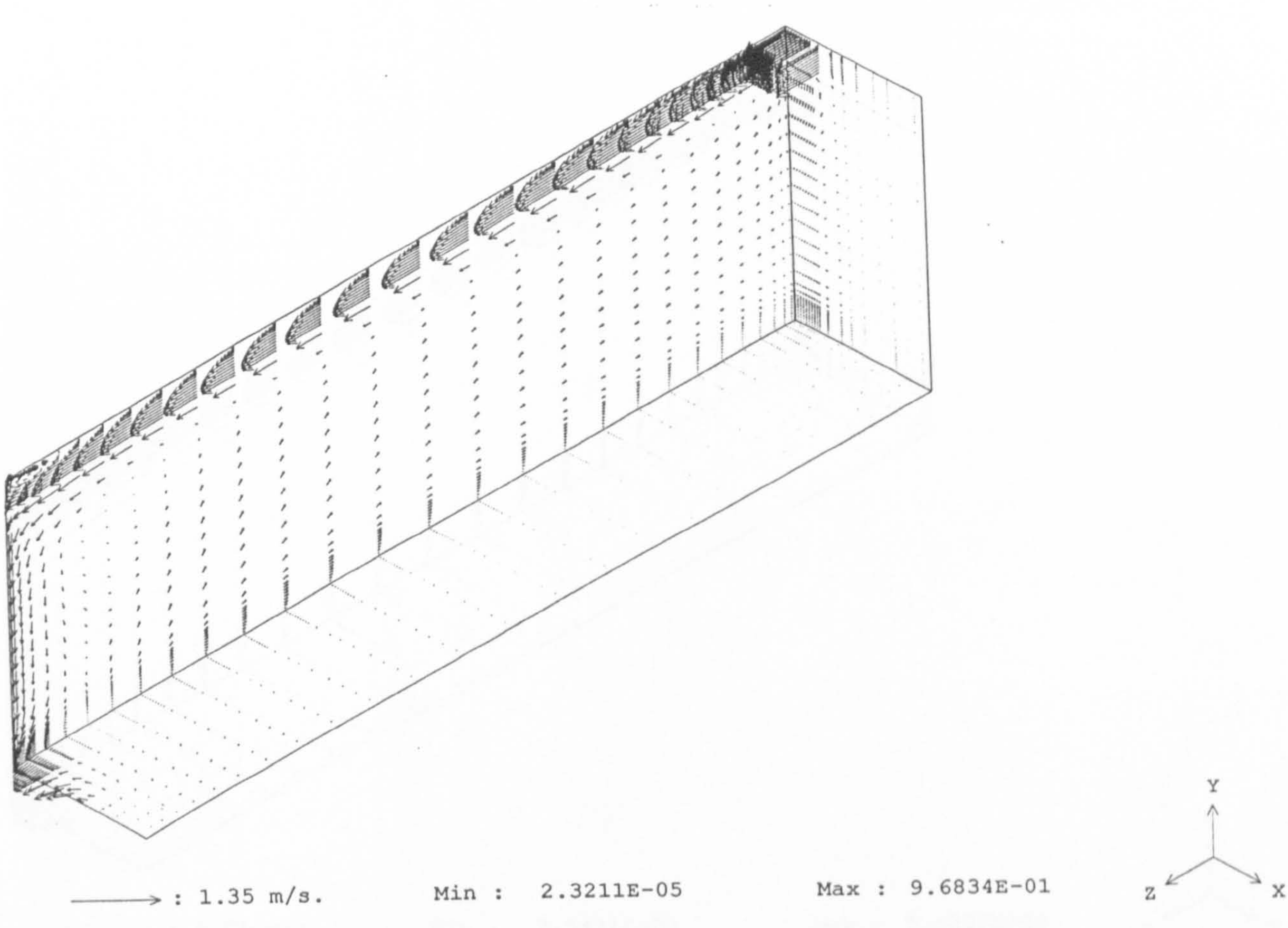

Figure 4.5 Velocity vector distribution in the planes x/W = 0.0, y/H = 0.0 and z/L = 0.0; Re = 600, standard κ–ε turbulence model.

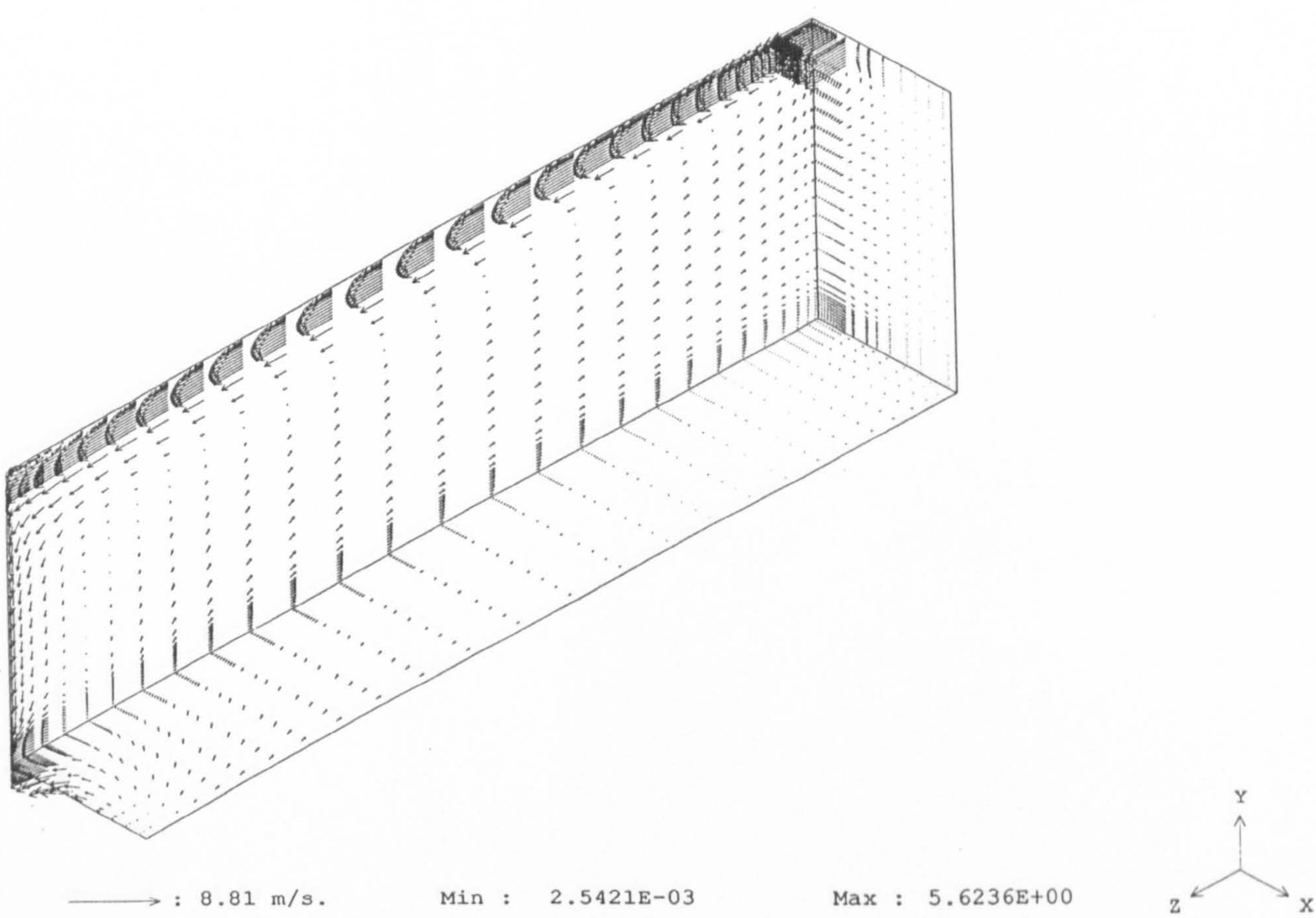

Figure 4.6 Velocity vector distribution in the planes x/W = 0.0, y/H = 0.0 and z/L = 0.0, Re = 3600; standard κ–ε turbulence model.

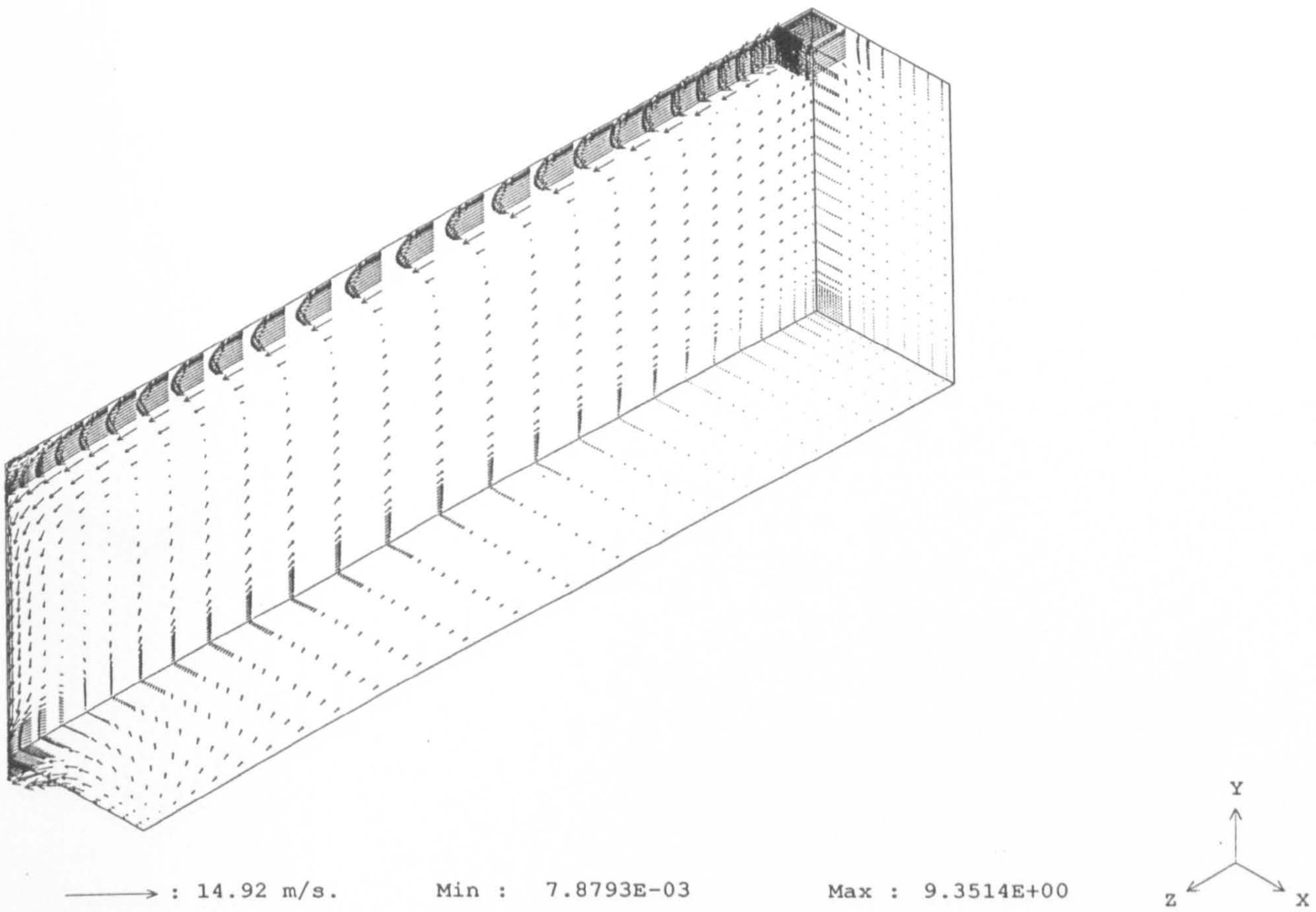

Figure 4.7 Velocity vector distribution in the planes x/W = 0.0, y/H = 0.0 and z/L = 0.0; Re = 6000, standard κ–ε turbulence model.

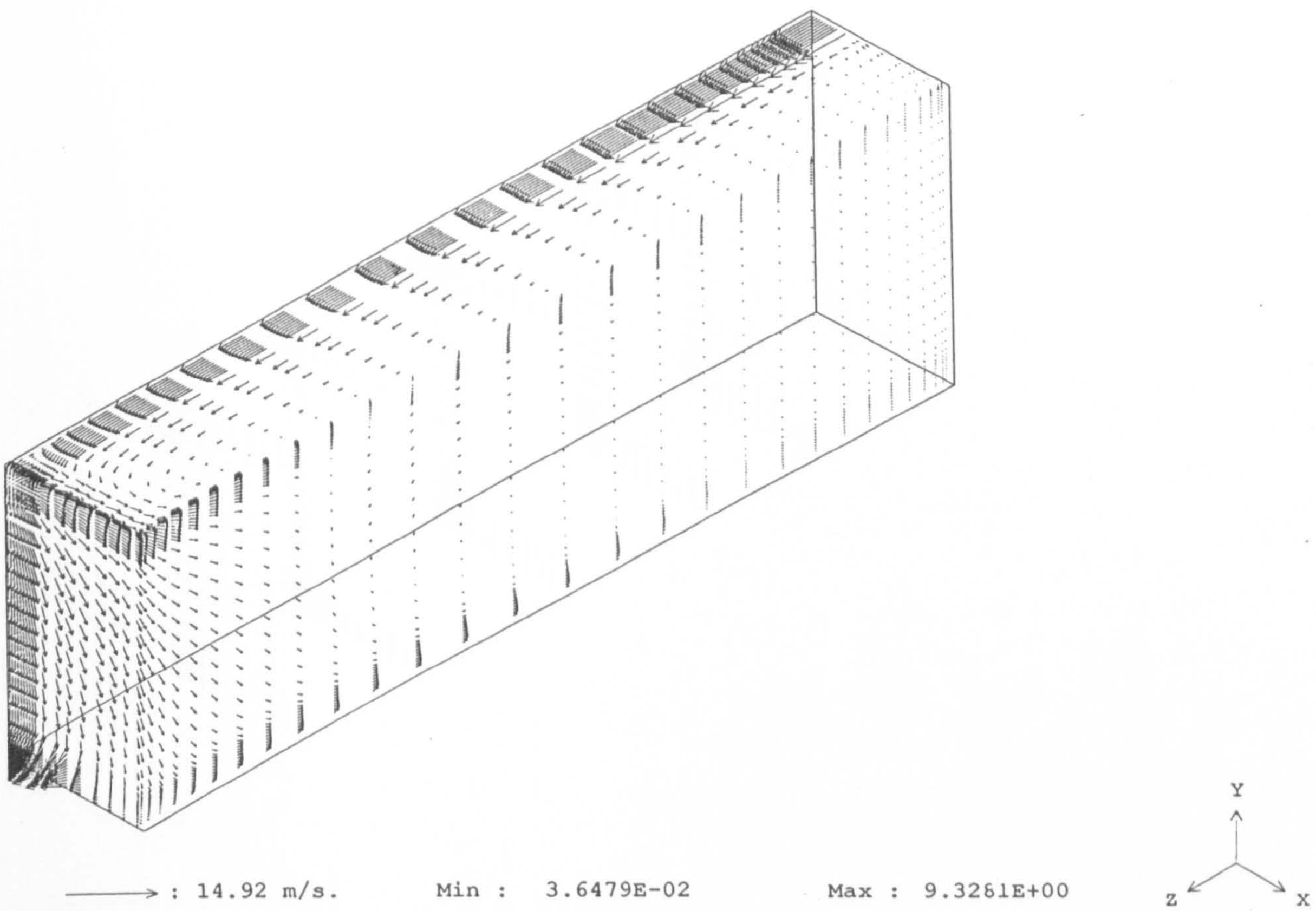

Figure 4.8 Velocity vector distribution in the planes x/W = 0.5, y/H = 1.0 and z/L = 3.0; Re = 6000, standard κ–ε turbulence model.

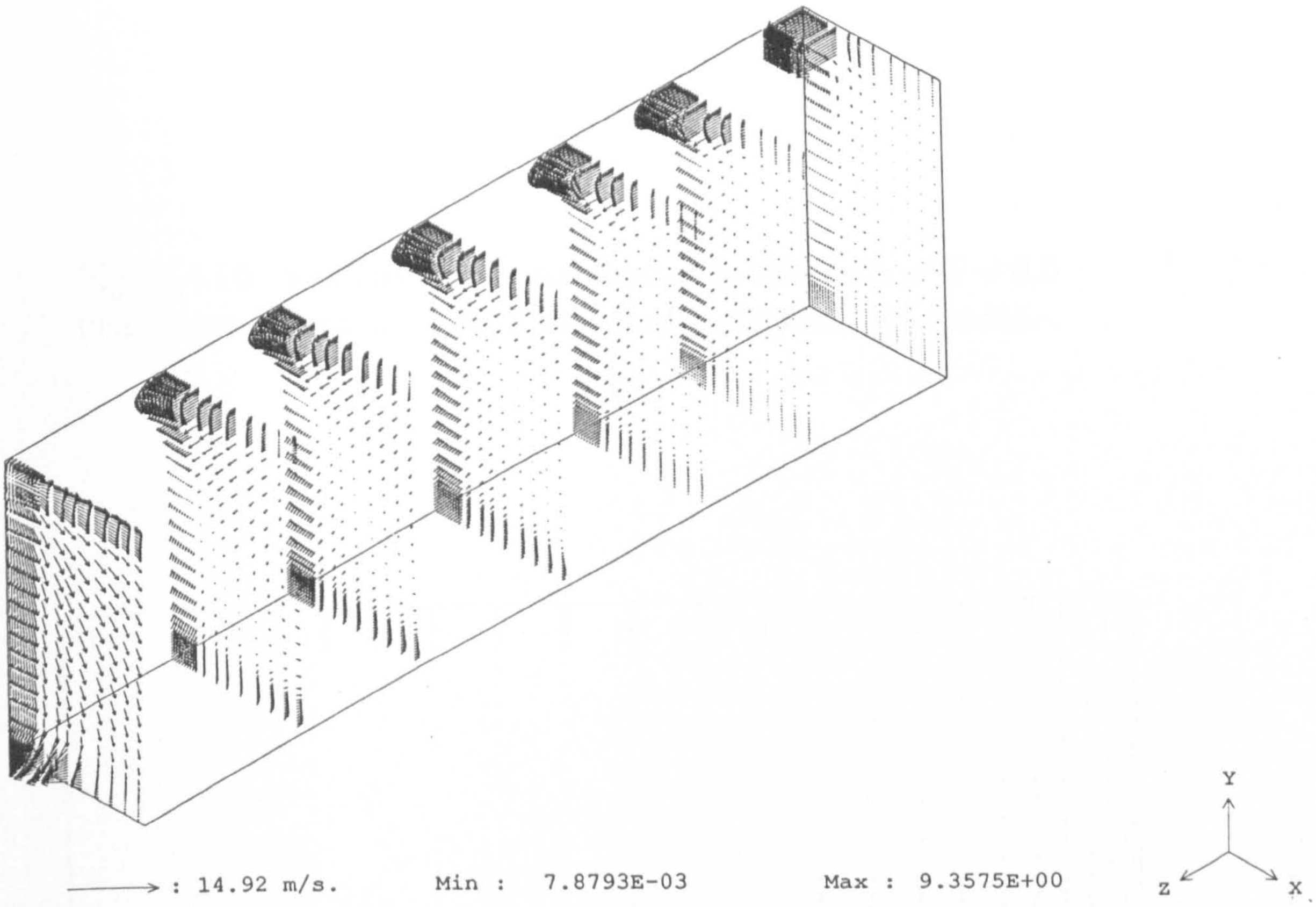

Figure 4.9 Velocity vector distribution in the planes z/L = 0.0, 0.5, 1.0, 1.5, 2.0, 2.5, and 3.0; Re = 6000, standard $\kappa-\varepsilon$ turbulence model.

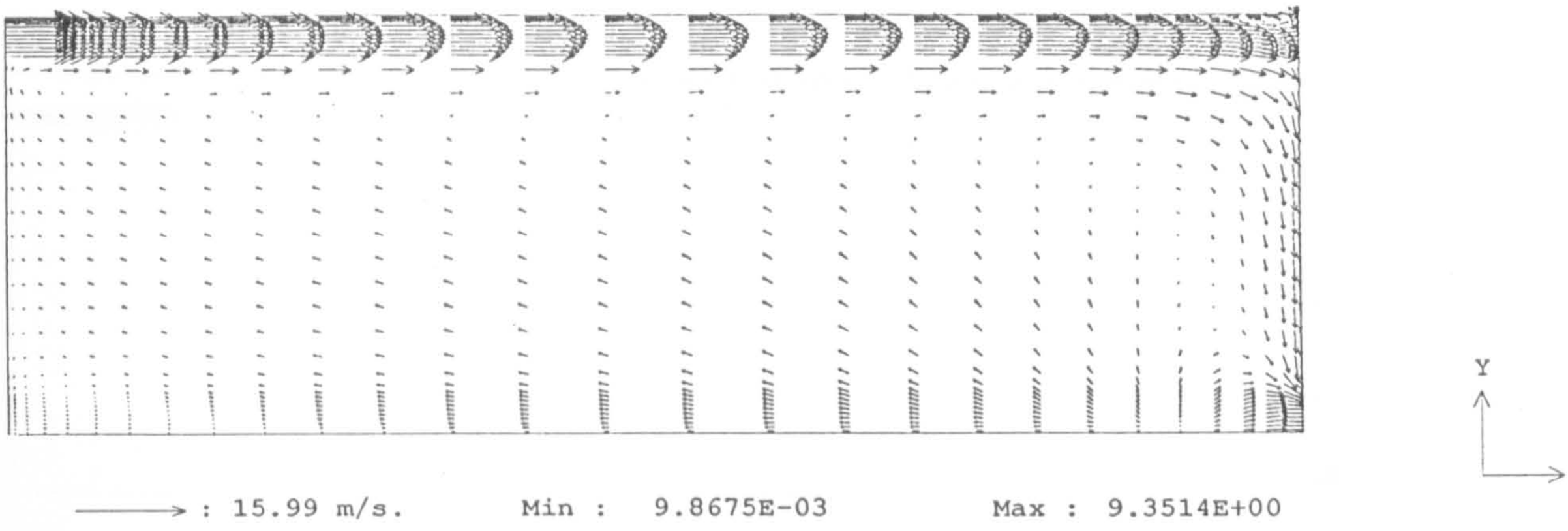

Figure 4.10 Velocity vector distribution in the plane x/W = 0.0 (symmetry plane); Re = 6000, standard κ–ε turbulence model.

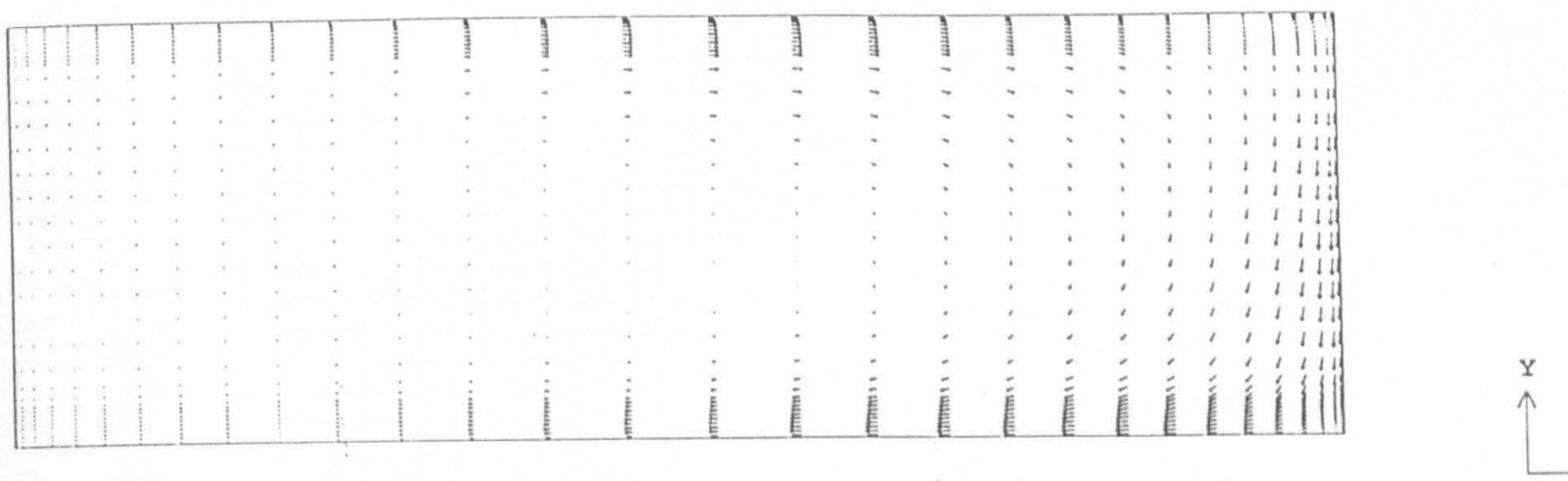

Figure 4.11 Velocity vector distribution in the plane x/W = 0.4; Re = 6000, standard κ–ε turbulence model.

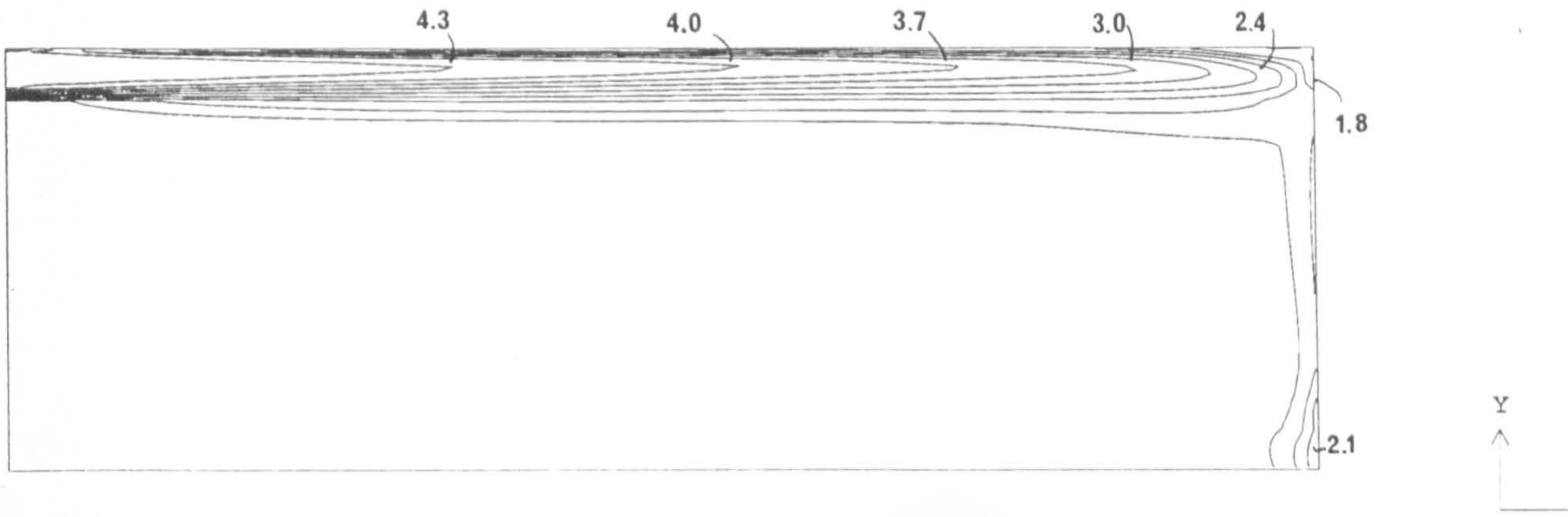

Figure 4.12 Turbulent kinetic energy contour in the plane x/W = 0.0 (symmetry plane); Re = 6000, standard κ–ε turbulence model. Contour values in m^2/s^2.

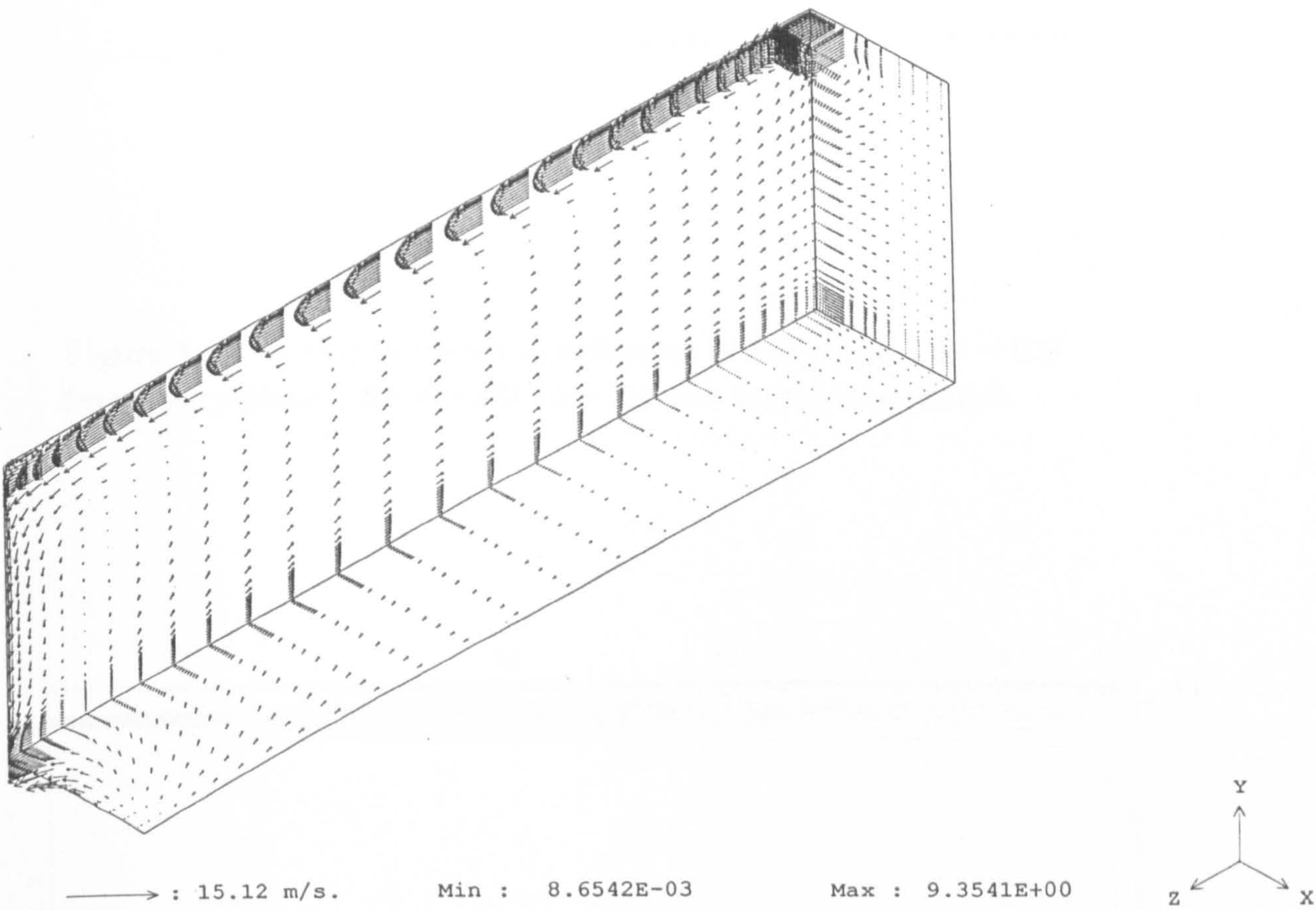

Figure 4.13 Velocity vector distribution in the planes x/W = 0.0, y/H = 0.0 and z/L = 0.0; Re = 6000, low-Re κ–ε turbulence model.

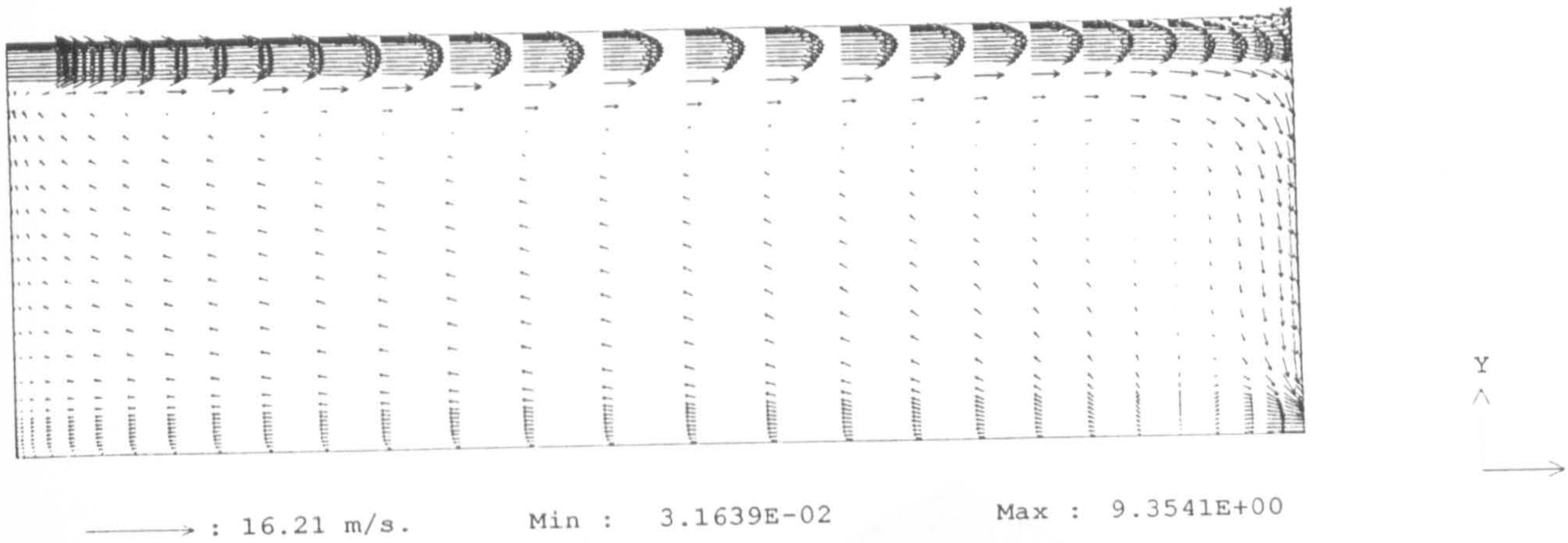

Figure 4.14 Velocity vector distribution in the plane x/W = 0.0 (symmetry plane); Re = 6000, low-Re κ–ε turbulence model.

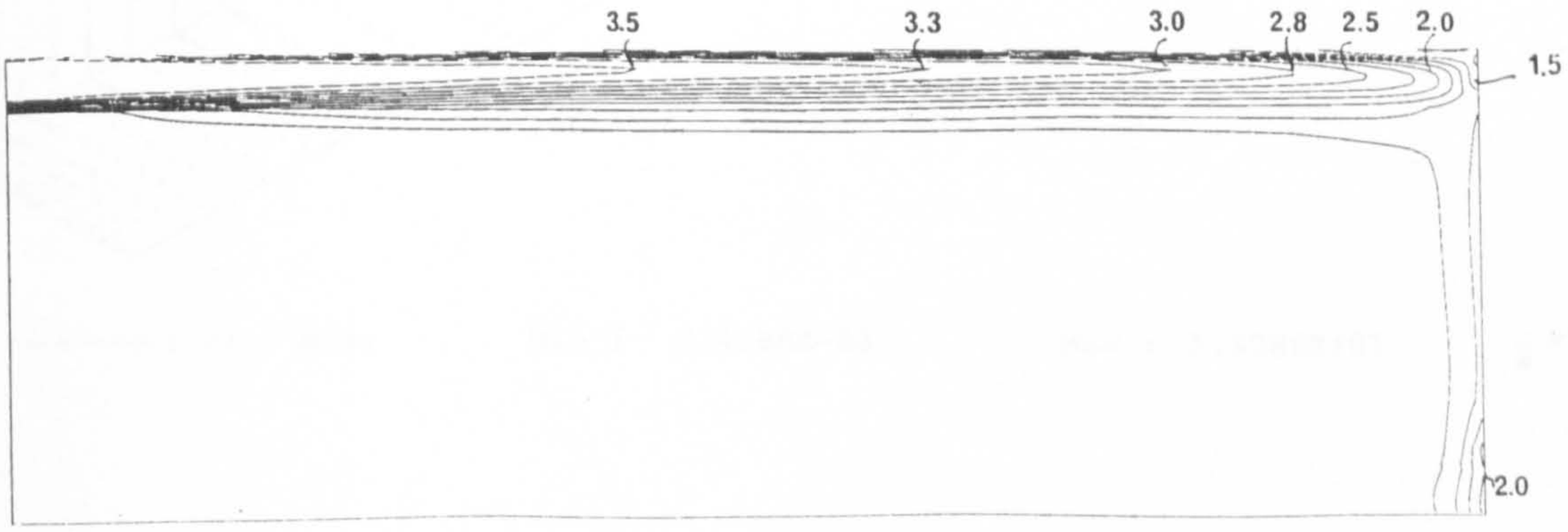

Figure 4.15 Turbulent kinetic energy contour in the plane x/W = 0.0 (symmetry plane); Re = 6000, low-Re κ–ε turbulence model. Contour values in m^2/s^2.

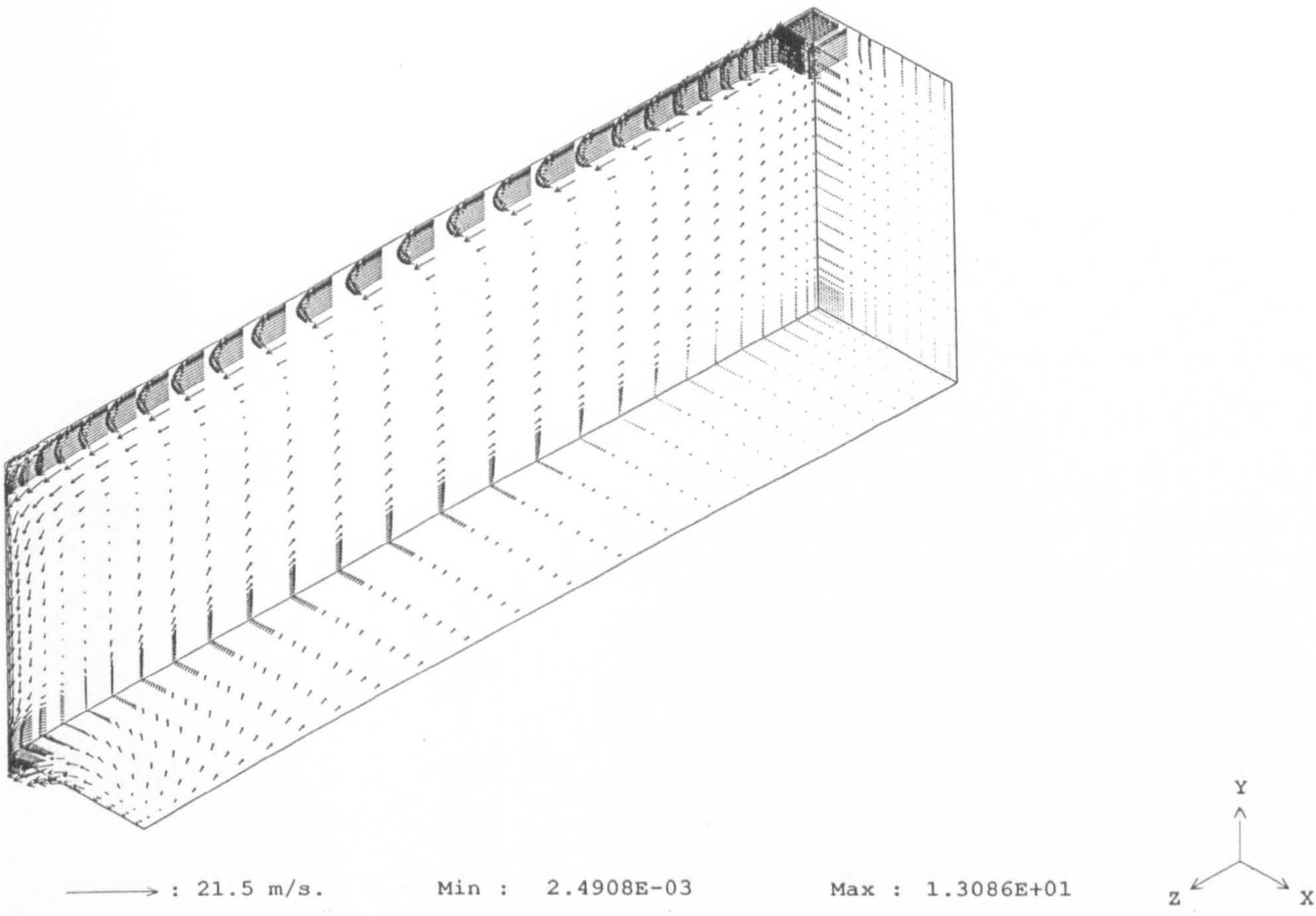

Figure 4.16 Velocity vector distribution in the planes x/W = 0.0, y/H = 0.0 and z/L = 0.0; Re = 8400, standard κ–ε turbulence model.

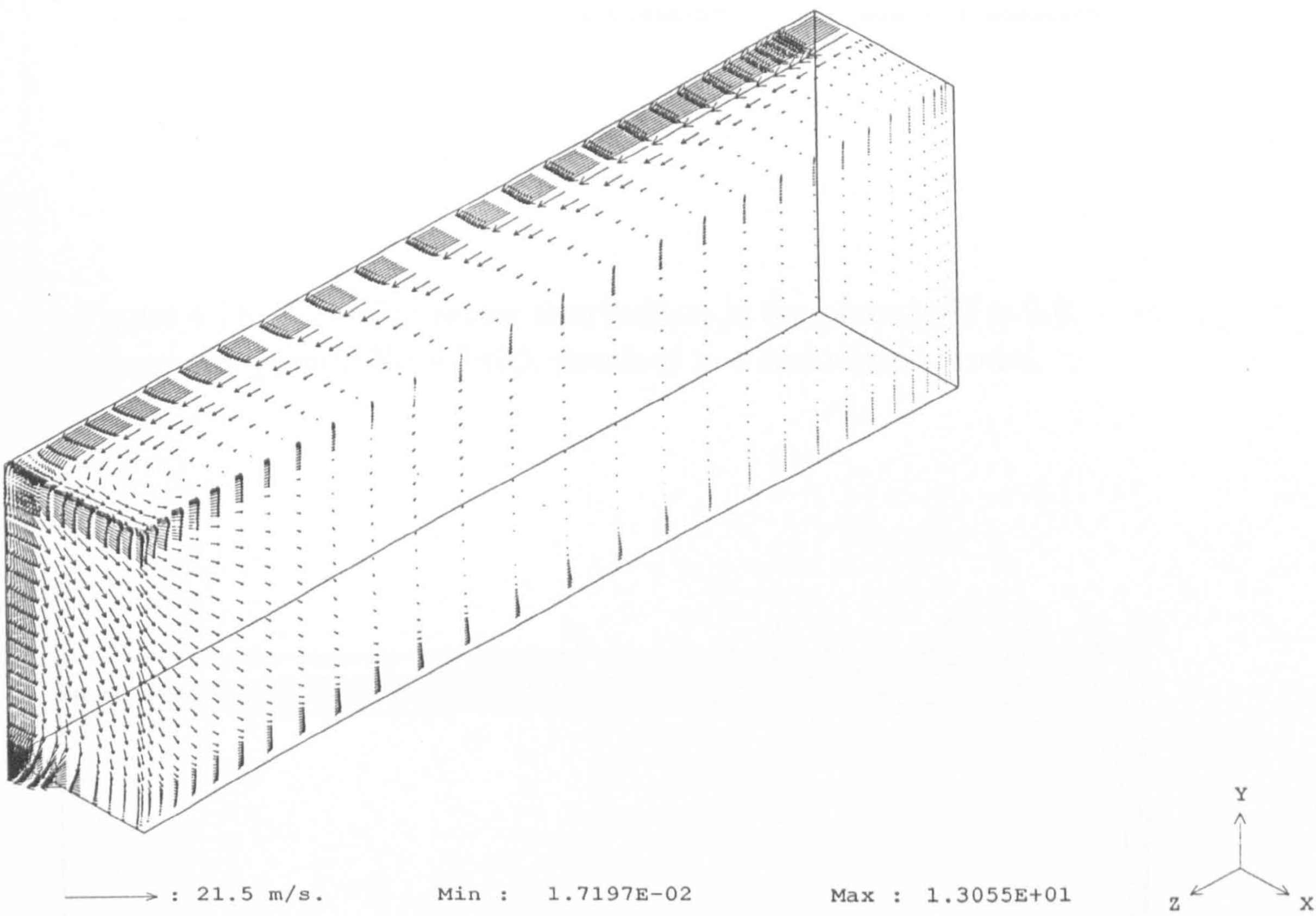

Figure 4.17 Velocity vector distribution in the planes x/W = 0.5, y/H = 1.0 and z/L = 3.0; Re = 8400, standard κ–ε turbulence model.

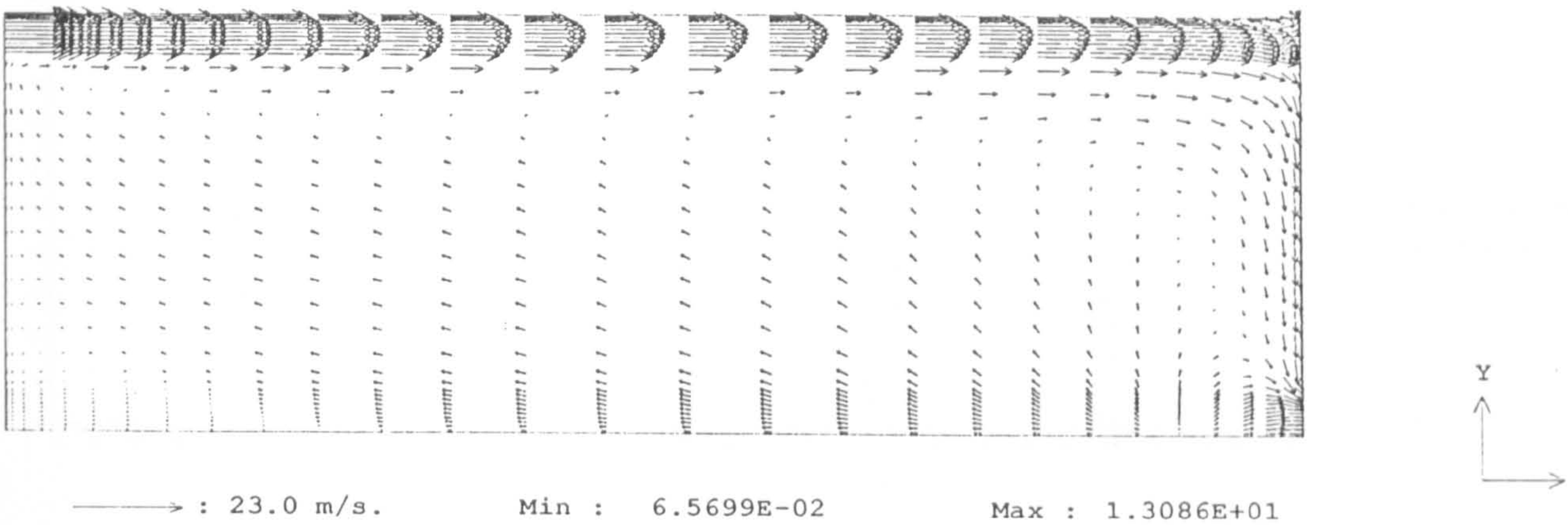

Figure 4.18 Velocity vector distribution in the plane x/W = 0.0 (symmetry plane); Re = 8400, standard κ–ε turbulence model.

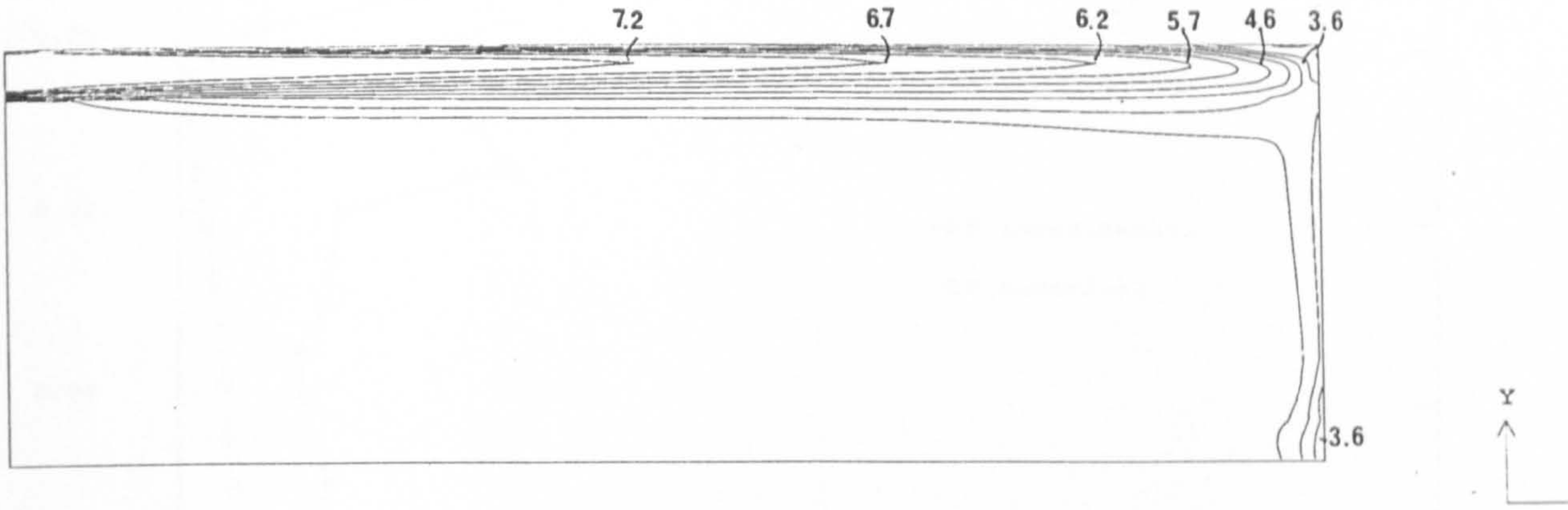

Figure 4.19 Turbulent kinetic energy contours in the plane x/W = 0.0 (symmetry plane); Re = 8400, standard κ–ε turbulence model. Contours values in m^2/s^2.

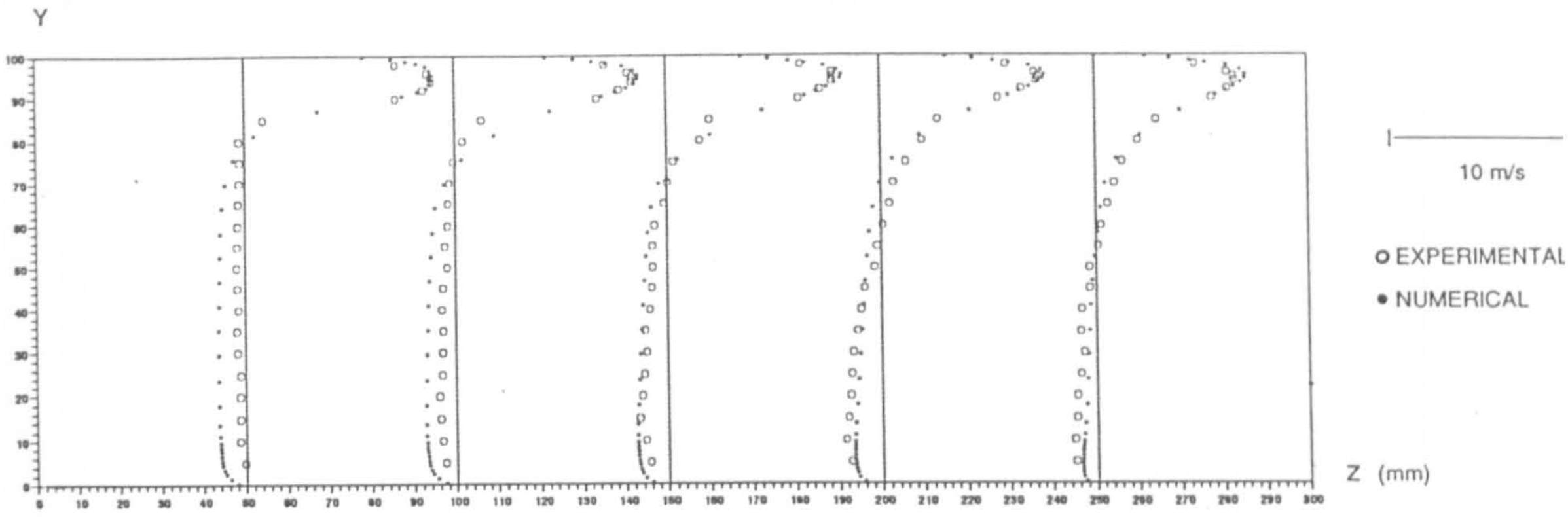

Figure 4.20 Measured and predicted mean velocity in the plane x/W = 0.0 (symmetry plane); Re = 6000.

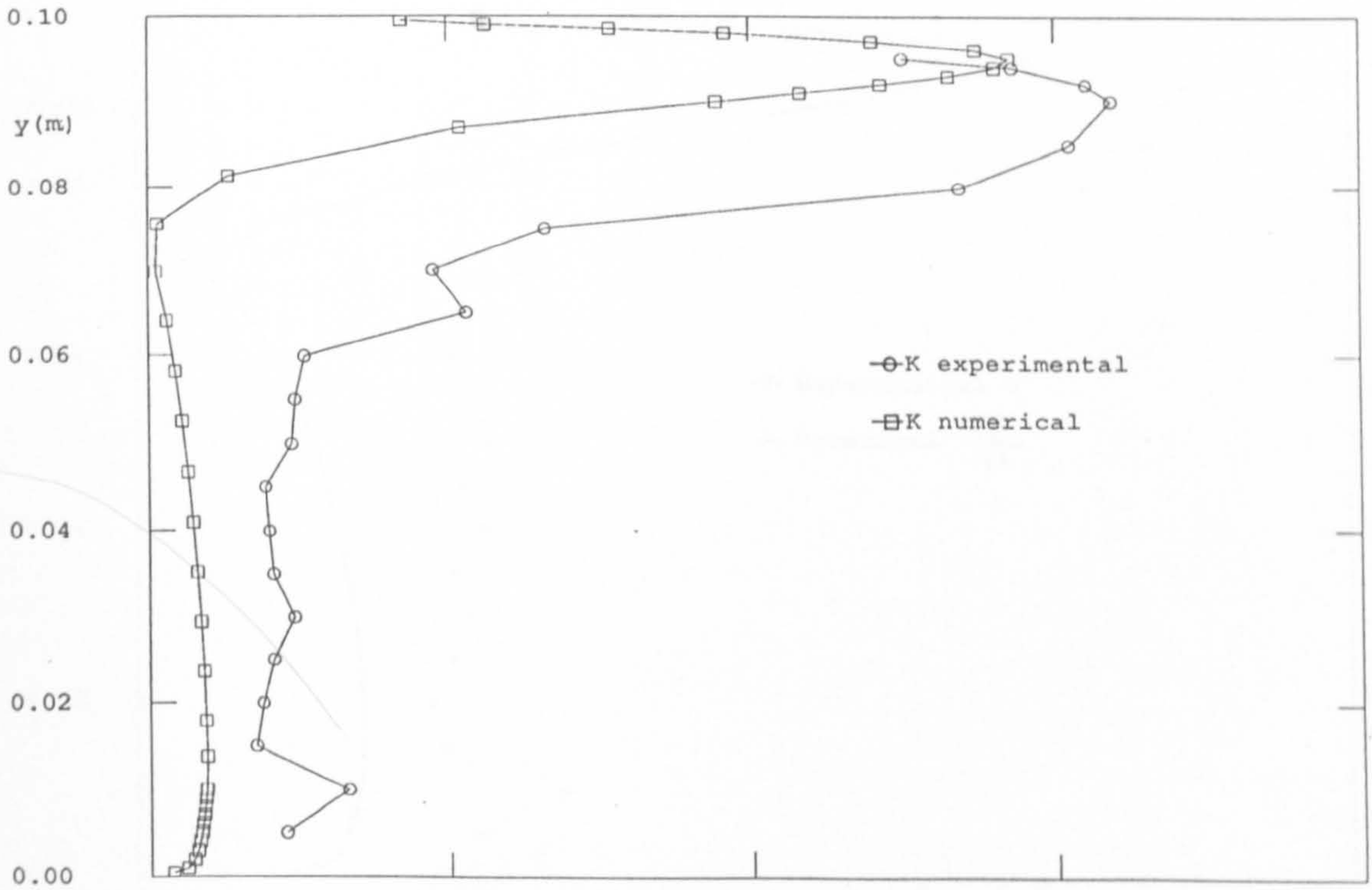

Figure 4.21 Measured and predicted kinetic energy of turbulence in the plane x/W = 0.0 at z = 150 mm, Re = 6000.

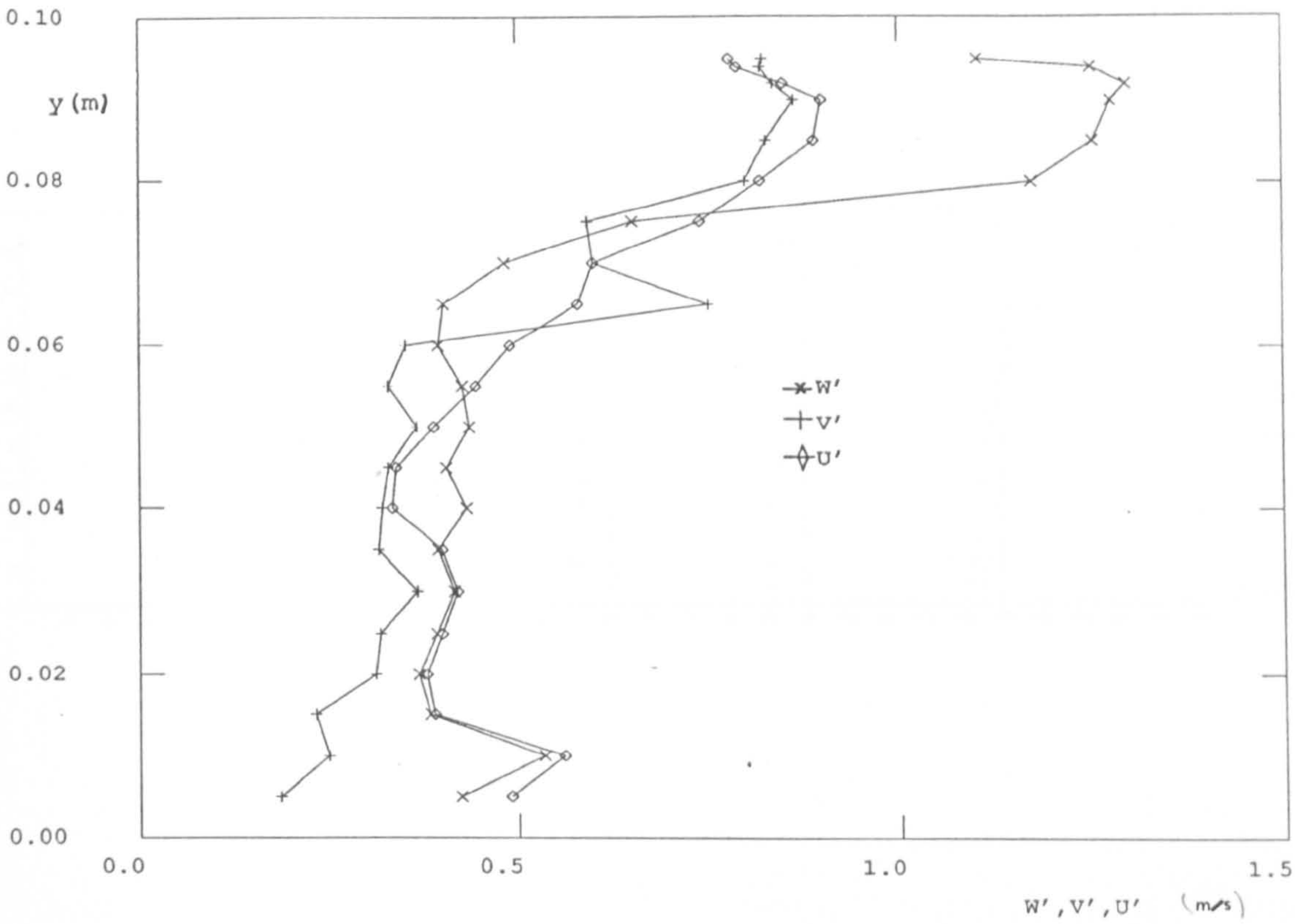

Figure 4.22 Measured rms velocities in the plane x/W = 0.0 at z = 150 mm, Re = 6000.

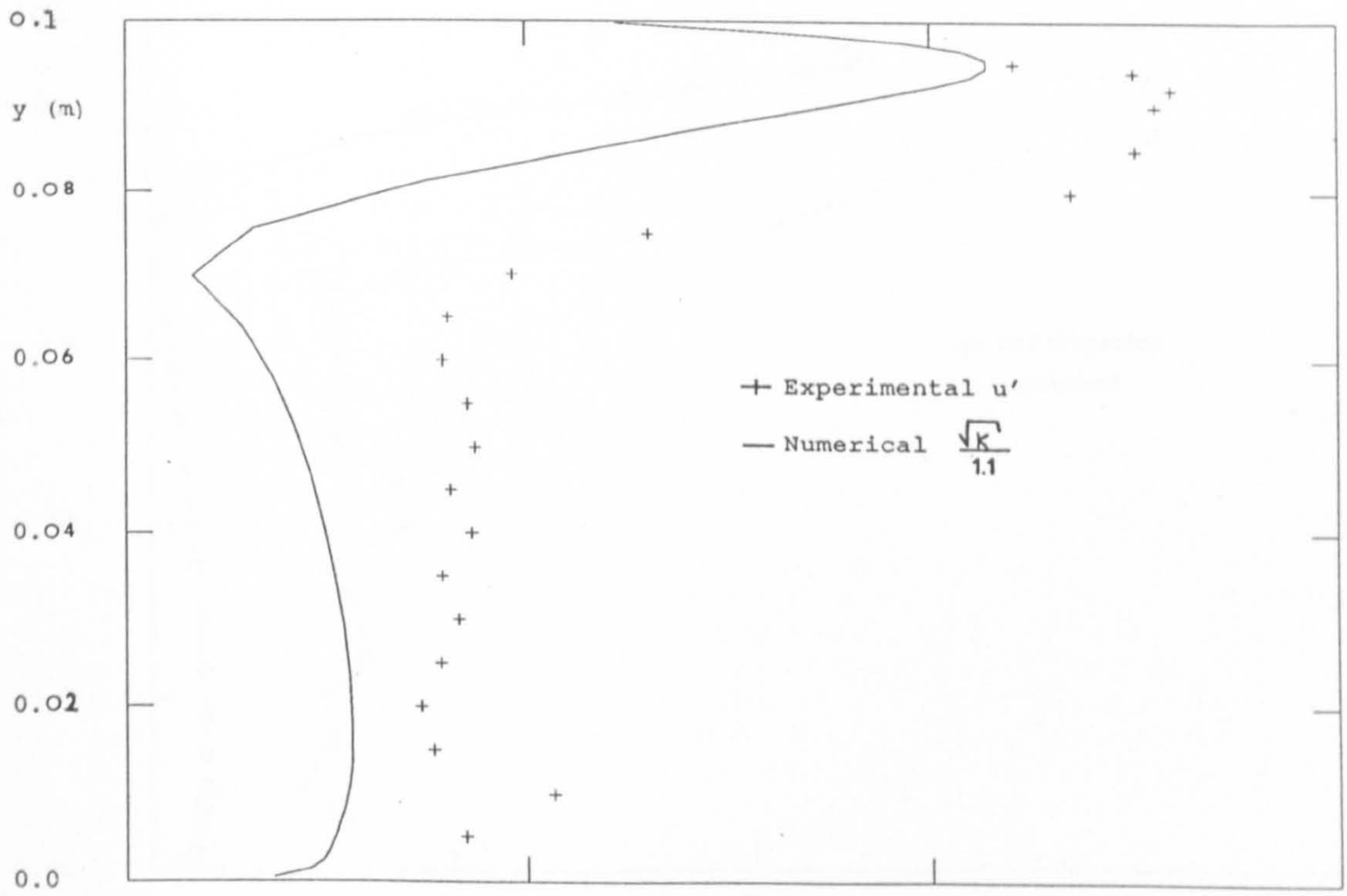

Figure 4.23 Measured and predicted rms velocities in the plane x/W = 0.0 at z = 150 mm, Re = 6000.

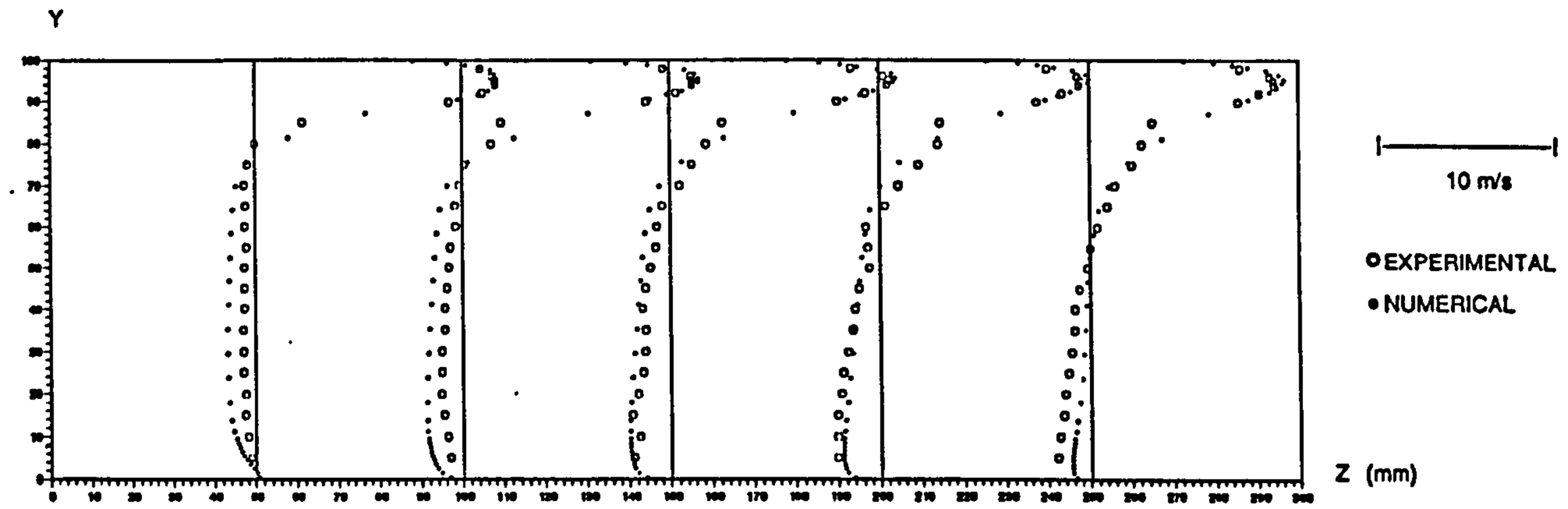

Figure 4.24 Measured and predicted mean velocity in the plane x/W = 0.0 (symmetry plane), Re = 8400.

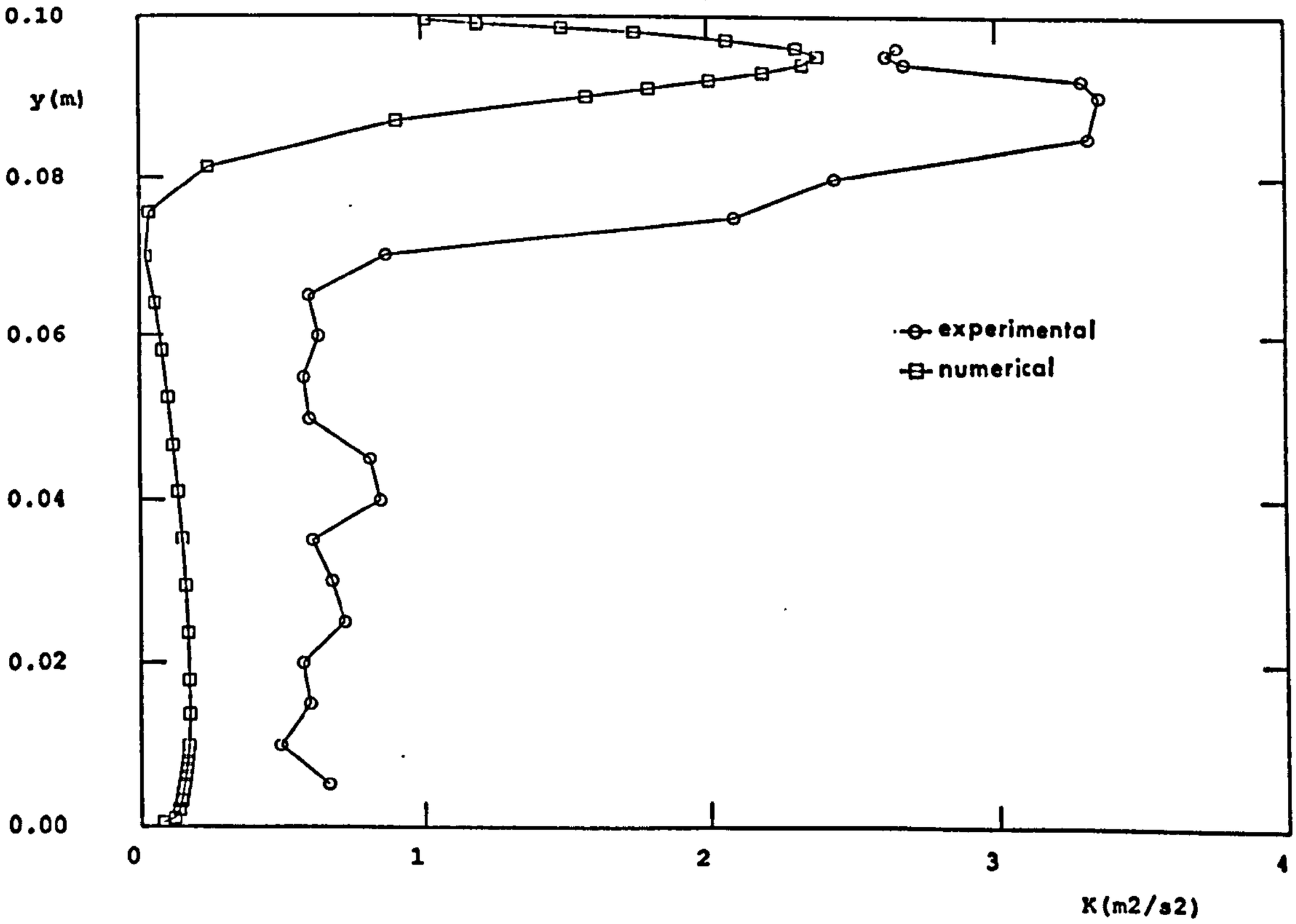

Figure 4.25 Measured and predicted turbulent kinetic energy in the plane x/W = 0.0 at z = 150 mm, Re = 8400.

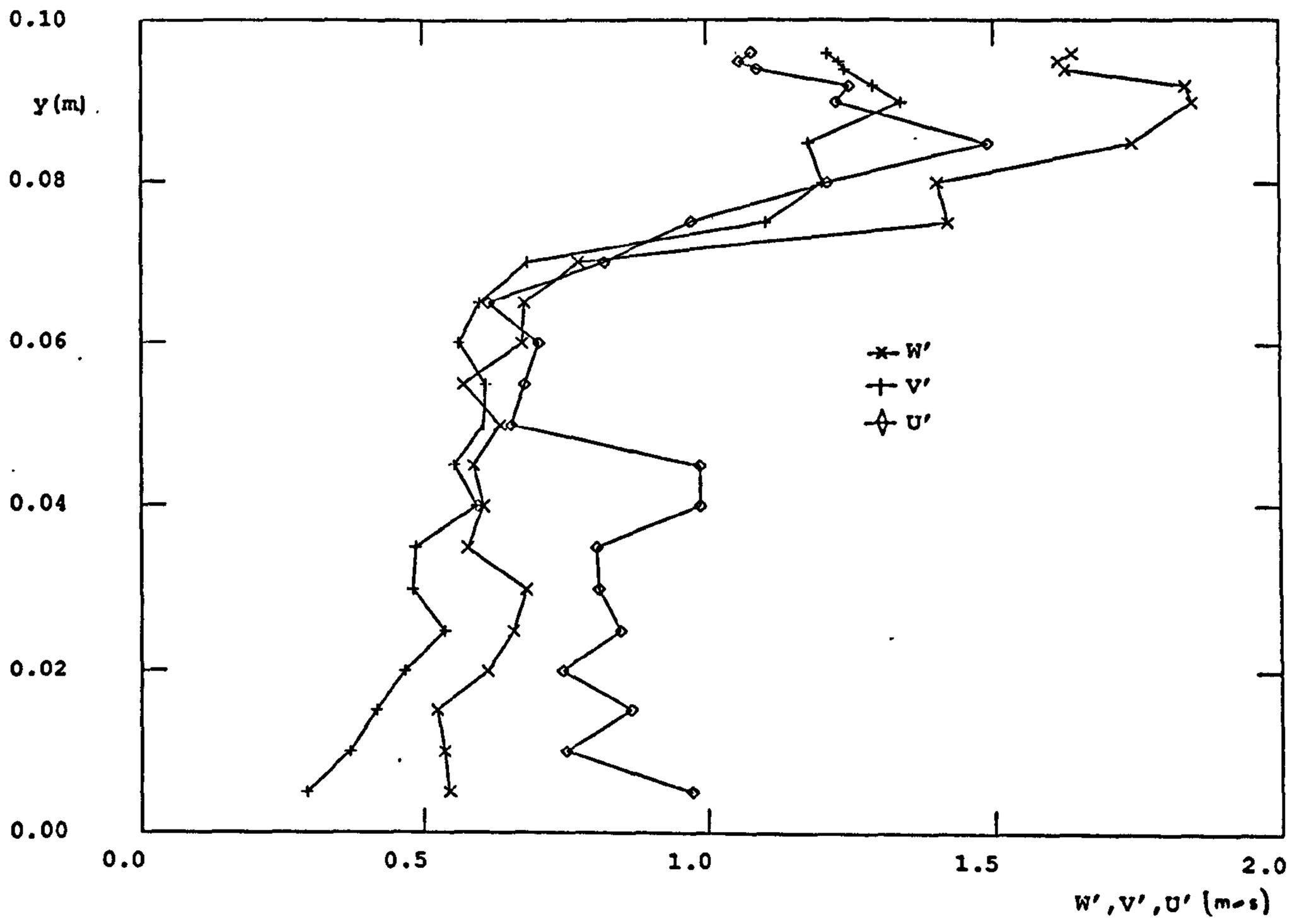

Figure 4.26 Measured rms velocities in the plane x/W = 0.0 at z = 150 mm, Re = 8400.

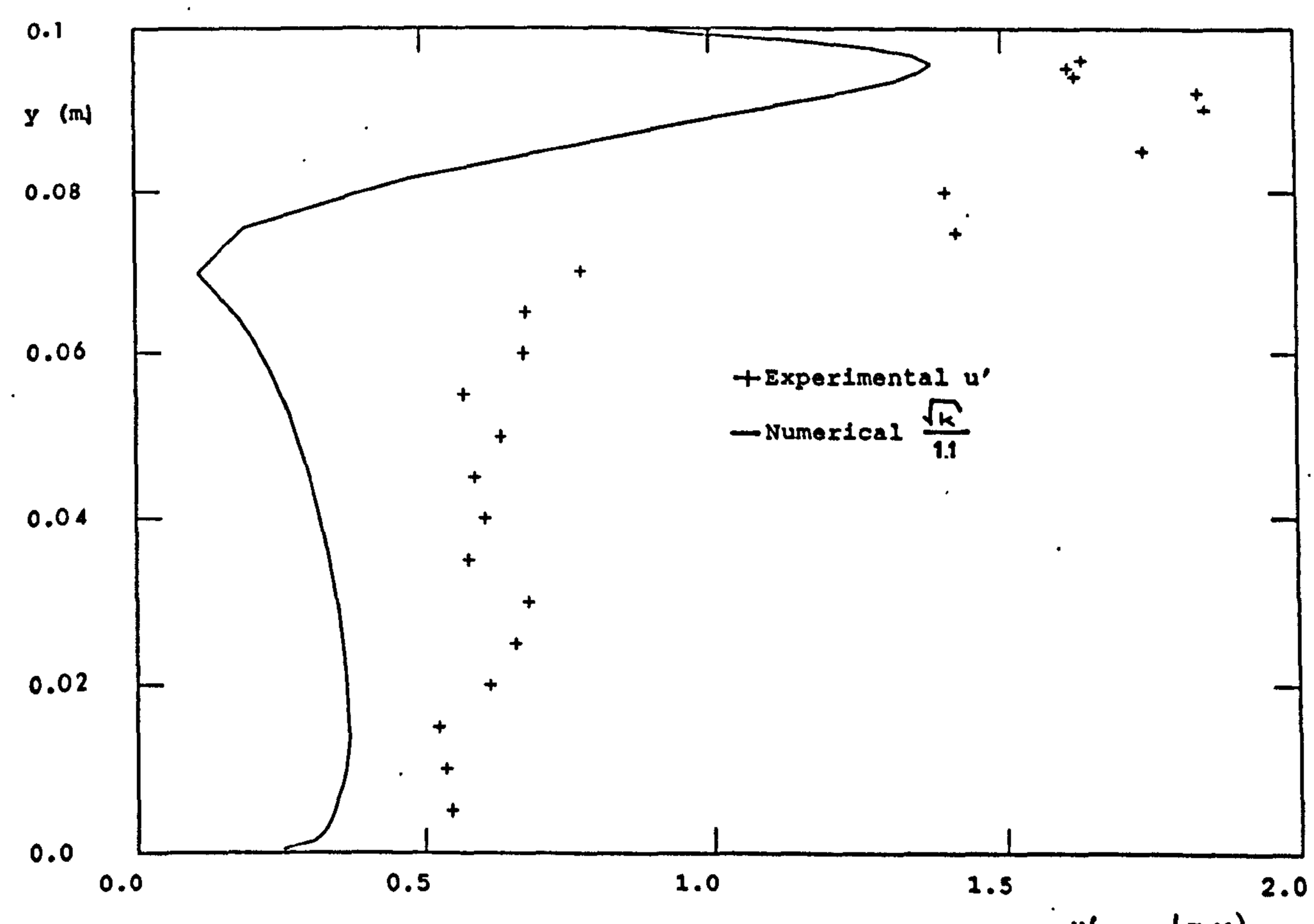

Figure 4.27 Measured and predicted rms velocities in the plane x/W = 0.0 at z = 150 mm, Re = 8400.

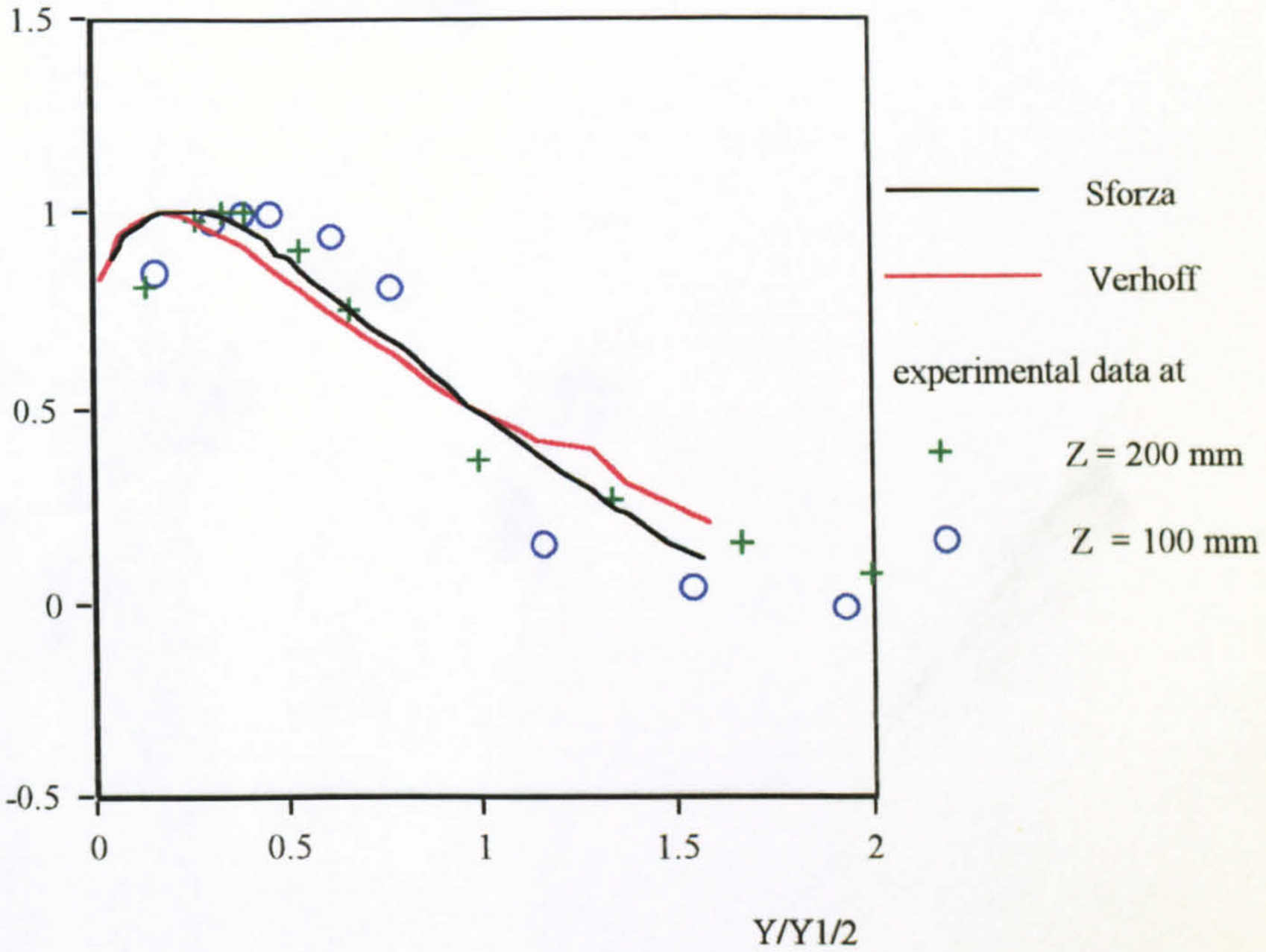

Figure 4.28 Comparison of measured non-dimensional velocity profiles at z = 100, 200 mm for Re = 6000 with data from Sforza and Herbst (1967), Verhoff (1963).

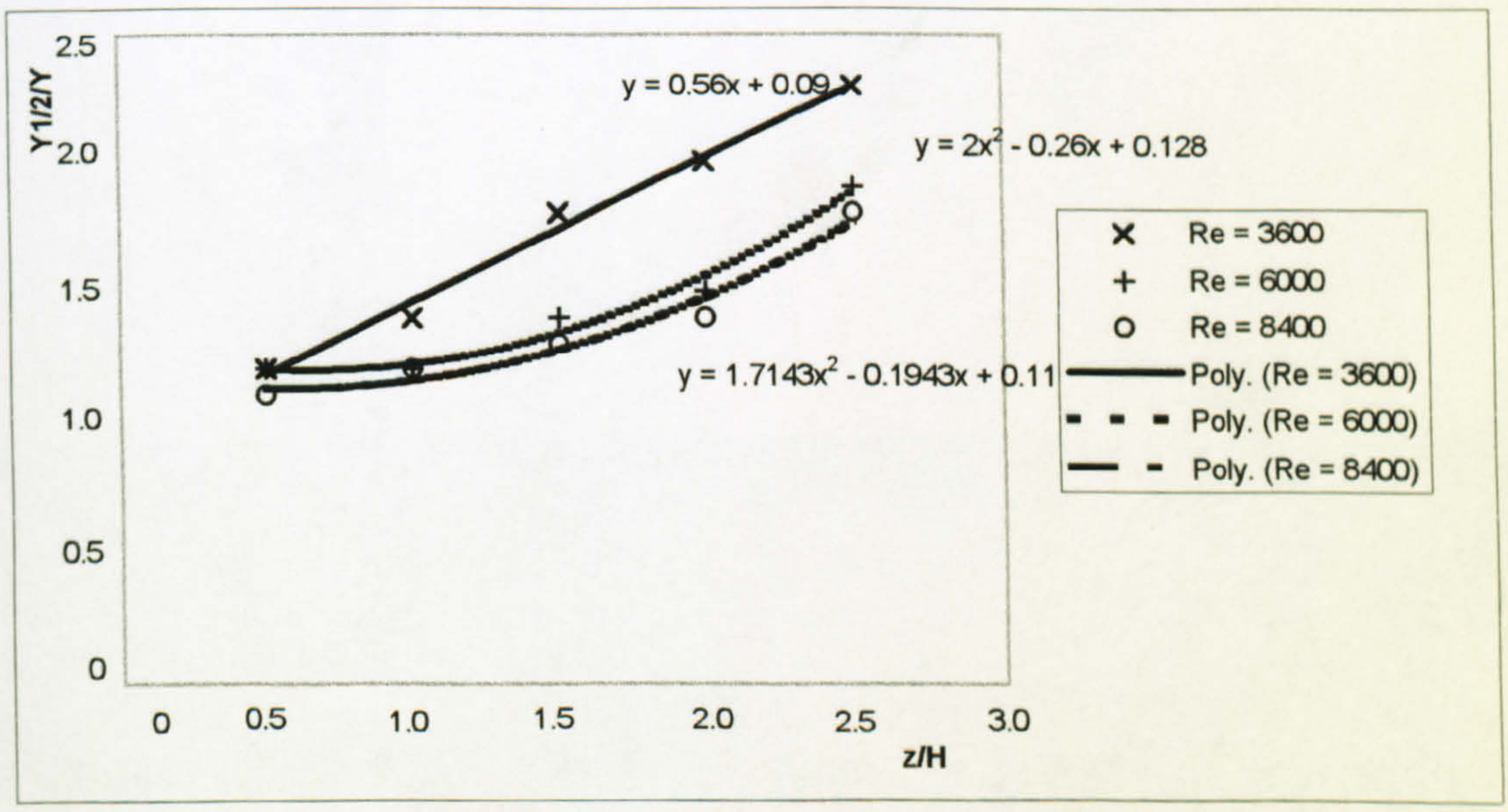

Figure 4.29 Variation of jet half width (horizontal jet spread) for different Re's numbers.

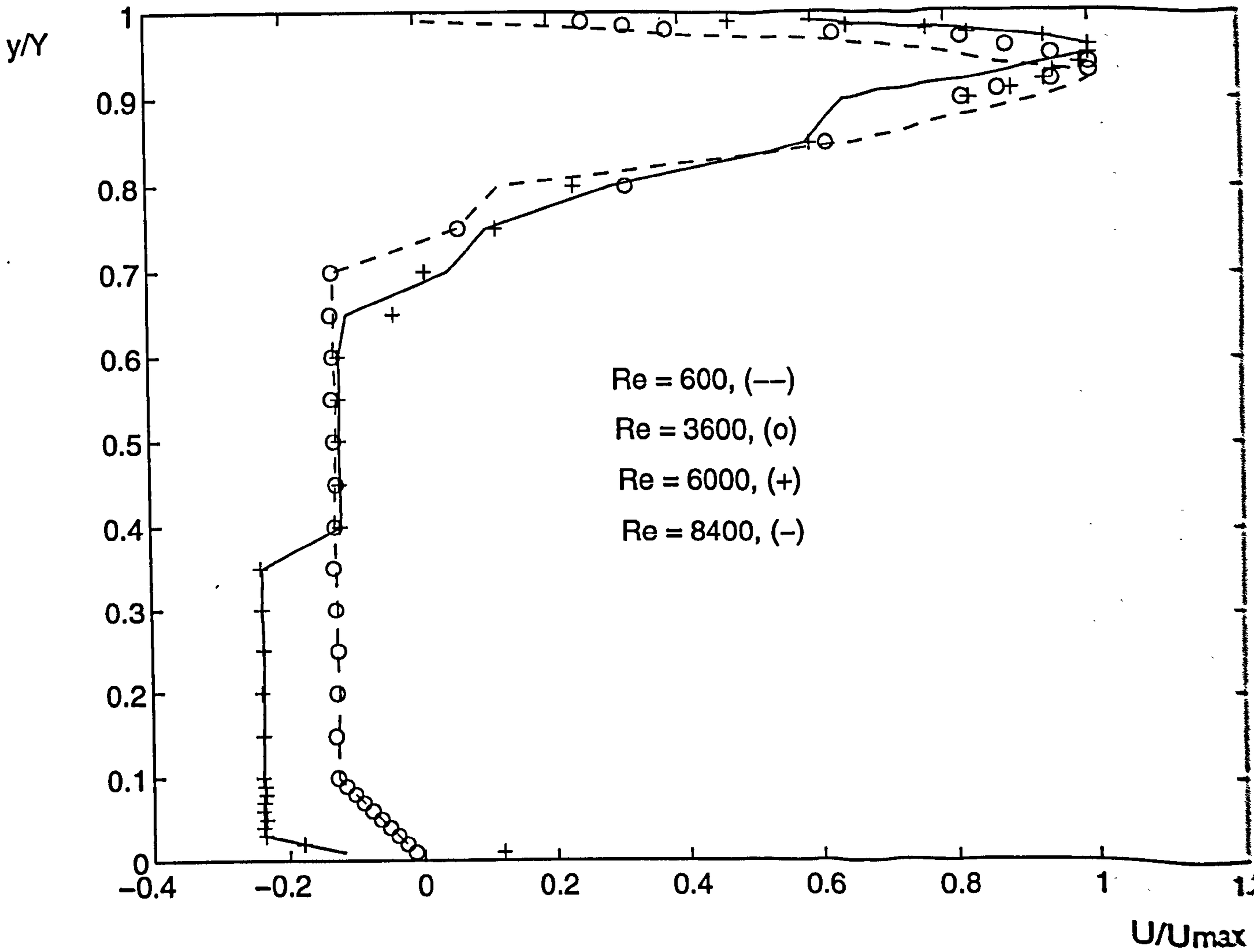

Figure 4.29b Non-dimensional air velocity profiles for Re = 600, 3600, 6000 and 8400.

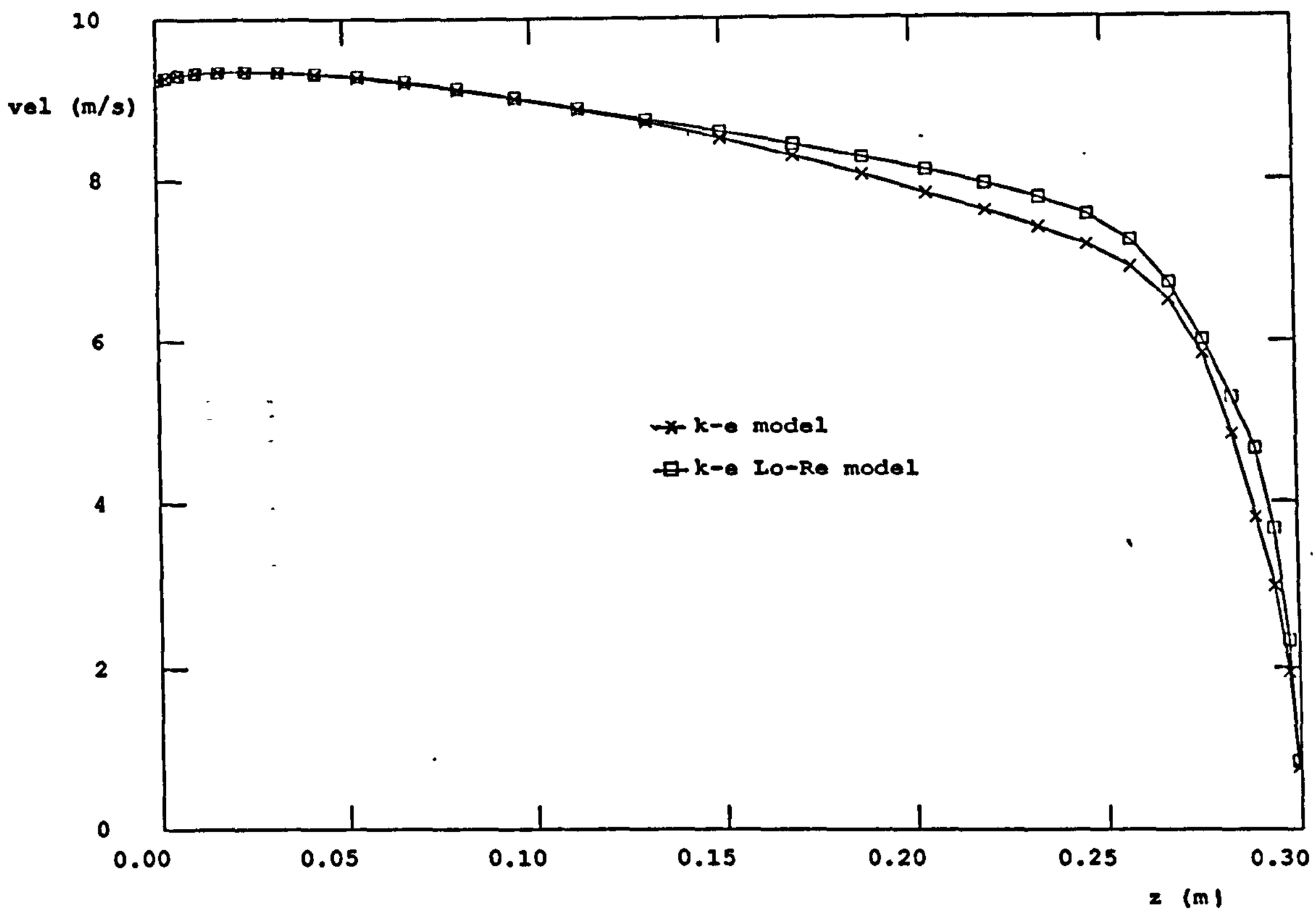

Figure 4.30 Predicted mean velocity decay in the plane x/W = 0.0 (symmetry plane) at y = (H-h)/2, Re = 6000.

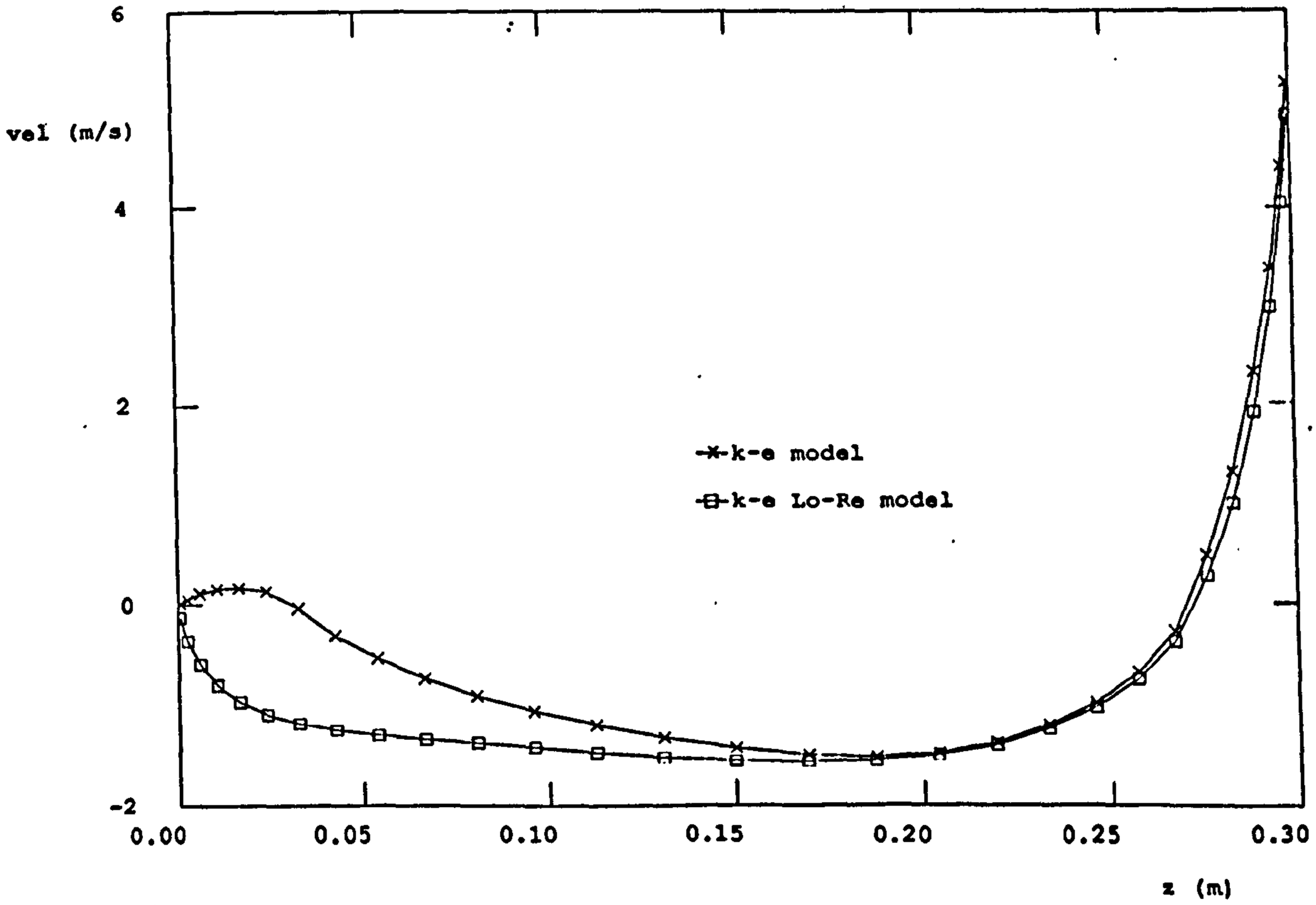

Figure 4.31 Predicted mean velocity in the occupied zone in the plane x/W = 0.0 at y = h/2, Re = 6000.

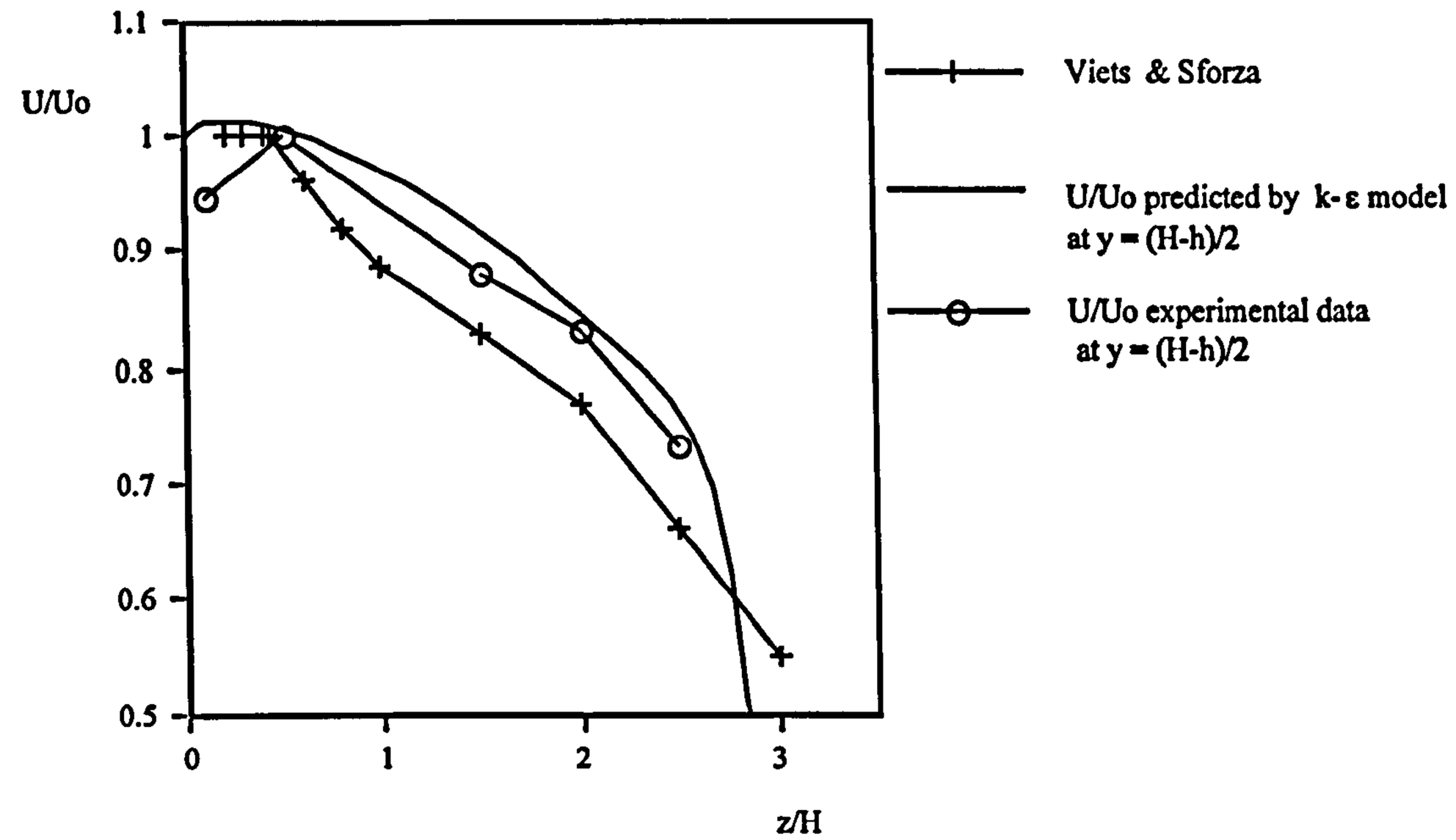

Figure 4.32 Measured and predicted velocity decay on symmetry plane and comparison with data of Viets and Sforza (1967).

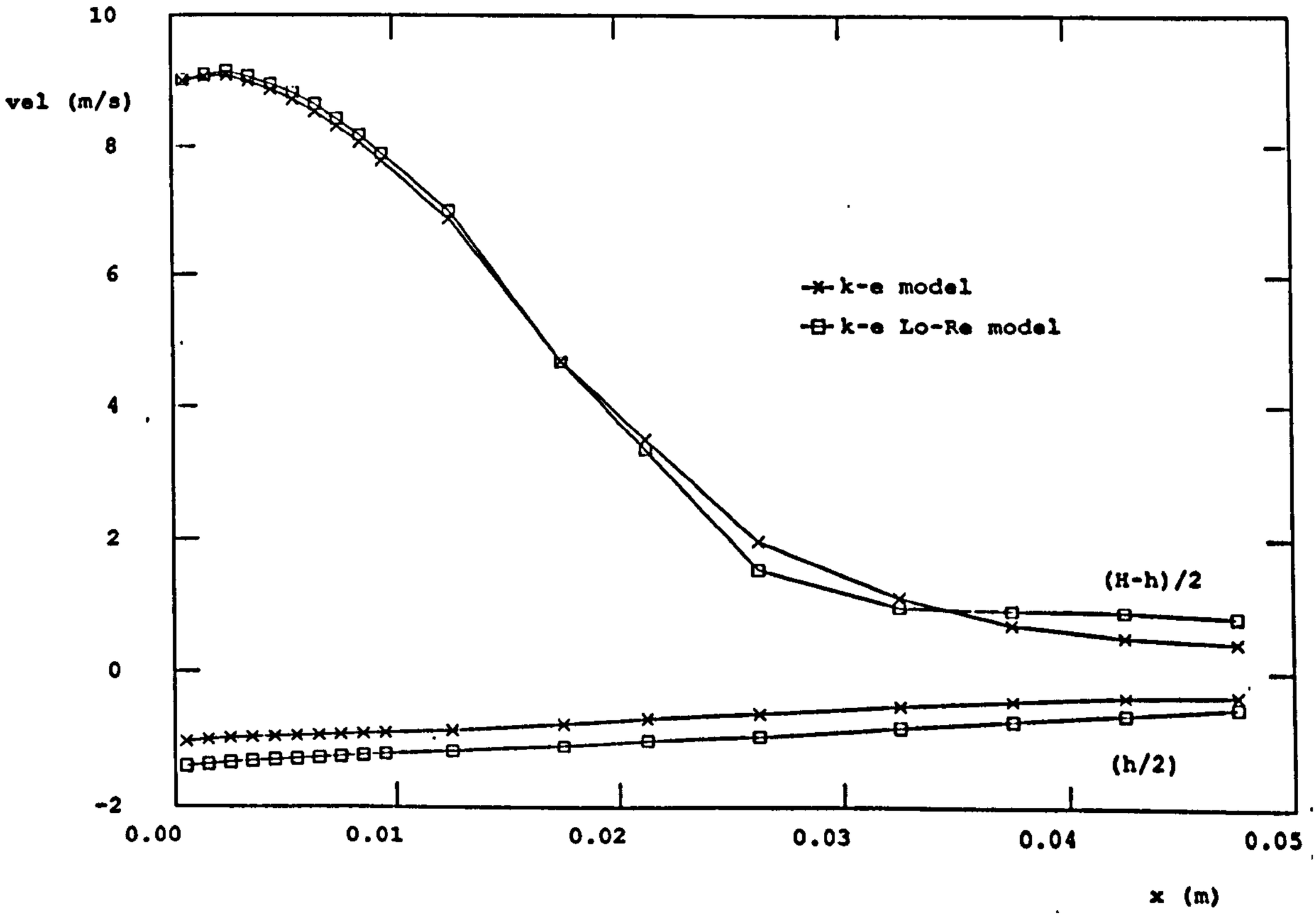

Figure 4.33 Predicted mean velocity at z = 100 mm on the horizontal planes y = (H-h)/2 and y = h/2, Re = 6000.

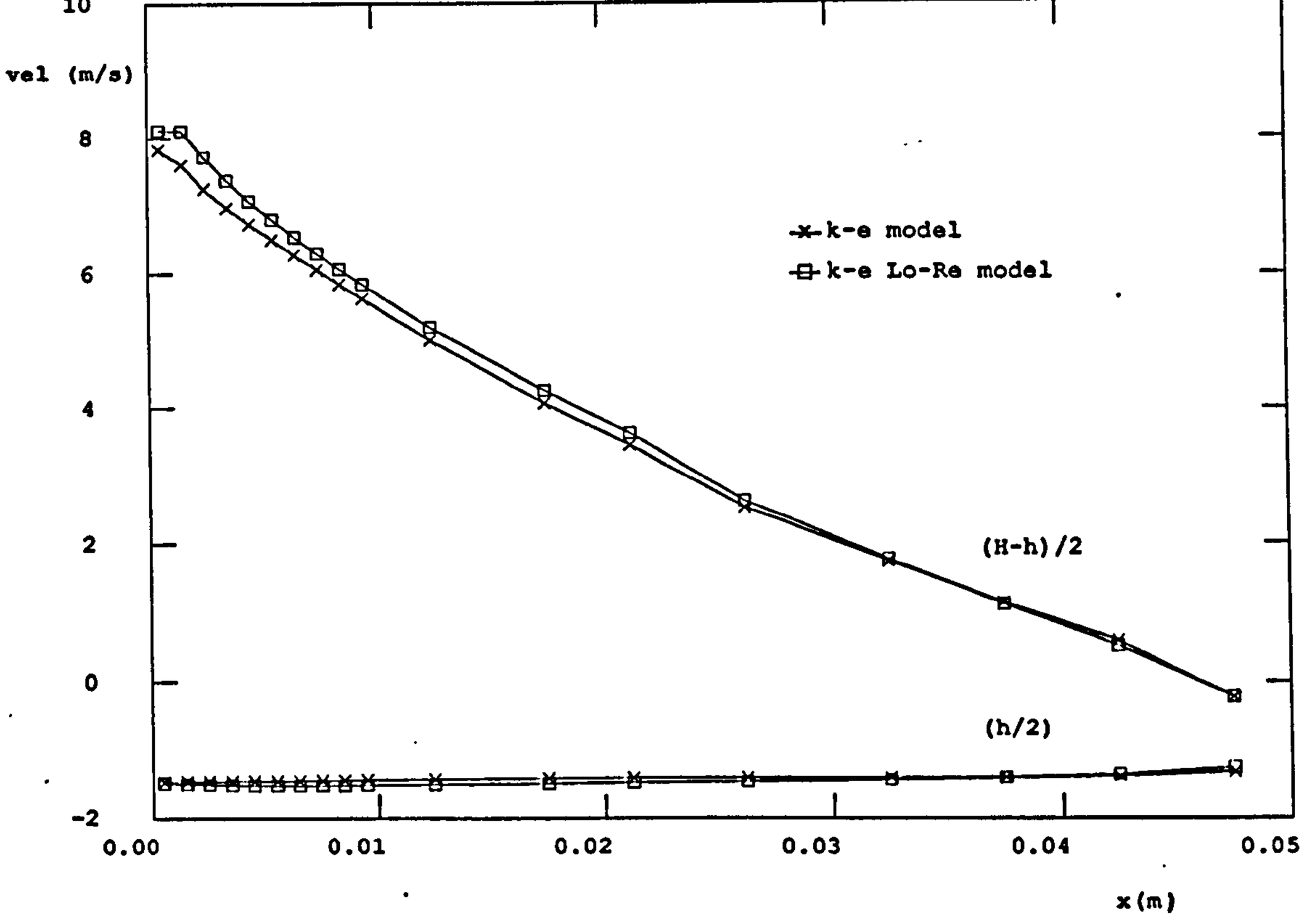

Figure 4.34 Predicted mean velocity at z = 200 mm on the horizontal planes y = (H-h)/2 and y = h/2, Re = 6000.

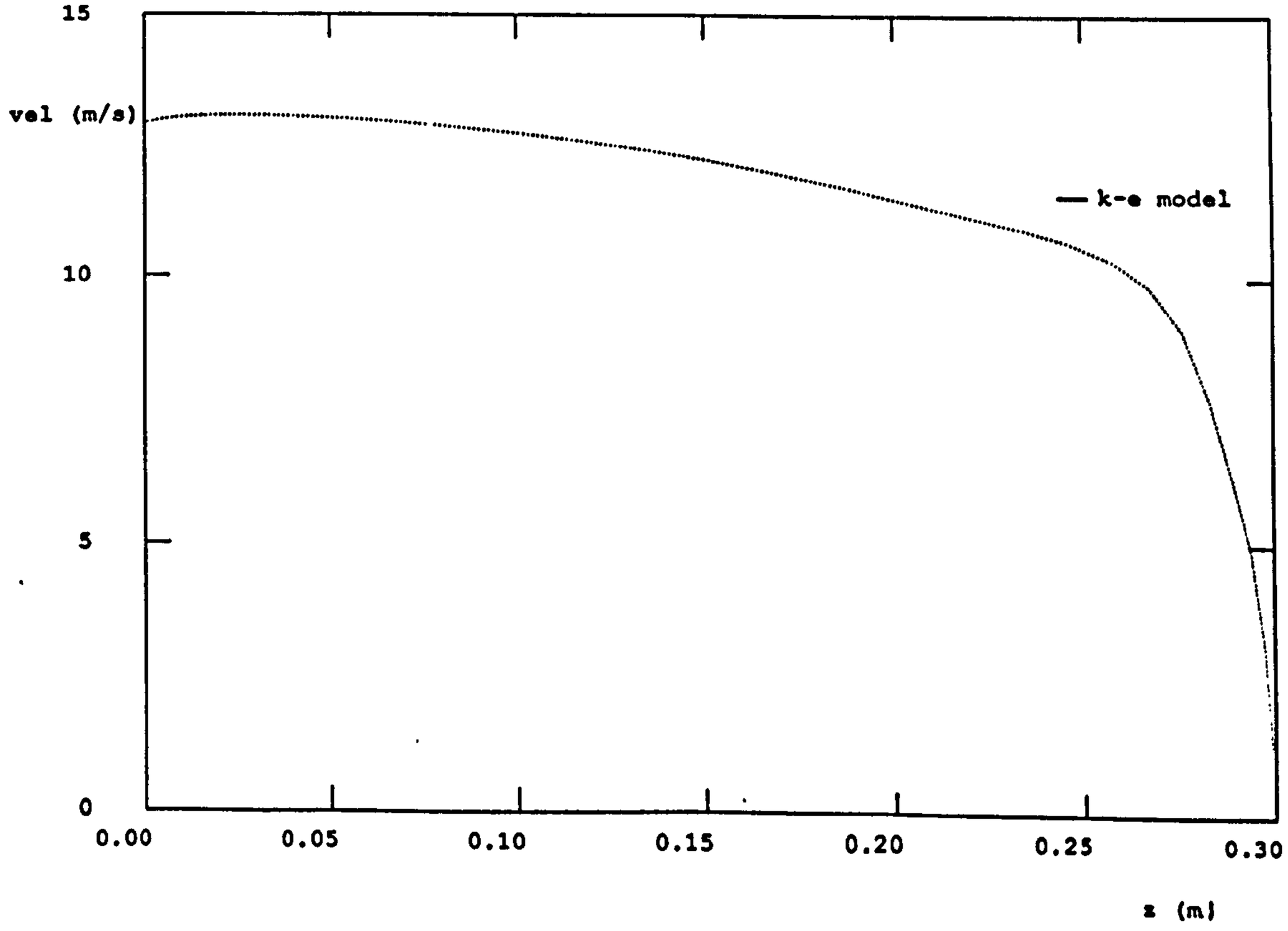

Figure 4.35 Predicted mean velocity decay in the plane x/W = 0.0 (symmetry plane) at y = (H-h)/2, Re = 8400.

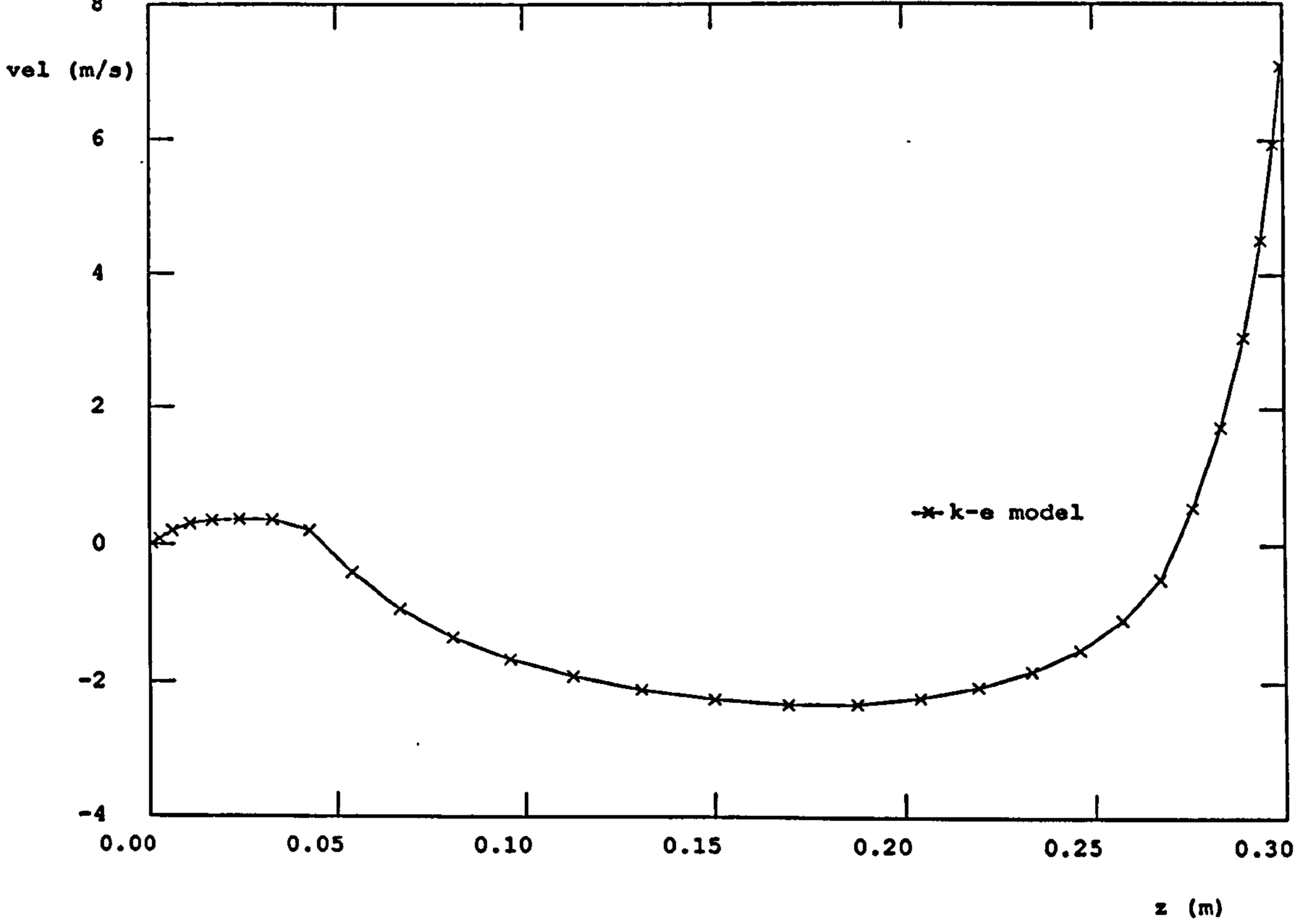

Figure 4.36 Predicted mean velocity in the occupied zone in the plane x/W = 0.0 at y = h/2, Re = 8400.

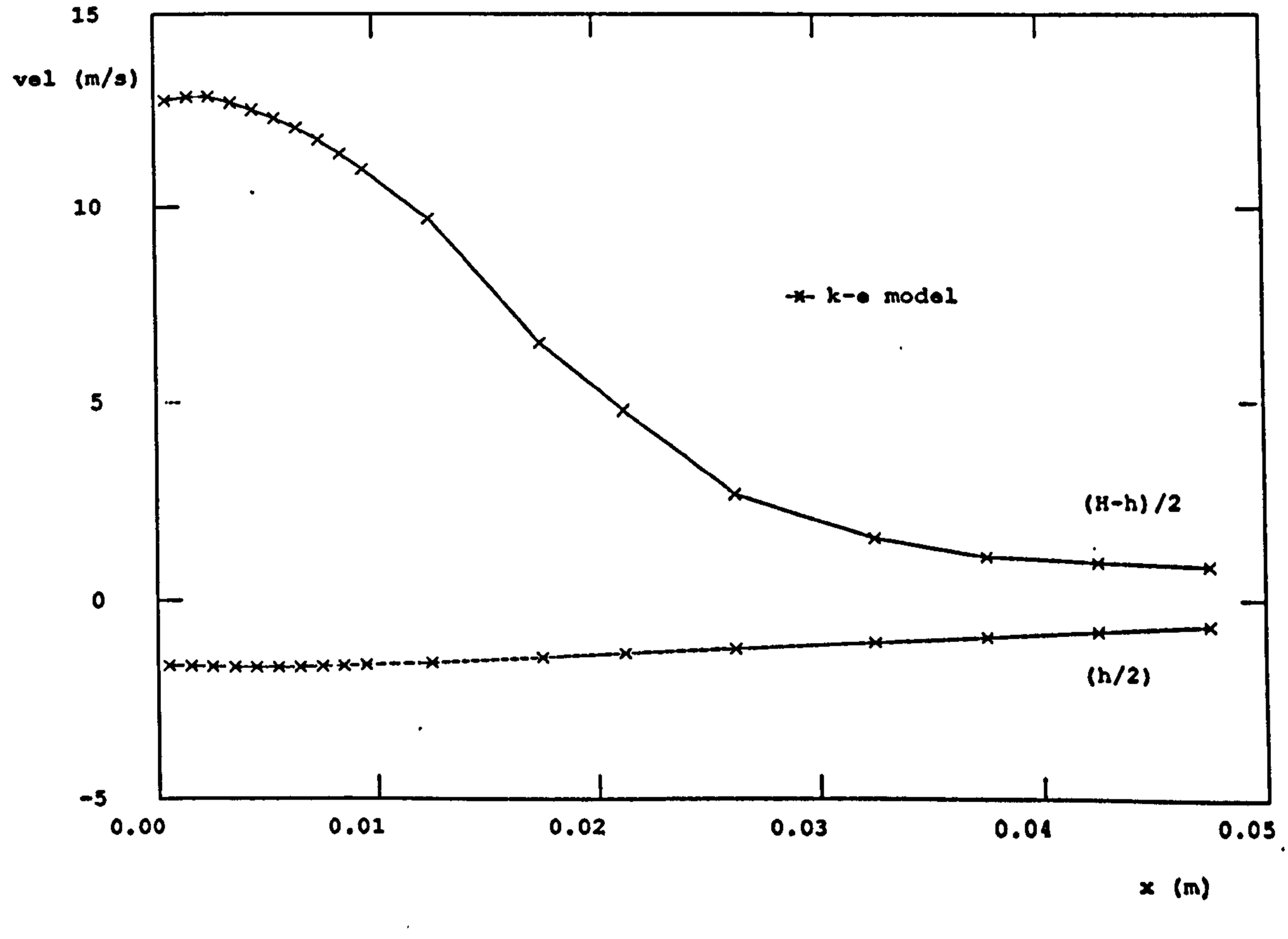

Figure 4.37 Predicted mean velocity at z = 100 mm on the horizontal planes y = (H-h)/2 and y = h/2, Re = 8400.

CHAPTER 5

MEASUREMENT AND PREDICTION OF THREE-DIMENSIONAL ISOTHERMAL FLOWS IN A CHAMBER VENTILATED BY A LOW-WALL JET.

5.1 Introduction

The results for the second flow configuration studied, a three-dimensional, square cross-section low-wall horizontal jet discharging into a rectangular chamber, are presented here. This second case corresponds to a side-wall mounted diffuser located close to the floor of a room, that forms a three-dimensional wall-jet. Several aspects of the flow are studied through numerical simulation and experiments. The predictions were assessed by comparison with the measured mean velocity components and the corresponding turbulence levels and the results comprise predictions of three-dimensional isothermal flows for two different flow rates. In particular the variations of the inlet jet throw, spread and drop with Re were quantified.

5.2 Experimental and computational details

5.2.1 Flow configuration and LDA measurement locations

Figure 5.1 shows the geometrical configuration of the second chamber studied, which has been described in detail in Chapter 2. Symmetry tests were made following the procedure explained in Chapter 4 for the first chamber. The tests corroborated the flow symmetry on either side of the symmetry plane. Four horizontal and four vertical locations were selected

where detailed profiles of the velocity and turbulence levels were obtained through LDA measurements. These where z/L = 1.0 and 2.0, in the x/H = 0.0 plane. LDA measurements of all three components of the velocity u, v, w, and the corresponding r.m.s. values u', v', w' were made, while for all other locations only the w and v components were measured.

5.2.2 Computational details

The numerical CFD code described in Chapter 3 was used to obtain the predictions shown in this chapter. The boundary conditions were the same as for the first chamber (Chapter 4), apart from the position of the inlet and outlet, which are located on the same walls but with the inlet being near the floor and the outlet near the ceiling (see Figure 5.1). The three components of the velocity were calculated as well as the pressure, the kinetic energy of turbulence (κ) and its dissipation rate (ε). Mesh independence tests were carried out and the same mesh of 18x36x30 volumes used for the first chamber was selected as it was found to provide a good compromise between accuracy and acceptable computer time cost. A characteristic comparison of velocity profiles at z = 200 mm calculated with four different mesh sizes is shown in Figure 5.2. It can be seen that with the 3 finer meshes the results are nearly identical. The flow over half of the chamber was simulated only, as the measurements showed that the flow was symmetrical about the x/W = 0.4 plane. Isothermal conditions were assumed throughout. The numerical mesh used for the calculation can be seen in Figure 5.3. Each numerical solution comprised 3000 iterations and took approximately 1.3 hours of CPU time on a VAX 4100 machine.

5.3 Flow visualisation

The same range of flow visualisation tests described for the first chamber were also carried out for this flow. Figure 5.4 shows three characteristic flow visualisation images obtained for a Reynolds number of 1500 to provide a qualitative description of the flow patterns. A sequence of images taken with a one second difference is presented, to show the instantaneous flow patterns under steady state conditions. It can be seen in Figure 5.4 that the air stream entering the chamber remains attached to the floor surface until it reaches the end wall, where it is deflected upwards. A small recirculation zone is formed on the lower corner and the end wall similar to that found opposite the inlet in the high-wall jet flow of Chapter 4 but again this cannot be distinguished in the images but could be clearly observed during the experiments. The main jet air stream is deflected upwards along the end wall, forming an ascending stream which is directed toward the exit located on the upper part of the end wall. Very close to the outlet the jet is divided in two parts, one of which exits the chamber, while the other forms a large recirculation zone in the chamber. As observed in the first chamber, the visualisation tests showed that the flow pattern formed inside the chamber is highly three-dimensional. Parcels of fluid can be observed, on the right side of all three images, to be entrained from the jet into the recirculation region. The air flow moves inside the recirculation region towards the ceiling. Subsequently, part of the recirculating flow moves backwards towards the inlet wall, while part of this flow is mixed with the main jet flowing along the floor of the chamber.

5.4 Predicted flow patterns

CFD predictions were performed for two flow rates, corresponding to Reynolds numbers of 3600 and 6600. The standard κ–ε turbulent model was used for these two predicted cases. For Re = 6600, a modified "low-Re" κ–ε turbulence model was also used in order to assess its suitability for this flow. The 3 cases predicted are listed in Table 5.1 below

Reynolds number	Inlet velocity (m/s)	Outlet velocity (m/s)	Flow rate (m^3/s)
3600	5.55	2.46	0.001665
6600	10.17	4.52	0.0030525
6600 low-Re κ–ε m.	10.17	4.52	0.0030525

Table 5.1

The computational results are presented below in a similar format to that used in Chapter 4, as velocity vector distributions, mean and r.m.s. velocity profiles, and contours of the kinetic energy of turbulence.

5.4.1 Predictions with the standard κ–ε turbulence model, Re = 3600

Figures 5.5 to 5.10 show the three-dimensional velocity vector distribution for Re = 3600. Figure 5.5 shows the velocity vector distribution in the x/W = 0.0, y/H = 0.0 and z/L = 0.0 planes. The air flow stream enters the chamber and remains attached to the floor surface until it has reached the end wall (Coanda effect). Subsequently as the air stream moves upwards along the end wall it is divided near the ceiling: one part of the stream exits through the chamber outlet, while the other part forms a large

recirculation zone. The centre of the recirculation zone on the symmetry plane is located at z = 274 mm and y = 47.6 mm.

Figure 5.6 shows the vectors on the x/W= 0.5, y/H= 1.0 and z/L = 3.0 planes. It can be observed that once the air flow reaches the end wall, it spreads diagonally toward the lateral wall and ceiling. At x/H = 0.5 (lateral wall), the flow moves towards the ceiling surface and the velocity magnitudes are 50% smaller compared with those found over the symmetry plane (Figure 5.5). Figure 5.7 shows velocity vectors in seven different vertical planes along the chamber length. The jet clearly remains attached to the floor surface, while the jet spread and throw are indicated by the vector distributions along the jet trajectory. The jet spreads before it reaches the end wall and although the velocities in the jet decay with increasing distance from the inlet stream, the jet maintains sufficient momentum to impinge on the end wall opposite the inlet.

Figure 5.8 shows the velocity vectors along the symmetry plane (x/W = 0.0). The recirculating zone formed on the lower/end wall corner can be seen to be around 10 mm long and 3 mm high. The vectors in the x/W = 0.4 plane close to the lateral wall are presented in Figure 5.9. In comparison with the velocities in Figure 5.8, it can be noticed that the magnitude of the vectors has decreased by around 60 to 70%. The main recirculation is evident in this plane as well, with its centre located at x = 54.0 mm and z = 196.0 mm.

The contours of the kinetic energy of turbulence along the symmetry plane (x/W = 0.0) can be seen in Figure 5.10. The highest values of κ are found, as expected, along the jet trajectory, and decrease with distance from the inlet from 1.07 m^2/s^2 in the jet core near the inlet to 0.08 m^2/s^2 at the edge of the jet.

5.4.2 Predictions with the standard κ–ε turbulence model, Re = 6600

Figures 5.11 to 5.16 present the results for Re = 6600. In Figure 5.11 the vectors in the x/W = 0.0, y/H = 0.0 and z/L = 0.0 planes are shown (as for Re = 3600 in Figure 5.5). The incoming air jet remains attached to the floor surface until it reaches the opposite wall, where a small recirculation zone, 17.54 mm long and 2 mm high, is formed. This region is smaller than for Re = 3600 by around 20% and its centre its located around 3 mm nearer the end wall than at the lower Re. The velocity magnitudes have increased by around 45 -50% compared with those predicted for Re = 3600. The overall flow pattern remains unchanged and the main differences are found along the jet core trajectory, where the shape of the boundary layer has changed.

Figures 5.12 and 5.13 may be compared with Figures 5.6 and 5.7 respectively to assess the corresponding spread and throw of the incoming jet as it flows towards the end wall. Once has reached the end wall the air stream spreads diagonally toward the lateral wall and ceiling, as for Re = 3600.

Figure 5.14 shows the velocity vectors on the symmetry plane (x/W = 0.0). The air jet seems to flow closer to the floor surface for Re =6600, than for Re = 3600, with steeper velocity gradients being present along the floor surface. Figure 5.15 shows the velocity vector distribution in the x/W = 0.4 plane. Comparing Figures 5.14 and 5.15, it can be observed that although a recirculating flow is evident at x/W = 0.4, the magnitude of the velocity vectors has decreased by around 60% between x/W = 0.0 and 0.4.

The contours of the kinetic energy of turbulence for Re = 6600 can be seen in Figure 5.16. The distribution of the kinetic energy is similar to that obtained for Re = 3600. The kinetic energy inside the chamber has doubled with a maximum value of 3.7 m^2/s^2.

5.4.3 Predictions with the low-Re κ–ε turbulence model, Re = 6600

In order to assess the suitability of the low Re κ–ε turbulence model for the simulation of the flow a second set of predictions were carried out for Re = 6600. Figures 5.17 to 5.22 show the corresponding results. No appreciable differences between these figures and the previous results obtained for this Re using the normal κ–ε turbulence model can be observed. However there was an increase of 25% on the CPU time required for the calculations due to the additional equations that had to be solved.

Figures 5.17 to 5.19 show three-dimensional velocity vector distributions, while Figure 5.20 and 5.21 present the vectors in the symmetry plane (x/W = 0.0) and in the x/W =0.4 plane near the lateral wall. Comparing Figure 5.20 (low Re κ–ε) and Figure 5.14 (standard κ–ε), only small differences can be found. For example, on the lower/end wall corner, the small recirculation zone is reduced in size to 15.25 mm in length by 1.5 mm in height, i.e. it is predicted to be around 15% smaller than with the standard κ–ε model.

Figure 5.22 presents the predicted contours of the kinetic energy of turbulence in the plane of symmetry. The low-Reynolds model has predicted values of κ which are larger than those obtained with the standard κ–ε, by around 10%. Otherwise the overall distribution of κ is similar to those described earlier for the Re = 3600 and 6600 cases.

5.5 Comparison of predictions and experimental data

5.5.1 Comparisons at Re = 3600

Comparisons between the predictions and the LDA measurements are presented in this section. In Figure 5.23 the mean velocities in the plane of symmetry (x/W = 0.0) for Re = 3600 are compared. There is good qualitative and quantitative agreement. The mean velocities in the recirculation zone have been predicted well at both z/L = 1.0 and z/L = 2.0: the predicted values are on average 10% lower. Along the incoming air jet core, the numerical method tended to overpredict the mean velocity by around 20% at z = 100 mm and 10% at z = 200 mm, while the core zone has been overpredicted by 10 to 15% at z = 100 mm. The predicted mean velocities near the ceiling match the measured data, while in the jet core zone the mean velocities have been overpredicted 15 to 20%.

A comparison of the predicted and measured kinetic turbulent energy at z = 200 mm in the x/W = 0.0 plane is shown in Figure 5.24. The kinetic turbulent energy has been underpredicted for 0.01 m < y <0.1 m but is overpredicted for y < 0.01 m. In contrast to the corresponding comparisons made in Chapter 4, the value of κ is overpredicted in the core of the jet. This may be related to the fact that the maximum of the predicted mean flow profile is located at a higher y location than in the experiment, and as result the near-wall velocity gradient where κ is high is also located higher than in the experiment. However, it is surprising that κ is overpredicted anywhere in the flow, especially as any broadening of the measured r.m.s. values due to 'flapping' of the jet would tend to produce higher κ values. The inability of the κ–ε model to account for the anisotropy of turbulence across most of the flow may also be a reason for the discrepancy, as already mentioned in the previous Chapter.

As can be seen from the comparison of the u', v' and w' levels shown in Figure 5.25, the present flow case is strongly anisotropic, particularly near the top and bottom walls. Similarly, comparing the predicted $\frac{\sqrt{k}}{1.1}$ values (Nielsen, 1991) with the measured u' levels (Figure 5.26), it can be seen there are large differences at most locations and clearly an assumption of isotropy is inappropriate.

5.5.2 Comparisons at Re = 6600

The numerical calculations for Re = 6600 using the standard κ–ε turbulence model were also compared with the LDA data. The results along the symmetry plane (x/W = 0.0) are plotted in Figure 5.27. It can be observed that the predicted mean velocity values have been overpredicted in the jet region around 15%. The mean velocity values in the recirculation zone are over- and under-predicted by 5 to 10% at z = 100 mm and z = 200 mm respectively. All qualitative features of the LDA profiles are well reproduced by the predictions.

Figure 5.28 shows the predicted and measured values of the kinetic energy of turbulence, at z = 200 mm in the x/W = 0.0 plane. In this case, the kinetic energy of turbulence is underpredicted. κ is overpredicted only near the floor of the chamber. This was ascribed in part to the location of the predicted mean velocity gradient in the previous section. However, it can be noted from Figure 5.27 that the predicted maximum mean velocity at both z = 100 mm and z = 200 mm is located nearer the floor of the chamber then in the measured profile, in contrast to the comparison made earlier for Re = 3600.

Figure 5.29 shows a comparison of three individual measured r.m.s. profiles at z = 150 mm and x/W = 0.0. The turbulence levels in the middle of the profile are more similar than for Re = 3600 and near the wall and floor the turbulence is clearly anisotropic. Using Nielsen's expression it can be seen in Figure 5.30 that the kinetic energy of turbulence has been underpredicted. This was also observed for Re = 6000 for the first chamber.

5.6 Discussion

5.6.1 Flow and turbulence structure

The results for the low-wall horizontal jet flow presented in sections 5.4 and 5.5, as well as the results obtained for the first chamber geometry, confirmed the presence of a three-dimensional flow inside the chamber. In both geometries the Coanda effect is present for Re > 2000. The flow patterns in both cavities shows many similarities. A comparison of the flow patterns, suggests that the air velocities inside the two cavities are of similar magnitudes. In both cases, the incoming air jet remains attached to the ceiling/floor surface until it has reached the chamber end wall. Close to the ceiling the jet profile for the low-wall jet seems to spread less.

The main feature of these flows is the recirculation zone which has its centre at around three-quarters of the chamber length from the inlet. The size of the recirculation zone in both cavities is similar, to within 5-10%. The centre of the large recirculation zone is located at the same distance, away from the inlet wall, and vertically it is at the same distance from either the floor (chamber 1) or the ceiling (chamber 2). The shape of the air jet core profile is different for chamber 1 and 2. This can be observed on the sharpest form of the velocity profile, for the jet core zone in chamber 2

(Figures 5.11 and 5.14), while the chamber 1 data (Figures 4.7 and 4.10) show a more rounded profile. The magnitude of the mean velocities increases across the whole domain with Re, but the flow pattern remains practically unaltered. In both chambers the numerical predictions show that a small recirculating zone is formed when the incoming air stream has reached the end wall. The maximum velocities have been found to be located along the incoming core jet and the maximum velocities in the return zone are located around 2/3 of the chamber length toward the outlet for both cavities.

The decay of the velocity with distance from the floor ceiling was similar for both cases. Figure 5.31 presents the experimental data with the velocity u and the distance from the floor y normalised with the maximum velocity (U_{max}) and the rate of spreading $(Y_{1/2})^3$ respectively. The velocity variations reported by Sforza and Herbst (1967) and Verhoff (1963) are also shown for comparison. The results indicate the presence of a typical wall jet that is in agreement with the findings of Nielsen (1972) and Restivo (1979) as also shown in Chapter 4 for chamber 1. There is still a small difference in the location of the peak velocity, which is found at $Y/Y_{1/2} = 0.25$ for the experimental data and at $Y/Y_{1/2} = 0.50$ for the approximation proposed by Sforza and Herbst (1967) and Verhoff (1963).

The experimental results for chamber 2 as well as those for chamber 1, showed that in some regions inside the chamber the turbulence is anisotropic and in some isotropic. All the results presented for the kinetic energy of turbulence for both cavities (apart from those for Re = 3600) showed that the numerical method has underpredicted the value of κ; this is possibly due to the type of implicit assumption of local isotropy made in

---

3 See footnote page 130

the formulation of the κ–ε model used or the presence of jet flapping which is interpreted as higher r.m.s. values in the LDA data.

The literature survey did not reveal any previous flow visualisation investigations within a geometrically similar chamber. Setrakian (1986) presented a study of the flow in an open chamber, in which the inlet is located beside the room floor. His study covered flow visualisation tests for different Reynolds numbers. However, most of the tests made by Setrakian were aimed at finding how the flow pattern is modified by the presence of an obstacle and direct comparisons with the present data cannot be made.

5.6.2 Effect of Reynolds number

A comparison of the experimental and numerical results obtained for the second chamber confirmed the assumption that the air flow patterns become independent of the Reynolds number for Re > 6000, as for the high-wall inlet configuration flow described in Chapter 4. Flow patterns of similar magnitude were found in both cavities. An increase of the Re produced an increase of the magnitude of the mean velocities and the κ values.

Figures 5.32.a and 5.32.b show the variation of the jet half width (jet spread) in the y and x directions respectively for two Re's. Figure 5.32.a shows the increase of the vertical jet spread with axial distance. $Y/Y_{1/2}$[4] is similar for both Re's at z = 0.1 m but around 5% greater for the lower Re at z = 0.2m. The horizontal jet spread is higher for Re = 3600 at x = 0.1 m but lower at x = 0.2 m.

---

[4] $Y_{1/2}$ the jet velocity half width (the distance from the wall normal to the ceiling at which the velocity is half that of $U_{max.}$).

5.6.3 Assessment of predictions and the effect of the turbulence models used

Further analysis of the predicted velocities and turbulence parameters is given in this section. The analysis is given along similar lines to that for chamber 1. Predicted variations of the decay of the maximum velocity (drop and throw), and of the maximum velocity in the recirculation zone (occupied zone) are shown in Figures 5.33 to 5.38.

Figure 5.33 shows the jet velocity decay predicted with the standard $\kappa-\varepsilon$ turbulence model at $y = (H-h)/2$ in the $x/W = 0.0$ plane. When these results for chamber 2 are compared with the corresponding results for chamber 1, the velocity decay exhibits a similar trend (Figure 4.30), but in the present case the velocity decays more rapidly.

For Re = 3600 the experimental results are also compared with the predicted mean velocities in Figure 5.34 which presents velocity profiles at $y = (H-h)/2$ and $y = h/2$ in the $z/L = 2.0$ plane. The maximum velocity decay (at $y = h/2$) for Re = 3600 has been overpredicted. On the other hand the mean velocities at $y = (H-h)/2$ have been underpredicted.

Figure 5.35 presents the predicted jet velocity decay along the symmetry plane at $x/W = 0.0$ for Re = 6600. When compared with the corresponding results for chamber one, the differences found between the two predicted cases are small: the same velocity decay behaviour as for chamber 1 is also observed in chamber 2. Figures 5.35.(a) and 5.35.(b) show the measured axial velocity decay compared with the rectangular wall jet decay results of Hammond (1982) and Viets and Sforza (1966) respectively. The measured velocity decay compares well with the data of Hammond and Viets and Sforza. Although the experimental data show a more rapid

decay, this is probably attributed to the geometrical differences between the present flow and those of Hammond and Viets and Sforza.

A comparison between the predicted mean velocity decay calculated by both turbulence models (standard κ–ε and low-Re κ–ε) is shown in Figure 5.36 in the x/W = 0.0 plane (symmetry plane) at y = (H-h)/2. Differences between the 2 models can be seen along the jet trajectory for z > 0.15 m. The low Re κ–ε model predicted lower (by 15%) mean velocities at the zone where the maximum velocity decay is found, between z = 0.15 and 0.27 m. Close to the end wall the standard κ–ε model has predicted mean flow velocities lower by 5% compared with the low Re κ–ε model.

The mean velocity profiles at y = (H-h)/2 and y = h/2 in the z = 1.0 mm and z = 200 mm planes are shown in Figures 5.37 and 5.38 respectively, for Re = 6600. The experimental data and predictions are similar to within 20% in the jet core zone (y = h/2) and in the reverse flow (y = (H-h)/2) to within 10%.

Finally it should be noted that the small recirculation zone near the end wall was predicted with both turbulence models. However, this recirculation has not been predicted in earlier numerical studies (Chen (1991), Heikkinen (1991), and Skovgaard (1991)), and such differences could be attributed to the size and distribution of the meshes or the numerical methods used.

5.7 Concluding remarks

1. Flow visualisation recordings in a chamber ventilated by a low-wall jet for Re up to 2000 showed the presence of a highly three-dimensional jet. The flow visualisation tests showed that the flow pattern in the second

chamber is in many ways similar to that in the first chamber. The flow pattern in both cavities shows a large zone of recirculation centred around 3/4 of the chamber length from the inlet. A smaller recirculation zone was observed on the lower/upper end wall corner respectively.

2. The predictions were assessed against the flow visualisation and LDA results and were compared qualitatively and quantitatively with the results obtained in chamber 1 where possible. The incoming air stream forms a wall type jet due partly to the Coanda effect. It was found that the numerical methods used, tended to overpredict the velocities in the air jet core zone, and underpredict them in the recirculating zone. The maximum velocities were found in the jet core, while in the recirculation zone they are located 3/4 of the length chamber from the inlet.

3. The highest values of the kinetic energy of turbulence are found in the jet core zone. The values are lower in the recirculation zone.

4. The agreement between experimental and predicted quantities is good for the results presented in this Chapter. Differences between the predictions with the 2 turbulence models used are not significant, apart from the CPU time used for each method to obtained a converged solution. The kinetic energy of turbulence was underpredicted by both the standard $\kappa-\varepsilon$ and the low Re $\kappa-\varepsilon$ models. The values of the kinetic energy of turbulence predicted by the low Re model were higher than those obtained through the standard $\kappa-\varepsilon$ method. The standard $\kappa-\varepsilon$ model proved to be more appropriate for the calculation, using less computational time and predicting more accurately the recirculation zones found near the upper end wall corner and the lower rear wall corner.

5. The experimental and numerical results presented in previous sections tend to help the assumption that the air flow patterns for the low-wall inlet geometry is essentially independent of the Reynolds number for Re numbers greater than 6000, these findings are supported by results not presented here, but are in agreement with those of Figure 4.29b.

6. An increase on the Re from 3000 to 6600 resulted in a corresponding increase of the velocity and κ magnitudes.

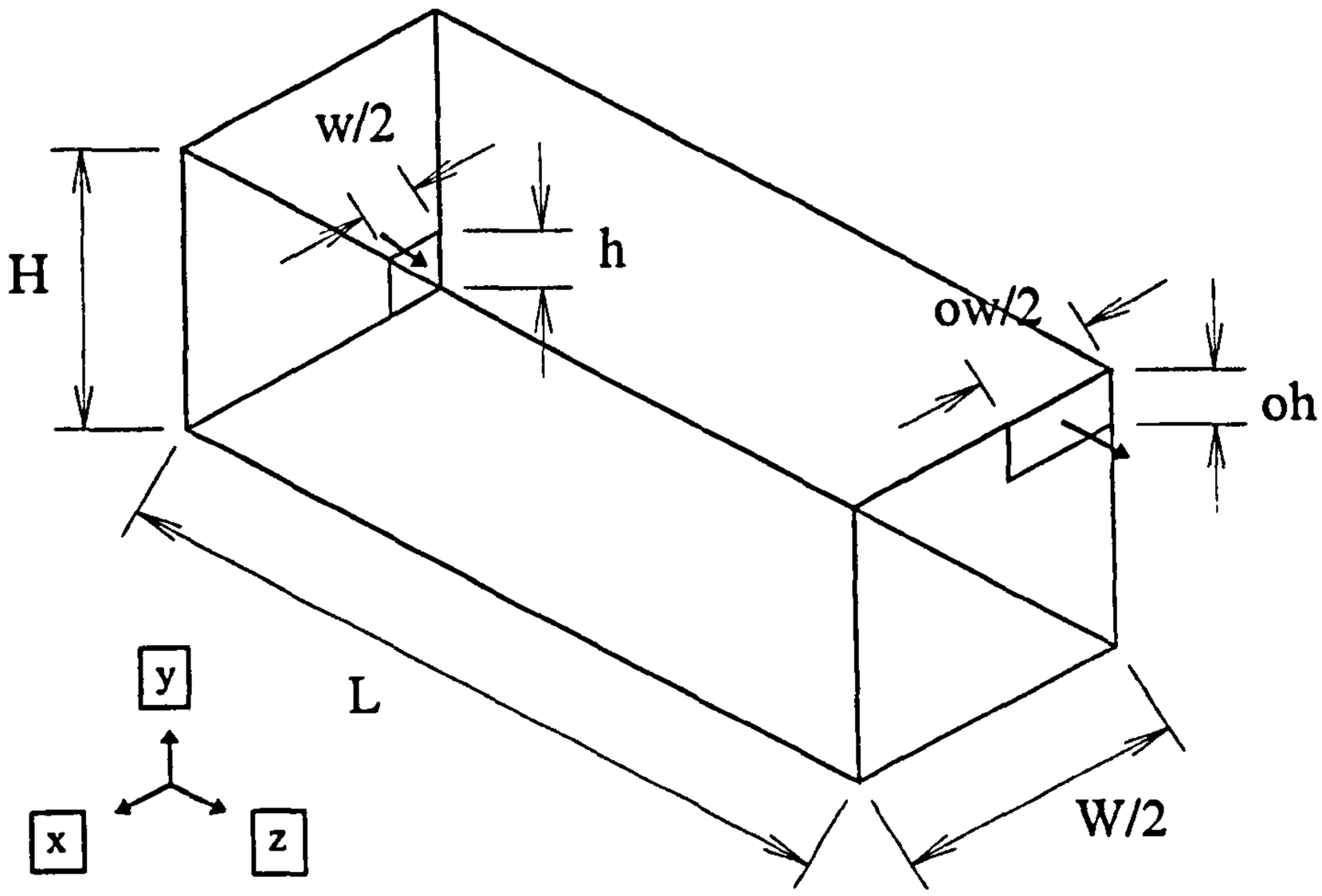

Figure 5.1 Flow configuration: schematic diagram of one-half of test section, chamber 2.

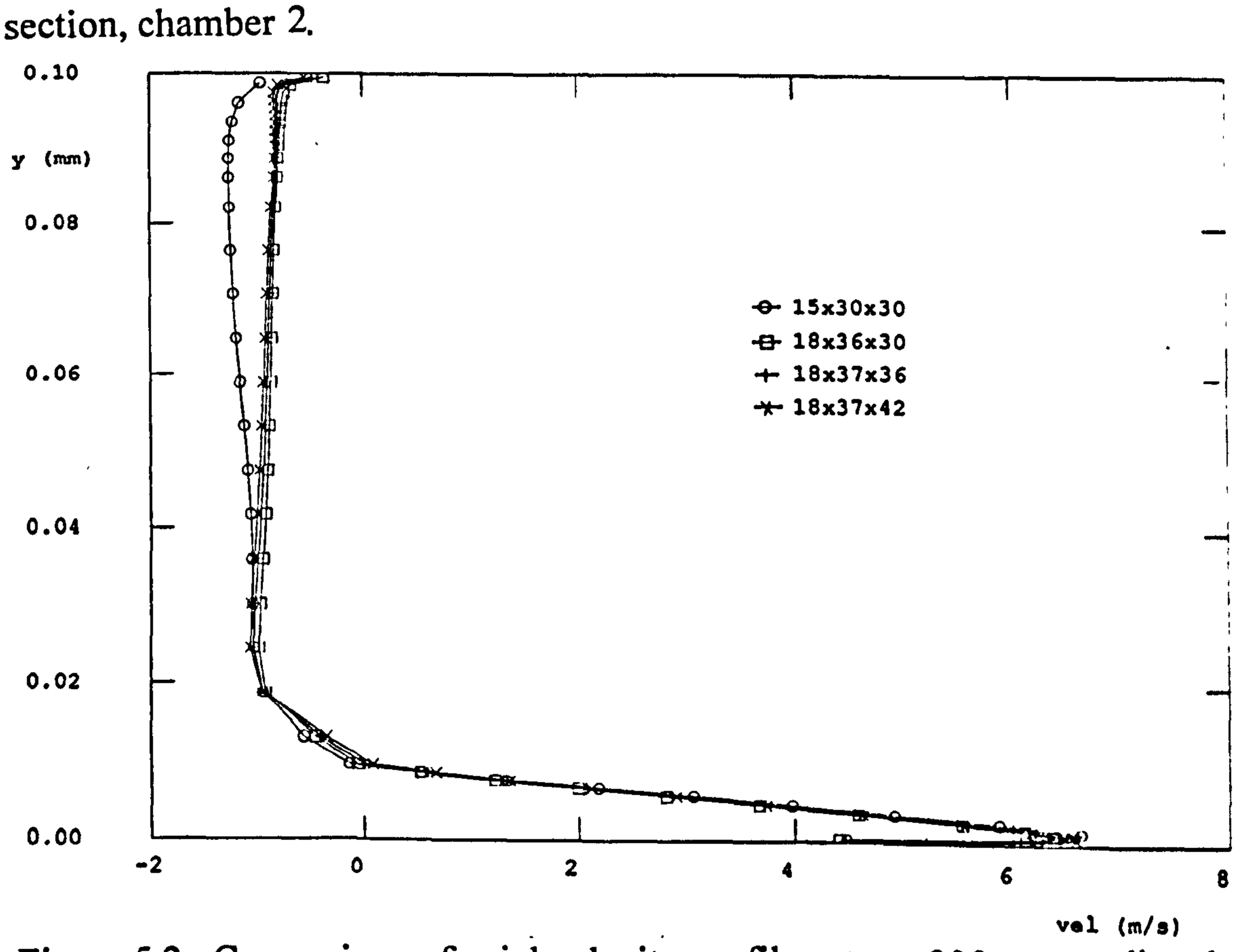

Figure 5.2 Comparison of axial velocity profiles at z = 200mm predicted with four different grid sizes; Re = 6600.

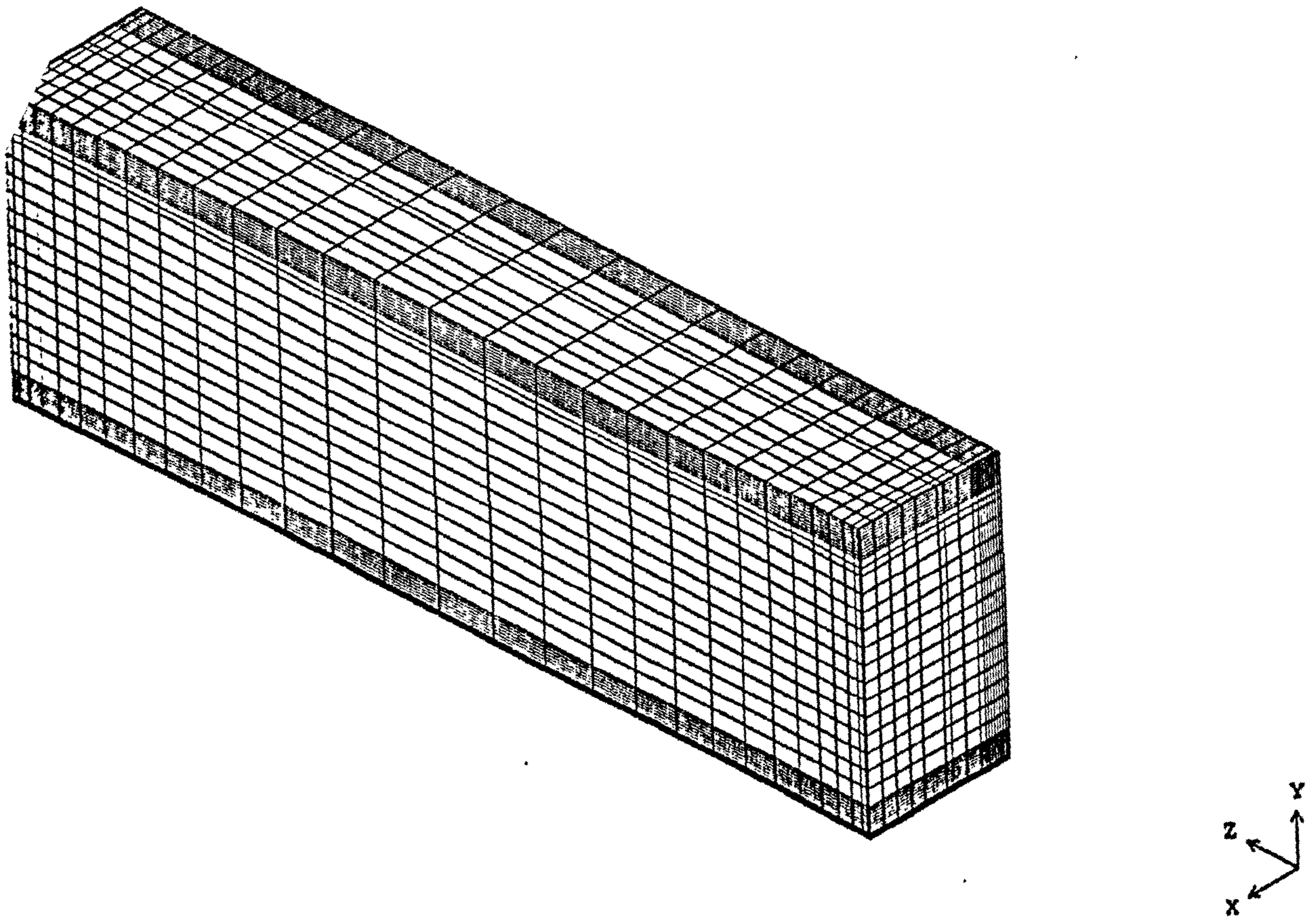

Figure 5.3 Numerical mesh

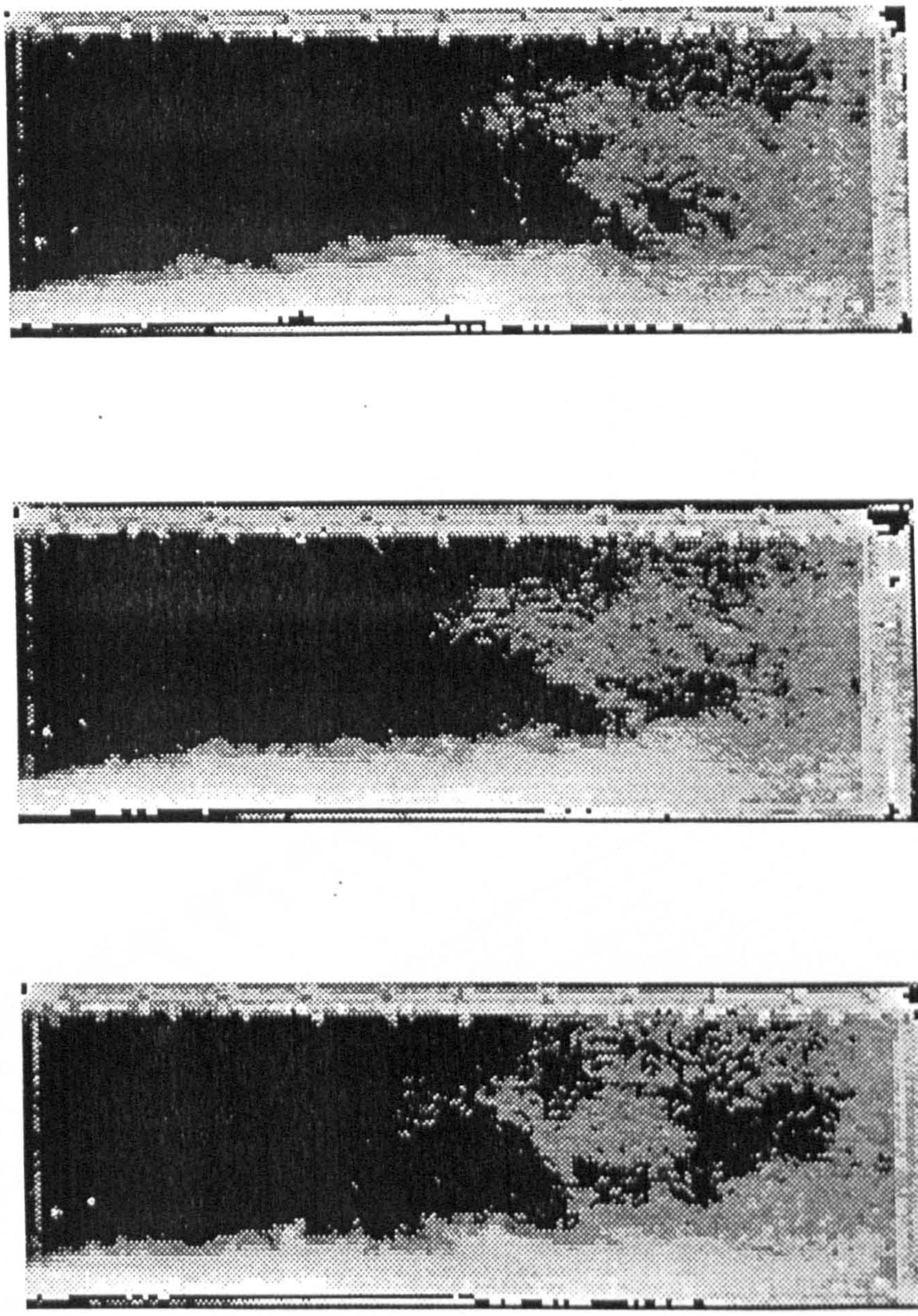

Figure 5.4 Flow visualization test at Re = 1500.

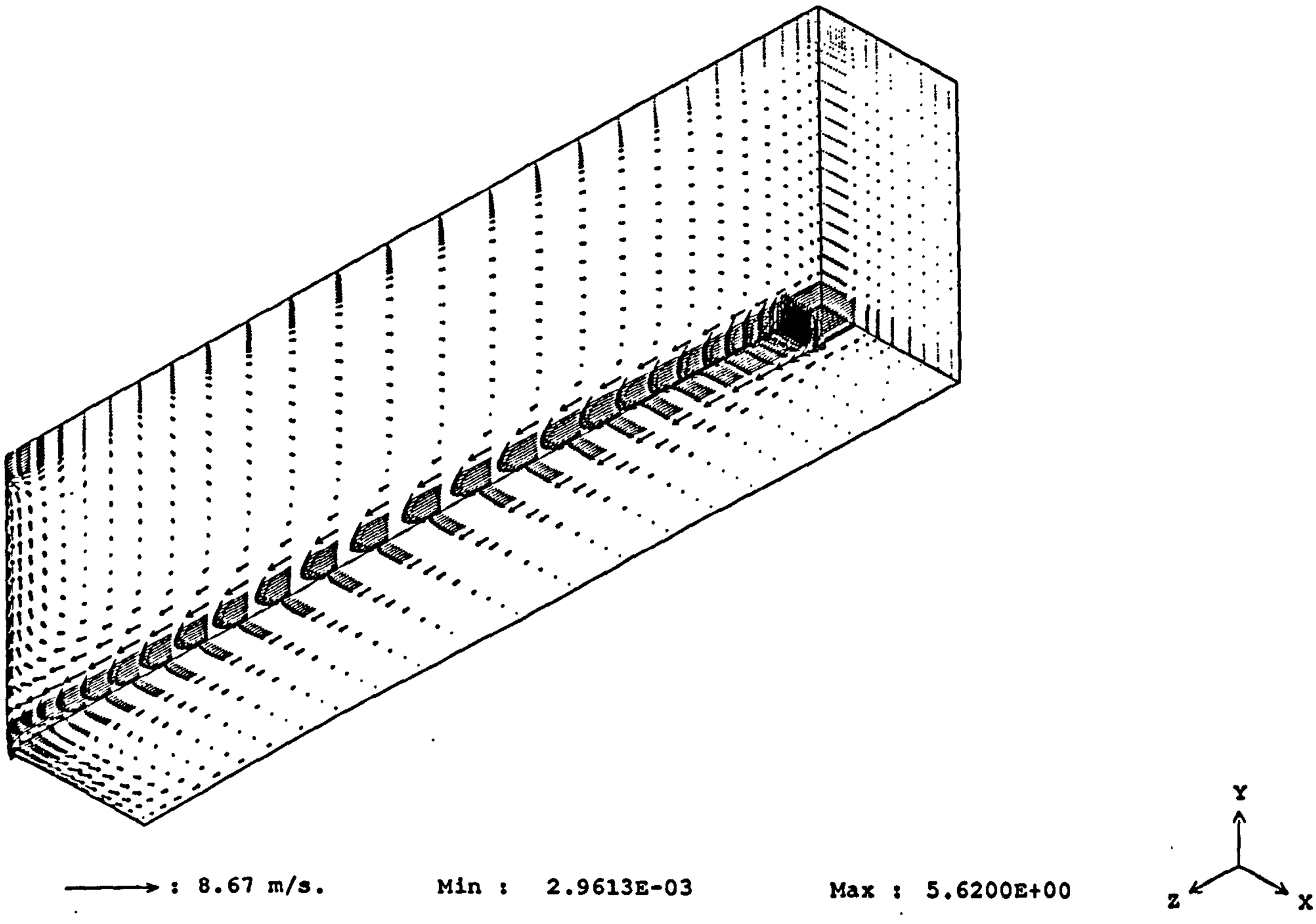

Figure 5.5 Velocity vector distribution in the planes x/W = 0.0, y/H = 0.0 and z/L = 0.0; Re = 3600, standard $\kappa-\varepsilon$ turbulence model.

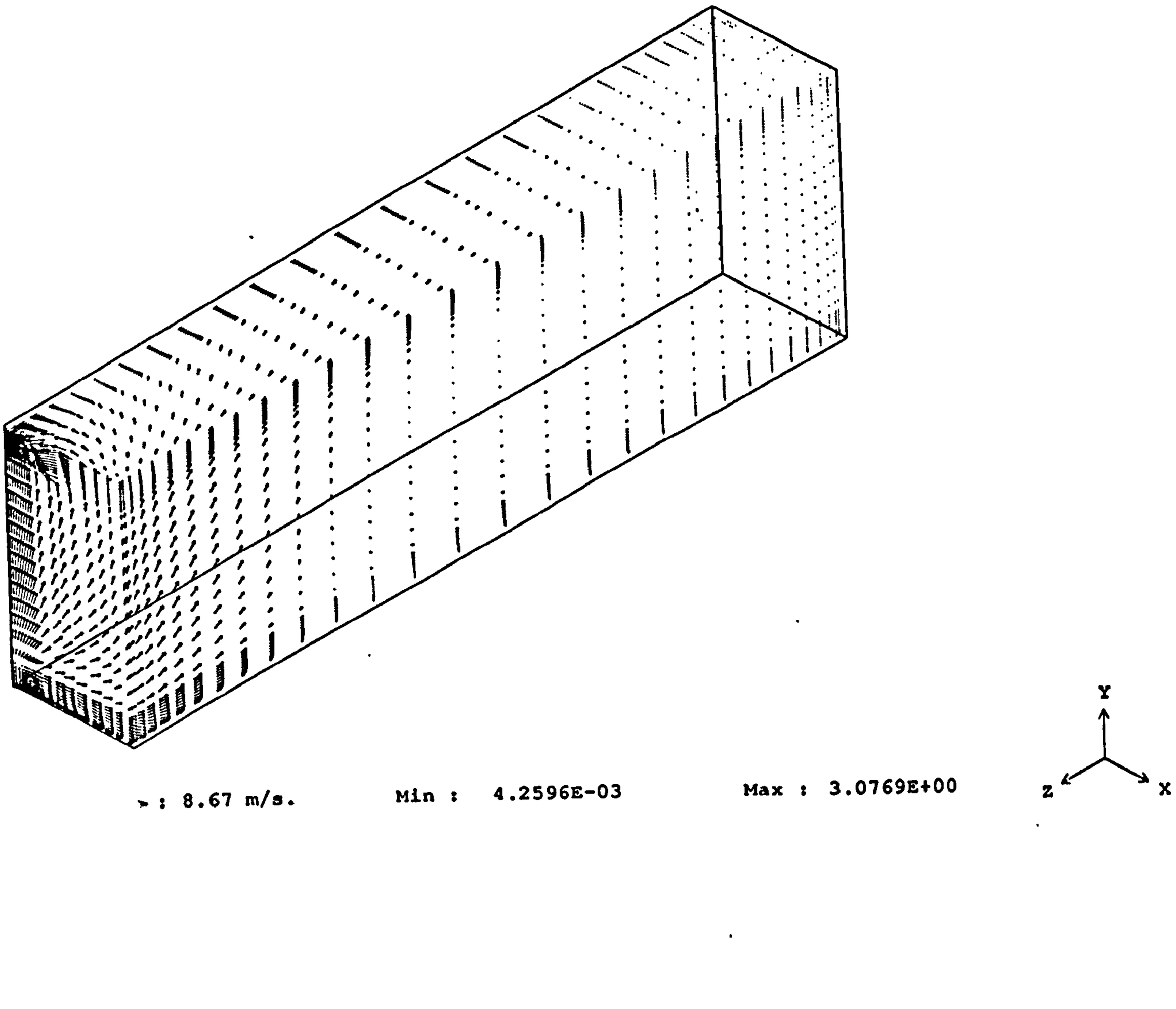

Figure 5.6 Velocity vector distribution in the planes x/W = 0.5, y/H = 1.0 and z/L = 3.0; Re = 3600, standard $\kappa-\varepsilon$ turbulence model.

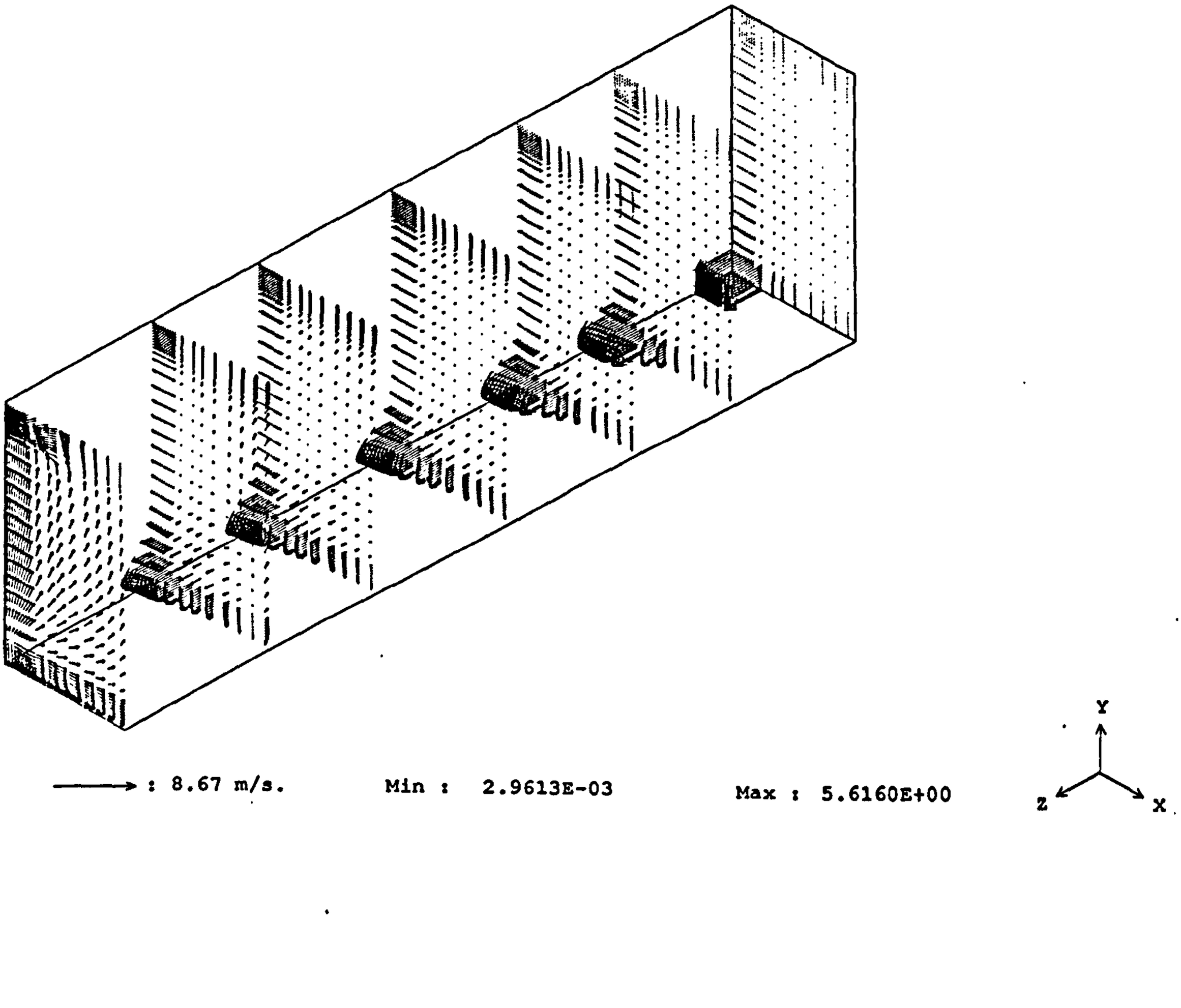

Figure 5.7 Velocity vector distribution in the planes z/L = 0.0, 0.5, 1.0, 1.5, 2.0, 2.5 and 3.0; Re = 3600, standard $\kappa-\varepsilon$ turbulence model.

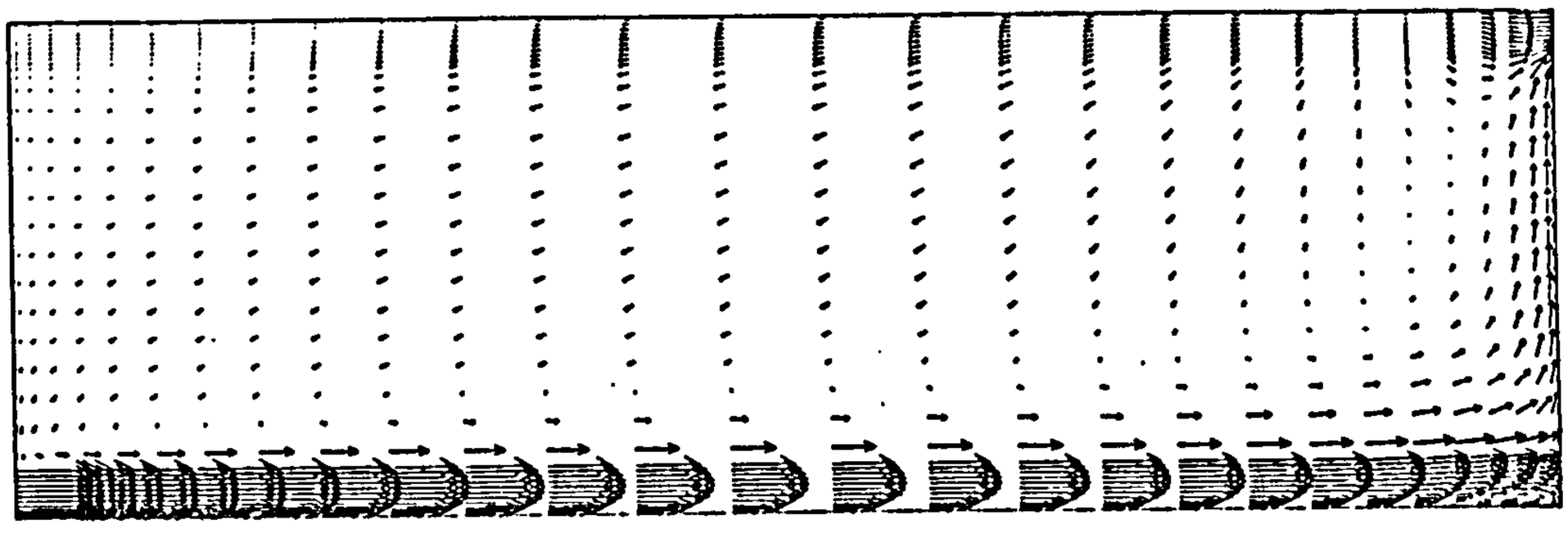

⟶ : 9.29 m/s. Min : 3.9913E-03 Max : 5.6200E+00

Figure 5.8 Velocity vector distribution in the plane x/W = 0.0 (symmetry plane); Re = 3600, standard κ–ε turbulence model.

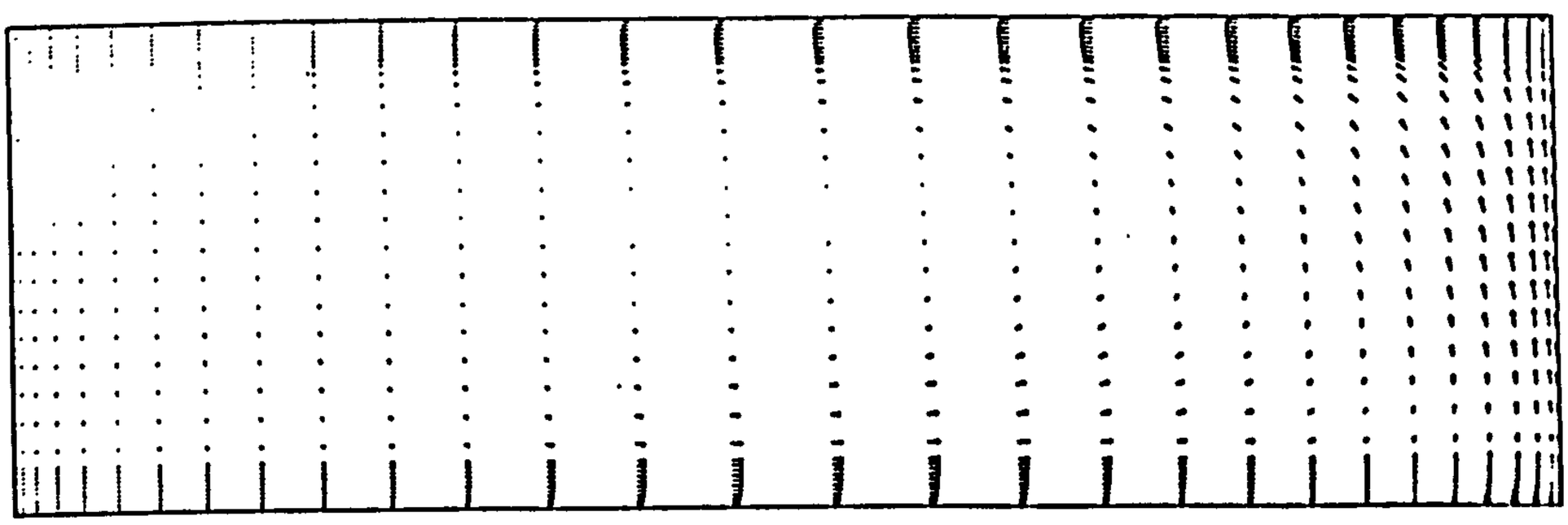

⟶ : 9.29 m/s. Min : 2.9613E-03 Max : 1.5832E+00

Figure 5.9 Velocity vector distribution in the plane x/W = 0.4; Re = 3600, standard κ–ε turbulence model.

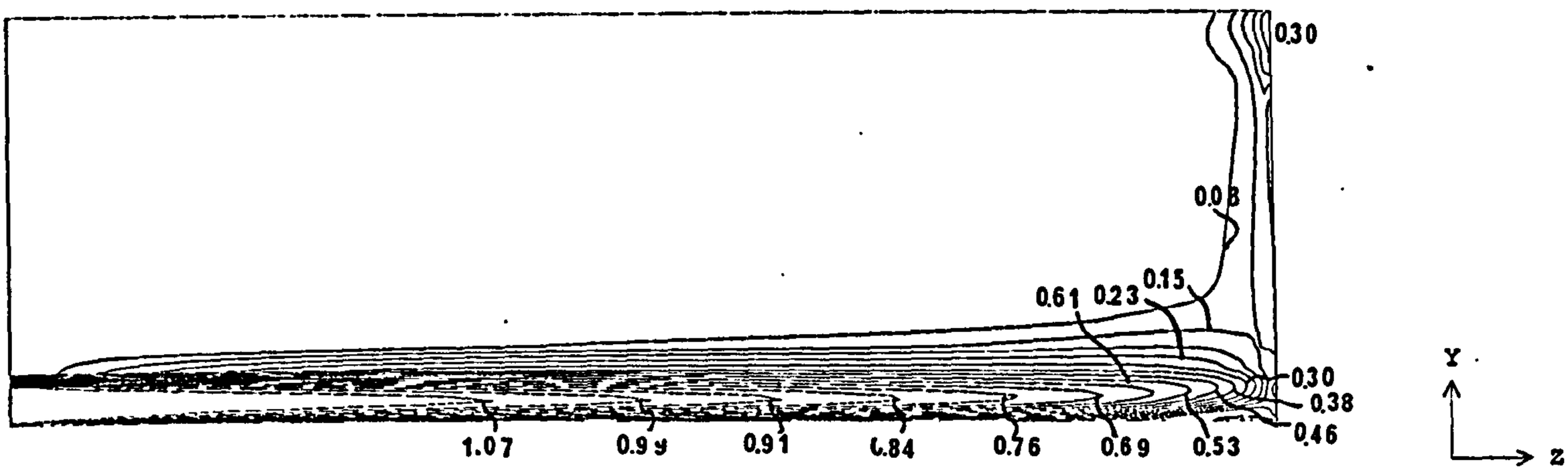

Figure 5.10 Turbulent kinetic energy contours in the plane x/W = 0.0 (symmetry plane); Re = 3600, standard κ–ε turbulence model. Contour values in m^2/s^2.

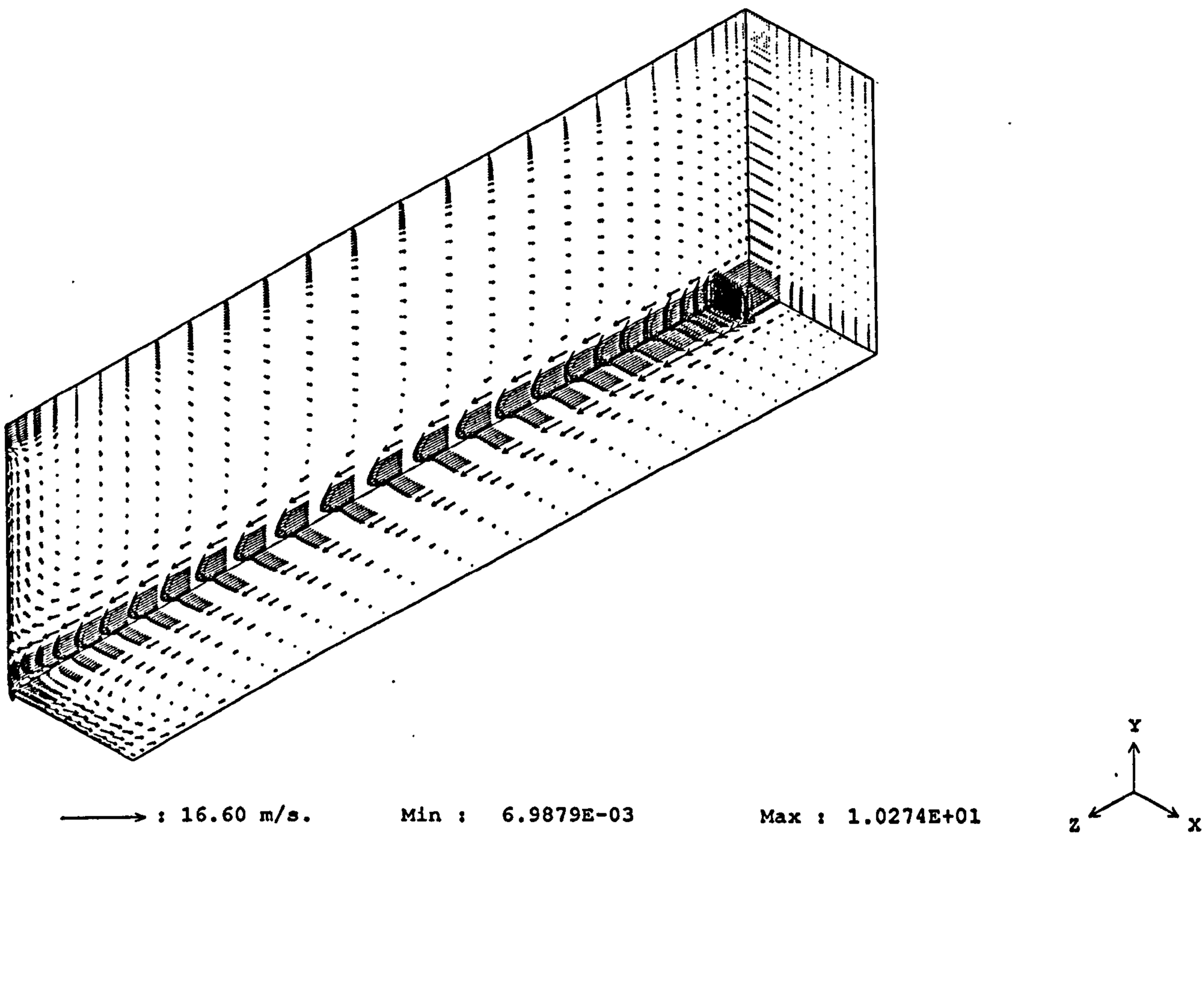

Figure 5.11 Velocity vector distribution in the planes x/W = 0.0, y/H = 0.0 z/L = 0.0; Re = 6600, Standard κ–ε turbulence model.

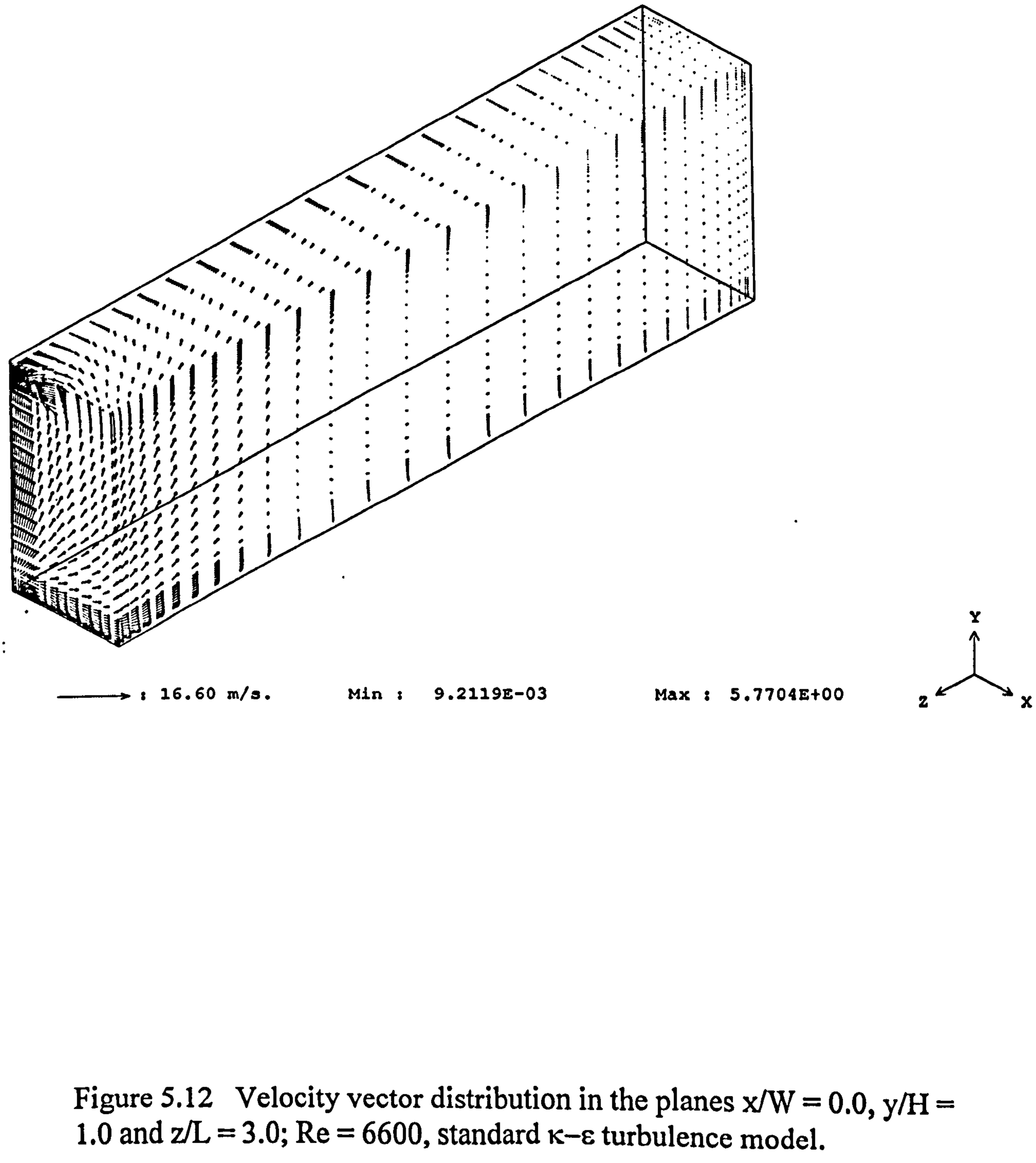

Figure 5.12 Velocity vector distribution in the planes x/W = 0.0, y/H = 1.0 and z/L = 3.0; Re = 6600, standard κ–ε turbulence model.

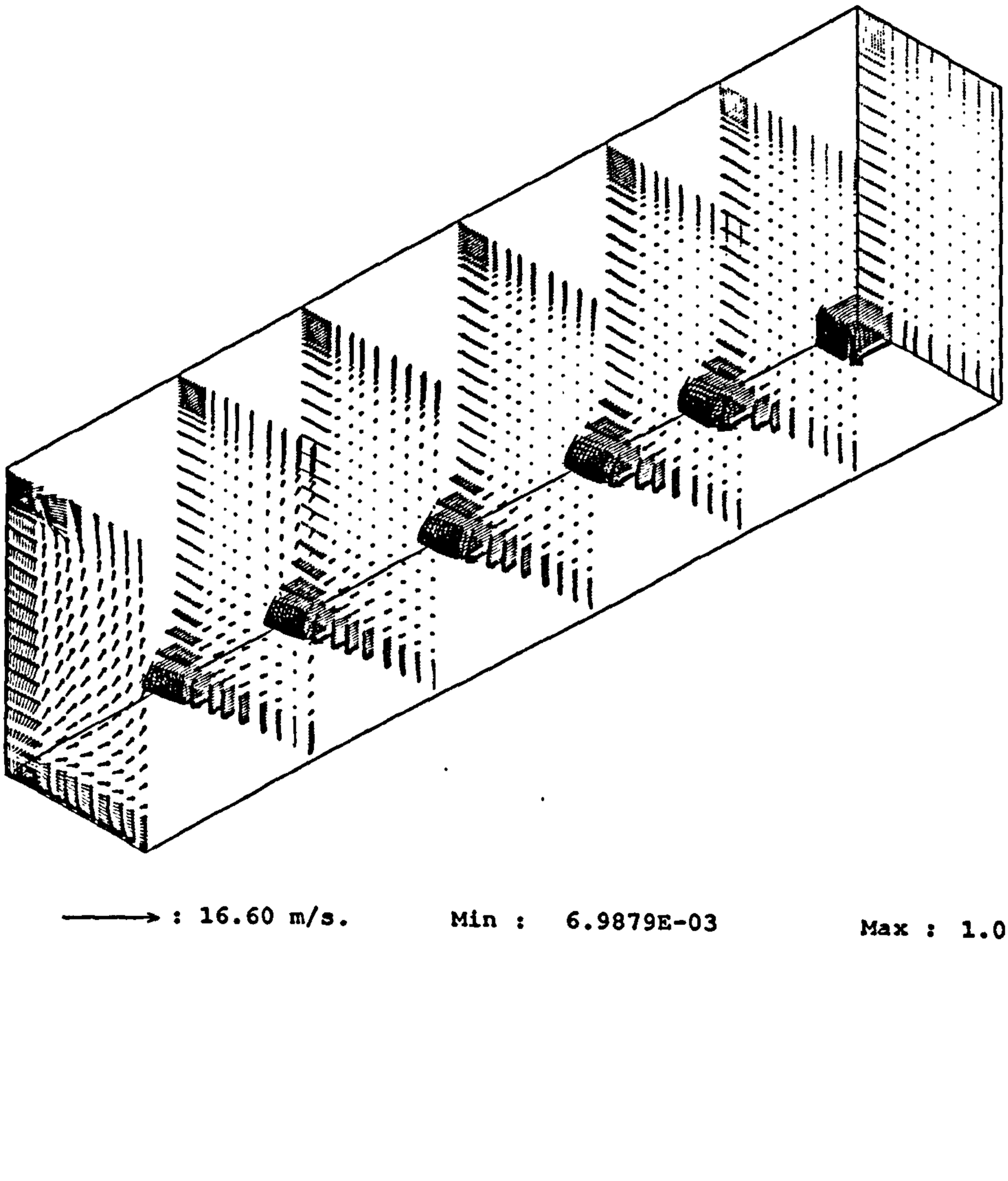

Figure 5.13 Velocity vector distribution in the planes z/L = 0.0, 0.5, 1.0, 1.5, 2.0, 2.5, 3.0; Re = 6600, standard $\kappa-\varepsilon$ turbulence model.

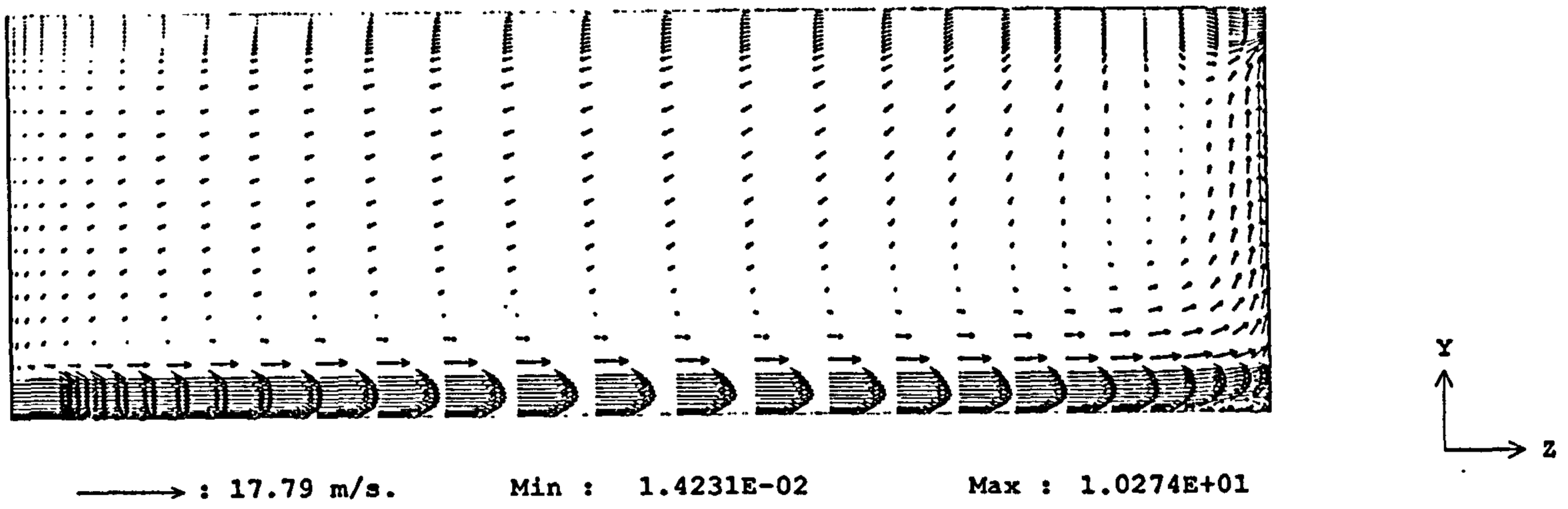

Figure 5.14 Velocity vector distribution in the planes x/W = 0.0 (symmetry plane); Re = 6600, Standard κ–ε turbulence model.

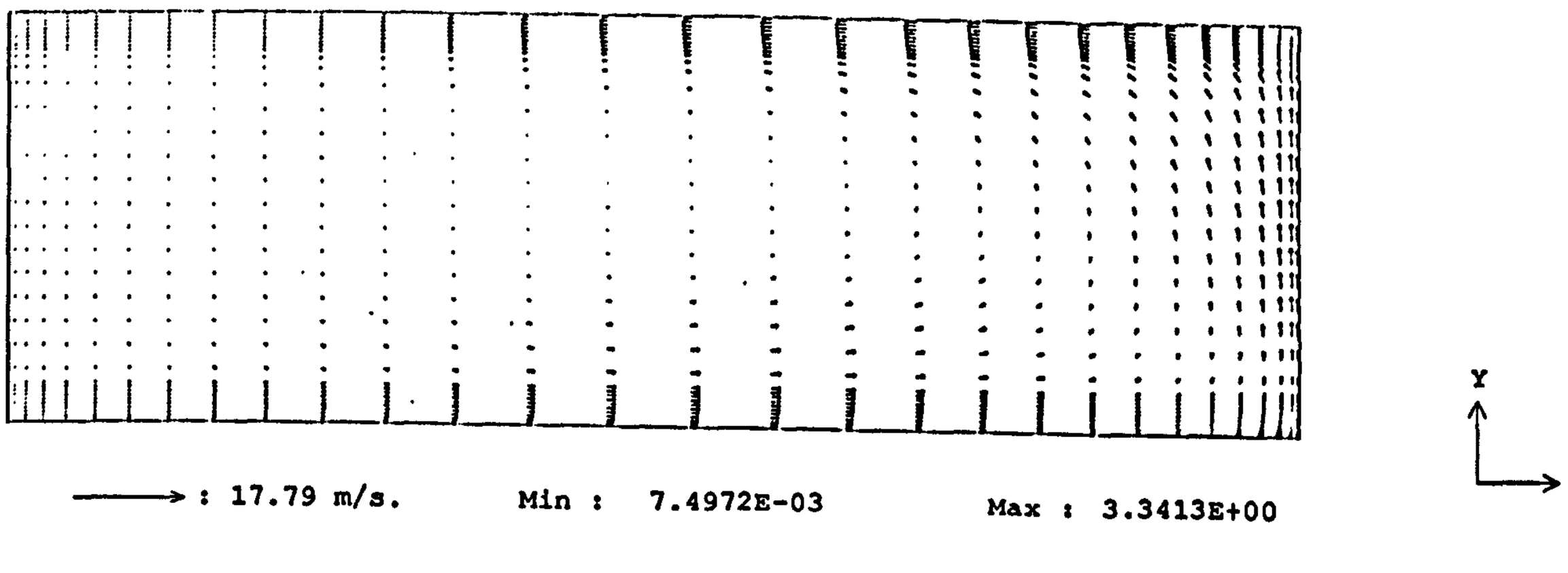

Figure 5.15 Velocity vector distribution in the plane x/W = 0.4; Re = 6600, standard κ–ε turbulence model.

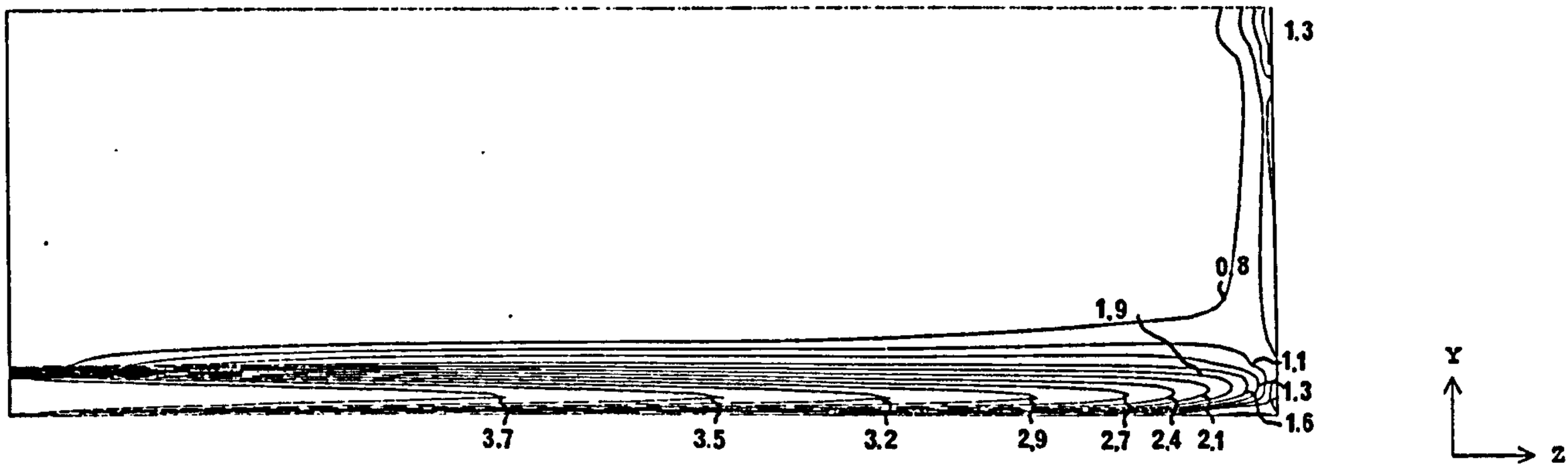

Figure 5.16 Turbulent kinetic energy contours in the plane x/W = 0.0. (symmetry plane); Re = 6600, standard κ–ε turbulence model. Contour values in m^2/s^2.

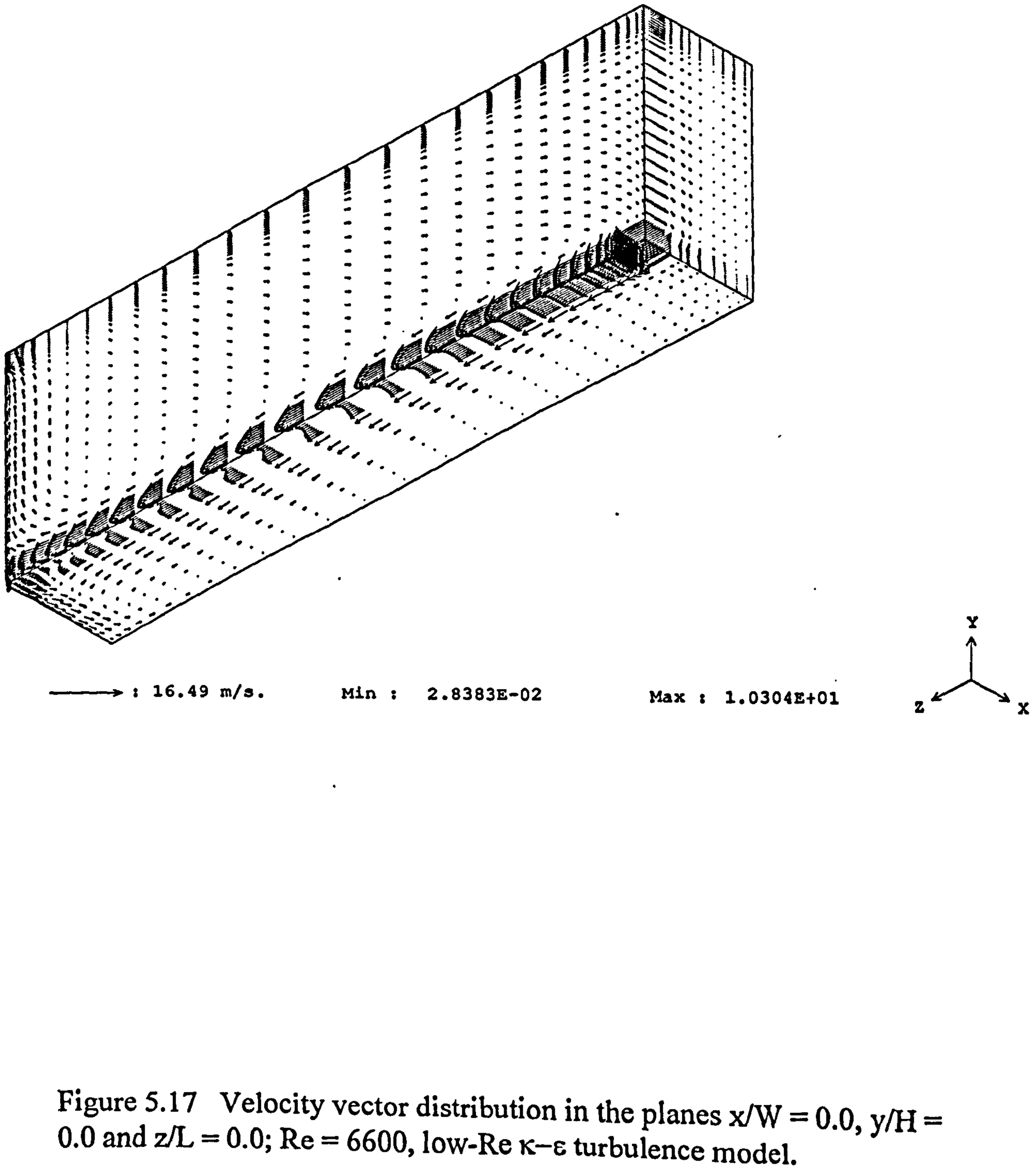

Figure 5.17 Velocity vector distribution in the planes x/W = 0.0, y/H = 0.0 and z/L = 0.0; Re = 6600, low-Re κ–ε turbulence model.

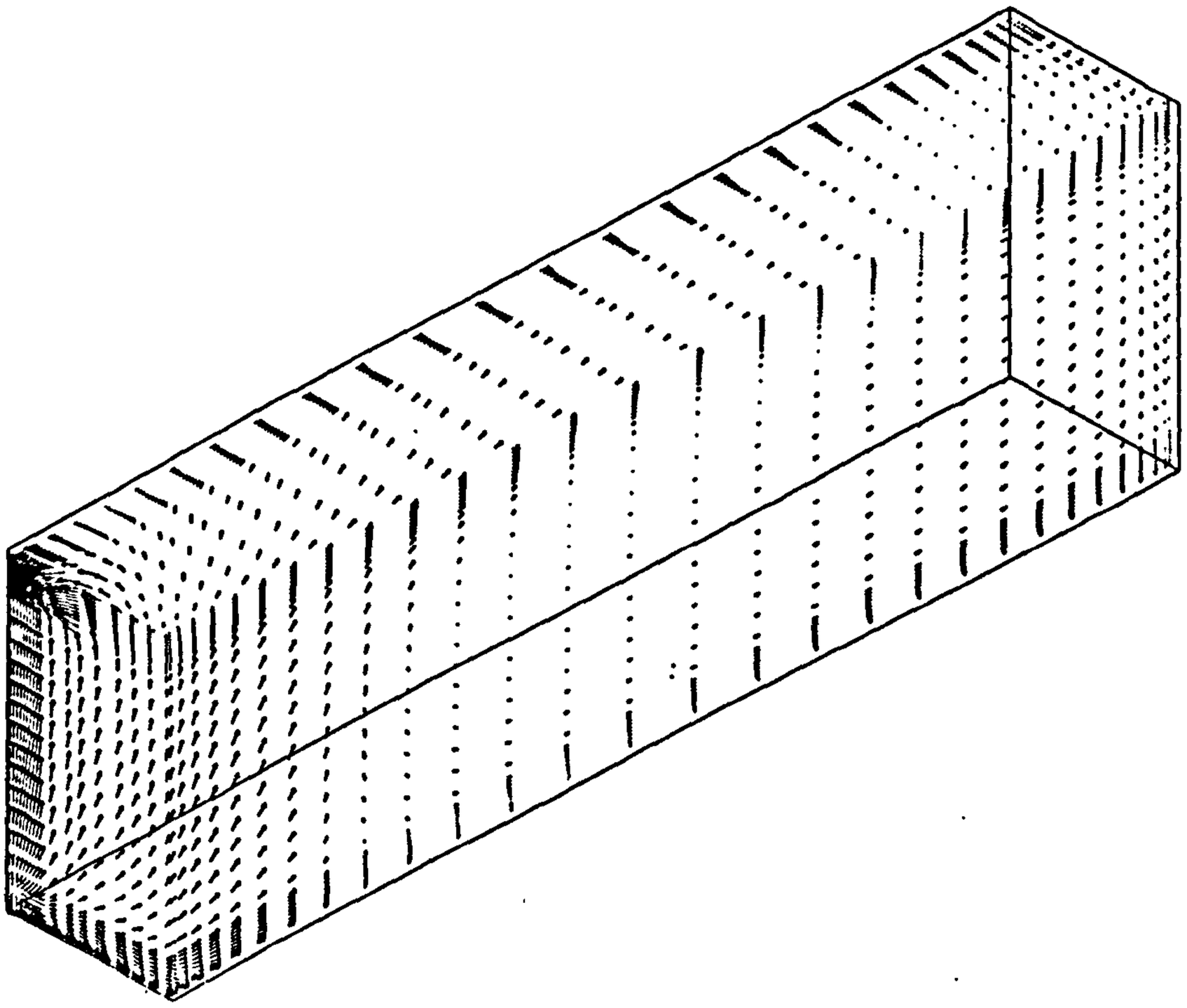

⟶ : 16.49 m/s. Min : 2.8383E-02 Max : 6.0239E+00

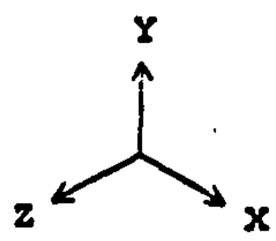

Figure 5.18 Velocity vector distribution in the planes x/W = 0.5, y/H = 1.0 and z/L = 3.0; Re = 6600, low-Re κ–ε turbulence model.

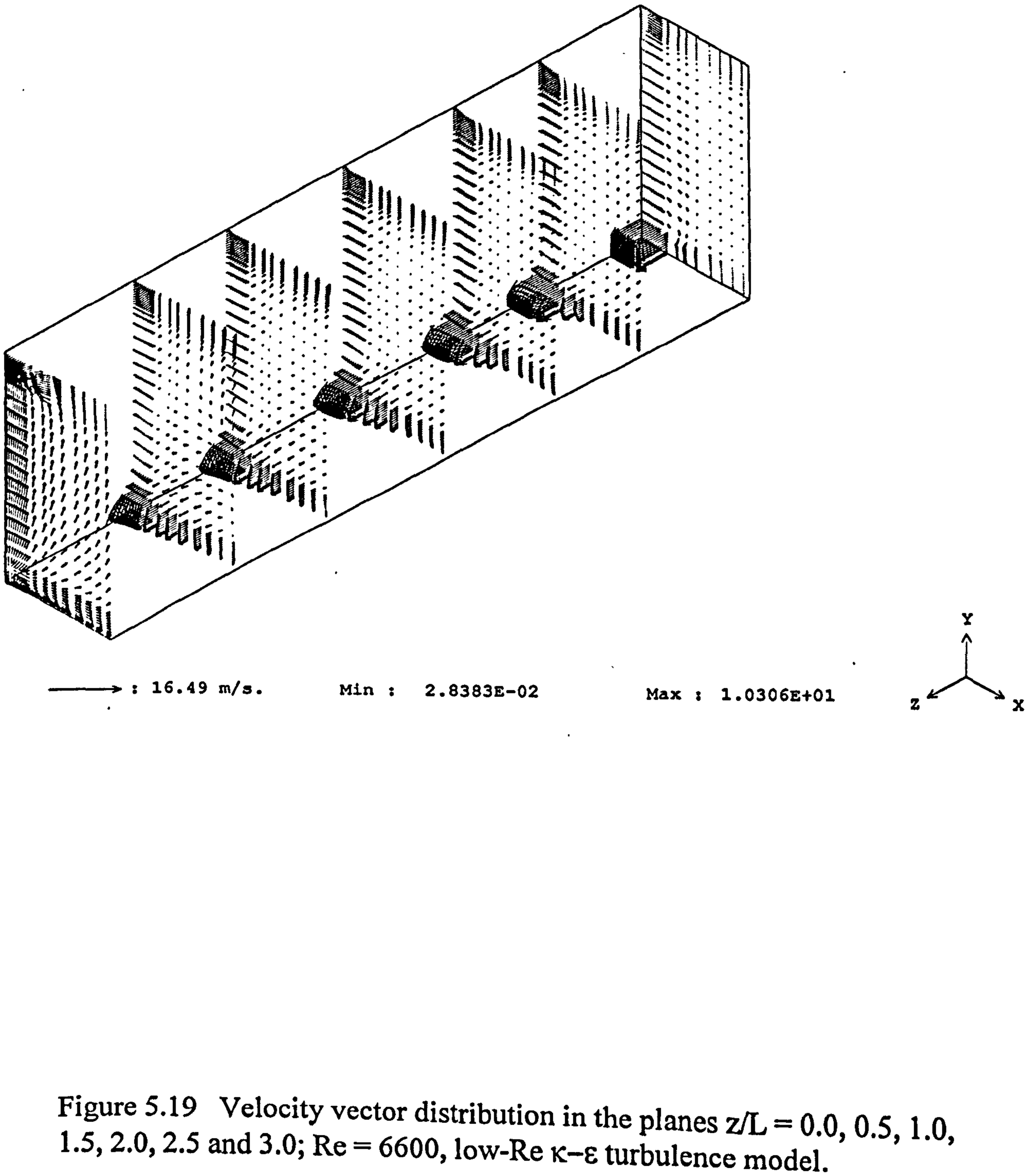

Figure 5.19 Velocity vector distribution in the planes z/L = 0.0, 0.5, 1.0, 1.5, 2.0, 2.5 and 3.0; Re = 6600, low-Re κ–ε turbulence model.

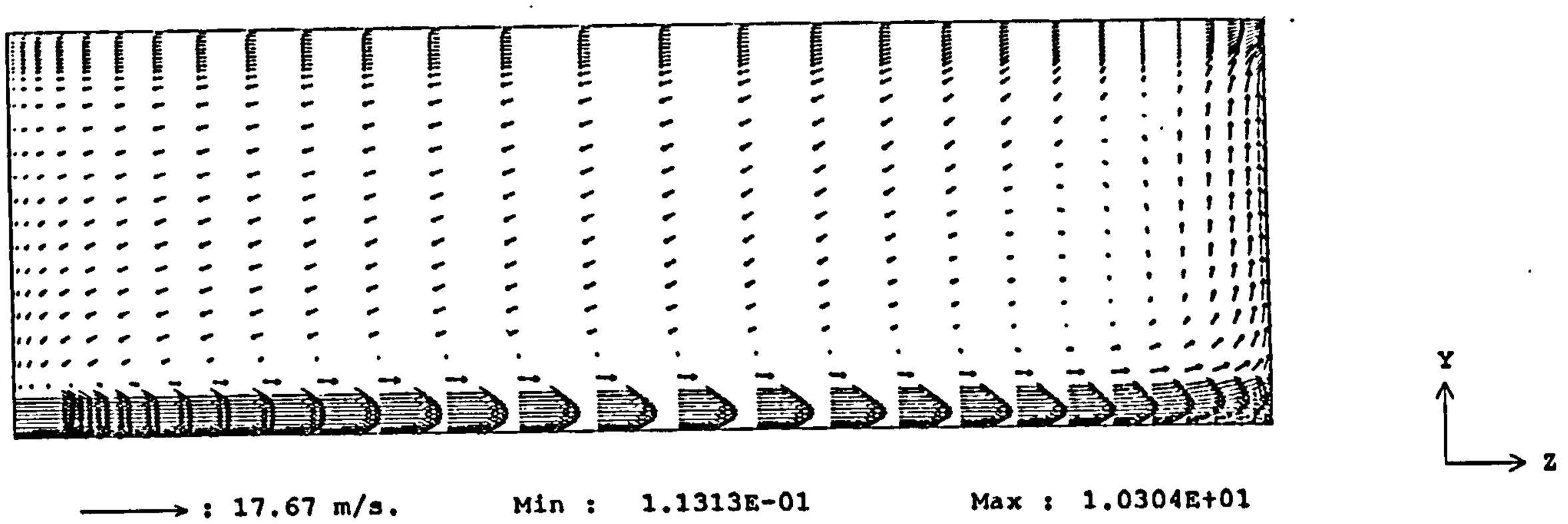

Figure 5.20 Velocity vector distribution in the planes x/W = 0.0 (symmetry plane); Re = 6600, low-Re κ–ε turbulence model.

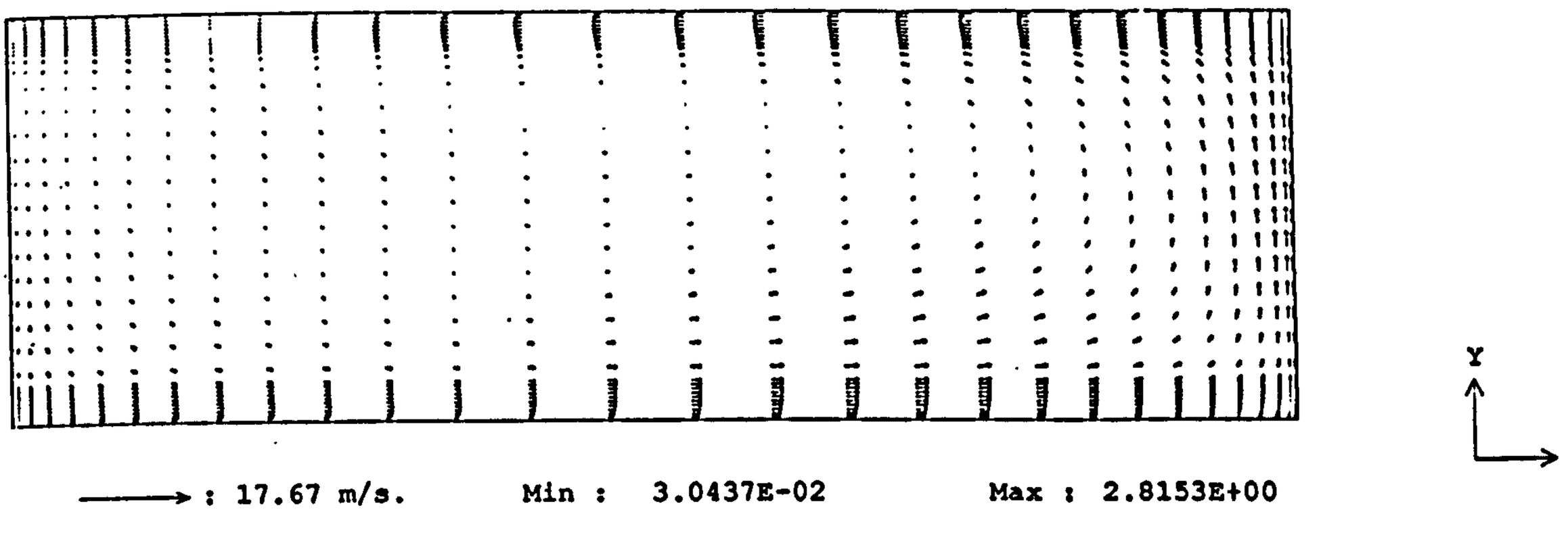

Figure 5.21 Velocity vector distribution in the plane x/W = 0.4; Re = 6600, low-Re κ–ε turbulence model.

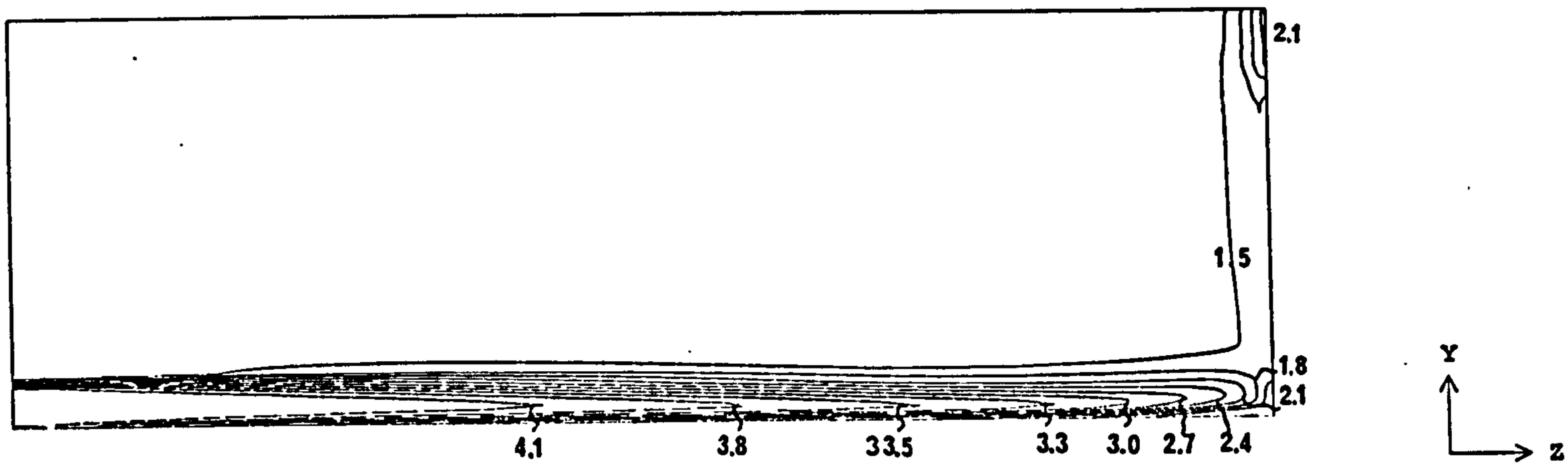

Figure 5.22 Turbulent kinetic energy contours in the plane x/W = 0.0 (symmetry plane); Re = 6600, low-Re κ–ε turbulence model. Contour values in m^2/s^2 .

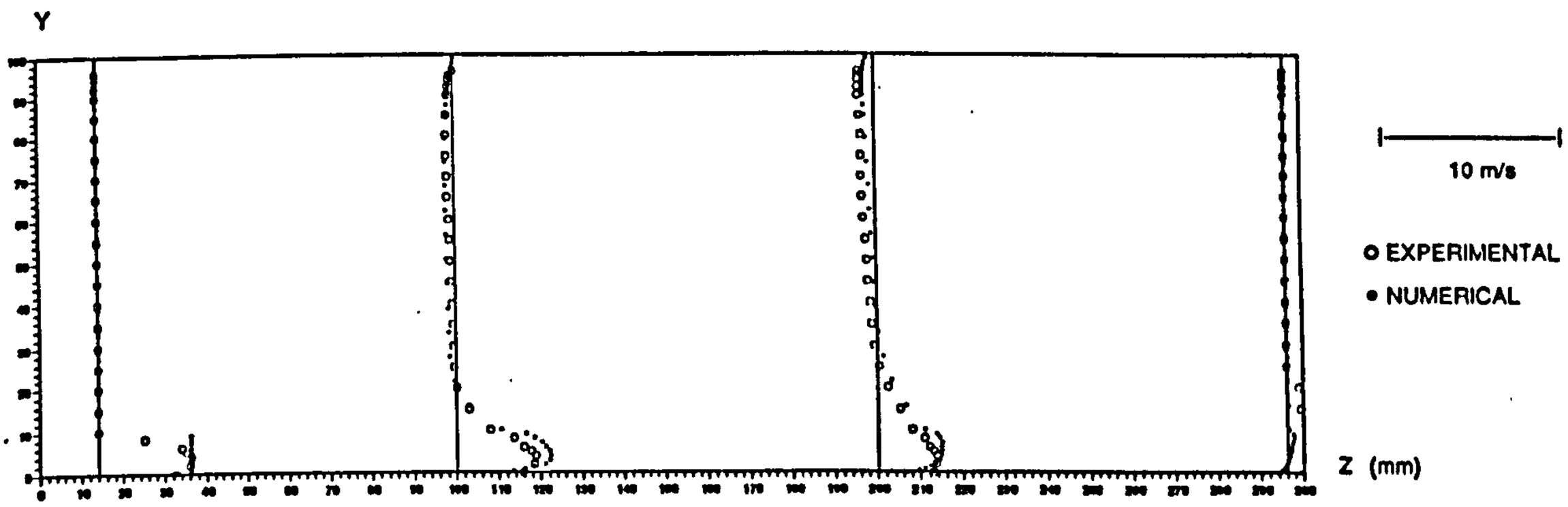

Figure 5.23 Measured and predicted mean velocity in the plane x/W = 0.0 (symmetry plane); Re = 3600.

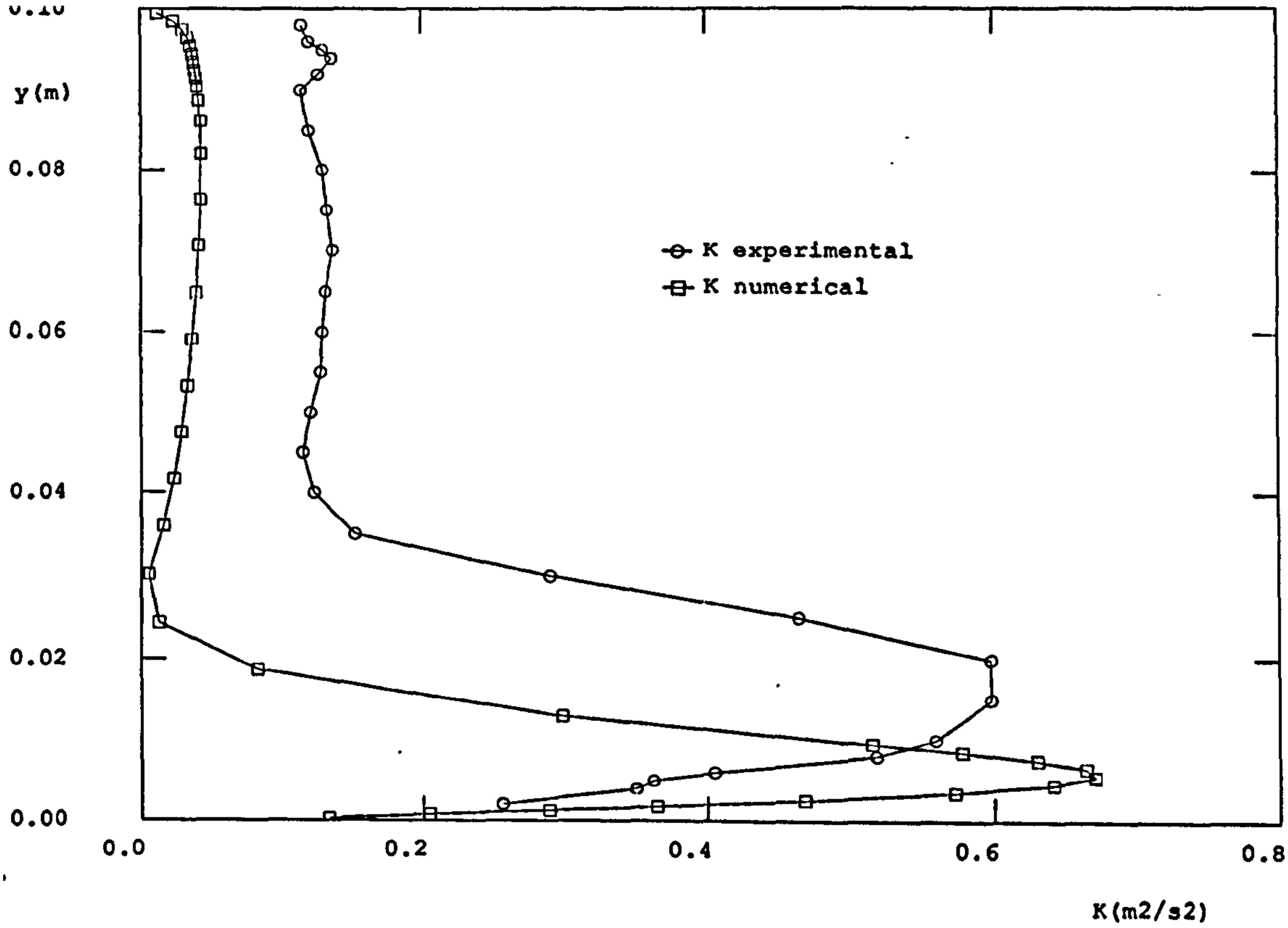

Figure 5.24 Measured and predicted kinetic energy of turbulence in the plane x/W = 0.0 at z = 200 mm; Re = 3600.

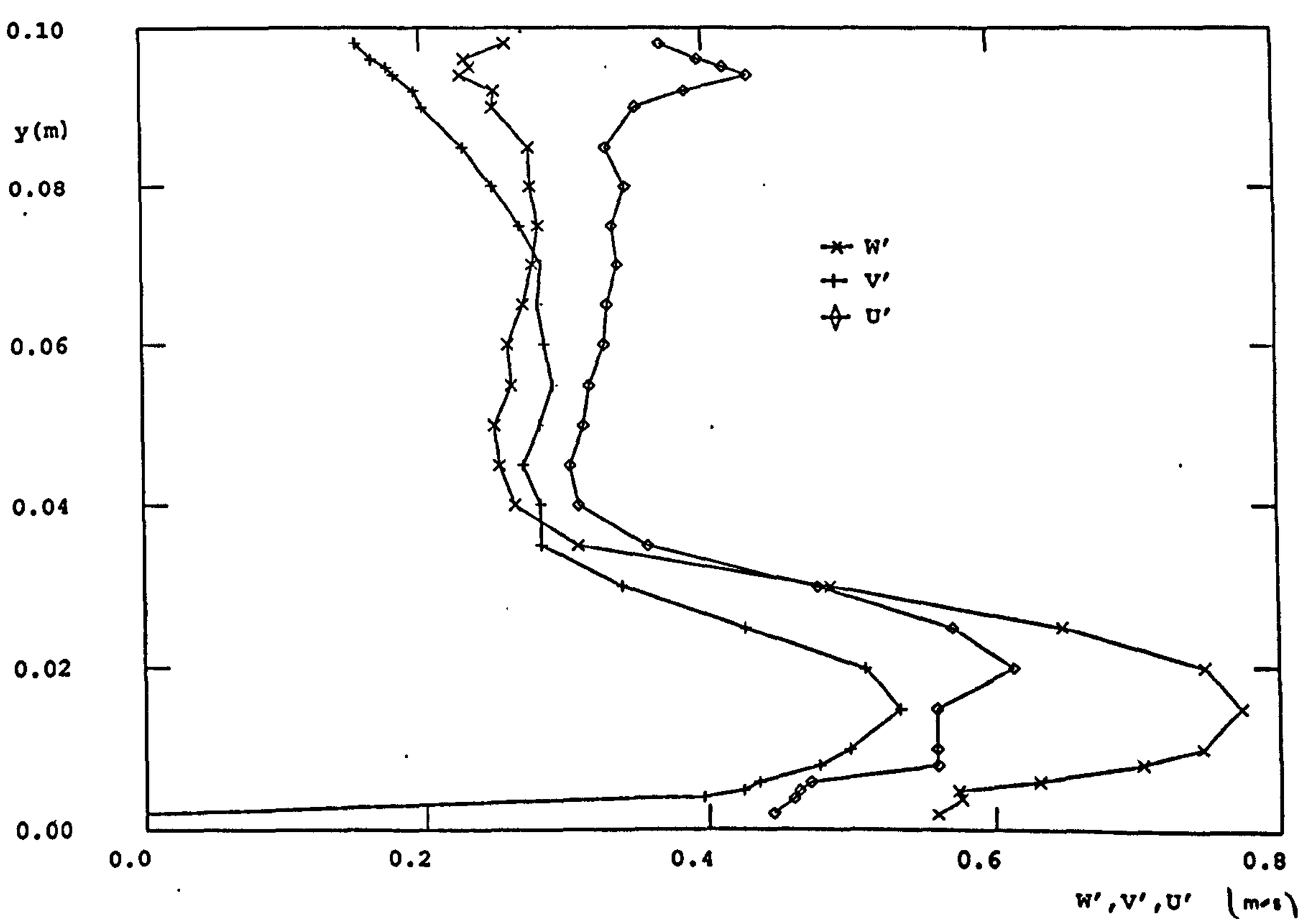

Figure 5.25 Measured rms velocities in the plane x/W = 0.0 at z = 150 mm; Re = 3600.

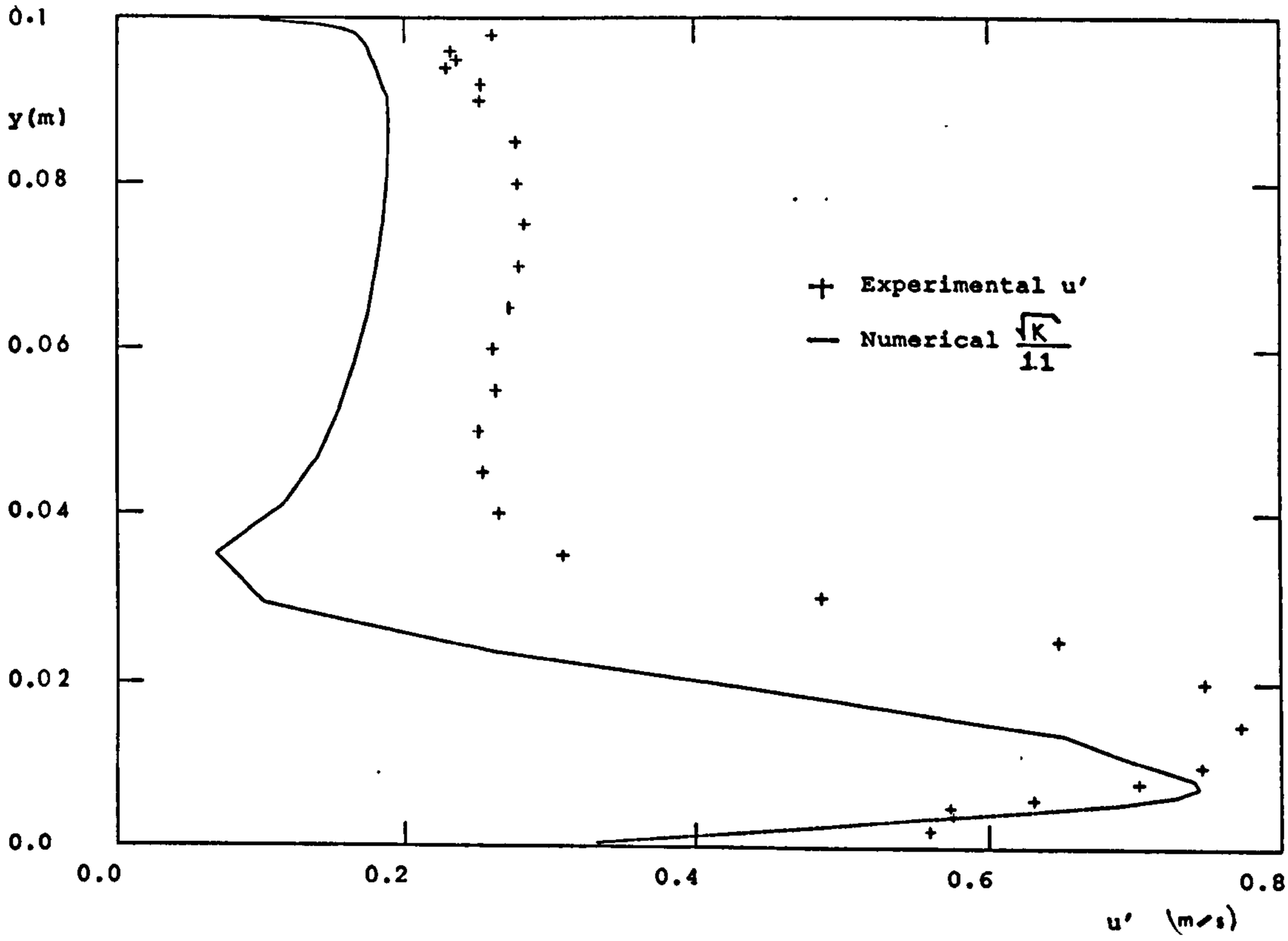

Figure 5.26 Measured and predicted r.m.s. velocities in the plane x/W = 0.0 at z = 150 mm; Re = 3600.

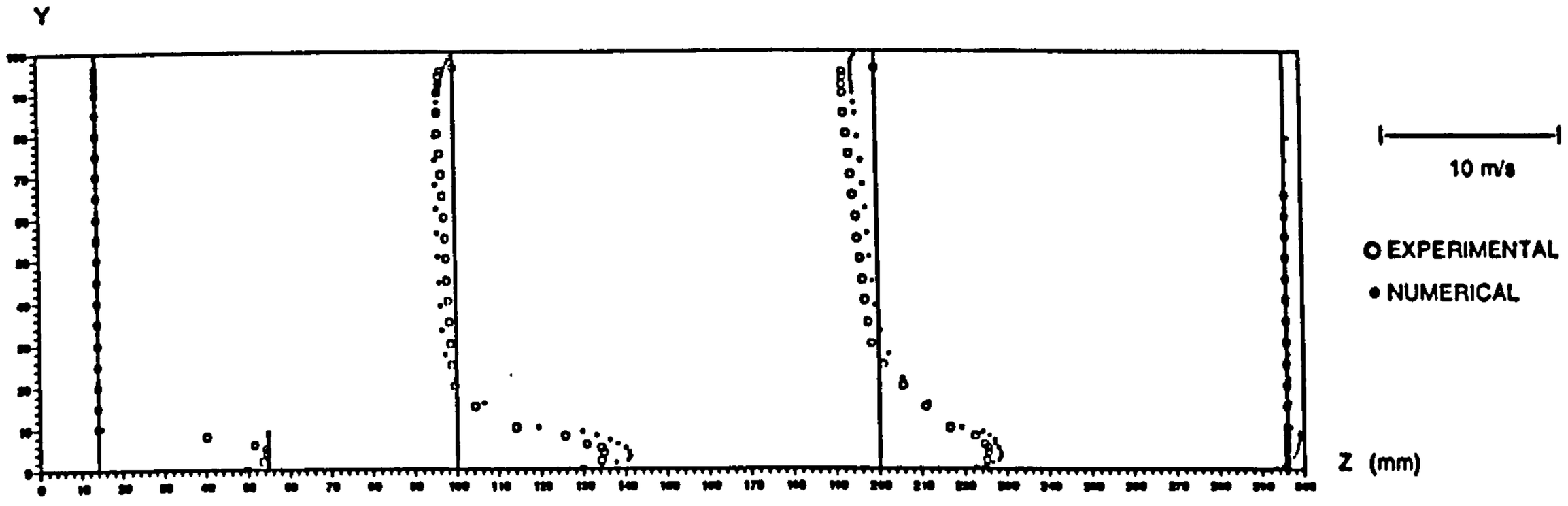

Figure 5.27 Measured and predicted mean velocity in the plane x/W = 0.0 (symmetry plane); Re = 6600.

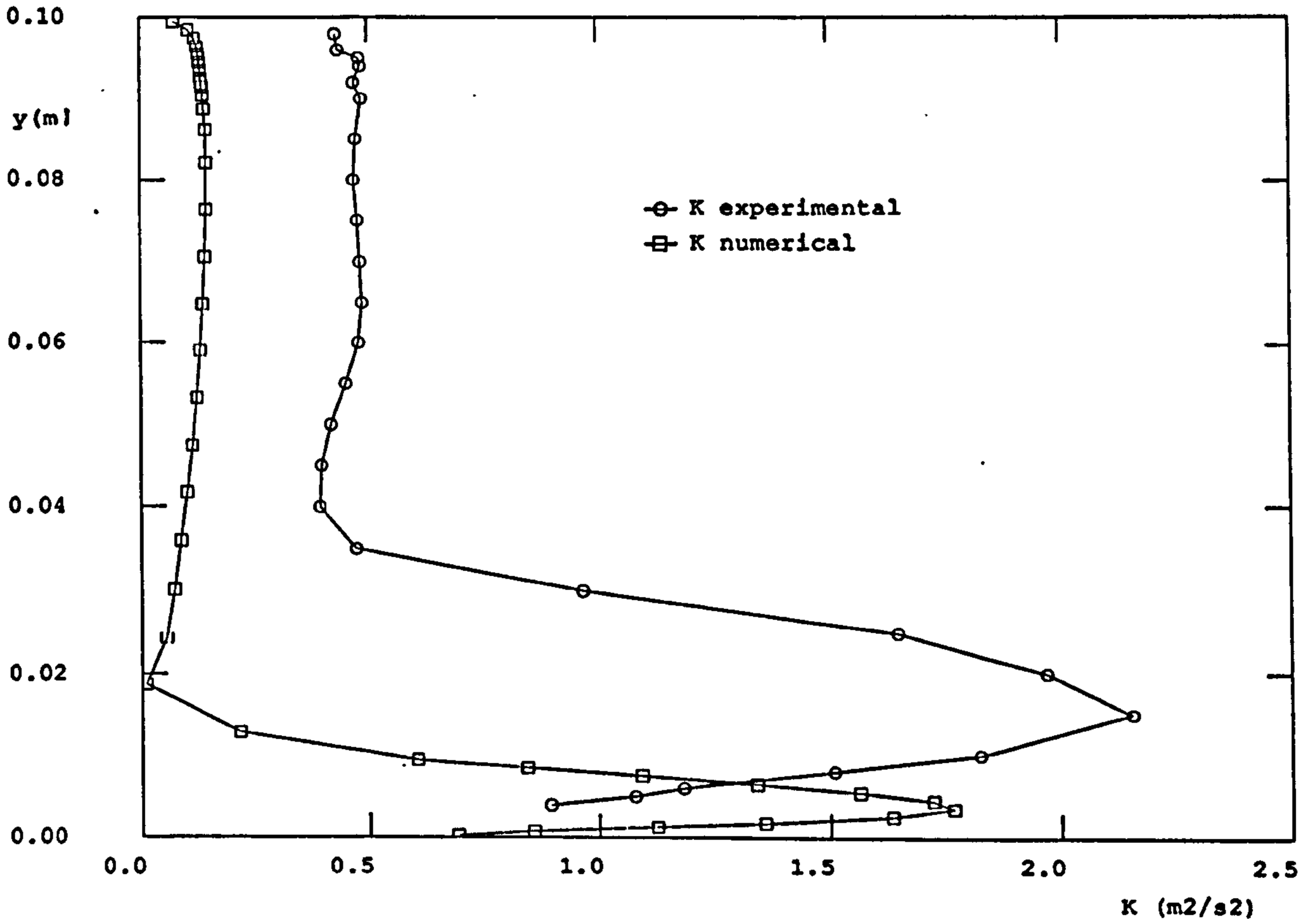

Figure 5.28 Measured and predicted kinetic energy of turbulence in the plane x/W = 0.0 at z = 150 mm; Re = 6600.

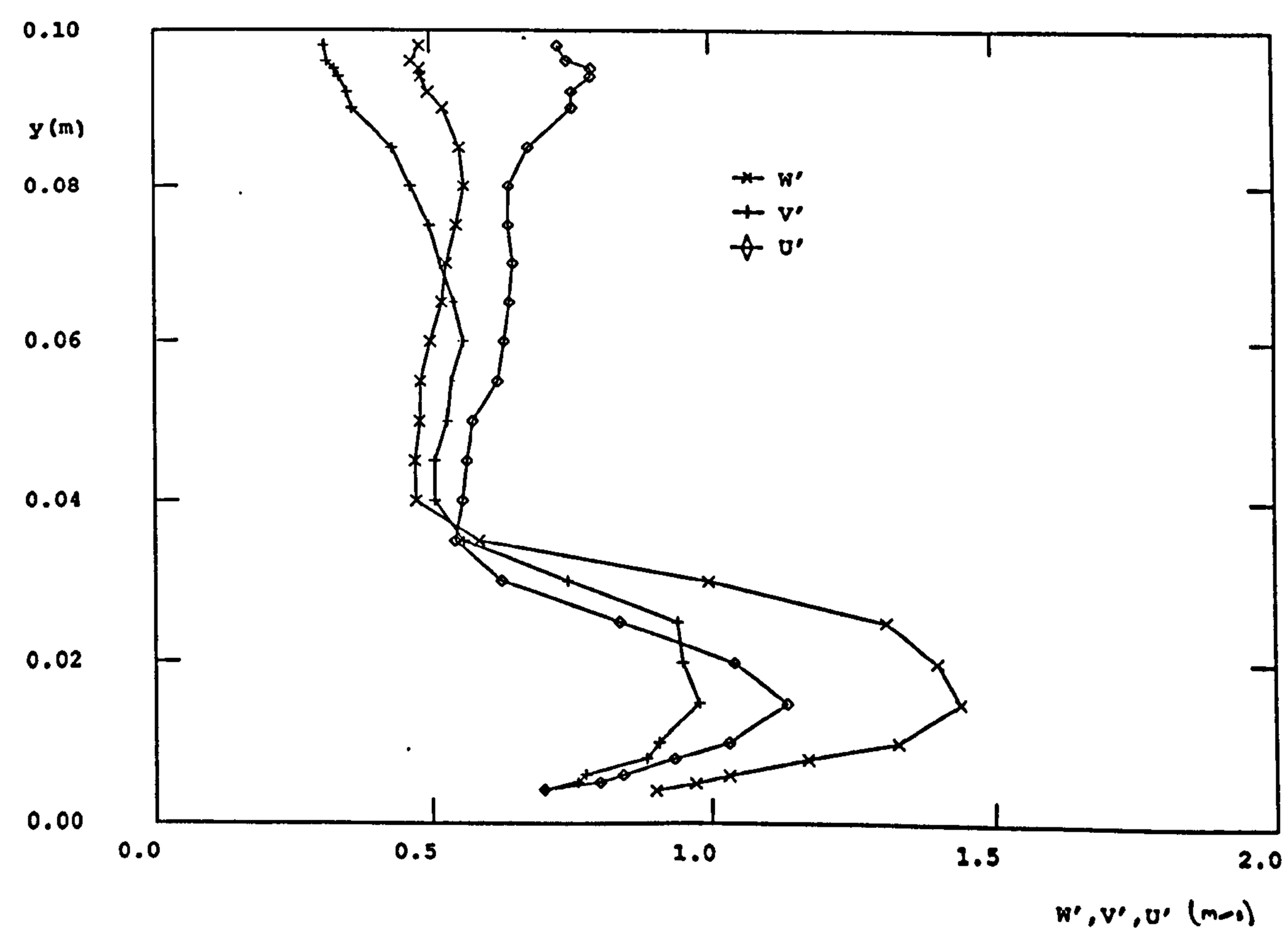

Figure 5.29 Measured rms velocities in the plane x/W = 0.0 at z = 150 mm; Re = 6600.

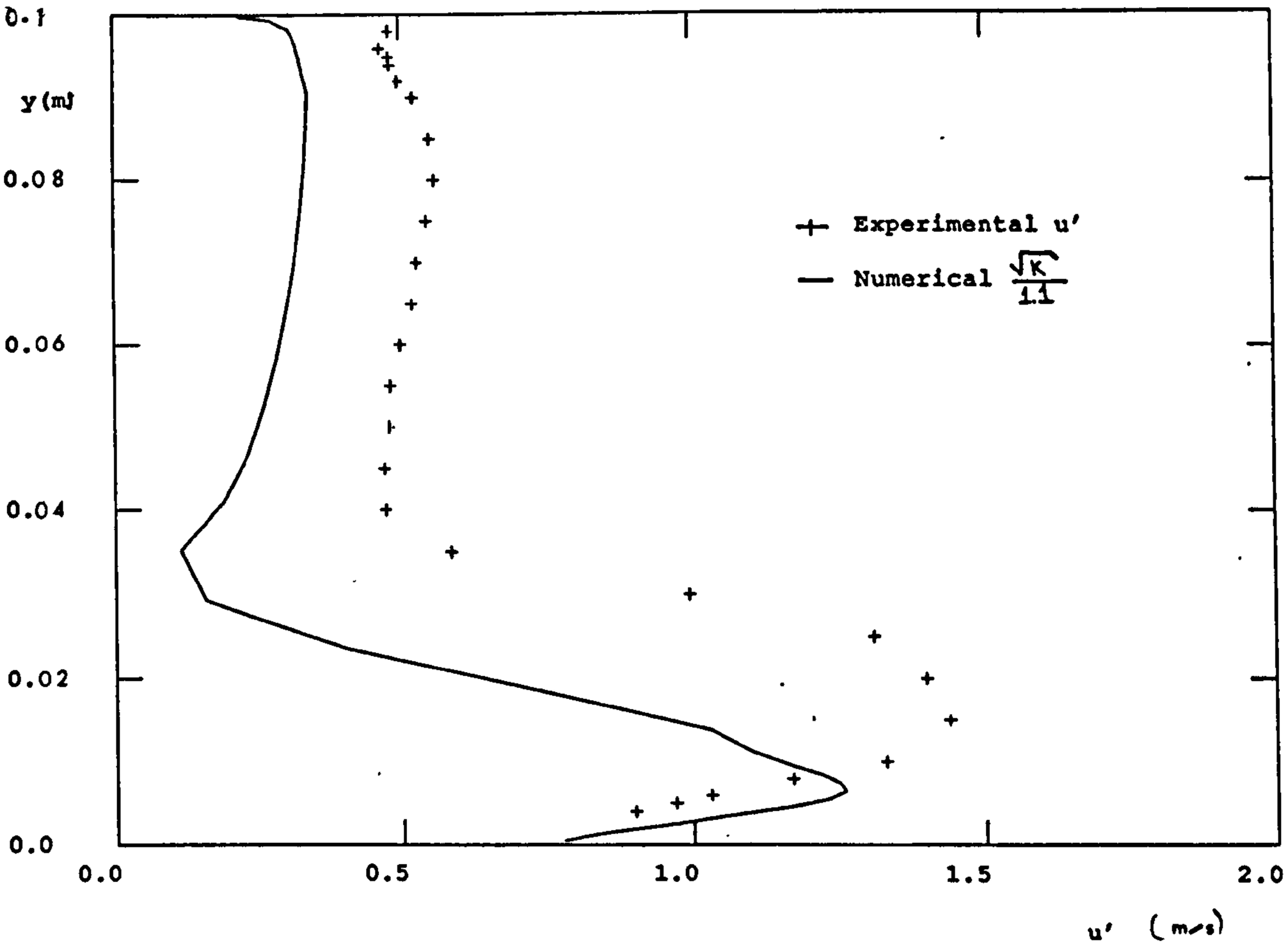

Figure 5.30 Measured and predicted r.m.s. velocities in the plane x/W = 0.0 at z = 150 mm; Re = 6600.

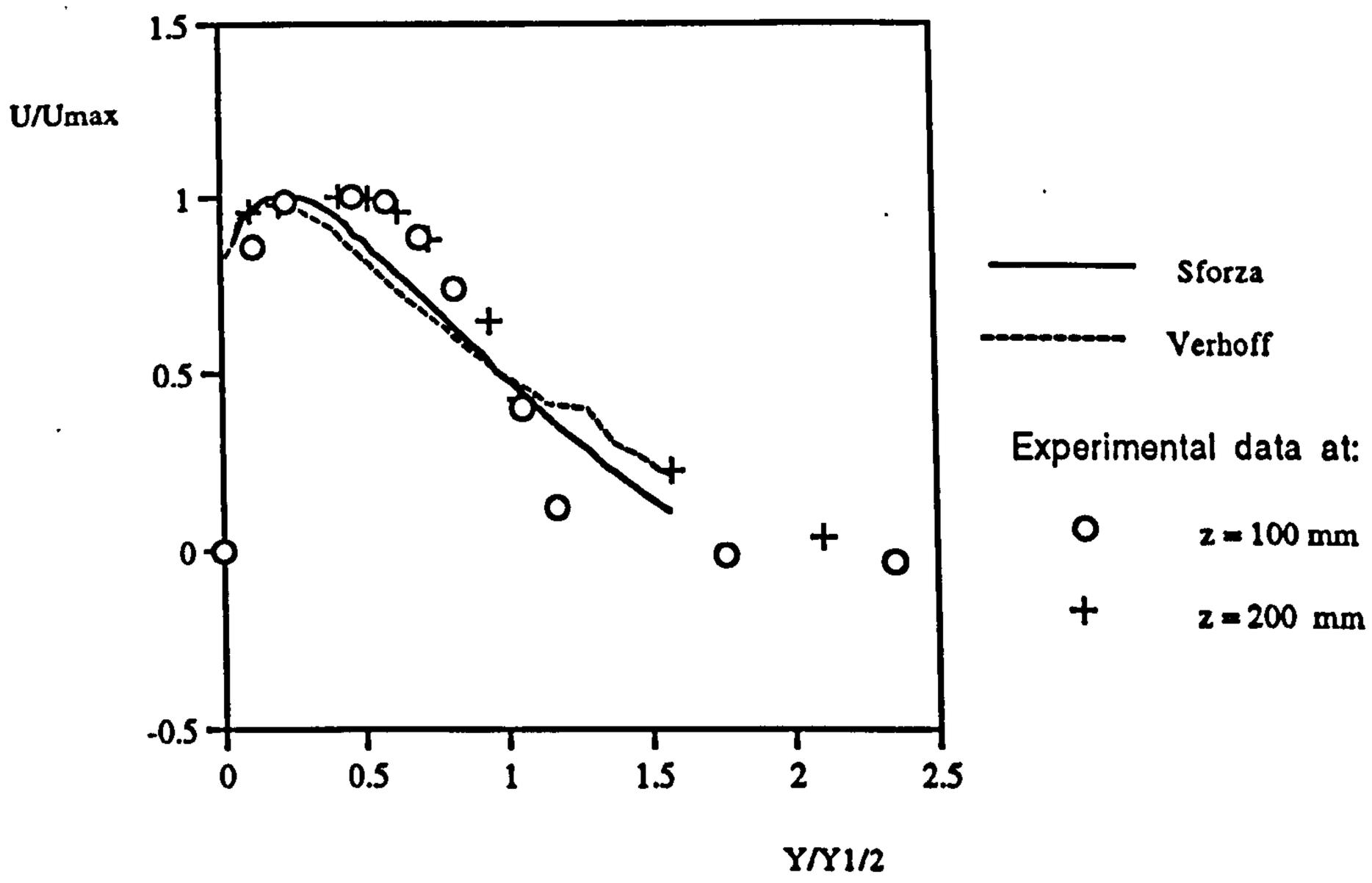

Figure 5.31 Comparison of measured non-dimensional velocity profiles at z = 100, 200 mm for Re = 6600 with data from Sforza and Herbst (1967), Verhoff (1963).

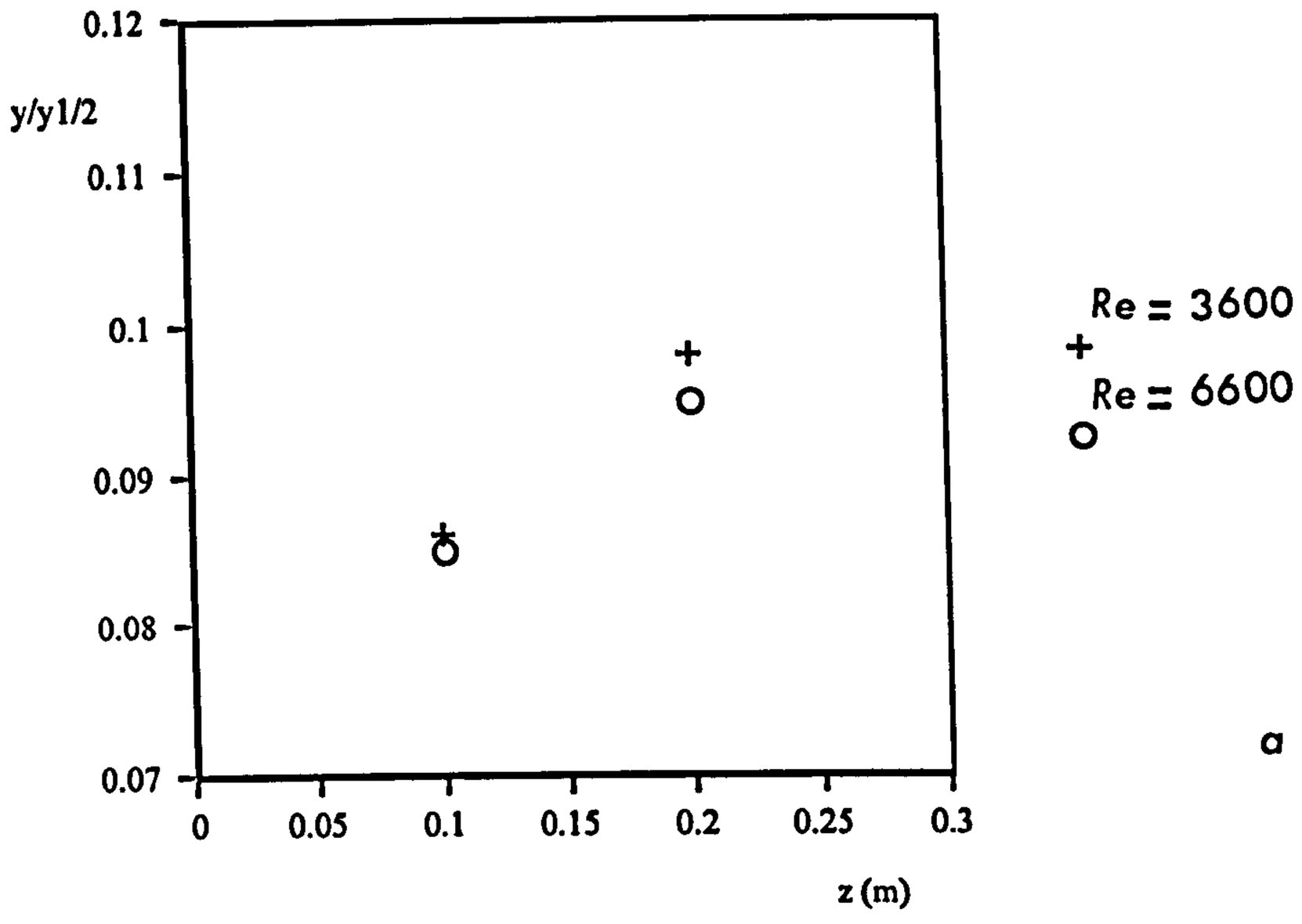

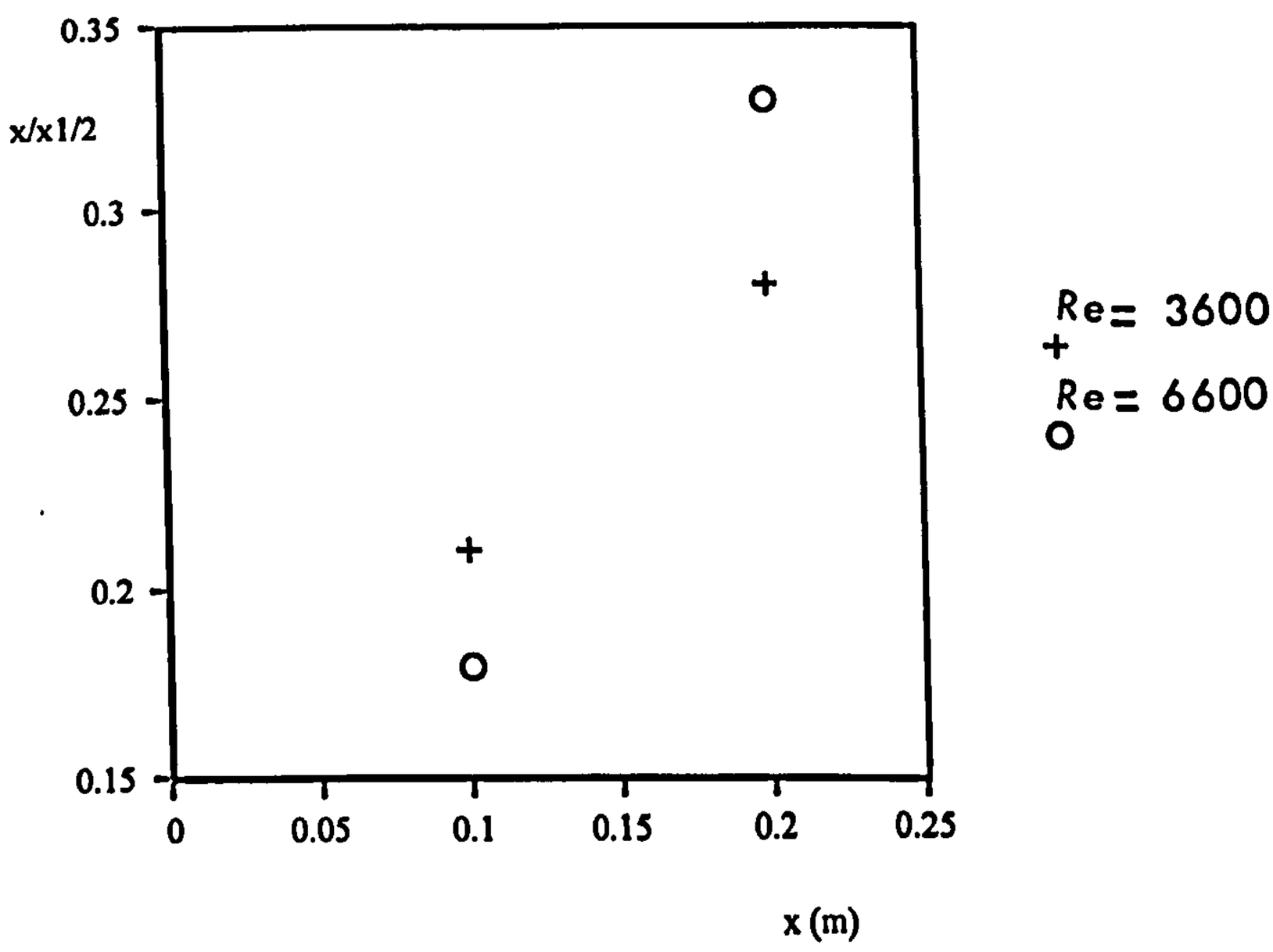

Figure 5.32 Variations of jet half width (horizontal and vertical jet spread) for different Re's numbers. a) $y/Y_{1/2}$, b) $x/X_{1/2}$.

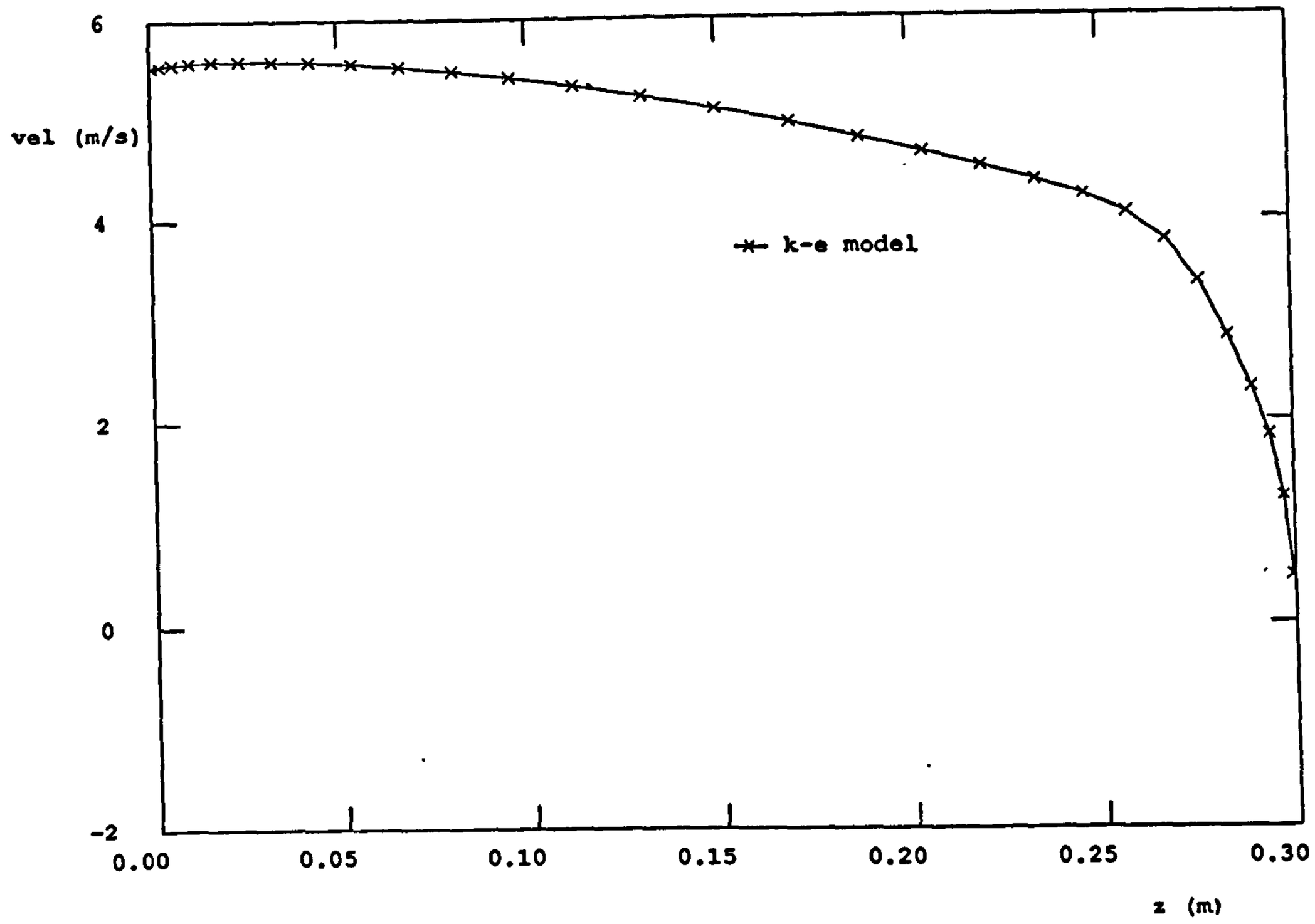

Figure 5.33 Measured mean velocity decay in the plane x/W = 0.0 (symmetry plane) at y = (H-h)/2; Re = 3600.

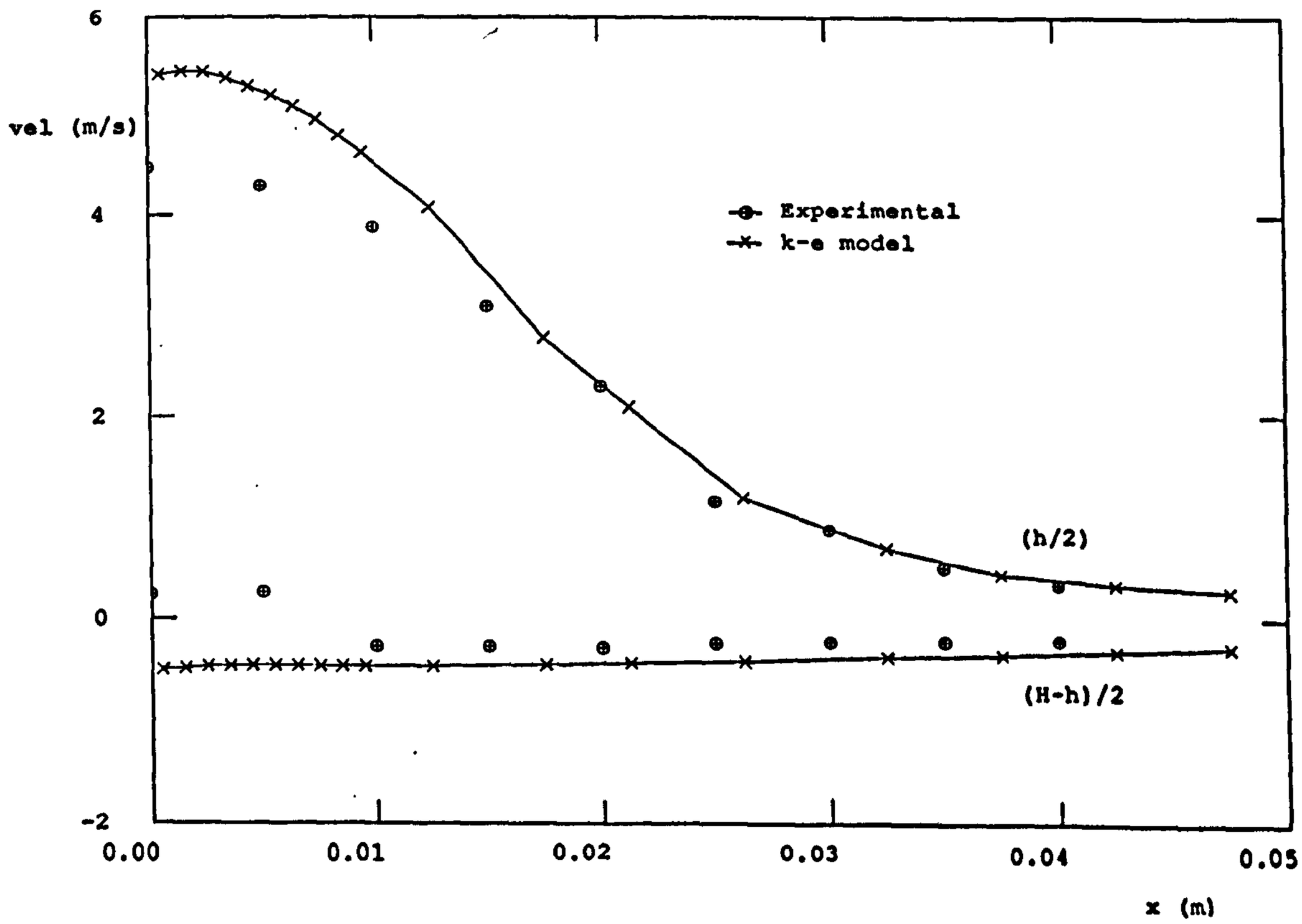

Figure 5.34 Predicted mean velocity in the occupied zone in the plane x/W = 0.0 at y = h/2; Re = 3600.

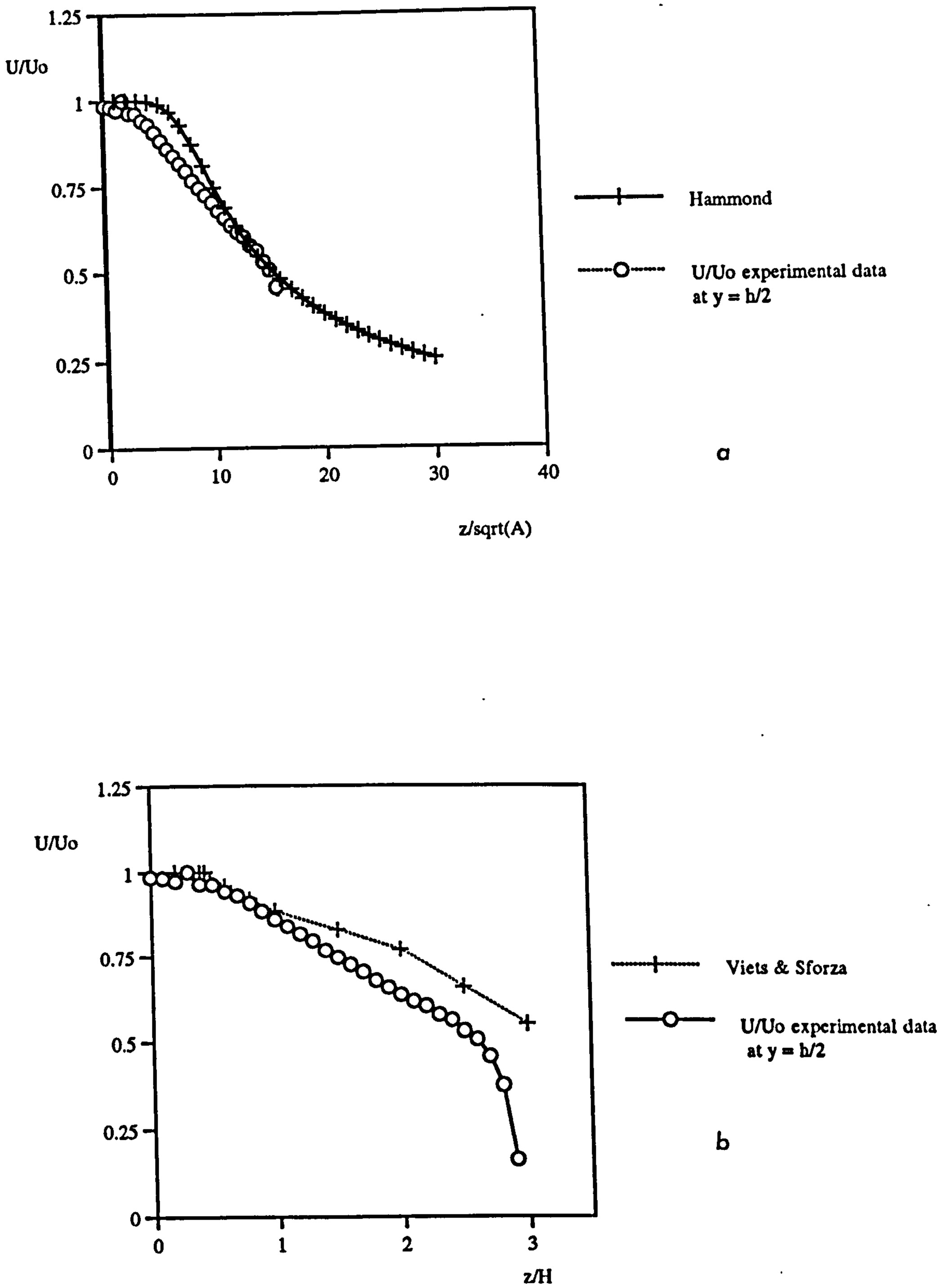

Figure 5.35 Measured and predicted velocity decay on symmetry plane. Comparison with data of (a) Hammond (1991), (b) Viets and Sforza (1964); Re = 6600.

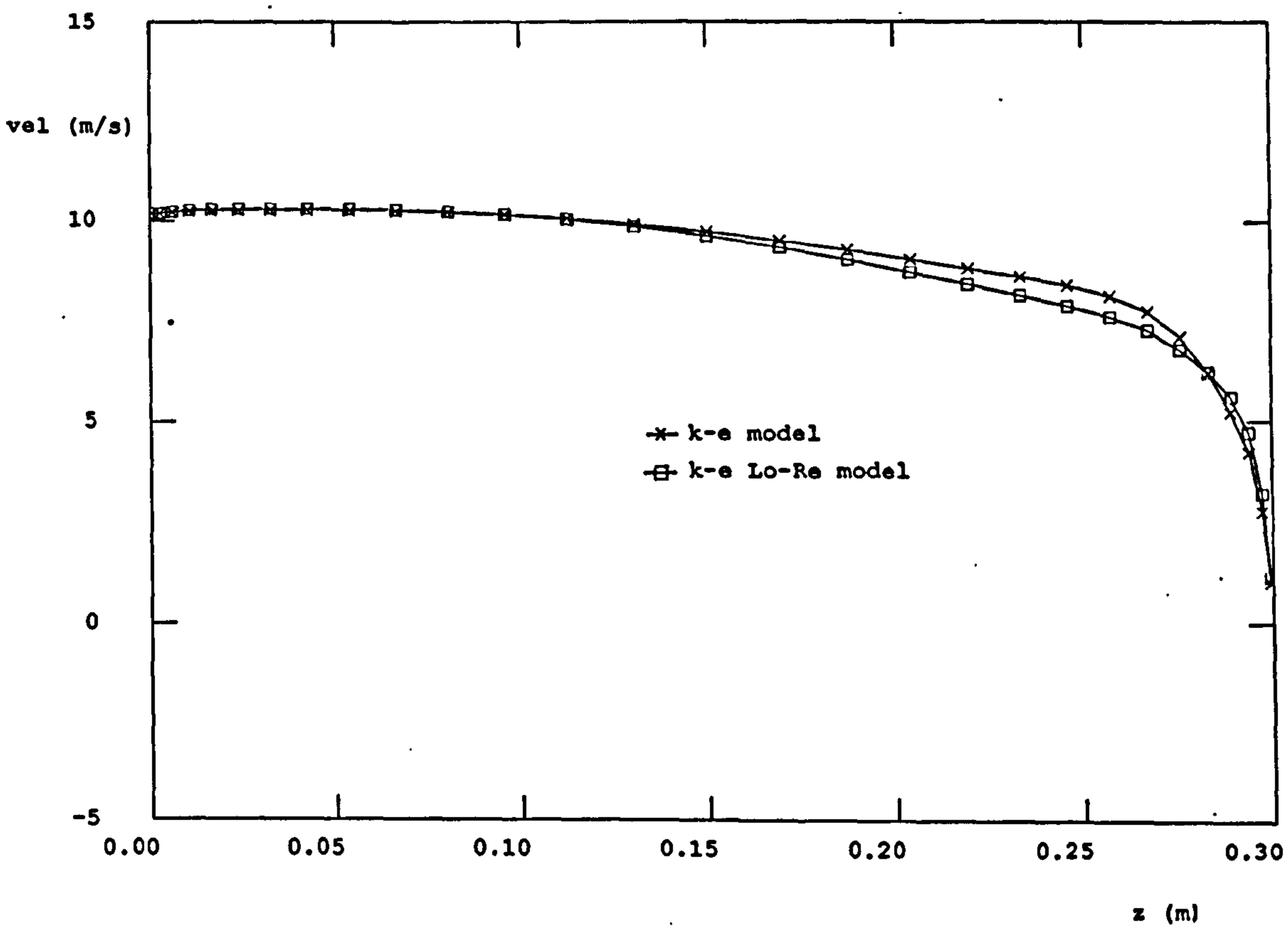

Figure 5.36 Predicted mean velocity decay in the plane x/W = 0.0 (symmetry plane) at y (H-h)/2; Re = 6600 calculated with the standard and the low-Re κ–ε turbulence models.

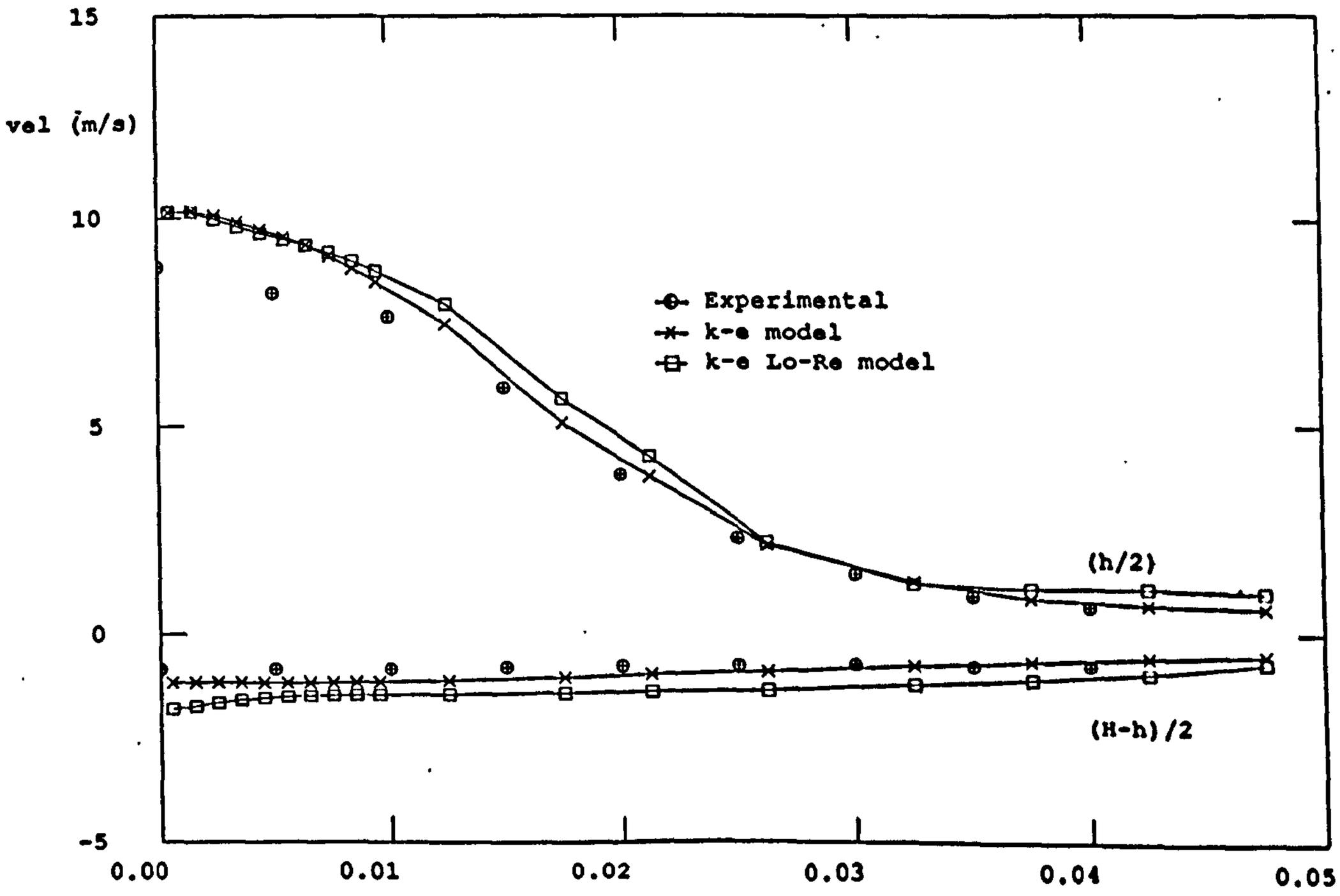

Figure 5.37 Predicted and measured mean velocity profile at z = 100 mm on the horizontal planes y = (H-h)/2 and y = h/2; Re = 6600.

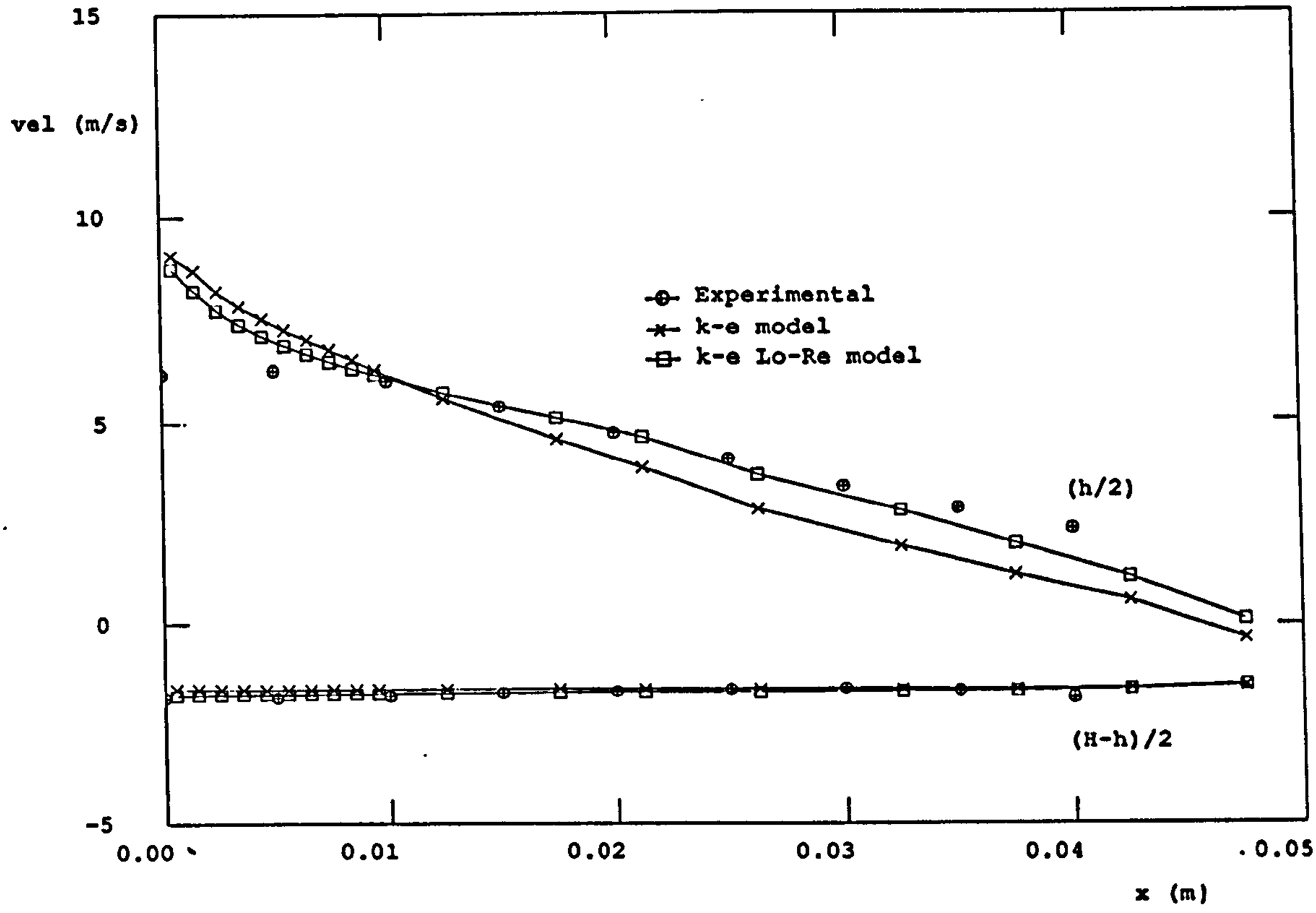

Figure 5.38 Predicted and measured mean velocity profiles at z = 200 mm on the horizontal planes y = (H-h)/2 and y = h/2; Re = 6600.

CHAPTER 6

MEASUREMENT AND PREDICTION OF THREE-DIMENSIONAL ISOTHERMAL FLOWS IN CHAMBERS VENTILATED BY VERTICAL JETS FROM CEILING AND FLOOR INLETS.

6.1 Introduction

The measured and predicted mean flow and turbulence distribution in the third and fourth chambers studied are presented in this Chapter. These chambers had the same inlet shape as those of Chapter 4 and 5: a three-dimensional square cross-section jet discharging into a rectangular chamber. The inlet was located at the chamber ceiling and floor for chambers 3 and 4 respectively. Through numerical simulations and experiments several aspects of the flow are studied. The measured mean velocities and the corresponding turbulence levels were used to assess the predictions obtained for both cases using two different turbulence models. Two different flow rates were studied for each chamber and the variations of the inlet jet throw, spread and drop with Re were quantified.

6.2 Experimental and computational details

6.2.1 Flow configurations and LDA measurement locations

The geometrical configurations for the third and fourth chambers are shown in Figures 6.1 (a) and (b) respectively. Their geometrical characteristics have been described in detail in Chapter 2. The symmetry of the flow patterns across the two chambers was established through LDA following the procedure explained in Chapter 4. The results showed that

the flow on either side of the symmetry plane was symmetrical to within the precision of the measurements. Two vertical and one horizontal locations were selected in the x/H = 0.0 plane where LDA measurements of all three components of the mean velocity (u, v, w) and the corresponding r.m.s. values (u', v' and w') were made for both cavities: For chamber 3 (C3) at z = 40 mm, y = 7 mm and y = 30 mm, and for chamber 4 (C4) at z = 40 mm, y = 97 mm and y = 70 mm.

6.2.2 Computational details

The CFD code used for the predictions shown in this Chapter has been described in Chapter 4. The boundary conditions used were identical to those set for chamber 1, apart from the locations of the inlet and outlet. For C3 the inlet is located at the ceiling, adjacent to the wall and the outlet is located centrally on the upper part of the end wall. The inlet in C4 is located on the floor, and the outlet located centrally on the lower part of the end wall.

The pressure, the three components of the mean velocity as well as the kinetic energy of turbulence (κ) and its dissipation rate (ε) have been calculated. The numerical mesh used for the prediction of the flows in both chambers is shown in Figure 6.2. Mesh independence tests were carried out with computational mesh sizes of 15x30x30, 18x36x30, 18x37x36 and 18x37x42 volumes (in the x, y, and z directions respectively). A mesh of 18x37x36 volumes was found to provide a good compromise between accuracy and computer time usage. Figure 6.3 shows for C3 a comparison of mean velocity profiles along the symmetry plane predicted with the four different meshes. The profiles predicted with all four meshes are very similar, and for the two finest meshes the differences are less than 5% in some locations (around z = 0.25 mm) and 2% across most of the profile.

The flow was assumed to be symmetrical, as verified by the LDA measurements, following the procedure described in Chapters 4 and 5. All gradients were set to zero across the symmetry plane and a slip condition was used in that plane. Only half of the domain was simulated. Isothermal conditions were assumed throughout. The numerical solutions comprised 3000 iterations and took approximately 1.40 hours of CPU time on a VAX 4100 machine.

6.3 Experiments and predictions of flows produced by a vertical jet issuing from a ceiling inlet

6.3.1 Flow visualisation

Using the flow visualisation technique described in Chapter 2 a qualitative description of flow patterns was obtained. As mentioned earlier, flow visualisation was possible for Re values up to 2000, as for Re > 2000 there was strong mixing inside the chamber and the water mist used as flow tracers diffused very rapidly. Characteristic results at Re = 1500 are shown in Figure 6.4.

The images shown in Figure 6.4 were taken under steady state conditions, with one second difference between them, in order to visualise the instantaneous flow patterns. It can be seen in Figure 6.4 that the incoming air stream remains attached to the vertical wall surface until it reaches the floor surface, where it is re-directed. One part of the air stream is deflected over the floor surface in the direction of the end wall. This horizontal flow moves along the floor surface for around 126 mm or 40% of the chamber length. The main part of this flow is then directed upward to form a recirculation zone. It was observed during the experiments that the air flow

deflected by the floor surface spreads in several directions, covering all the floor surface between the symmetry plane and the lateral walls, before leaving the chamber through the outlet.

The visualisation experiments showed that the flow pattern formed inside the chamber resulted in strong mixing of the inlet jet with the air already in the chamber across 40% of the volume near the inlet and that the flow was highly three-dimensional. The flow pattern over the remaining 60% of the chamber volume, across which the jet deflected by the floor spread, was difficult to distinguish.

6.3.2 Predicted flow patterns for chamber 3

CFD predictions were performed for two flow rates (Re's); predictions were made for the higher flow rate, using both the standard $\kappa-\varepsilon$ turbulent model and the "low-Re" $\kappa-\varepsilon$ turbulence model. The inlet and outlet velocities, flow rates and Re's are tabulated below.

Reynolds number	Inlet velocity (m/s)	Outlet velocity (m/s)	Flow rate (m^3/s)
3600	5.55	2.46	0.001665
6600	10.17	4.52	0.0030525
6600 low-Re $\kappa-\varepsilon$ m.	10.17	4.52	0.0030525

In the subsequent sections the same format as that used in Chapters 4 and 5 is employed for the presentation of the results. The predictions are presented in the form of velocity vector distributions, mean velocity and r.m.s. profiles, as well as contours of the kinetic energy of turbulence. The predicted results are compared with the LDA data obtained. The results for

Re = 3600 are described briefly, while those for Re = 6600 are discussed in more detail.

Predictions with the standard κ–ε turbulence model, Re = 3600

The predicted mean velocity vectors in the x/W = 0.0, y/H = 0.0 and z/L = 0.0 planes for Re = 3600 are shown in Figure 6.5. The air flow stream can be seen entering through the inlet located on the ceiling of the room. The air stream moves towards the floor, with the jet remaining attached to the lateral wall up to 14.5 mm from the floor surface. In the corner of the wall and floor, a recirculation region is formed, centred around the symmetry plane. The dimensions of this region are 3.4 mm, 14.5 mm and 3.6 mm, in the x, y and z directions respectively.

The jet, after it becomes detached from the wall, reaches the floor where it is deflected and subsequently spreads along the floor surface. A large recirculation zone is formed over the symmetry plane.

It can be clearly observed in the Figure that the velocities decrease significantly as the flow moves across the half of the chamber located near the outlet. Typically, velocity magnitudes in that region are around 10-20% of those near the inlet and in general do not exceed 1m/s. The mean velocities are around 0.60 m/s close to the outlet zone where part of the air stream exits through the chamber outlet.

Steep velocity gradients can be observed along the jet trajectory. The velocities vary from 5.6 m/s to 0.1 m/s in the boundary layer near the inlet and from 0.0 - 0.6 m/s over the second half of the chamber. The large recirculation region occupies around 30% of the area of the symmetry plane and has its centre at z = 47.3 mm and y = 10.9 mm.

Predictions with the standard κ–ε turbulence model, Re = 6600

The predicted velocity vectors and κ contours for several planes at Re = 6600 are presented in Figures 6.6 - 6.13. The velocity vector distribution for Re =6600 is shown in Figure 6.6. The velocity distributions show similar patterns as those for Re = 3600; such as the large recirculation zone, the inlet jet remaining attached to the wall and the small recirculation zone near the corner formed by the floor and the inlet wall. The velocity magnitudes are around 50% larger due to the higher flow rate. The Coanda effect is in evidence along the inlet wall surface to which the air stream remains attached.

The centre of the large recirculation zone is located at z = 33.0 mm and y = 10.9 mm for this Re. The recirculation zone at the lower corner is reduced in size to 9.9 mm long and 2.6 mm wide as the increased momentum of the inlet jet at this Re results in higher velocities.

The velocity gradients along the inlet jet edges are steeper than for Re = 3600, but the shape of the boundary layer is similar. The air stream flowing along the floor surface reaches 3/4 of the length chamber. Across half of the chamber the magnitudes of the mean velocity vectors are small, ranging from 1.6 m/s near the outlet to 1.0 m/s in the boundary layer and near zero in the vicinity of the stagnation point on the floor.

The mean velocity vectors at the z/L = 3.0, y/H = 1.0 and x/W = 0.5 planes are shown in Figure 6.7. It can be seen that the air jet spreads sideways as it flows along the x/W = 0.5 lateral wall. The velocity vectors along the lateral wall do not indicate the presence of a recirculation zone and the main direction of the flow is towards the end wall. The magnitudes of the

velocities in this plane are 20-60% higher that those observed along the symmetry plane outside the boundary layer. The mean velocities over the ceiling surface are smaller, varying from 0.1 to 0.5 m/s, and are in general around 40% lower than the velocities near the lateral wall.

Figure 6.8 shows the velocity vector distributions in several vertical planes along the chamber length. The results in the plane z/L = 0.0 show the air stream entering the chamber spreading towards the x/W = 0.5 wall. A recirculation zone is formed by the air flow deflected by the floor, occupying almost 70% of the plane. The centre of this elongated recirculation appears to comprise a long region at around 10.9 mm < y < 90.9 mm. Along the end wall, the mean velocity magnitudes have decreased by around 70%. As might be expected, the largest velocities are found near the outlet (1.6 m/s).

The mean velocity vectors in the symmetry plane (x/W) = 0.0 are shown in Figure 6.9 and those in the plane x/W = 0.4 close to the lateral wall in Figure 6.10. In Figure 6.9 the small recirculation zone on the corner formed by the floor and the inlet wall can be seen. The shape of boundary layer along the vertical wall changes as the flow approaches the stagnation point. Along the floor surface the jet is considerably narrower due to he spread in the x direction observed in Figures 6.6 and 6.8. This floor jet motion persists for three-quarters of the chamber length: the stagnation point is located at z = 220 mm. The centre of the large recirculation zone formed in the half of the chamber nearer the inlet is at z = 38 mm and y = 14 mm. Comparing Figure 6.9 with Figure 6.10 it can be observed that in the latter the recirculating flow extends across over almost the entire plane.

The kinetic energy of turbulence contours in the plane of symmetry are presented in Figure 6.11. Along the incoming air jet trajectory the highest

values of κ are 4.5 m^2/s^2. As the jet flows into the chamber the levels of kinetic energy decrease rapidly with values of 1.9 m^2/s^2 at z = 91 mm near the floor. Steep gradients can be observed along the inlet wall and floor surfaces on the left half of the chamber. Across the rest of the chamber the values of κ are below 1.9 m^2/s^2 . Near the outlet the predicted κ values were around 0.6 m^2/s^2 .

Predictions with the low-Re κ–ε turbulence model, Re = 6600

The results for Re = 6600 using the low-Re κ–ε turbulence model are shown in Figures 6.12 to 6.17. It can be seen in Figure 6.12 that there are some appreciable differences between these and the previous results (Figure 6.6) with the standard κ–ε model. In this case, the velocity magnitudes decrease more rapidly along the floor; the stagnation point located at around 130 mm from the inlet wall; the magnitude of the vectors over the half of the chamber nearer the outlet are 20-30 % lower than in Figure 6.6.

Comparing Figures 6.13 and 6.14 with Figures 6.7 and 6.8 it can be seen that the magnitude of the velocity vectors near the ceiling surface and the symmetry plane is higher by 5-10% when the low-Re model is used. Although the differences between the two sets of predictions are not large, it is interesting to note that the low-Re model yields lower velocities near the floor and higher near the ceiling and the centre of the chamber. This will be discussed further later in this chapter.

Figure 6.15 shows the vectors in the symmetry plane, and Figure 6.16 the corresponding ones in the x/W = 0.4 plane. When these results are compared with the predictions presented in Figures 6.9 and 6.10 respectively, it can be seen that the small recirculation region on the corner

formed between the inlet wall and the floor surface has been reduced in size by 5%. The centre of the large recirculation zone is located in the same position, but the magnitudes of the velocity vectors along the floor surface are lower by 10 to 30%. Conversely, the velocities over the second half of the chamber (for $z > 130.0$ mm) are predicted to be larger by 20% to 30% with the low- Re $\kappa-\varepsilon$ turbulence model.

As for the previous calculations the CPU time required for the predictions increased due to the additional equations that had to be solved by 25% in comparison with the standard $\kappa-\varepsilon$ turbulent model calculations.

Figure 6.17 shows the contours of the kinetic energy of turbulence at the plane of symmetry. The overall distribution is similar to that predicted for the same Re with the standard $\kappa-\varepsilon$ turbulence model. When Figure 6.17 is compared with Figure 6.11 it can be observed that with the low-Re model κ values lower by around 5% are predicted in most parts of the jet.

6.3.3 Comparison of predictions and measured data at Re = 6600

The predictions with the standard $\kappa-\varepsilon$ turbulence model are assessed in this section by comparison with the LDA measurements. Predicted and measured mean velocity profiles at $y = 97$ mm, $y = 70$ mm and $z = 40$ mm in the plane of symmetry for Re = 6600 are compared in Figure 6.18.

In general the predicted mean velocities are similar to the measured values, to within 10%. Agreement between measured and predicted values is quantitatively good for the $y = 70$ mm and $z = 40$ mm profiles. The measured inlet profile at $y = 97$ mm exhibited a parabolic profile, while the predicted one is akin to plug flow, clearly due to the effect of the inlet boundary condition specified. From this observation it may be concluded

that the small discrepancies between measurements and predictions further downstream are due primarily to the inlet conditions specified.

The measured and predicted kinetic turbulent energy profiles at z = 40 mm are compared in Figure 6.19. As in previous cases (Chapters 4 and 5), κ has been underpredicted by the numerical model by 10-15% for y>0.02 m and 20-25% at y = 0.01 m. The measured kinetic turbulent energy was calculated from the three r.m.s. components. (u', v' and w') which are shown in Figure 4.20. In the jet core the turbulence is anisotropic while across the rest of the profile it is nearly isotropic. As has been explained in Chapters 4 and 5, the differences between the measured and predicted κ values (Figure 6.19) may be attributed to the implicit assumption of local isotropy made for the standard κ–ε turbulence model and possible 'flapping' of the jet. A comparison of u' with Nielsen's (1991) expression for the normal stress is shown in Figure 6.21. The comparison of the measured u' levels with the predicted ($\sqrt{\kappa}/_{1.1}$) values shows that the κ values have been under predicted as observed previously from the results shown in Figure 6.19.

6.4 Experiments and predictions of flows produced by a vertical jet issuing from a floor inlet

6.4.1 Flow visualisation

The air flow for C4 (Figure 6.22) follows a similar flow pattern to that observed for C3, but due to the position of the inlet, the incoming air in this case is, of course, flowing from the floor towards the ceiling. The flow is then deflected by the ceiling surface and moves along it until approximately 126 mm from the lateral wall, were it descends. The visualisation experiments showed that the flow pattern formed is highly

three-dimensional. In the first half of the chamber there is intense mixing. The flow pattern over the remainder of the chamber volume was difficult to distinguish.

6.4.2 Predicted flow patterns for chamber 4

Predictions with the standard κ–ε turbulence model, Re = 3600

The mean velocity vectors distributions for Re = 3600 in the x/W = 0.0, y/H = 0.0 and z/L = 0.0 planes are shown in Figure 6.23. The incoming air stream can be seen moving from the floor surface towards the ceiling. The air jet remains attached to the inlet wall until y = 83.3 mm, where a recirculation is formed. The jet is deflected sharply by the ceiling surface along the symmetry plane and towards the lateral wall.

Three recirculations can be observed. The first is formed by the air stream flowing along the symmetry plane; its centre is located at z = 47 mm and y = 12 mm and this region occupies almost the entire half of the chamber nearest to the inlet. The second recirculation is formed by the flow deflected by the ceiling and redirected towards the lateral wall; the centre of this recirculation is elongated as for the ceiling jet case described earlier. The third recirculation is that created over the symmetry plane in the corner formed by the ceiling and the inlet wall; this recirculation zone is the smaller of the three, around 0.3 mm wide and 10 mm long.

Along the jet trajectory steep velocity gradients can observed. The steepest gradient is found, just before the air stream reaches the ceiling surface. Subsequently the velocities decrease to values of 0.2 m/s to 5 m/s in the boundary layer and the recirculation zone. The magnitudes of the velocity vectors in the second half of the chamber, near the outlet, are between 60

and 80% lower. Near the outlet the mean velocities increase from 0.29 m/s at z =150 mm (near the floor surface) to 1.1 m/s at the outlet before the flow leaves the chamber.

Predictions with the standard κ–ε turbulence model, Re = 6600

Figures 6.24 to 6.29 show the predicted results for Re = 6600. Figure 6.24 shows the velocity vector distribution for Re =6600 at x/W = 0.0, y/H = 0.0 and z/L = 0.0. The behaviour is similar to that predicted for Re = 3600; there are three recirculations in evidence and the velocity magnitudes decrease over the half chamber near the outlet of course. The velocity magnitudes are around 50% larger than for Re = 3600 because the flow rate has been increased.

In Figure 6.24, the incoming air jet remains attached to the inlet wall and it is deflected by the ceiling surface. The large recirculation over the first half of the chamber has its centre at z = 38 mm and y = 12 mm. Because the inlet momentum has increased, the size of the small recirculation zone has decreased by 10%, and along the ceiling surface the velocity gradients are steeper by 50 to 60% compared to the Re = 3600 flow case. The air flow along the ceiling extends to half of the distance to the end wall. The shape of the boundary layer along the ceiling surface can be seen in Figure 6.24 to change, especially over the second half, for z > 150 mm. It should be noted that for Re = 3600 the shape of the boundary layer in this region could not be discerned. Steep velocity gradients are again present along the inlet air jet. Smaller velocities (0.1 m/s to 2 m/s) are found over the chamber second half.

Figure 6.25 shows at the z/L = 3.0, y/H = 1.0 and x/W = 0.5 planes the air flow patterns at the cell layers closest to the lateral wall, the end wall and

the ceiling. It can be seen that a large part of the incoming air stream is deflected toward the lateral walls, and large velocity vectors (1 m/s to 4 m/s) can be seen along the x/W = 0.5 plane. The air flowing close to the lateral wall moves primarily in one direction towards the end wall without forming a recirculation zone. Velocities magnitudes are in general 20 to 60% higher that those in the symmetry plane. Along the ceiling surface mean velocities vary from 0.1 to 4.0 m/s but their distributions are different from those on the lateral wall.

The mean velocity vector distributions over 7 vertical planes along the chamber length are shown in Figure 6.26. The spread of the inlet jet and the reduction of velocity magnitudes with increasing distance from the inlet can be observed in all planes.

Figures 6.27 and 6.28 show the vectors in the x/W = 0.0 symmetry plane and in the x/W = 0.4 plane respectively. Figure 6.27 shows velocity close to the ceiling surface, with vector magnitudes varying from 0.1 to 5.80 m/s. The small recirculation zone on the corner formed by the floor and the inlet wall can also be observed. Along the ceiling velocity magnitudes reduce near to zero when the air stream has travelled almost 3/4 of the chamber length. A large recirculation zone is formed on the first half of the chamber; this region is centred at z = 37.8 mm and y = 14.0 mm. Figure 6.28 shows a small recirculation similar to that observed in the symmetry plane. The air flow after being deflected by the ceiling is seen moving towards the chamber centre.

Figure 6.29 shows contours of the kinetic energy of turbulence on the x/W = 0.0 plane. The highest value is 4.1, located in the core of the incoming air jet Outside the jet core region, κ values are low and do not exceed 1.2 m^2/s^2.

Predictions with low-Re κ–ε turbulence model, Re = 6600

The predictions obtained using the low Re κ–ε turbulent model for Re = 6600 can be seen in Figures 6.30 to 6.35. Figure 6.30 shows that, compared with the results shown in Figure 6.24, the jet does not penetrate the chamber volume to the extent predicted with the standard κ–ε model. The boundary layer near the ceiling is around 5% smaller compared to that predicted by the standard κ–ε turbulent model. The jet penetrates to around 50% of the chamber length; after z = 150 mm the mean velocities drop to around 0.5 m/s. The vector magnitudes along the large recirculation zone in x/W = 0.0 plane decrease gradually to 0.5m/s (compared with 10.25 m/s at the inlet). Over the second half of the chamber near the outlet, the mean velocities have values around 1.0 m/s, but near the outlet they increase to 1.6 m/s.

In Figure 6.31 the vectors in the x/W = 0.5, y/H = 1.0 and z/L = 3.0 planes are shown, and indicate a pattern similar to that of Figure 6.25. The vectors shown in Figure 6.32 confirm previous findings and indicate a decrease of velocity magnitudes near the ceiling of 20-30%, compared with the predictions with the standard κ–ε turbulence model.

The flow pattern in the symmetry plane can be seen in Figure 6.33. Differences can be observed when the vectors are compared with the predictions using the standard κ–ε turbulence model, for example along the ceiling after the air stream has been deflected. The flow pattern over the second half of the chamber is also different. However the flow pattern in the x/W = 0.4 plane, Figure 6.34 is similar to that shown earlier in Figure 6.28, albeit with same velocities magnitudes being 10% lower in

this case. The CPU time used by the low Re model was around 25% higher, due to the additional equations that had to be solved.

The contours of the kinetic energy of turbulence in the plane of symmetry are shown in Figure 6.35. The κ present the same distribution as in Figure 6.29, but the high κ values along the ceiling surface, extend over a shorter distance. The differences between the κ values predicted with the two models are small, 2 - 5%.

6.4.3 Comparison of predictions and measured data at Re = 6600

In Figure 6.36 predicted and measured mean velocity profiles in the symmetry plane (in the y = 7 mm, y = 70 mm and z = 40 planes) are compared. The mean velocities are underpredicted, with differences of the order of 10%.

The measured and predicted turbulent kinetic energy profiles at z = 40 mm in the x/W = 0.0 plane are plotted in Figure 6.37. The κ values have clearly been underpredicted do not follow the same trend as the measured ones. The corresponding r.m.s. values can be observed on Figure 6.38, showing that turbulence is anisotropic along the ceiling but isotropic over the rest of the profile. A comparison of measured u' and predicted ($\sqrt{\kappa}/_{1.1}$) is shown in Figure 6.39: the profiles are qualitatively similar to those in Figure 6.37 and the observations made for the predicted and measured κ apply to the comparison of u' and ($\sqrt{\kappa}/_{1.1}$) as well.

6.5 Discussion

6.5.1 Flow and turbulence structure

The interaction between the geometrical characteristics in both chambers studied, and the momentum of the incoming air jet help the formation of a highly three-dimensional and turbulent flow. For the two chambers studied the main features of the flow are as follows: 1. A large recirculation zone formed over the first half of the chamber ($z < 150$ mm). 2. A small recirculation zone located in the corner formed by the symmetry plane and the inlet wall. The predicted size of this region varies depending on the turbulence model employed. 3. A recirculation predicted over the plane $z/L = 0.0$, formed by the deflected flow moving towards the lateral wall and the flow close to the lateral wall surface moving towards the end wall. The behaviour previously described can be observed for both chambers investigated in this chapter.

Along the jet core zone the measurements suggested that the flow is anisotropic. Although the three r.m.s. velocities components were only measured for one profile, the results show evidence that parts of the flow away from the jet region may be considered isotropic.

Andrade and Restivo (1982) investigated an air jet entering from the bottom of the cavity. The geometrical configuration is different, a square cavity, and due to the location of the outlet below the inlet position, helps the formation of a large recirculation zone. Due to strong mixing the flow visualisation tests were limited to $Re < 500$. The length of the inlet slot occupied the whole wall length, thus the mean flow measured was nearly two dimensional. This geometrical configuration was restricted to the measurement of only two velocity components due to the lack of a

frequency shifting device to avoid directional ambiguity. Therefore only measurements on the symmetry plane were done. Results shown for chamber 3 and 4 suggested the presence of a highly three dimensional flow. Andrade and Restivo also found out that the maximum velocity on the occupied zone is about 40% of the inlet velocity. They also reported that the r.m.s. values measured presented nearly uniform distributions of fluctuating velocity in the occupied zone, higher that those found under the ceiling.

6.5.2 Effect of Reynolds number

For the two flows studied, it is not possible to establish if the air flow pattern is independent of the Reynolds number. Strong mixing takes place over both halves of the chamber. The level of mixing increases with the Reynolds number, as observed during the flow visualisations tests. The air flow patterns in the jet core zone for different Reynolds numbers are similar, with some variations of the velocity magnitudes and the size of the recirculations zones. The air flow patterns close to the lateral wall remained unchanged in size and direction. The air jet remains attached to the inlet wall surface.

Andrade and Restivo's (1982) LDA results are in some cases 20% higher when compared with the results obtained in a full scale room. He found out that between $100 < Re < 910$ the flow pattern observed was independent of Re.

6.5.3 Assessment of predictions and of the effect of the turbulence models used

The agreement between predictions and measured mean velocity values was found to be good, within 10%. The level of turbulence was predicted to within 20%.

The previous sections show differences in the mean velocity flow patterns predicted for the two turbulence models used. The differences were found on the jet of the air stream that has been deflected by the ceiling/floor surface. With the two turbulence models used, different flow patterns for the central zone of the air flow were predicted (over the symmetry plane), while the flow patterns closer to the lateral wall remained unaffected by the changes observed on the boundary layer close to the ceiling/floor surface.

The size of the small recirculation zone formed when the jet is deflected by the ceiling/floor surface predicted with both models is similar to within 5%. Each turbulence model predicted a qualitatively similar air flow pattern for the large recirculation zone with quantitative differences of 20 - 30 % between the two predictions.

The kinetic energy of turbulence was underpredicted by the turbulence models by 20%. Renz and Terhaag (1990) studied the effect of two turbulence models ($\kappa-\varepsilon$ and algebraic stress) on the predictions of the flow patterns in a room ventilated by a vertical air jet. They did not find differences between the 2 wall functions used as long as the requirement of the minimum distance of the first grid point from the wall is observed. When predictions where compared with experimental data, the predictions with the algebraic Reynolds stress model were closer. They assumed that

the differences could be attributed to the false assumption in the κ–ε model of isotropy. They proposed the use of an algebraic Reynolds stress model for near-anisotropic flows. They also found that an increase in mesh size around the inlet showed a substantial improvement within the jet, but it didn't show a remarkable effect on the mean values elsewhere in the chamber. The inclusion of the buoyancy effect on the κ–ε model did not improve the predictions. However, as they used hot-wire anemometry for the measurement of velocities, some of the discrepancies may be attributed to the experimental technique. The present calculations as well as those of Renz and Terhaag indicate that a model which does not implicitly assume isotropic turbulence may provide improved predictions of the flows.

6.6 Concluding remarks

1. A highly three-dimensional jet flow was observed through flow visualisation for Reynolds numbers up to 2000. Flow visualisation showed a small recirculation in the corner formed by the inlet wall and the ceiling/floor surface. A large recirculation zone was shown in the first half of the chamber, and a mixing zone over the second half of the chamber was also shown.

2. The assessment of predictions has been made against the LDA results. It was found that the two turbulence models used predicted slightly different flow patterns for the two chambers studied, with the main differences in the boundary layer zone. This is possibly due to the wall approximation used for the turbulence models. However, with both models the velocity in the air jet core is well predicted.

3. The highest κ values were found in the vicinity of the incoming jet. Elsewhere, κ values decreased and remained at low values over the

remainder of the chambers. The kinetic energy of turbulence was underpredicted by both turbulence models. Values of the kinetic energy of turbulence predicted by the low Reynolds model were lower than those obtained through the standard $\kappa-\varepsilon$ model. As has been concluded with the results presented in Chapters 4 and 5, the standard $\kappa-\varepsilon$ turbulence model seems to be the most appropriate for the purposes of the calculation.

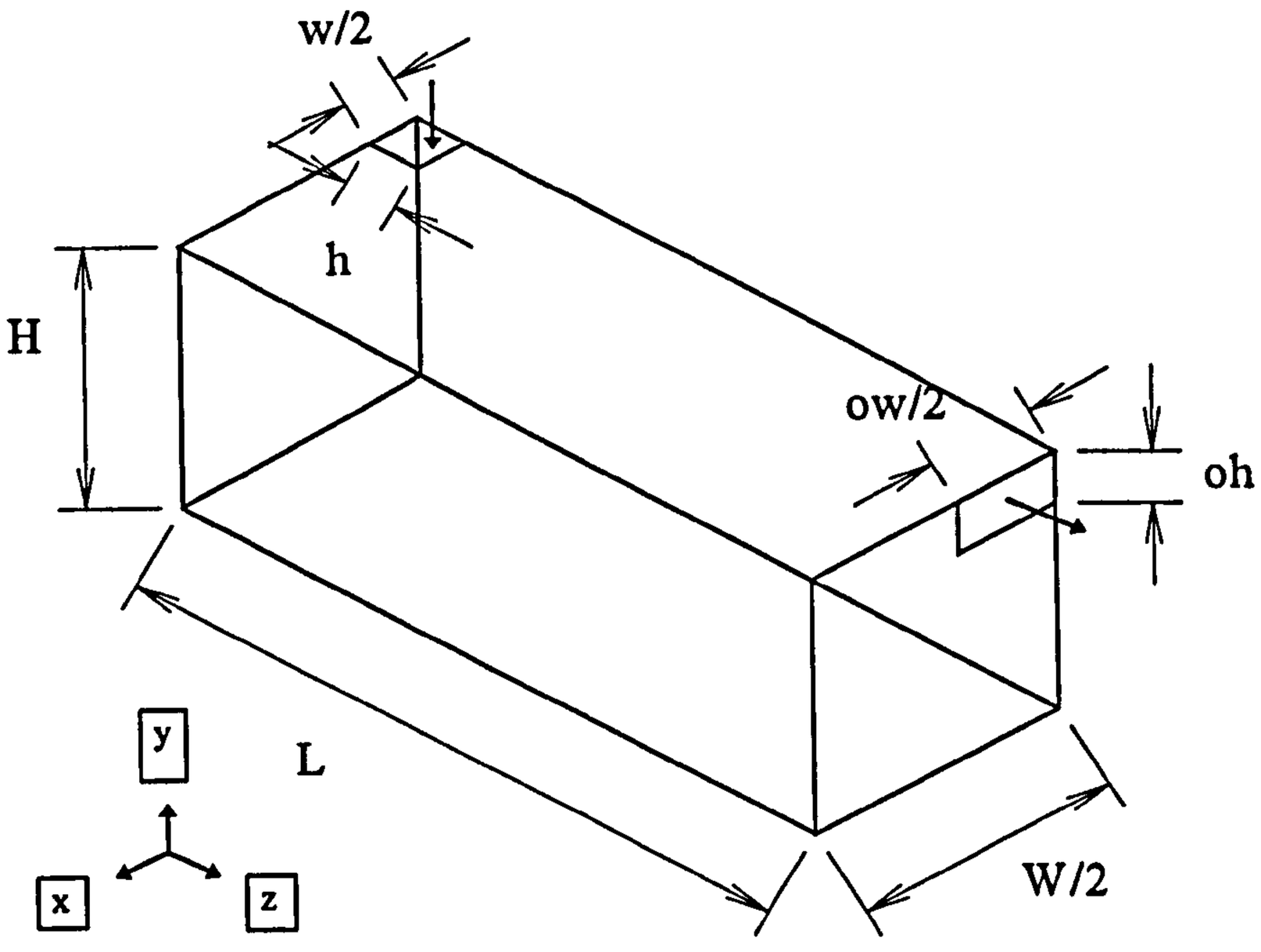

Figure 6.1a Flow configuration: schematic diagram of one-half of test section, chamber number 3.

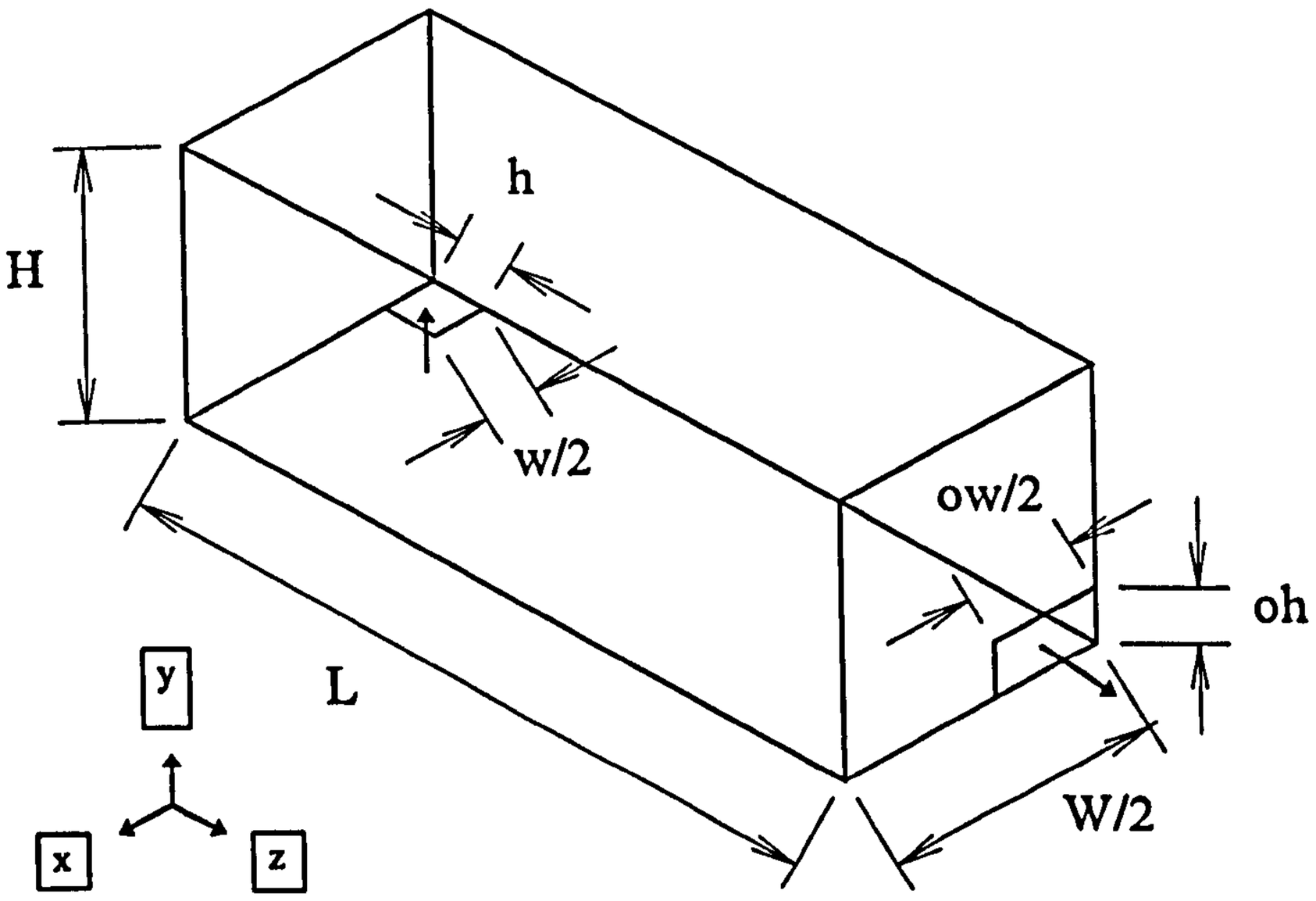

Figure 6.1b Flow configuration: schematic diagram of one-half of test section, chamber number 4.

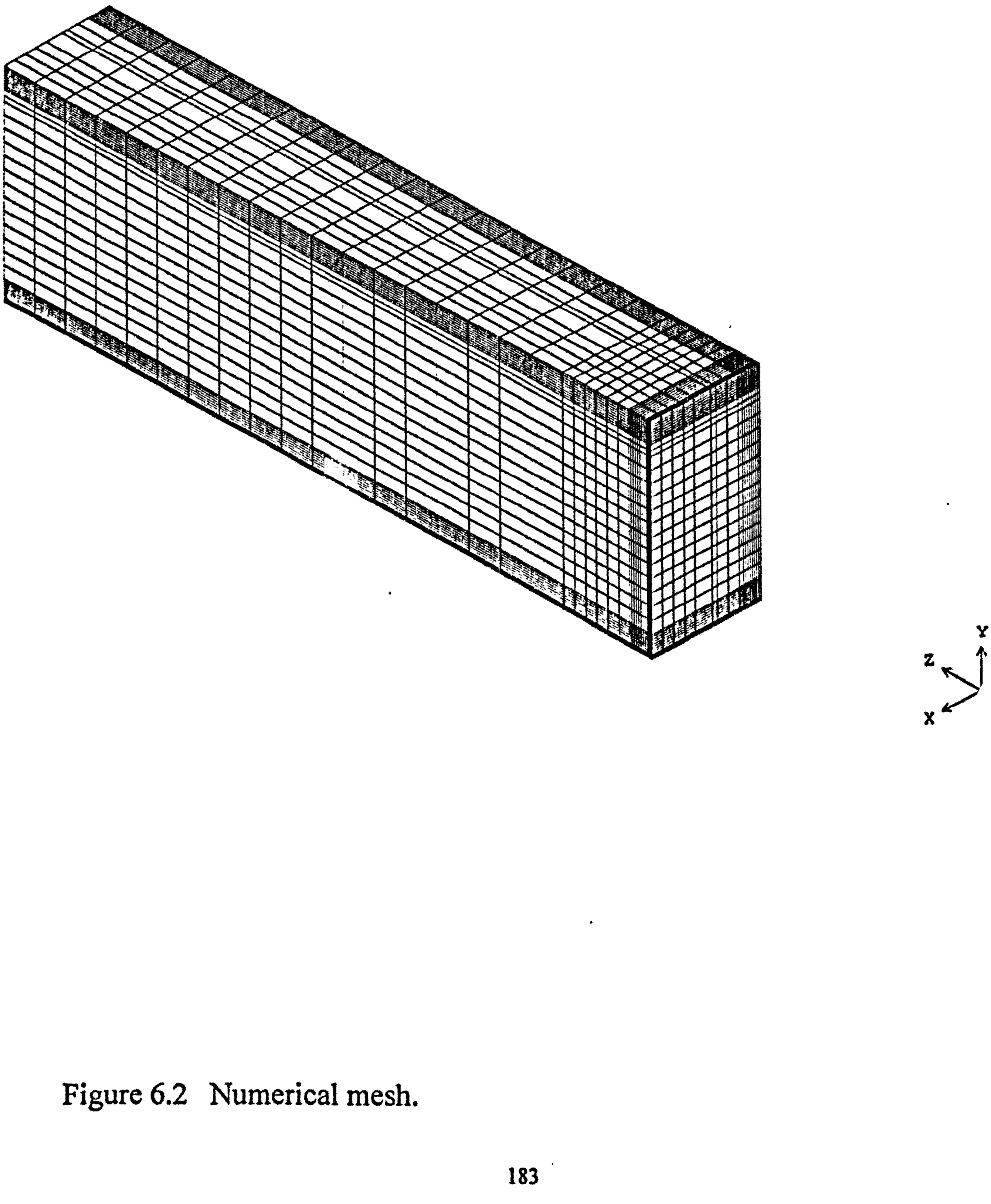

Figure 6.2 Numerical mesh.

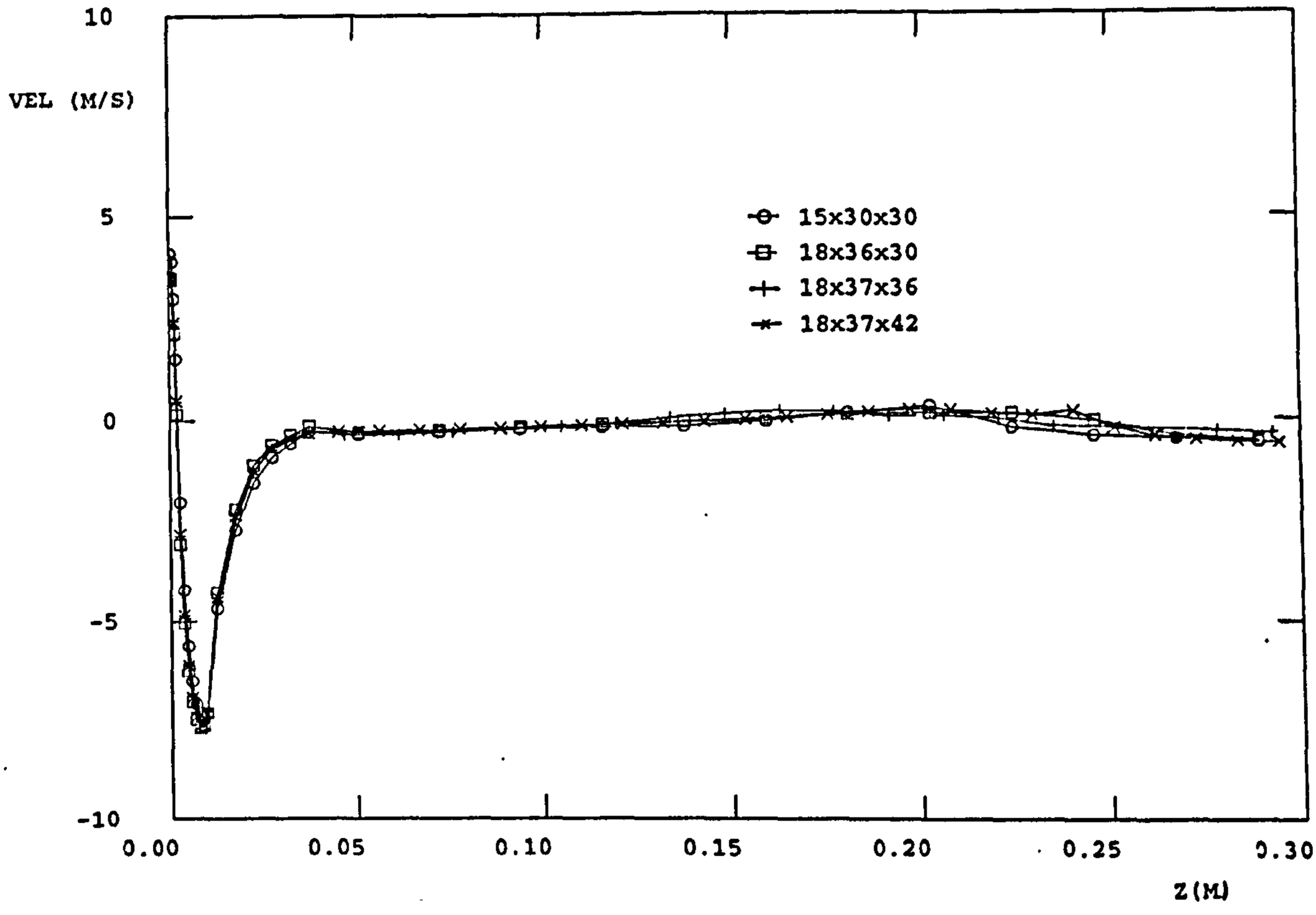

Figure 6.3 Comparison of axial velocity profiles at the symmetry plane predicted with four different grid sizes; Re = 6600.

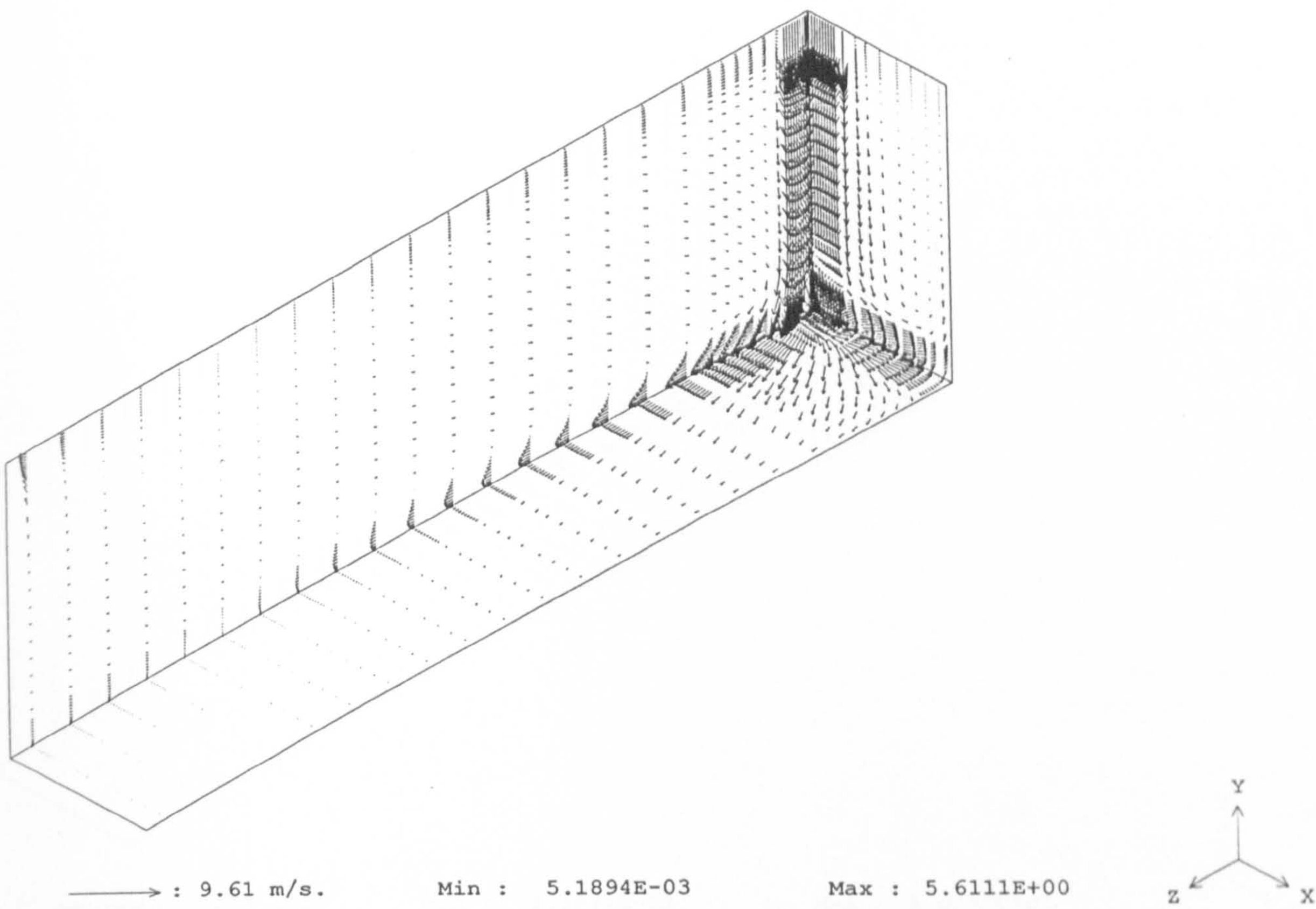

Figure 6.5 Velocity vector distribution in the planes x/W = 0.0, y/H = 0.0 and z/L = 0.0; Re = 3600, standard κ–ε turbulence model.

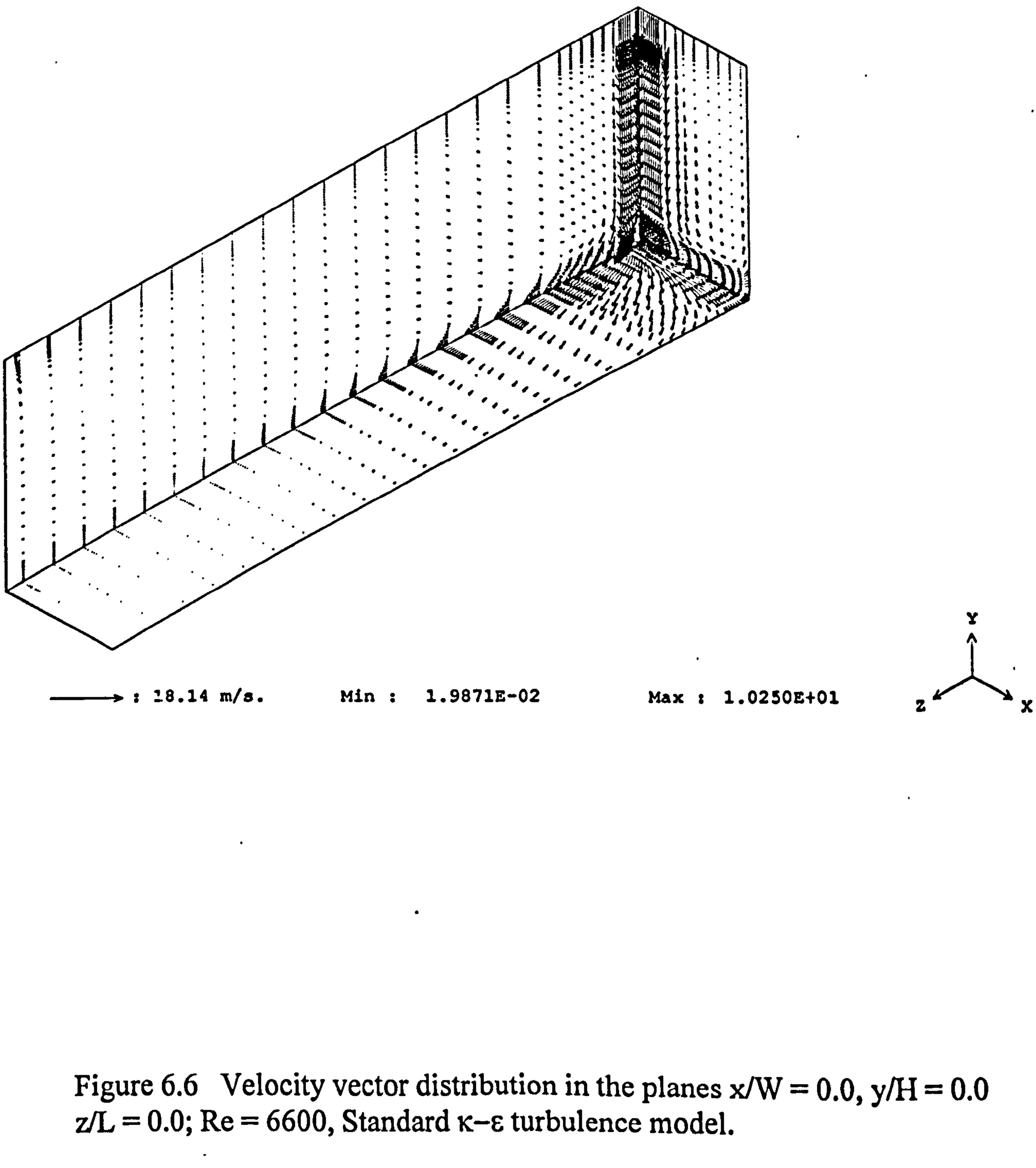

Figure 6.6 Velocity vector distribution in the planes x/W = 0.0, y/H = 0.0 z/L = 0.0; Re = 6600, Standard κ–ε turbulence model.

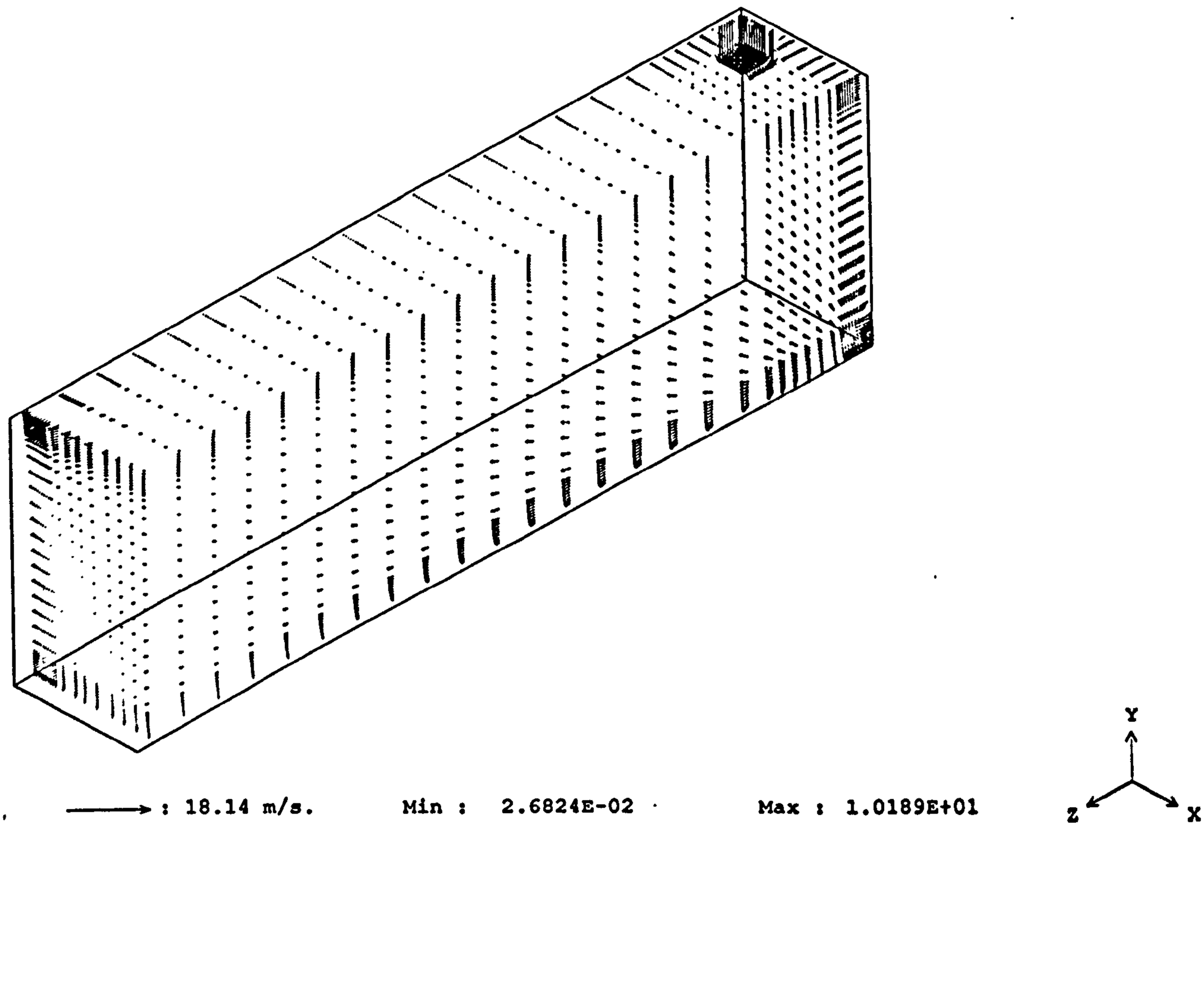

Figure 6.7 Velocity vector distribution in the planes x/W = 0.5, y/H = 1.0 and z/L = 3.0; Re = 6600, standard κ–ε turbulence model.

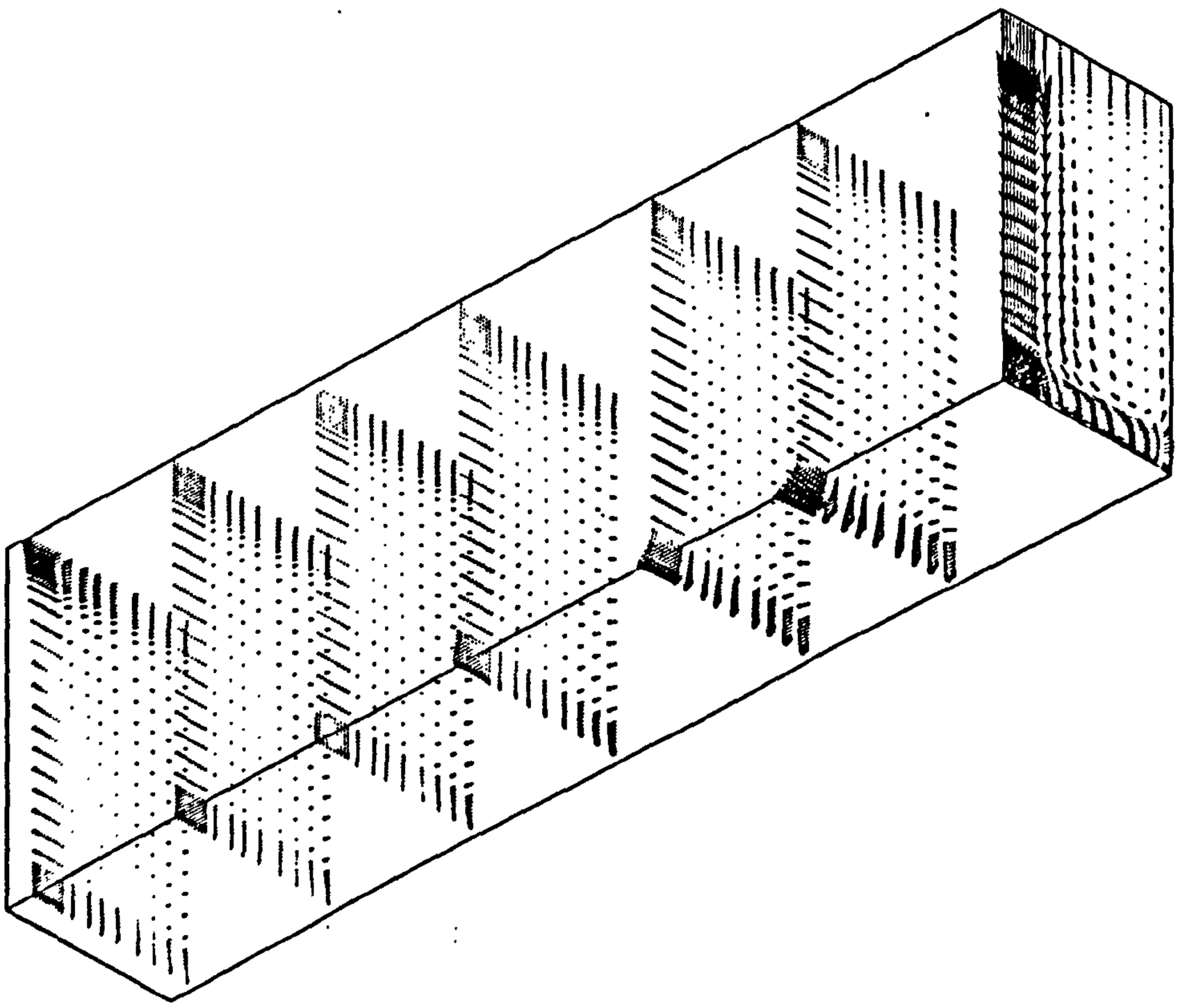

Figure 6.8 Velocity vector distribution in the planes z/L = 0.0, 0.5, 1.0, 1.5, 2.0, 2.5 and 3.0; Re = 6600, standard $\kappa-\varepsilon$ turbulence model.

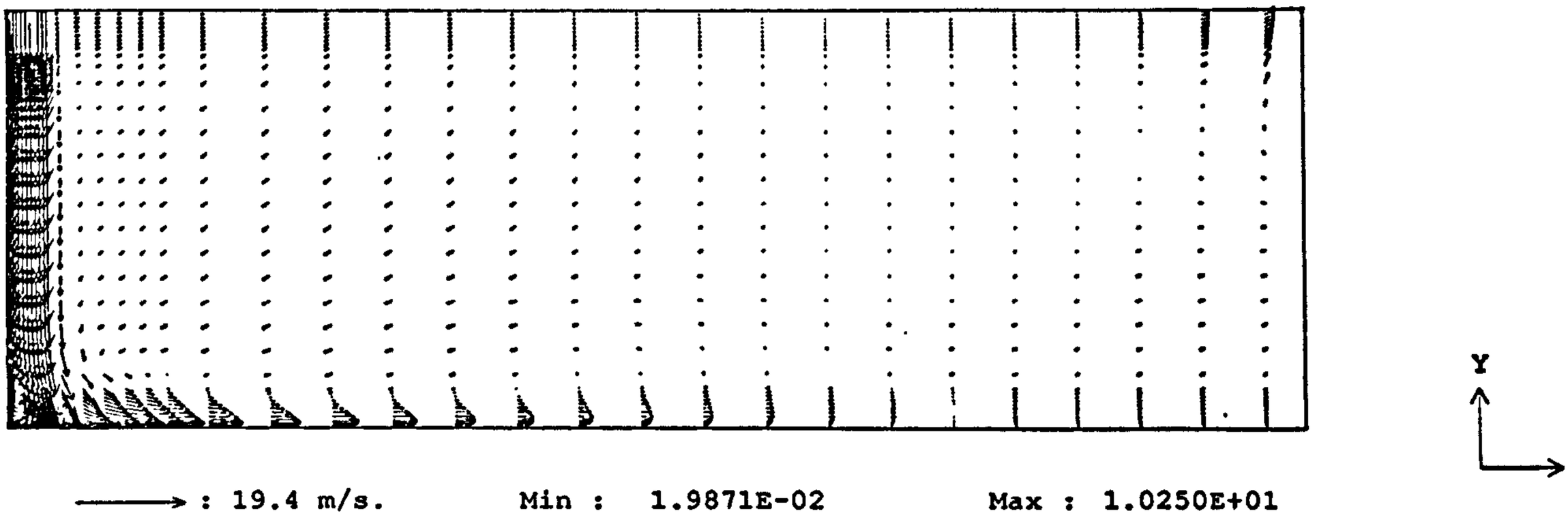

Figure 6.9 Velocity vector distribution in the plane x/W = 0.0 (symmetry plane); Re = 6600, Standard κ–ε turbulence model.

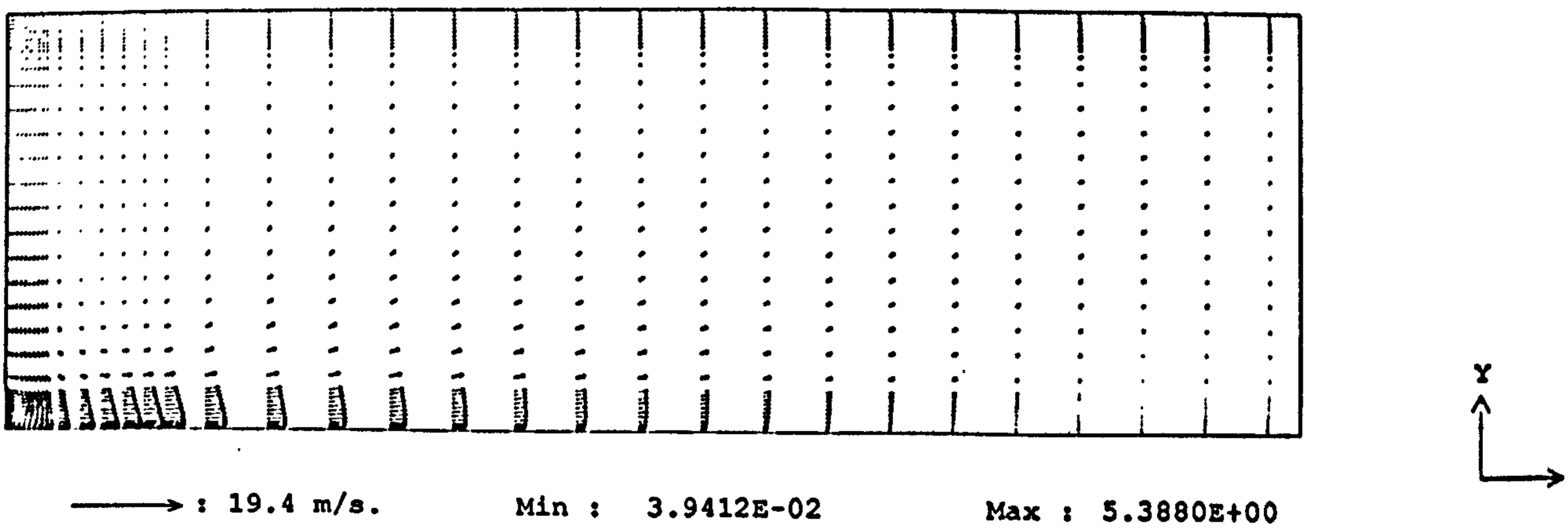

Figure 6.10 Velocity vector distribution in the plane x/W = 0.4; Re = 6600, standard κ–ε turbulence model.

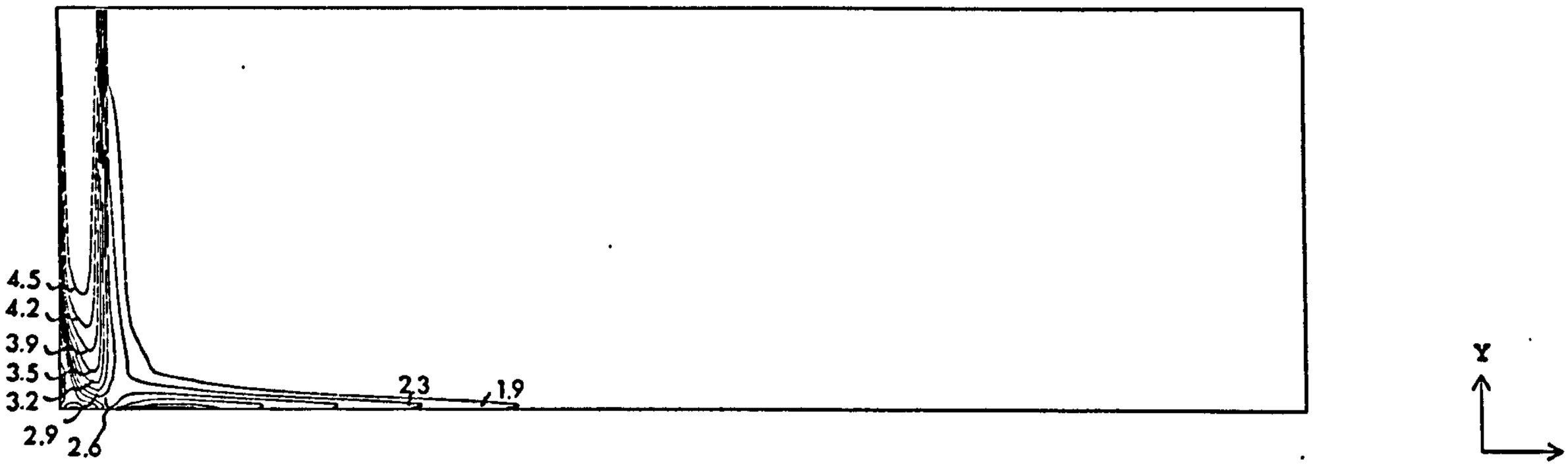

Figure 6.11 Turbulent kinetic energy contours in the plane x/W = 0.0 (symmetry plane); Re = 6600, low-Re κ–ε turbulence model. Contour values in m^2/s^2.

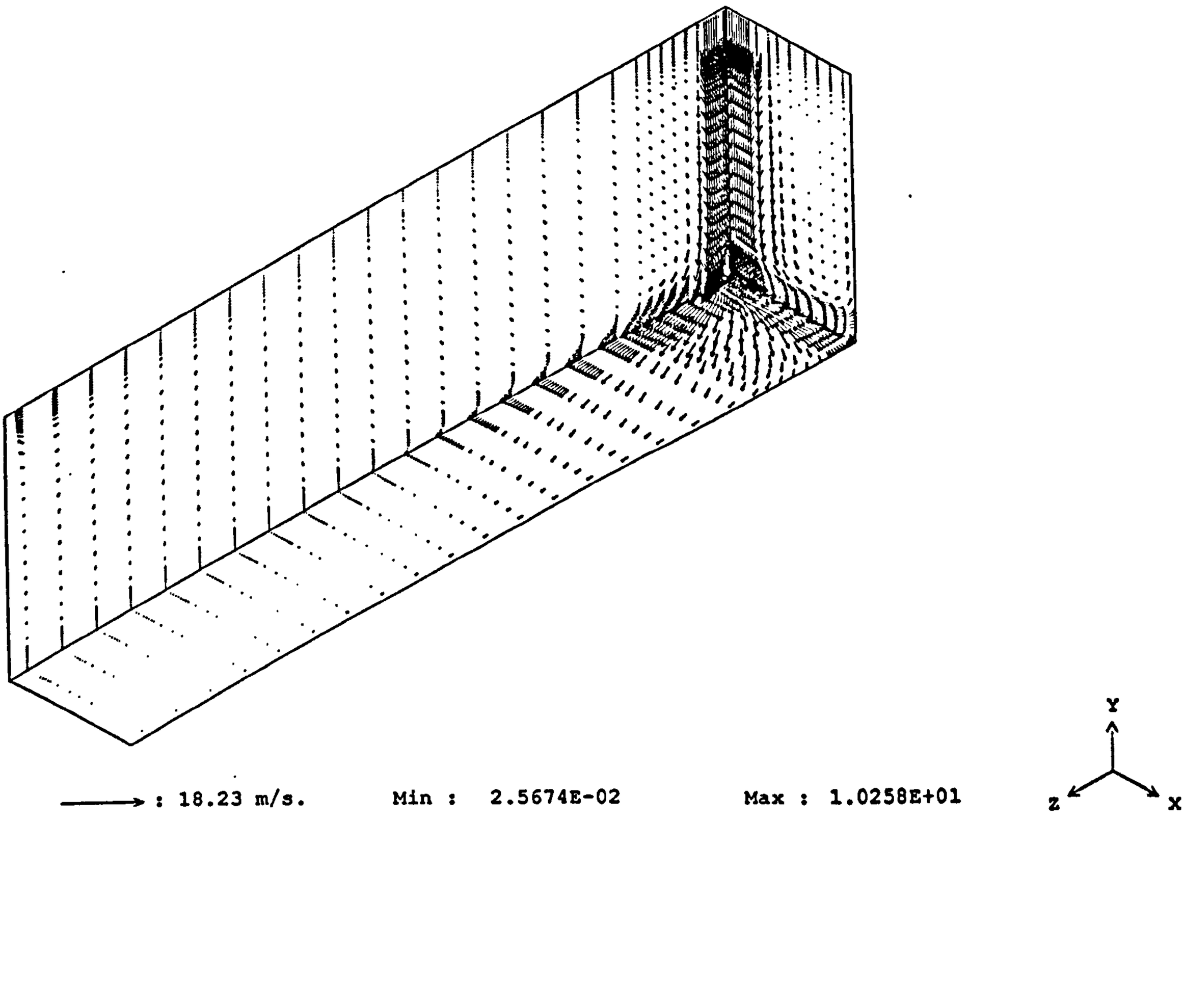

Figure 6.12 Velocity vector distribution in the planes x/W = 0.0, y/H = 0.0 and z/L = 0.0; Re = 6600, low-Re $\kappa-\varepsilon$ turbulence model.

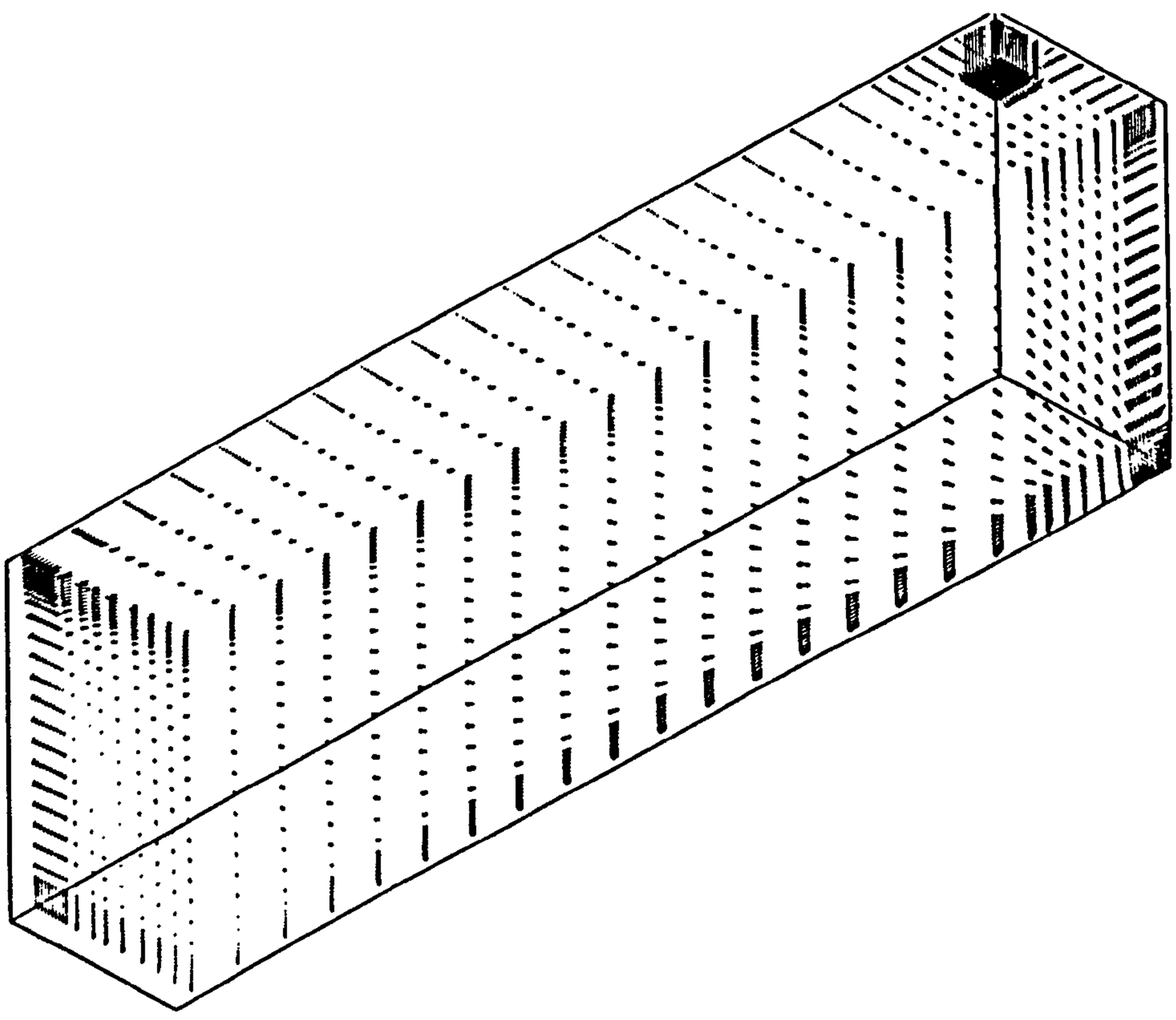

⟶ : 18.23 m/s. Min : 2.3337E-02 Max : 1.0188E+01

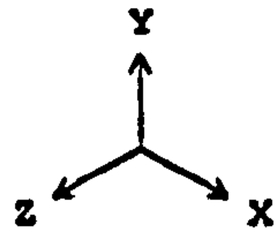

Figure 6.13 Velocity vector distribution in the planes x/W = 0.5, y/H = 1.0 and z/L = 3.0; Re = 6600, low-Re κ–ε turbulence model.

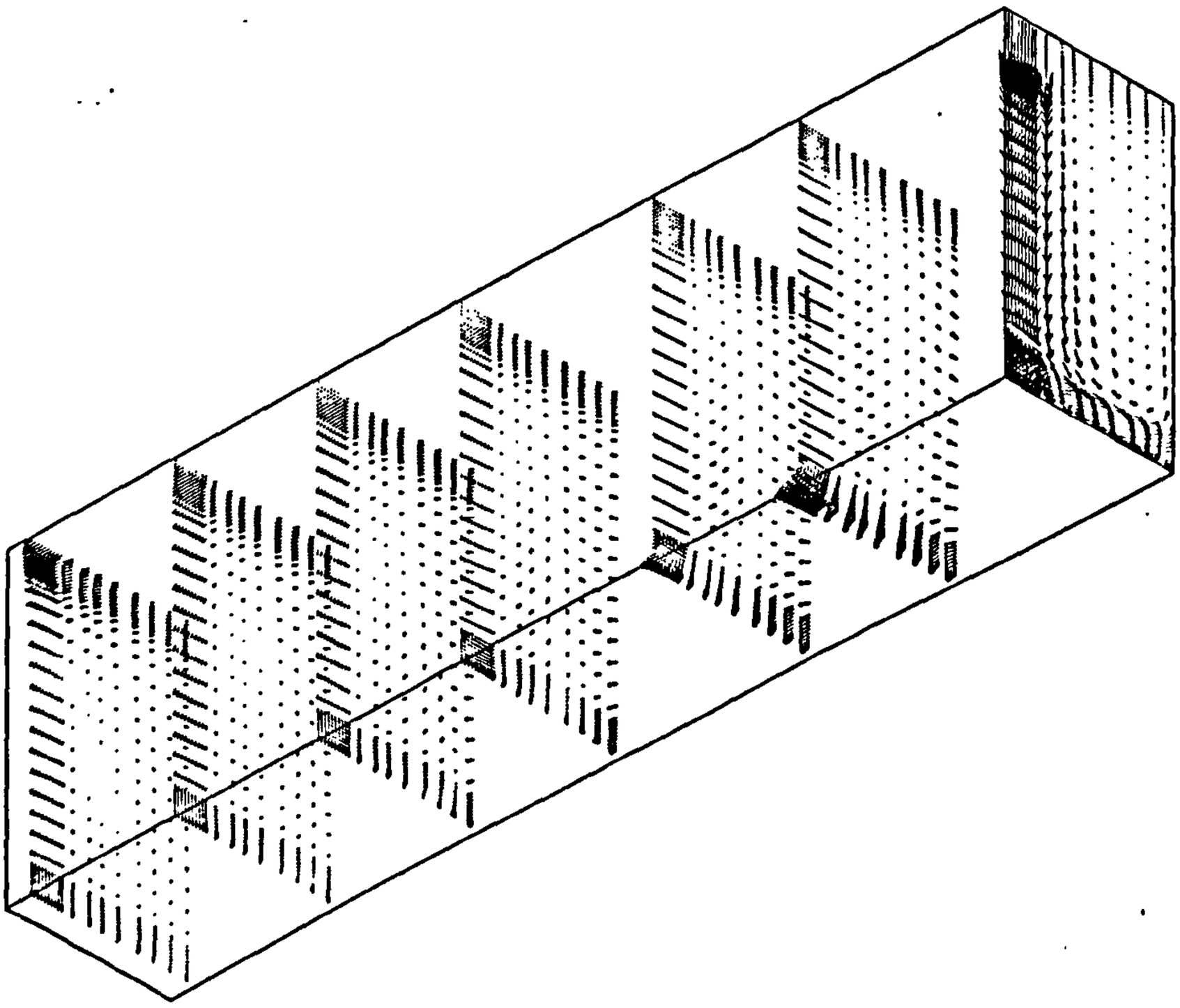

Figure 6.14 Velocity vector distribution in the planes z/L = 0.0, 0.5, 1.0, 1.5, 2.0, 2.5, 3.0; Re = 6600, low-Re $\kappa-\varepsilon$ turbulence model.

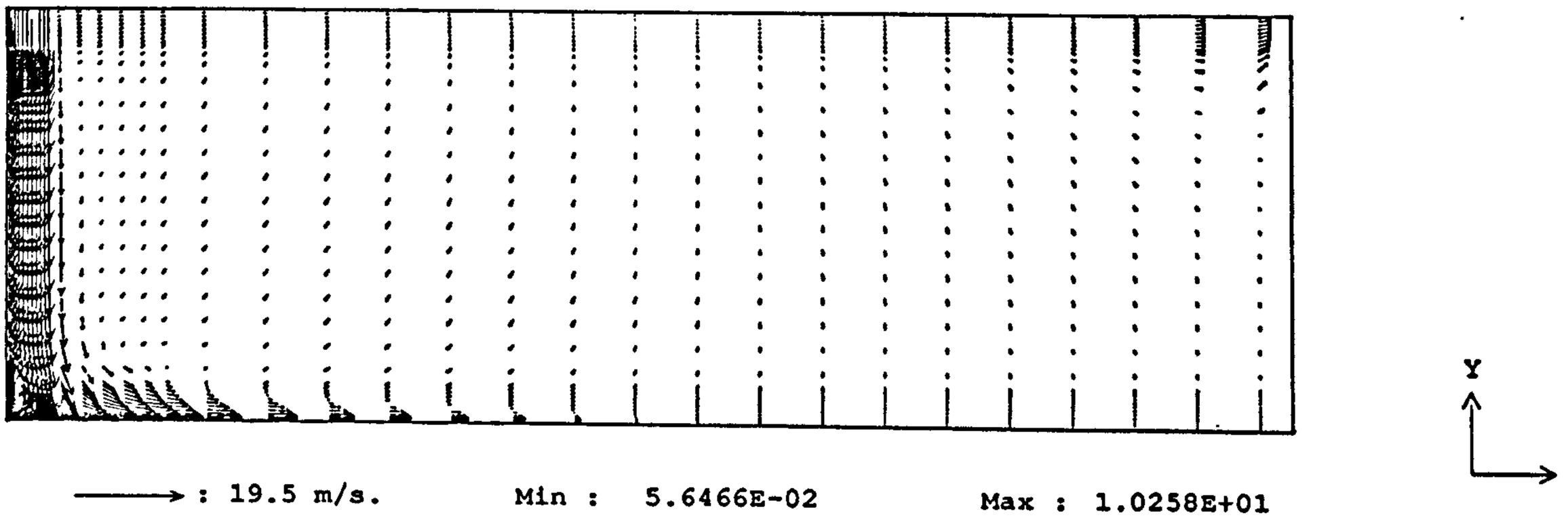

Figure 6.15 Velocity vector distribution in the planes x/W = 0.0 (symmetry plane); Re = 6600, low-Re κ–ε turbulence model.

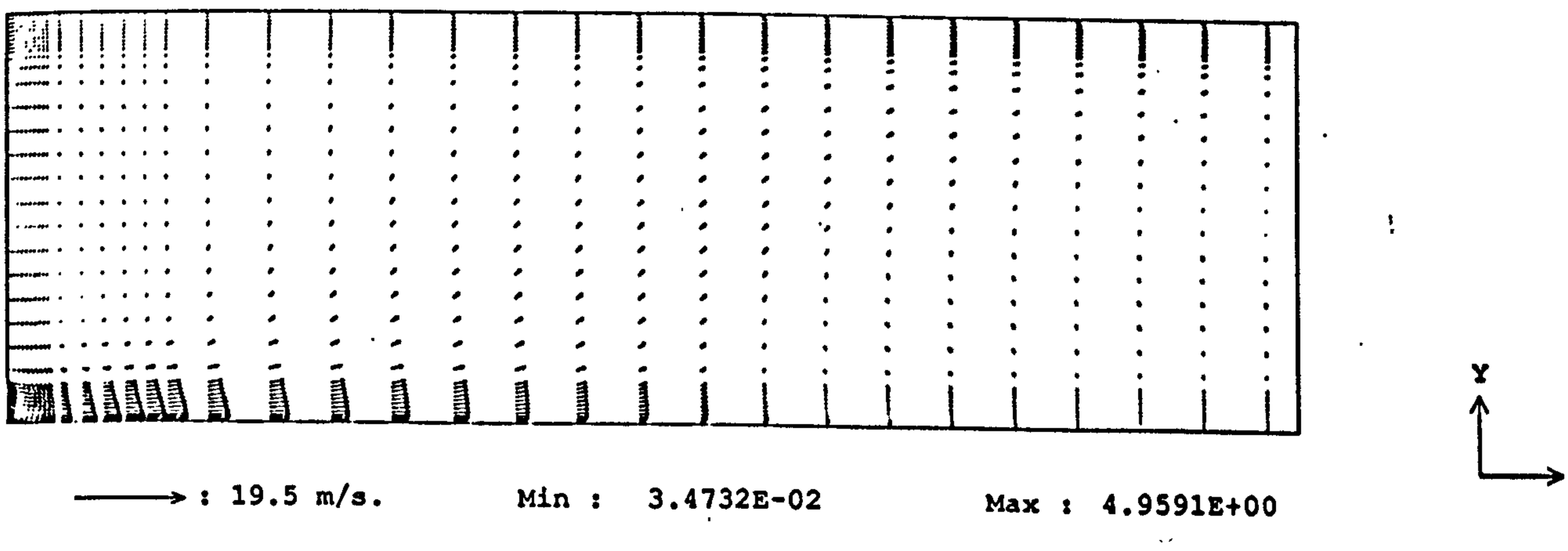

Figure 6.16 Velocity vector distribution in the plane x/W = 0.4; Re = 6600, low-Re κ–ε turbulence model.

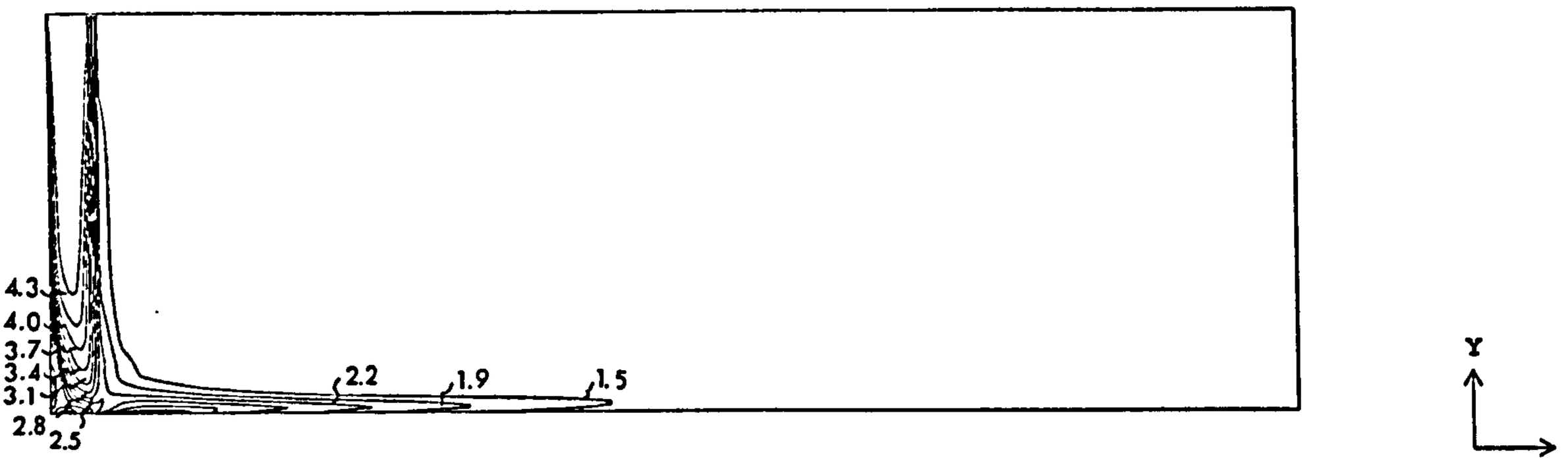

Figure 6.17 Turbulent kinetic energy contours in the plane x/W = 0.0 (symmetry plane); Re = 6600, low-Re κ–ε turbulence model. Contour values in m^2/s^2 .

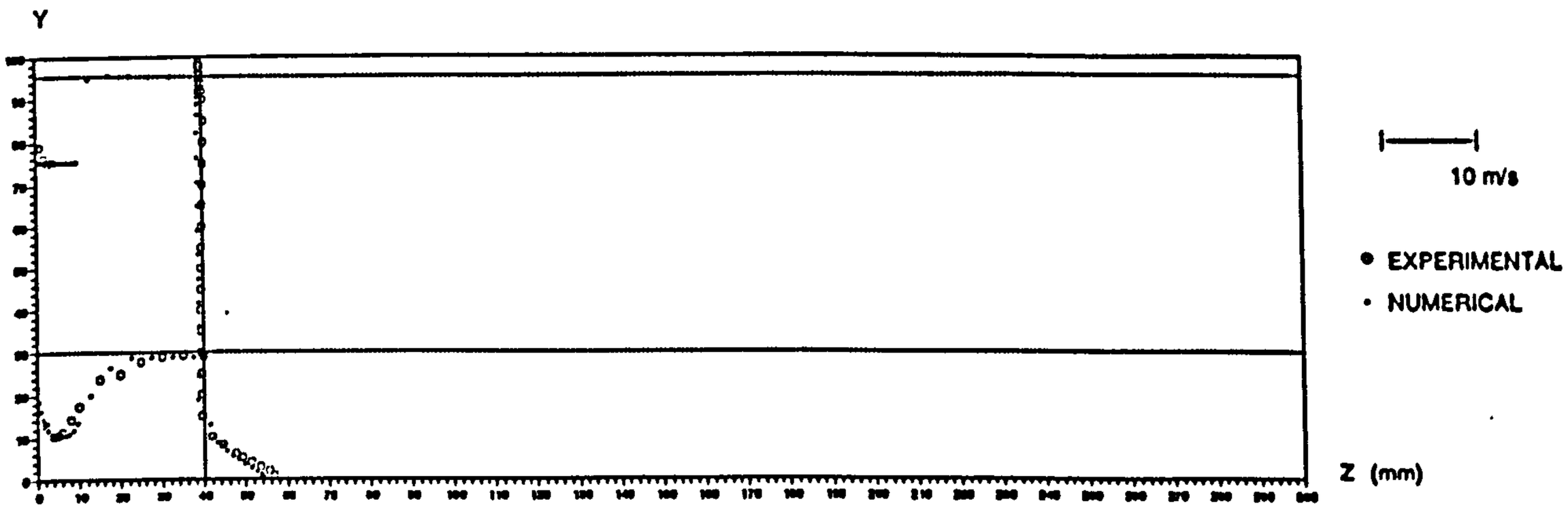

Figure 6.18 Measured and predicted mean velocity in the plane x/W = 0.0 (symmetry plane); Re = 6600.

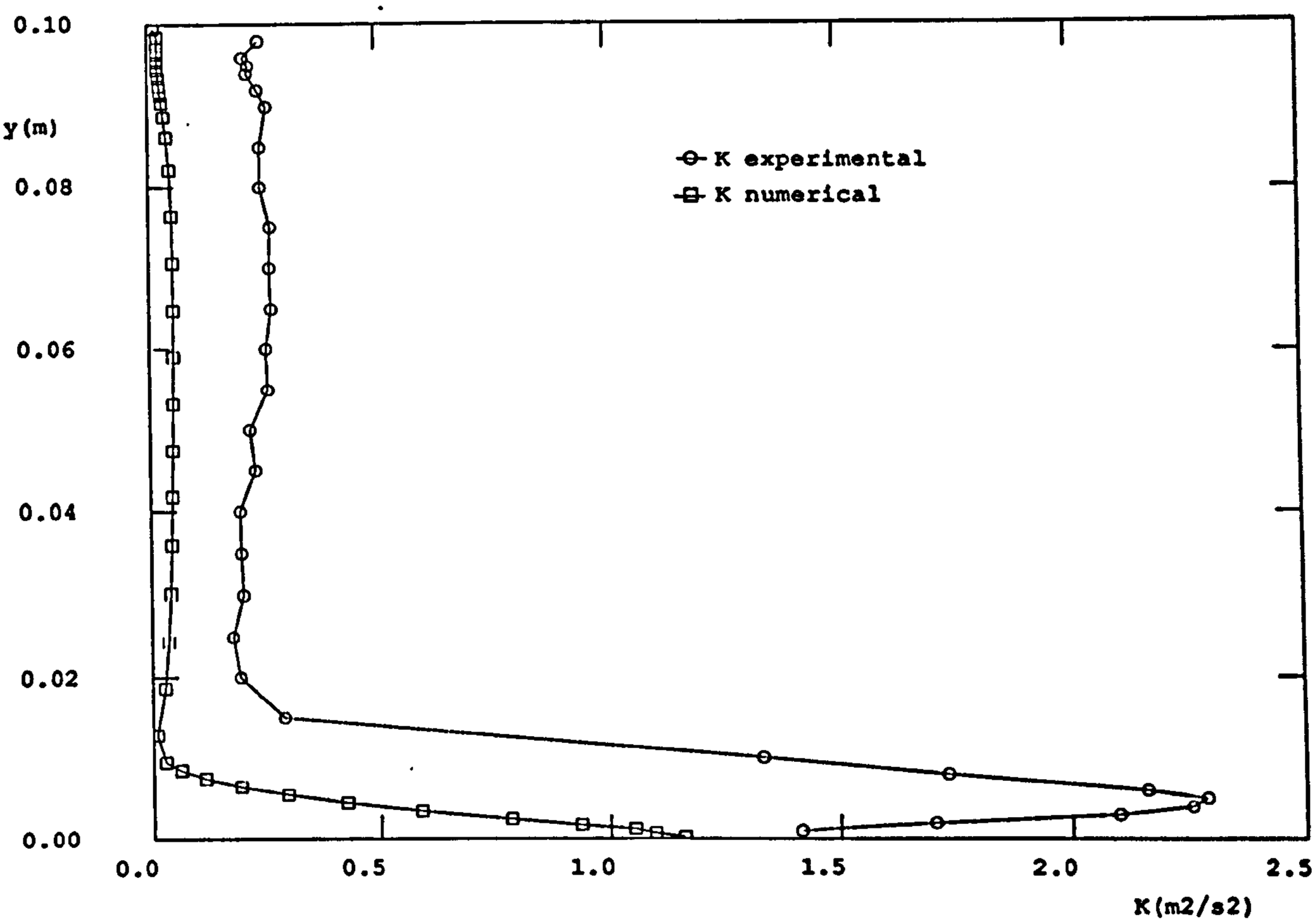

Figure 6.19 Measured and predicted kinetic energy of turbulence in the plane x/W = 0.0 at z = 40 mm; Re = 6600.

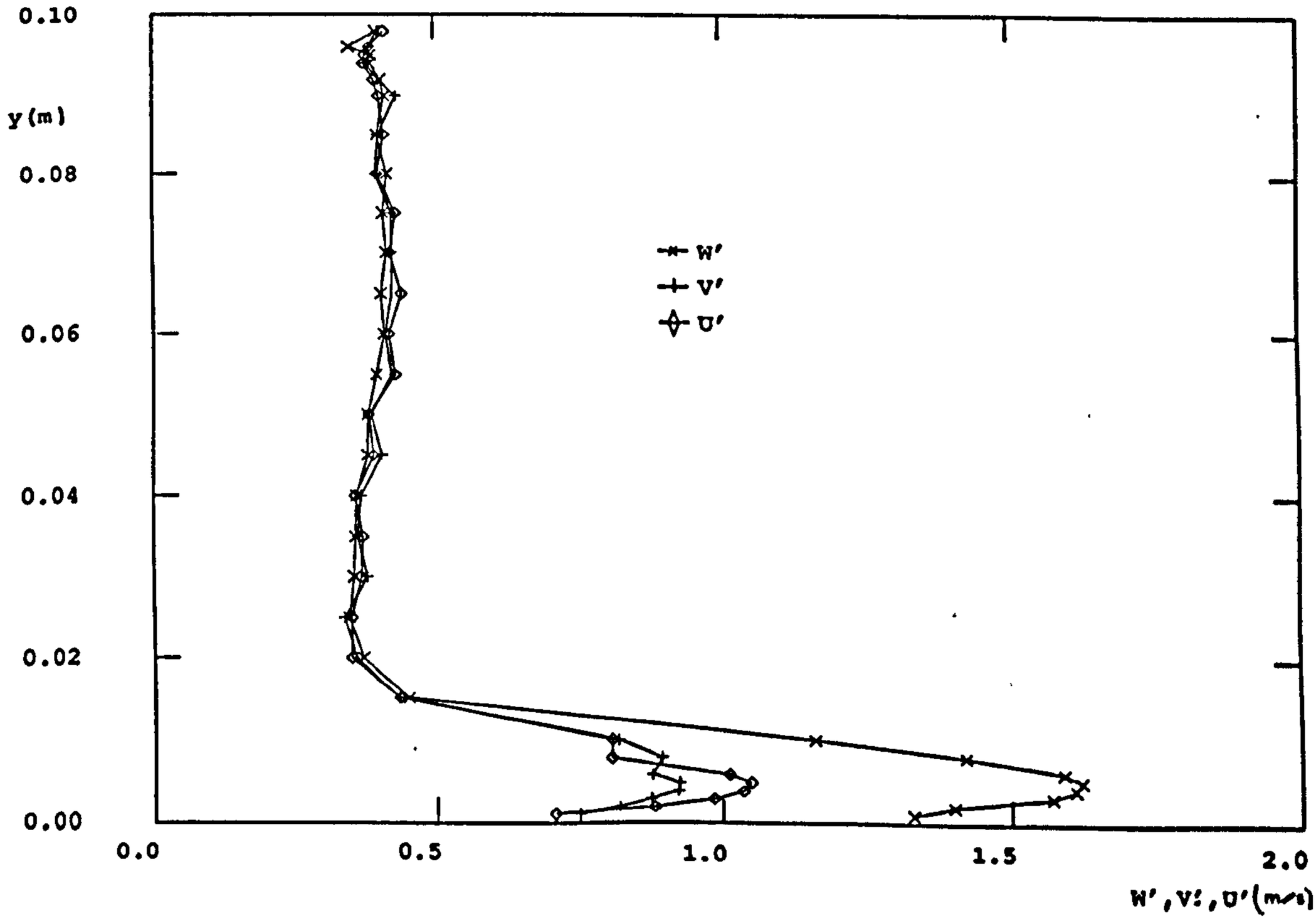

Figure 6.20 Measured rms velocities in the plane x/W = 0.0 at z = 40 mm; Re = 6600.

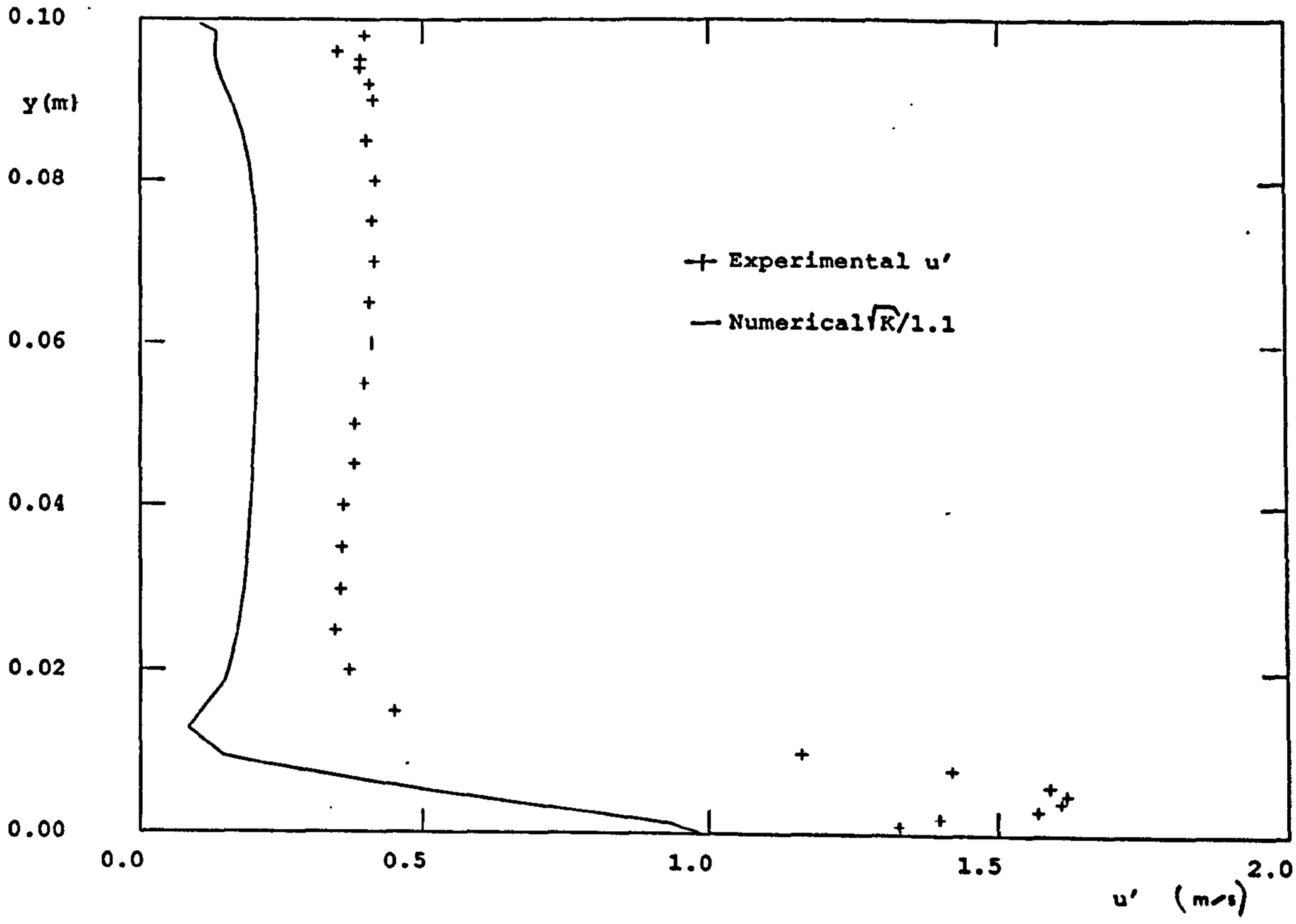

Figure 6.21 Measured and predicted r.m.s. velocities in the plane x/W = 0.0 at z = 40 mm; Re = 3600.

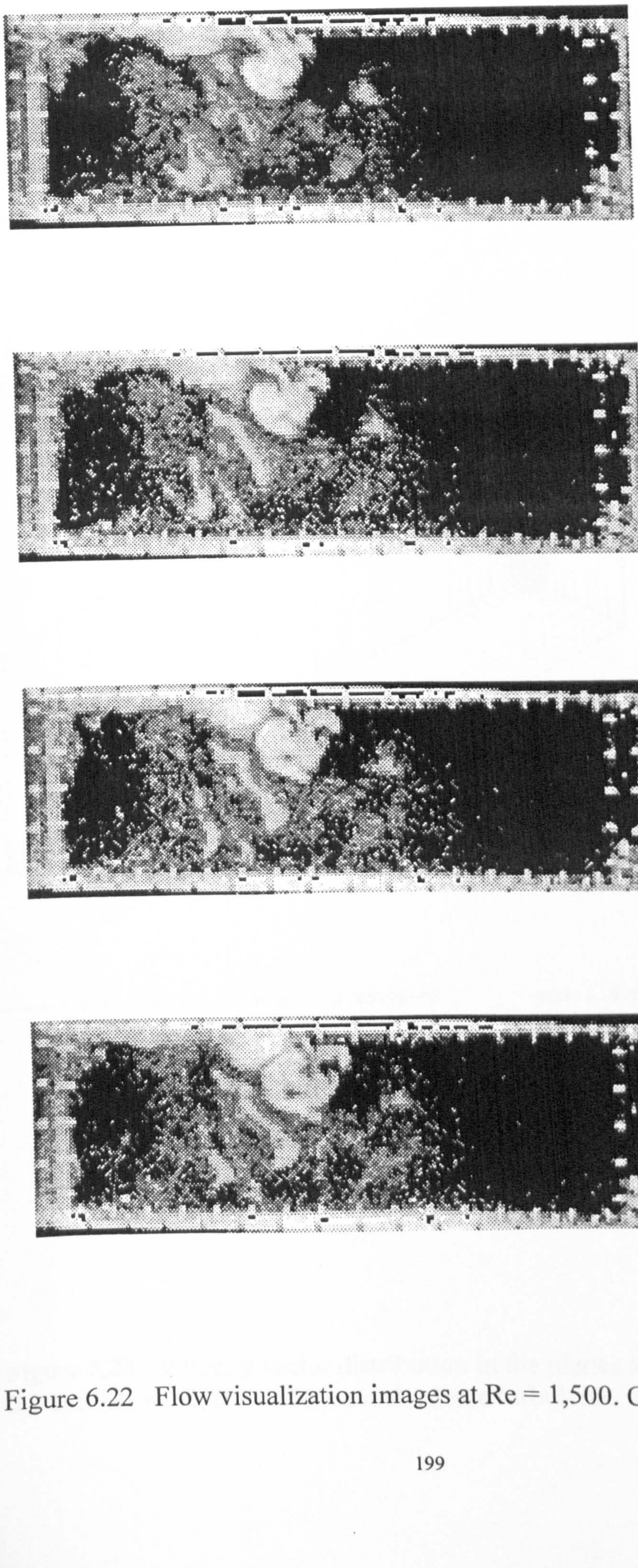

Figure 6.22 Flow visualization images at Re = 1,500. Chamber 4

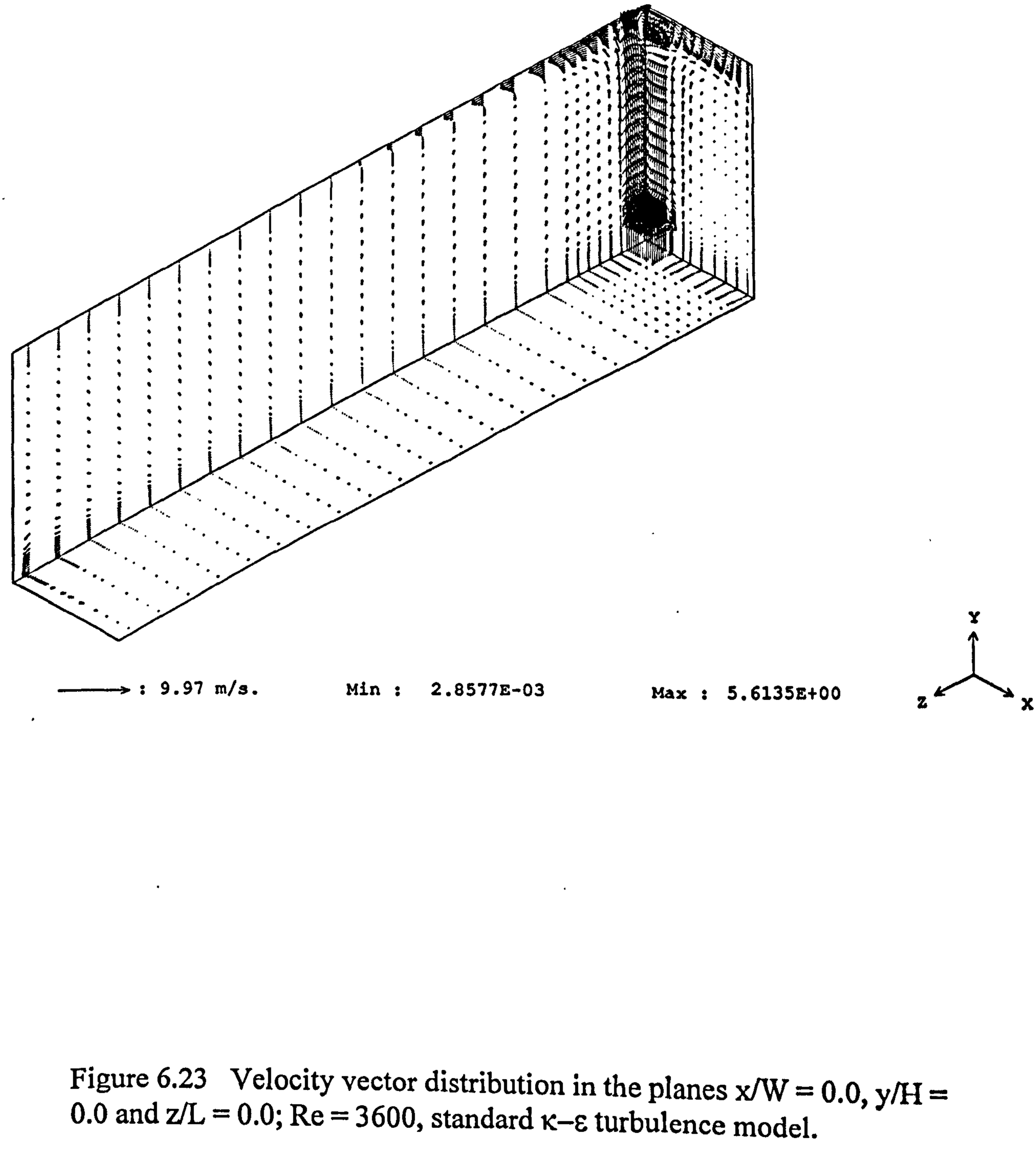

Figure 6.23 Velocity vector distribution in the planes x/W = 0.0, y/H = 0.0 and z/L = 0.0; Re = 3600, standard κ–ε turbulence model.

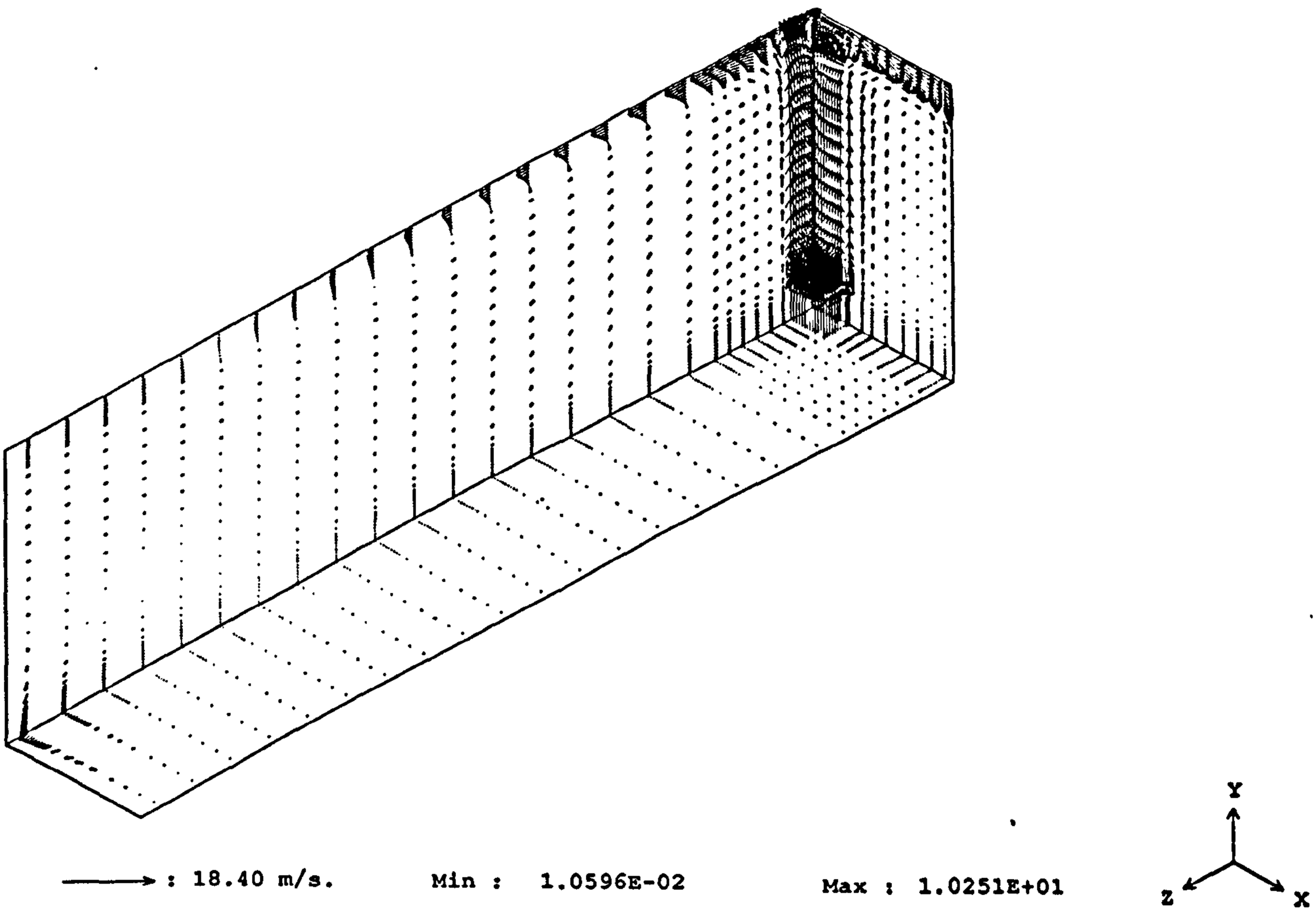

Figure 6.24 Velocity vector distribution in the planes x/W = 0.0, y/H = 0.0 z/L = 0.0; Re = 6600, Standard κ–ε turbulence model.

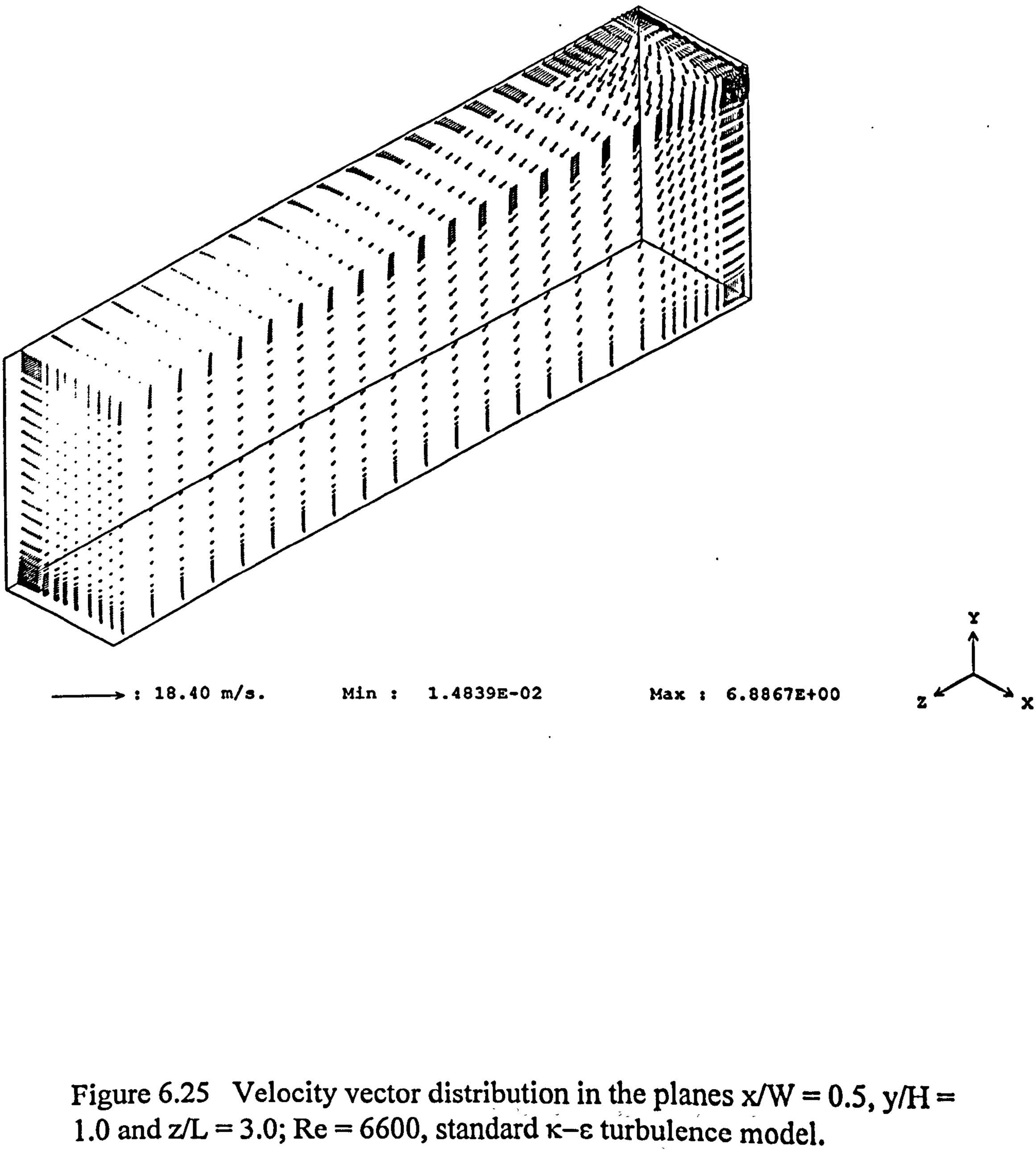

Figure 6.25 Velocity vector distribution in the planes x/W = 0.5, y/H = 1.0 and z/L = 3.0; Re = 6600, standard $\kappa-\varepsilon$ turbulence model.

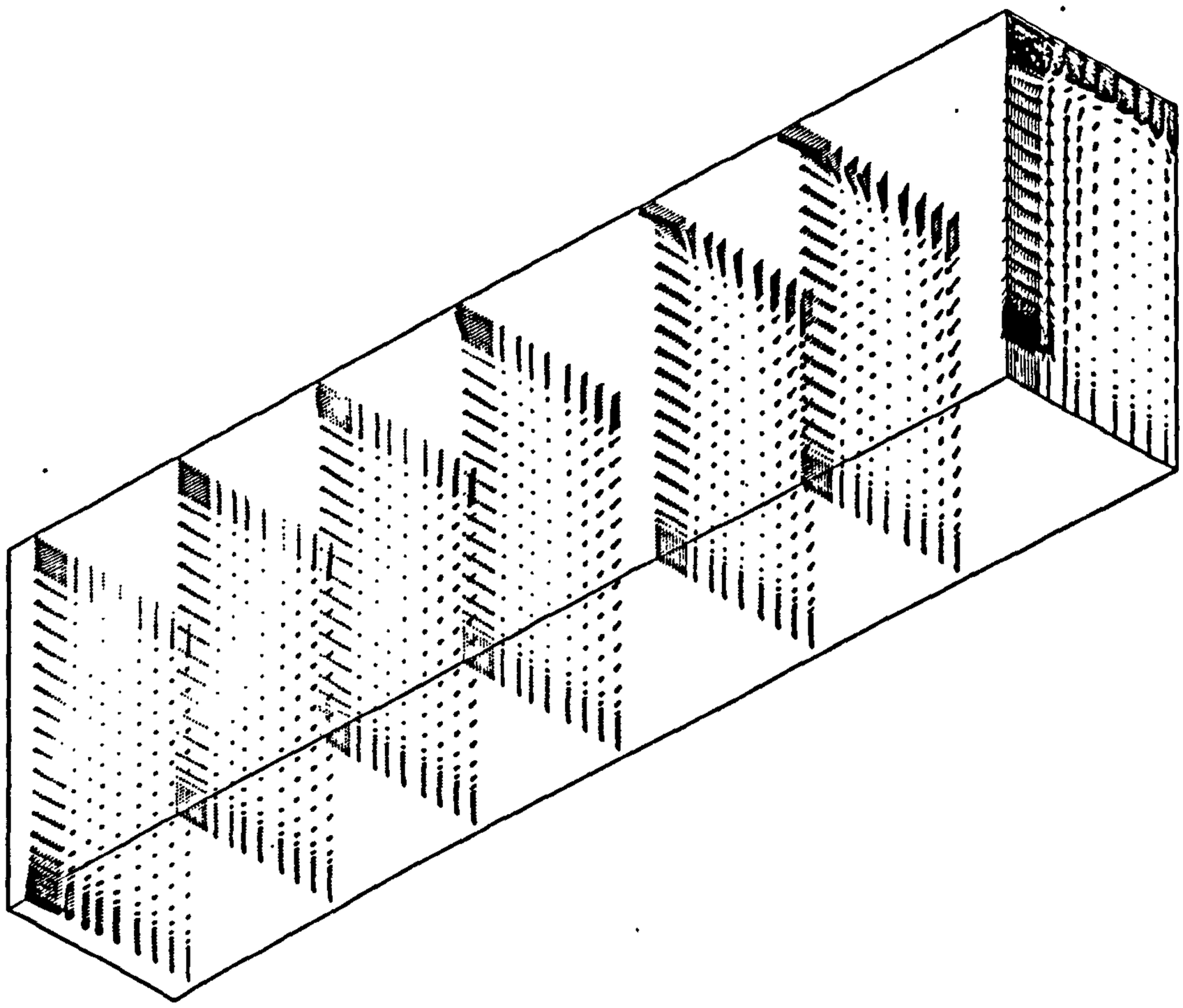

Figure 6.26 Velocity vector distribution in the planes z/L = 0.0, 0.5, 1.0, 1.5, 2.0, 2.5 and 3.0; Re = 6600, standard κ–ε turbulence model.

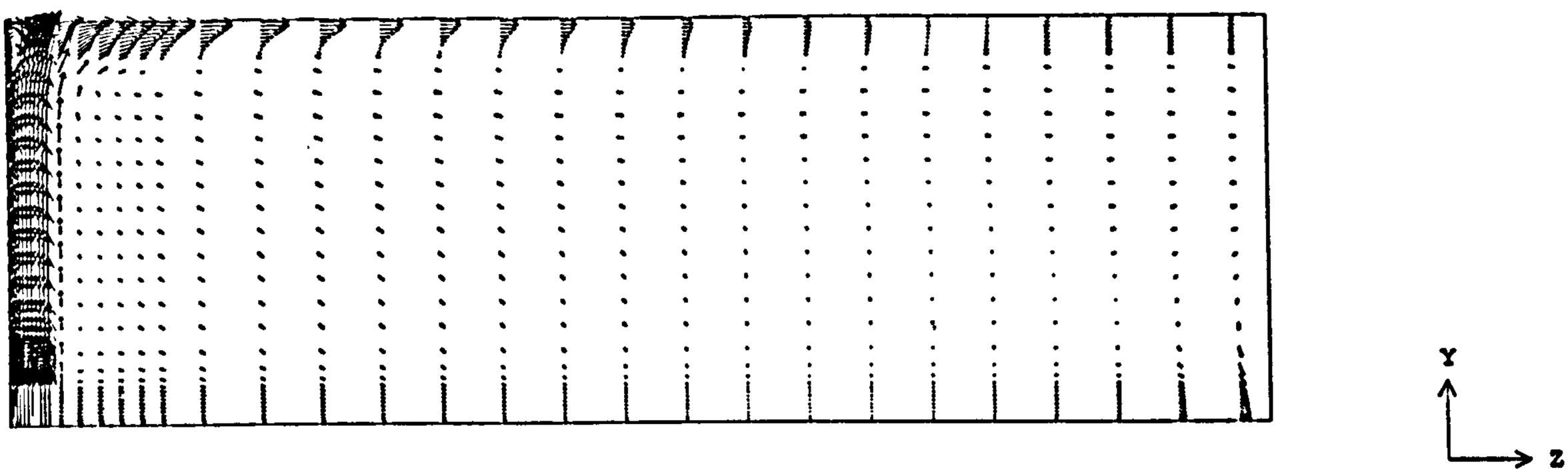

Figure 6.27 Velocity vector distribution in the planes x/W = 0.0 (symmetry plane); Re = 6600, Standard κ–ε turbulence model.

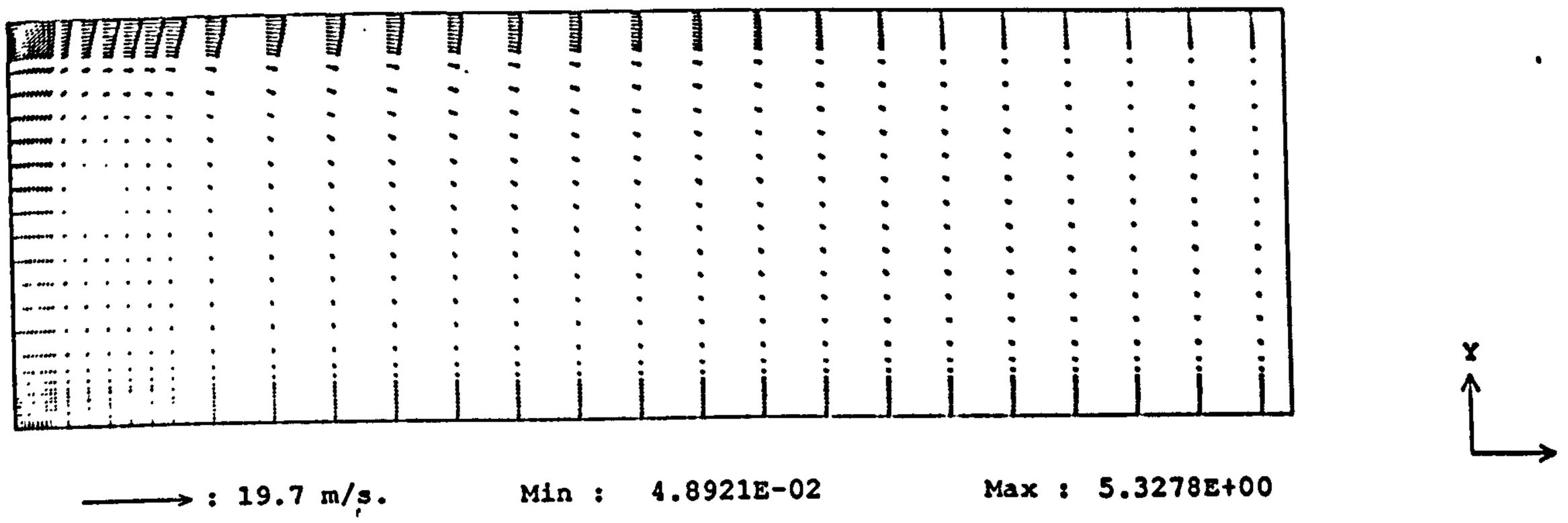

Figure 6.28 Velocity vector distribution in the plane x/W = 0.4; Re = 6600, standard κ–ε turbulence model.

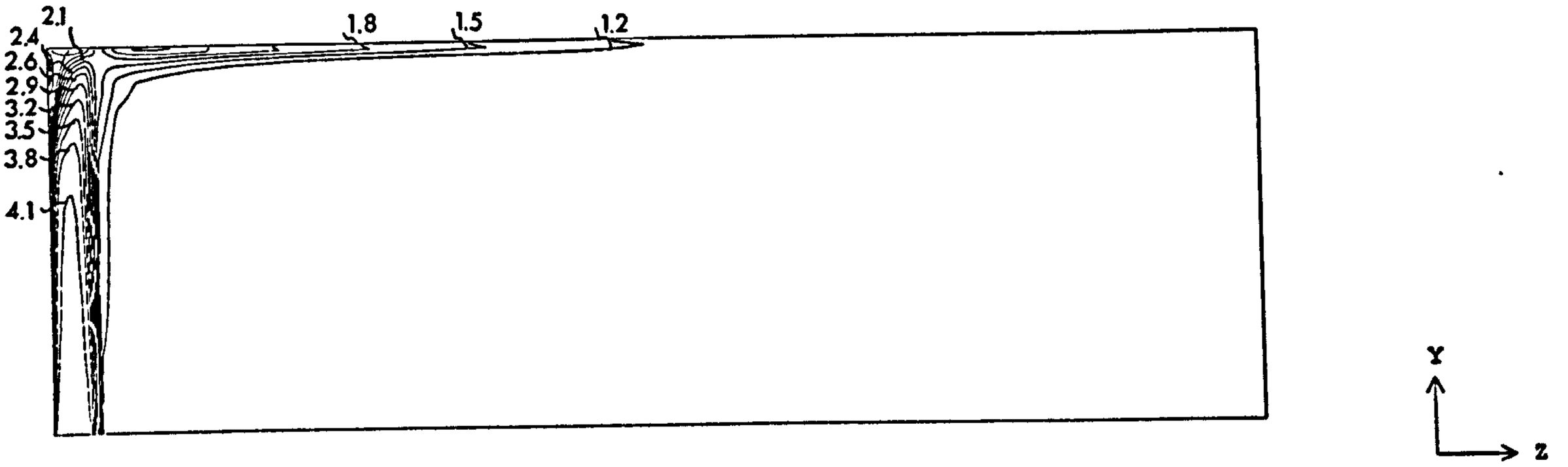

Figure 6.29 Turbulent kinetic energy contours in the plane x/W = 0.0 (symmetry plane); Re = 6600, low-Re $\kappa-\varepsilon$ turbulence model. Contour values in m^2/s^2.

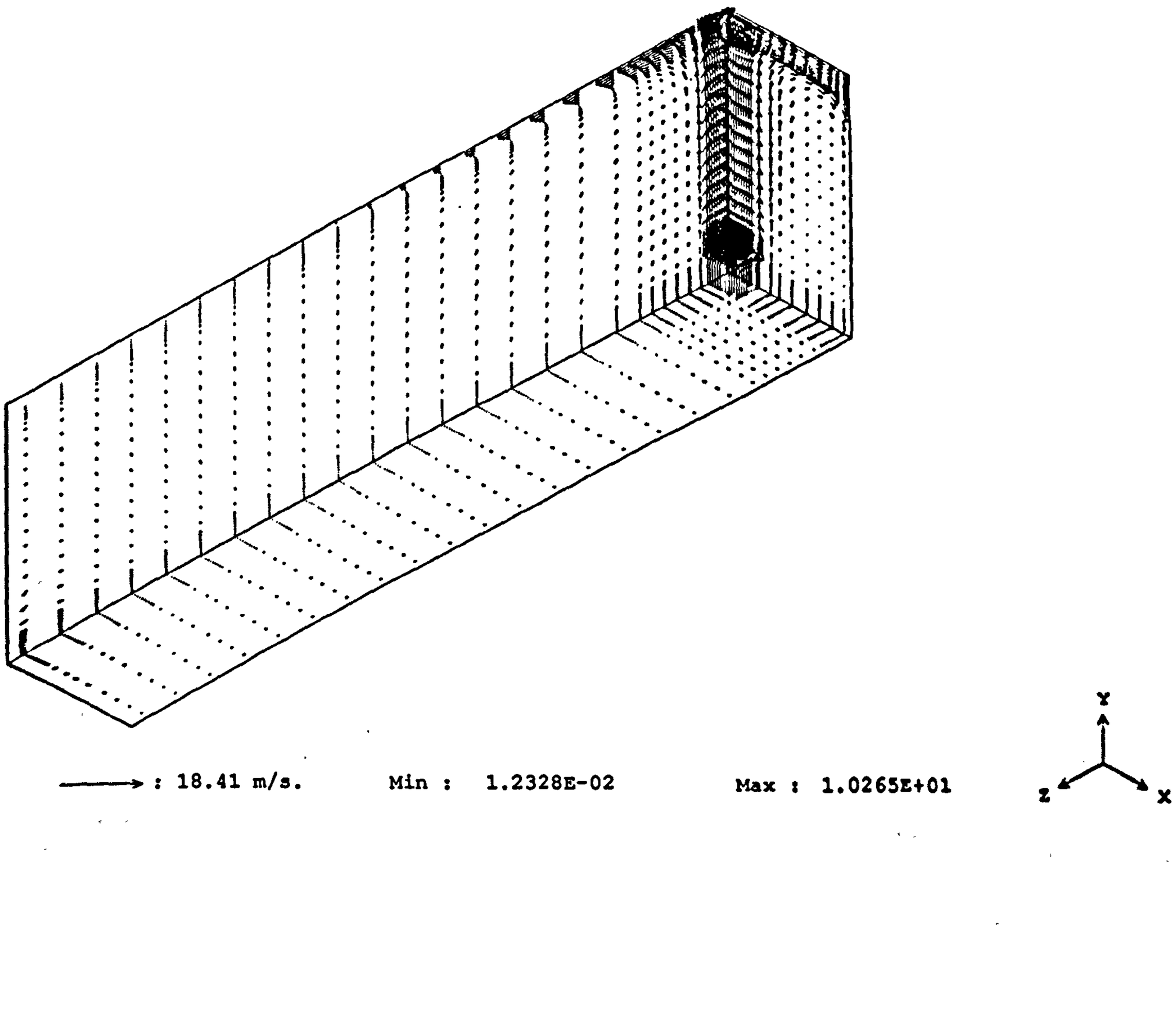

Figure 6.30 Velocity vector distribution in the planes x/W = 0.0, y/H = 0.0 and z/L = 0.0; Re = 6600, low-Re κ–ε turbulence model.

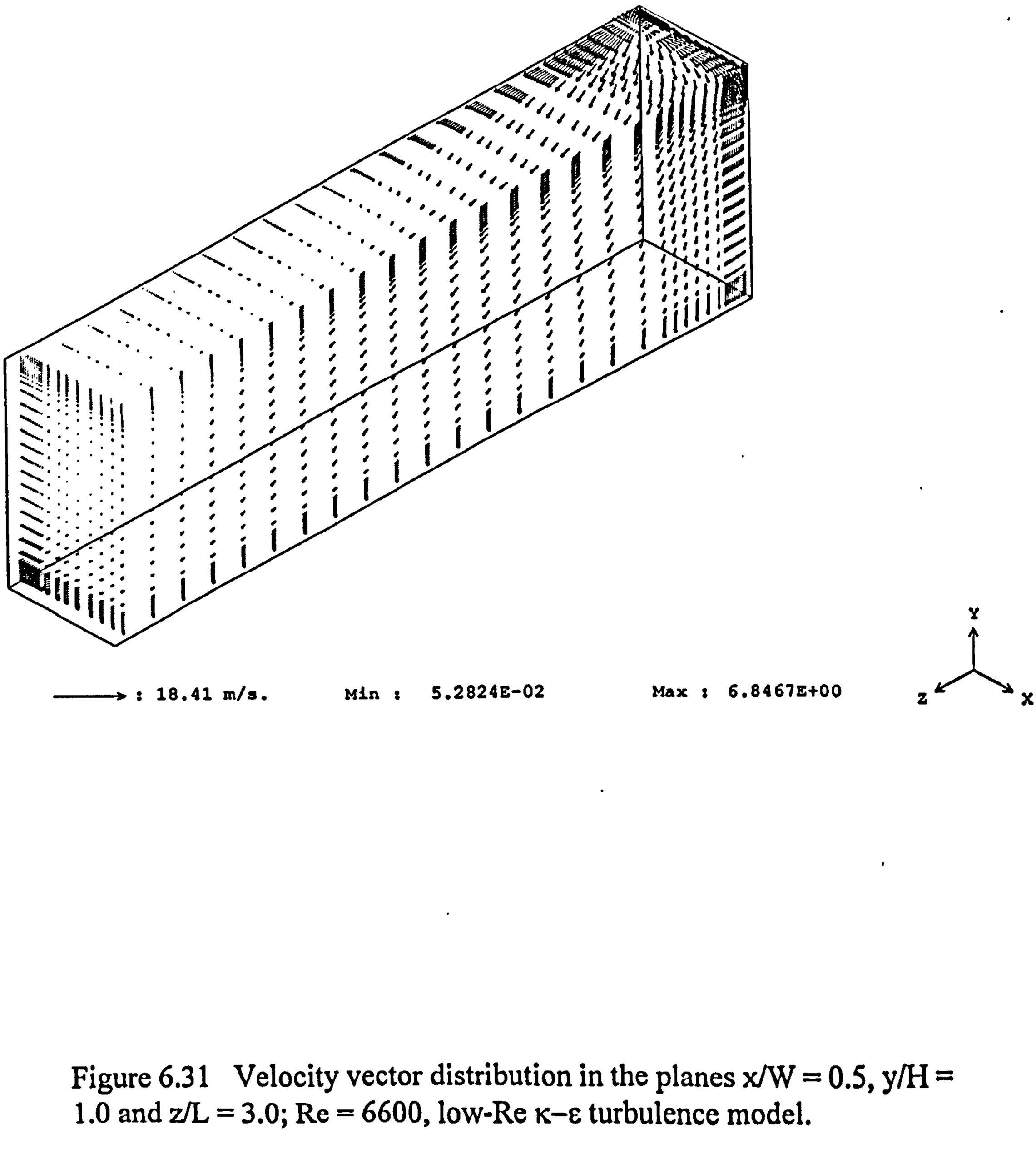

Figure 6.31 Velocity vector distribution in the planes x/W = 0.5, y/H = 1.0 and z/L = 3.0; Re = 6600, low-Re $\kappa-\varepsilon$ turbulence model.

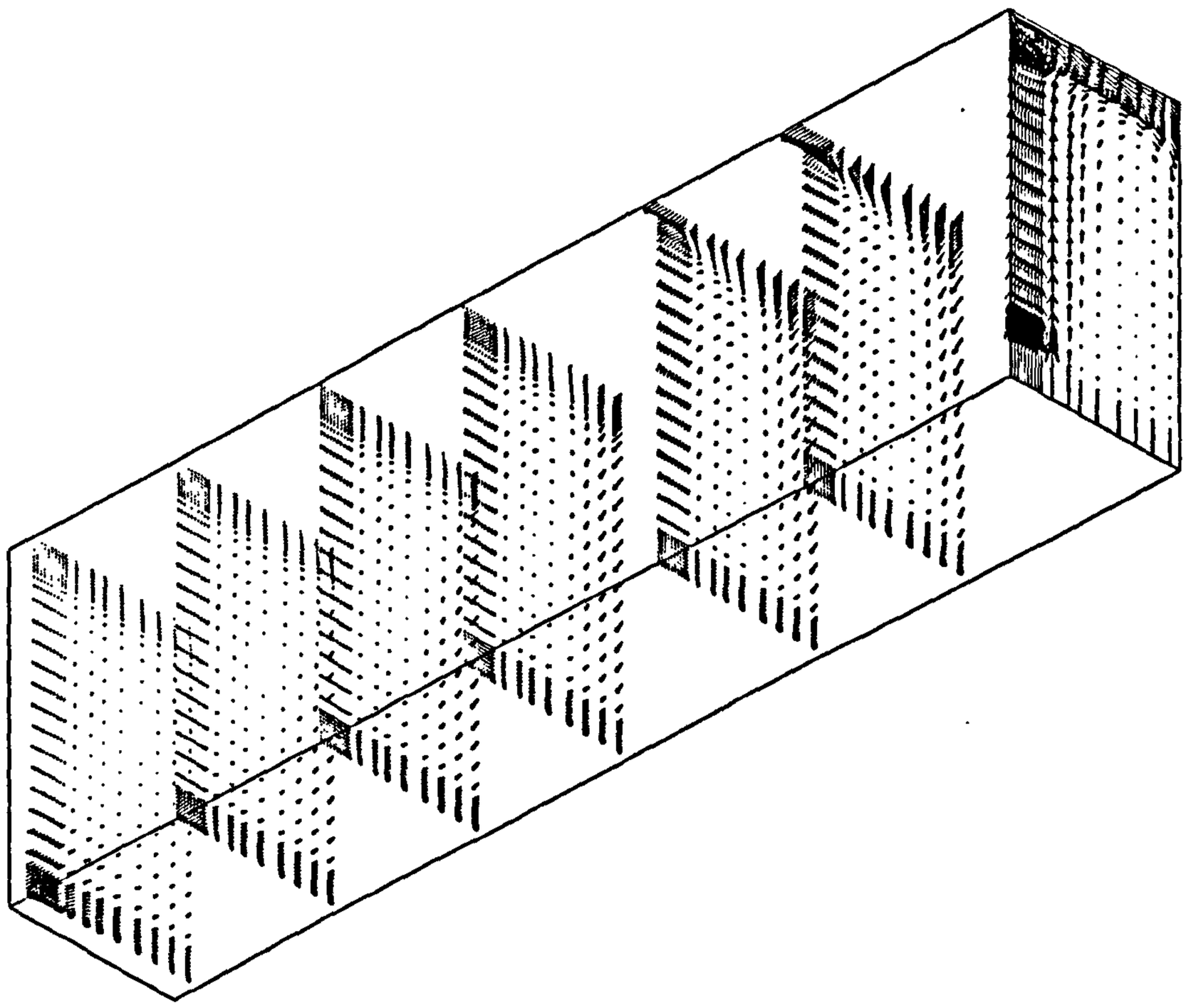

Figure 6.32 Velocity vector distribution in the planes z/L = 0.0, 0.5, 1.0, 1.5, 2.0, 2.5 and 3.0; Re = 6600, low-Re κ–ε turbulence model.

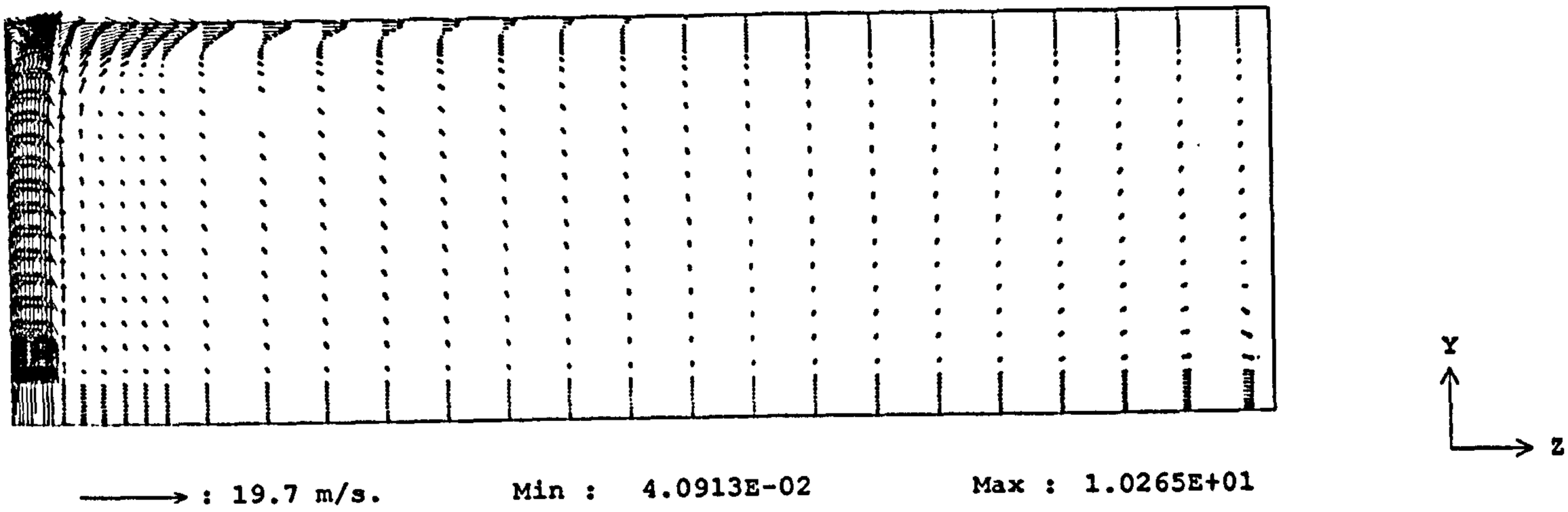

Figure 6.33 Velocity vector distribution in the planes x/W = 0.0 (symmetry plane); Re = 6600, low-Re κ–ε turbulence model.

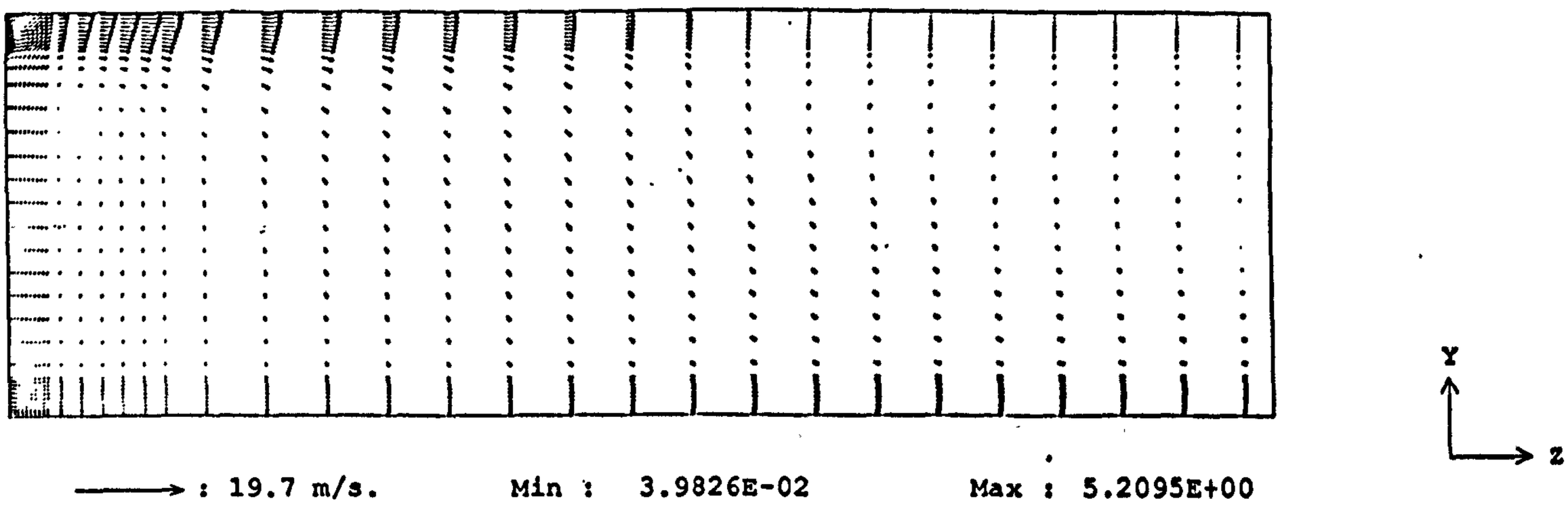

Figure 6.34 Velocity vector distribution in the plane x/W = 0.4; Re = 6600, low-Re κ–ε turbulence model.

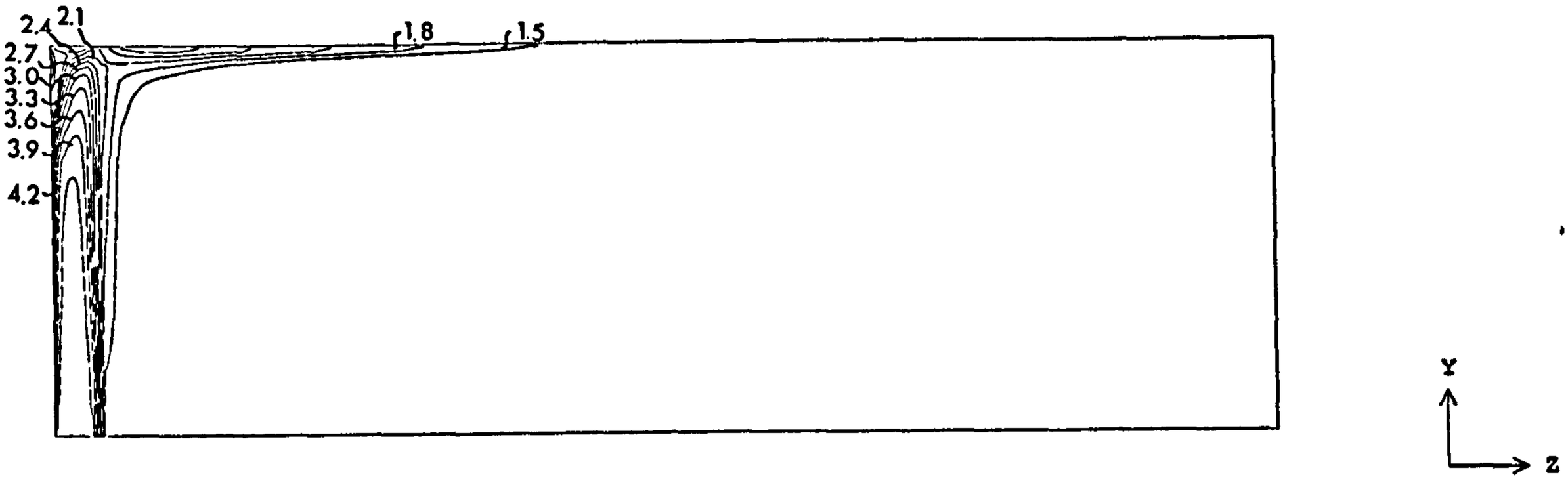

Figure 6.35 Turbulent kinetic energy contours in the plane x/W = 0.0 (symmetry plane); Re = 6600, low-Re κ–ε turbulence model. Contour values in m^2/s^2 .

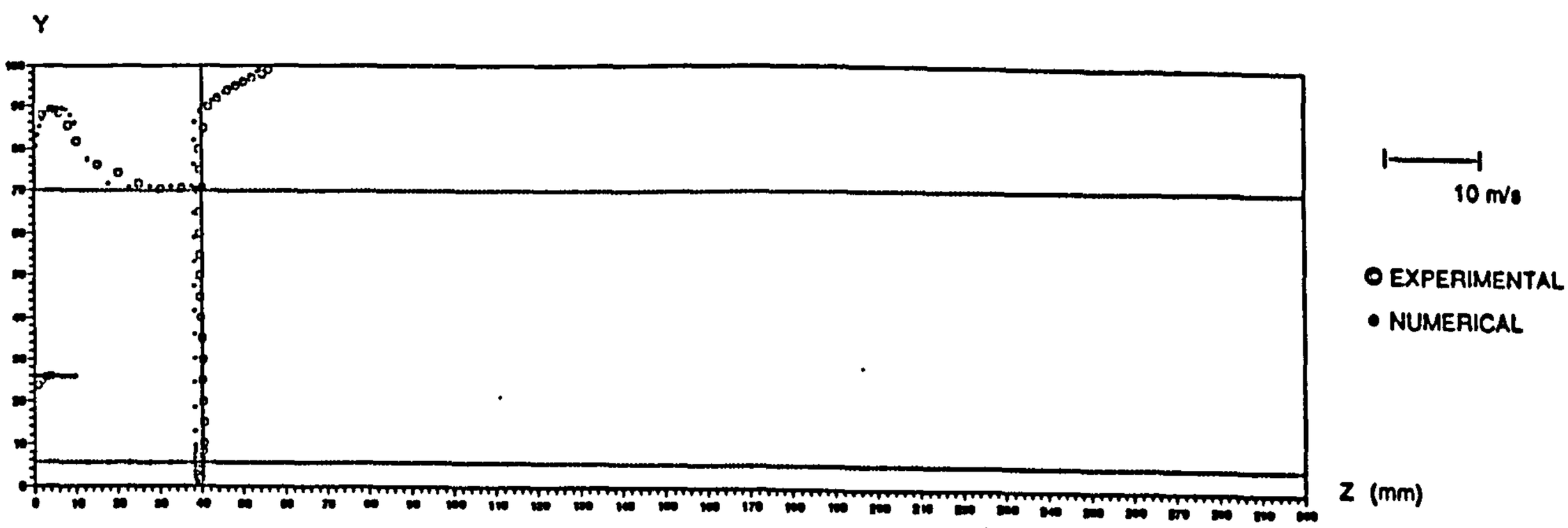

Figure 6.36 Measured and predicted mean velocity in the plane x/W = 0.0 (symmetry plane); Re = 6600.

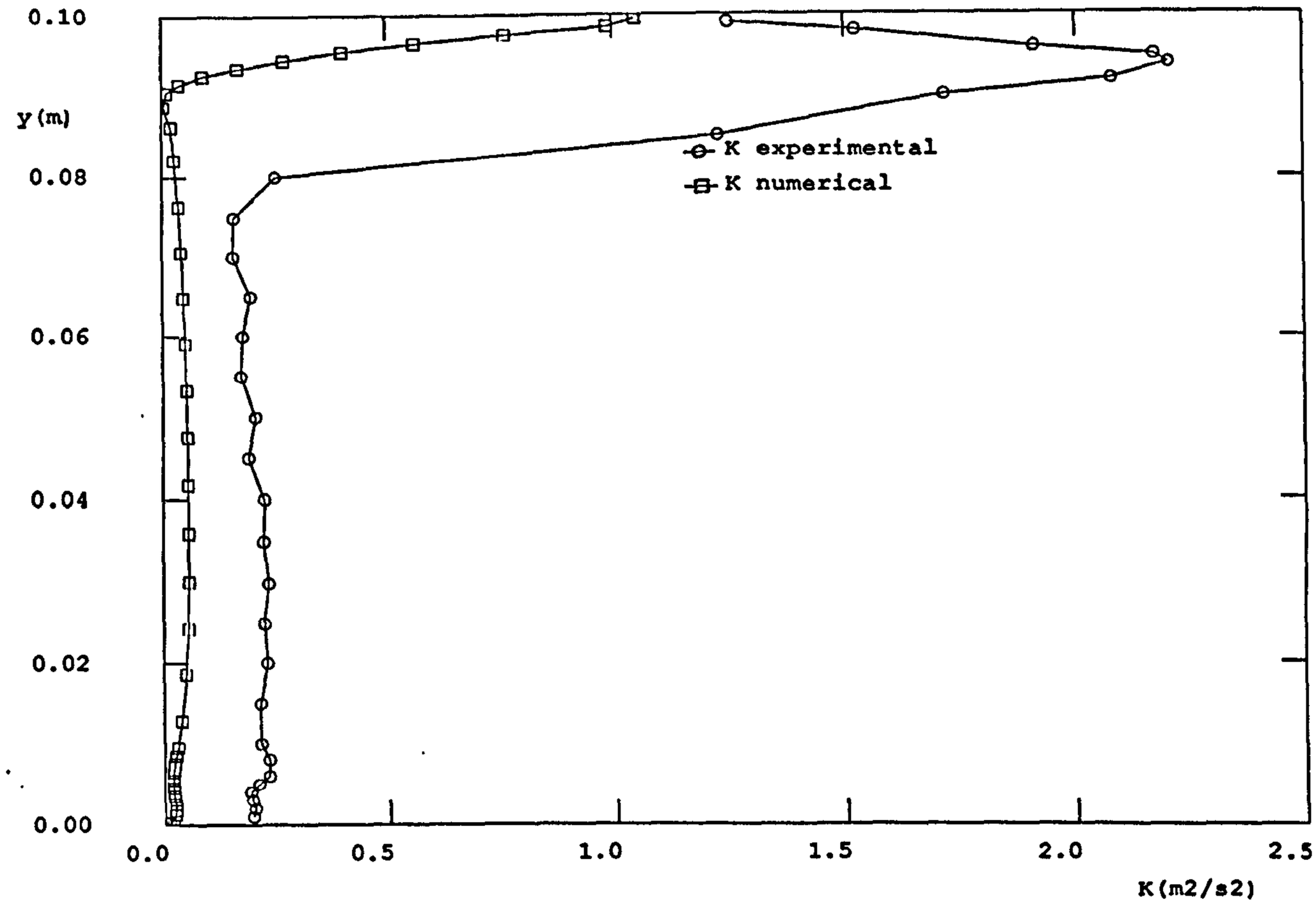

Figure 6.37 Measured and predicted kinetic energy of turbulence in the plane x/W = 0.0 at z = 40 mm; Re = 6600.

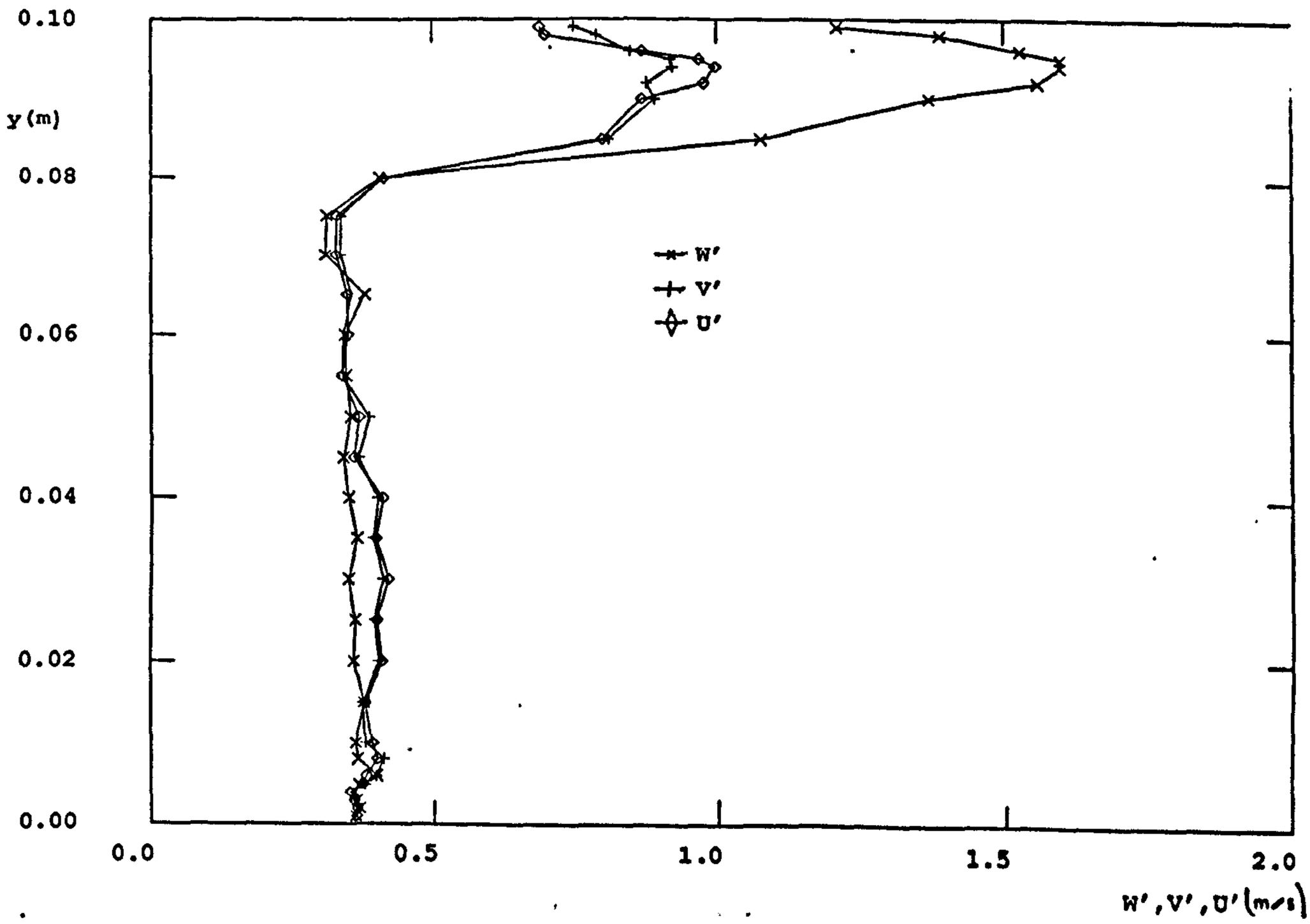

Figure 6.38 Measured rms velocities in the plane x/W = 0.0 at z = 40 mm; Re = 6600.

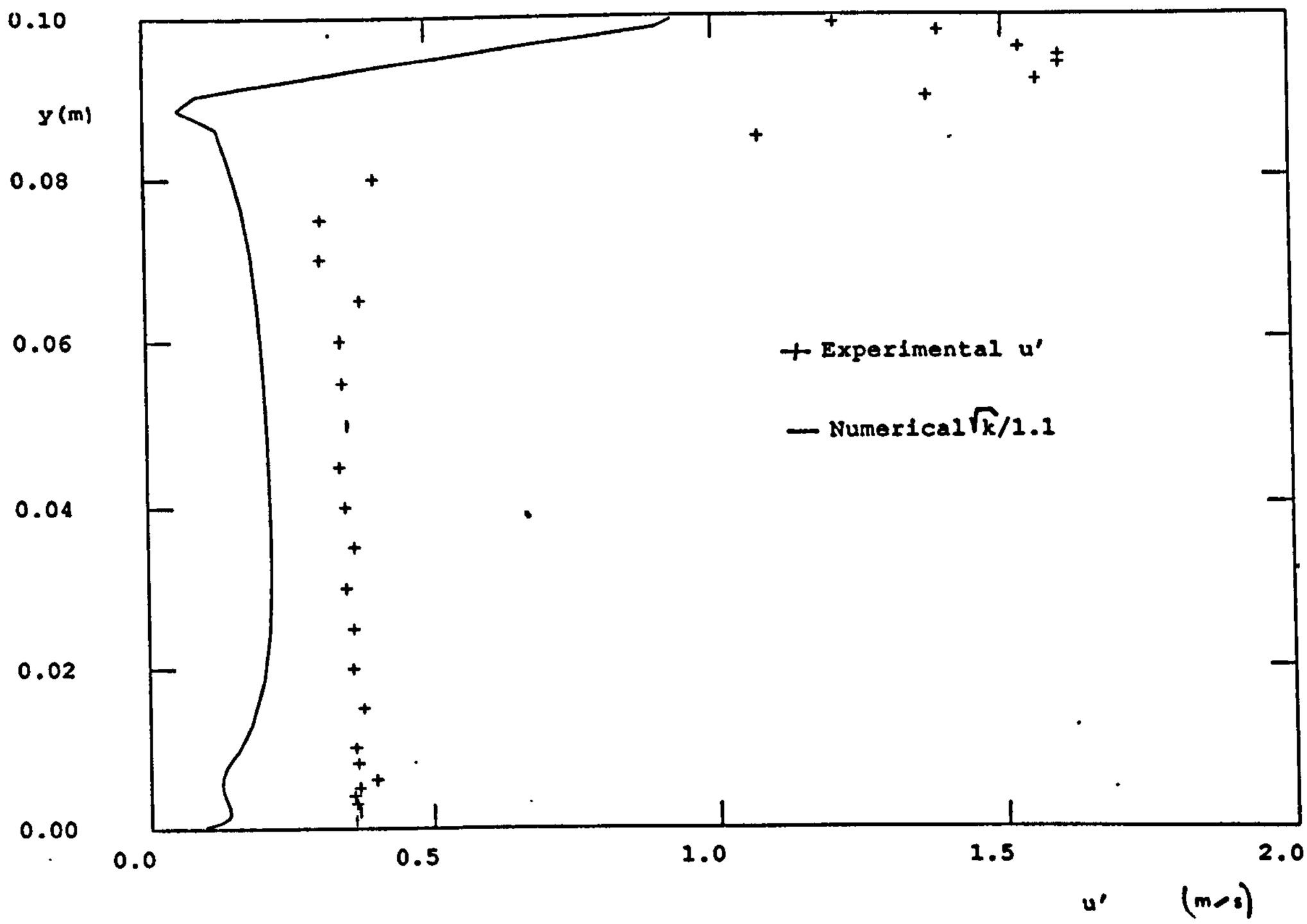

Figure 6.39 Measured and predicted r.m.s. velocities in the plane x/W = 0.0 at z = 40 mm; Re = 3600.

CHAPTER 7

EFFECT OF INLET JET ANGLE , CONTAMINANT DISPERSION AND ARCHIMEDES NUMBER ON THE MEAN FLOW AND TURBULENCE STRUCTURE.

7.1 Introduction

In this Chapter a series of CFD studies of the effects of the inlet jet angle, of contaminant dispersion from a pollutant source and of Archimedes number on the mean flow and turbulence structure is described and discussed. Inlet jet angle effects were studied for two geometrical configurations, namely chambers 1 and 3. In particular, the effects of inlet jet angle on the throw, drop and spread of the incoming air jet, and on the overall flow pattern were studied. Predictions of contaminant dispersion and of the effect of the Archimedes number (Ar) on the flow were performed in a full scale chamber, as it has been established that small scale studies of such effects are not appropriate (Nielsen (1991)). Contaminant dispersion was studied for six different locations along the cavity length. All but the Ar studies were performed for isothermal conditions. The effect of Ar was investigated by determining the influence of heating an internal surface (the floor of the chamber) on the air flow patterns.

7.2 Computational details

The numerical CFD code used to obtain the predictions shown in this Chapter was described in Chapter 3. The geometrical configuration, the mesh sizes and the boundary conditions used for the inlet jet angle

predictions for chambers 1 and 3 were identical to those described previously in chapters 4 and 6 respectively. Following the procedure described in Chapters 4 and 6, the flow was assumed to be symmetrical, and only half of the chamber was simulated for each case. All the gradients were set to zero across the symmetry plane, where the slip condition was used.

The contaminant dispersion and Archimedes number calculations, were made for the full scale configuration shown in Figure 7.1, where H = 3.0 m, L = 9.0 m, W = 3.0 m, h = 0.168 m and t = 0.48 m. A mesh similar to that suggested by Chen (1991) was used, containing 30 x 36 x 15 volumes in the z, y and x directions respectively. The contaminant dispersion predictions were carried out for isothermal conditions and all the usual variables (p, u, v, w, κ, and ε) were calculated as well as the distribution of the scalar contaminant in the chamber. For the Ar effect predictions, the energy equation was also solved. The buoyancy term was included in an additional term in the momentum equation. The buoyancy effect was introduced by means of buoyancy source terms in the κ and ε equations.

The numerical solutions for the inlet jet angle, contaminant distribution and Archimedes number studies required 400, 600 and 6000 iterations respectively. The corresponding computational times were 1.44, 1.28 and 1.50 hours of CPU time on a VAX 4100 machine.

In the following section 7.3 the predictions concerned with the effect of the inlet jet angle are presented. Subsequently in section 7.4 the contaminant dispersion study and in section 7.5 the investigation of the effect of the Archimedes number is described. The predictions are presented in the form of mean velocity vector distributions and kinetic energy of turbulence

contours and additionally in sections 7.4 and 7.5 as concentration and temperature contours respectively.

7.3 Effect of inlet jet angle

In earlier chapters the flow patterns produced with a 0° inlet jet angle (chamber 1) and 90° (chamber 3) were presented. In order to determine the flow structure with intermediate inlet jet angles, two cases (with jet angles of 10° and 45° to the horizontal) were studied with the chamber 1 configuration (high side-wall inlet) and two (with jet angles of 10° and 45° to the horizontal) with the chamber 3 configuration (ceiling inlet).

7.3.1 Predicted flow patterns and turbulence structure.

The study was made for the following conditions:

Reynolds number	inlet velocity (m/s)	outlet velocity (m/s)	Flow rate (m^3/s)
3600	5.55	2.46	0.001665

Figure 7.2 shows the predictions obtained for an incoming air jet angle of 10 degrees to the horizontal. The air flow can be seen entering the chamber and spreading in the direction towards the end wall. Large velocities, around 2.3 m/s, can be observed all along the jet trajectory. The velocities close to the ceiling surface are 50-70% smaller, with gradients along the roof of the chamber. The air jet spreads considerably as it flows through the central zone of the chamber. When the jet has reached the opposite wall, it has spread in the vertical direction by 70-80 mm. The jet is deflected by the end wall in two directions. One part of the jet moves toward the chamber ceiling, forming a recirculation zone. This region is

43.6 mm wide and 11.0 mm high, with velocities between 0.2 and 0.9 m/s. The second part of the air jet moves downwards towards the outlet. Part of the air jet reaches the floor and moves backwards in the direction of the inlet wall. The velocities along the occupied zone have values in the range 0.14 - 0.42 m/s.

Figure 7.3 shows the corresponding predicted contours of the kinetic energy of turbulence. High values of around 0.67 m^2/s^2 can be observed near the inlet. Further downstream the kinetic energy of turbulence decays along the air jet trajectory. Large areas of the occupied zone present a uniform distribution of κ values of around 0.14 m^2/s^2.

Figure 7.4 shows the velocity vector distribution predicted with a jet inlet angle of 45 degrees. The incoming air jet flows towards the floor area where it is deflected towards the lateral wall. The jet spreads over approximately 25% of the floor area with floor velocities of 2.5 m/s near the symmetry plane and decreasing to 0.4 m/s near the lateral wall. Along the symmetry plane the velocities decrease from 4.0 m/s near the inlet to 1.8 m/s at z = 200.0 mm. In the half of the chamber nearest the outlet the velocities are low, around 0.55 m/s compared to 4.0 m/s near the inlet. Close to the ceiling surface velocities are small everywhere, around 0.1 m/s. The predictions for this inlet angle show clearly that the flow consists of two regions, one near the inlet with velocities around 1-2 m/s and one near the outlet where the velocities are uniformly low (near-zero). Only very close to the outlet are larger velocities found as the flow accelerates to leave the chamber.

The corresponding kinetic energy of turbulence contours can be seen in Figure 7.5. In the area close to the inlet the largest values of κ (0.49 m^2/s^2)

are found. Further away, κ values decrease by 50 to 60 % while over most of the chamber κ does not exceed 0.1 m^2/s^2

The predictions made with the chamber 3 geometry (ceiling inlet) are shown in Figures 7.6 to 7.9. Figure 7.6 shows the velocity vectors predicted for an inlet jet angle of 10 degrees to the horizontal, which may be compared with the corresponding case for a 10^o angle jet from the side-wall inlet (Figure 7.2). Large velocities between 1.0-2.0 m/s can be seen along the jet trajectory and close to the ceiling surface. The shape of the boundary layer along the ceiling is considerably different to that in Figure 7.2, with steeper gradients present along the ceiling surface. The incoming jet flow moves toward the end wall and then it is deflected towards the floor surface. A large recirculation zone is formed in the chamber, centred on y = 47.5 mm and z = 271.2 mm. The reverse air velocities have values between 0.02 m/s and 0.33 m/s over most of the chamber. Uniform velocities of around 0.3 m/s can be seen moving in the direction of the outlet. The predicted flow pattern is similar to that obtained for chamber 1 (Chapter 4). However the small recirculation zone found in the upper end wall corner in chamber 1 (Figure 4.7) cannot be observed in the present case.

Figure 7.7 shows the predicted κ contours. The values of κ are large, around 0.71 m^2/s^2 close to the inlet. They remain high near the ceiling along the trajectory of the jet, decreasing to 0.30 m^2/s^2 at z = 250.0 mm. Similarly to the chamber 1 predictions (Figure 4.8), κ values over most of the chamber cross-section do not exceed 0.1 m^2/s^2.

Figure 7.8 shows the predictions for a ceiling inlet with a jet angle of 45 degrees. They may be compared with the corresponding side-wall inlet predictions shown in Figure 7.4. The incoming air jet in Figure 7.8 can be

seen flowing toward the floor surface. The jet spreads considerably before it reaches the floor surface. The floor surface deflects the jet in the direction of the outlet and a large recirculation zone is formed over the half of the chamber nearest to the outlet. Velocities of around 1.5-2.0 m/s are predicted along the jet trajectory. In the recirculation region the velocities do not exceed 0.25 m/s. Part of the deflected air flow moves over the floor surface towards the lateral walls, with velocities of 0.1 - 0.2 m/s. In the occupied zone the velocities vary from 0.8 - 1.1 m/s.

The corresponding values of the kinetic energy of turbulence are shown in Figure 7.9. The maximum value of κ is 0.54 m^2/s^2 in the inlet area. κ values along the jet trajectory decrease to 0.23 m^2/s^2 at a distance of 145 mm from the inlet. As in the previous cases, κ values are uniformly low over most of the chamber cross-section.

7.3.2 Discussion

The predictions presented in the previous section have shown that the air flow pattern is modified considerably when the inlet jet angle is altered. The results obtained with both geometries (chambers 1 and 3) have shown clearly that the velocity distribution in the chamber depends strongly on the angle of the incoming air jet.

The CFD predictions for an incoming jet angle of 10 degrees to the horizontal, show that the jet remains relatively close to the ceiling surface. A comparison of Figures 7.2 and 7.6 shows that with the side-wall inlet, a 10° inclination of the inlet jet results in the velocity decreasing to 2.5 m/s at z = 250 mm, compared with 3.0 m/s at the same z-location for the ceiling-inlet jet. In addition, the jet spread is considerably larger in the former case, e.g. 75 mm at z = 250 mm, compared to 10 mm at the same

location with a ceiling inlet. In the occupied zone, both configurations produce similar velocities of 0.2 - 0.3 m/s.

For a jet angle of 45 degrees (Figures 7.4 and 7.8), the predicted jet spread is larger (50 to 70 mm) for both ceiling and side wall inlets than with the 10º jet angle. Velocities of around 1.08 m/s (Figure 7.4) and 1.29 m/s (Figure 7.8) are predicted over the occupied zone, considerably larger than with the 10° jet angle. Large velocities will, of course, produce an undesirable draught over the occupants exposed directly to the incoming air jet. The maximum turbulence levels, 0.49 and 0.54 m^2/s^2 for Figures 7.5 and 7.9 respectively, are lower than the corresponding ones, 0.67 and 0.54 m^2/s^2, for Figures 7.3 and 7.7 respectively. Figures 7.3 and 7.7 show the largest values of κ along the jet trajectory and close to the ceiling chamber, while Figures 7.5 and 7.9 exhibit κ larger values close to the floor surface and in the middle of the chamber. The chambers with a 10° jet angle produce a more homogeneous air velocity distribution over the occupied zone.

Based on the above observations, it is clear that the maximum reverse velocity in the occupied zone decreases as the discharge angle is increased. This maximum velocity reduction was observed by Henstad (1971, 1974) who worked with jet angles of 10 degrees to the horizontal and a 90 degree jet deflected by a horizontal surface, in order to assess wall jet assumptions, and Restivo (1979) who assessed the effect of the inlet jet angle on the maximum reverse velocity. Restivo (1979) found that the maximum reverse velocity decreased as the jet angle increased, and that a 20 degree jet angle affected the velocity by around 10%. The levels of the kinetic energy of turbulence levels were not reported by Restivo. In ventilated chambers where the objective is to reduce the effects of draught over the occupants produced by the discharging air flow, the geometrical

configuration of chamber number 1 for 10° is more appropriate. This configuration presented the lowest velocity values over the occupied zone.

7.4 Contaminant dispersion

7.4.1 Flow and turbulence structure

Due to the problems associated with the scaling of contaminant sources and temperature effects (see chapter 1), the full scale geometry of the chamber (the benchmark test case suggested by Nielsen (1991)), was simulated in the predictions presented in this section and in the following section 7.5. The chamber is ventilated by an air jet discharging from a high side-wall rectangular inlet. The Reynolds number, inlet velocity and flow rate employed for the predictions shown in this and in the next section were:

Reynolds number	Inlet velocity (m/s)	Flow rate (m^3/s)
5000	0.455	0.229

A schematic diagram of the full-scale chamber can be seen in Figure 7.1. Five different locations of the pollutant source were simulated. The same contaminant concentration was used for each case: 5 olf, corresponding to 0.30 ml/s or decipol (i.e. corresponding to the pollution caused by one 'standard' person, 1 olf ventilated by 10 l/s of unpolluted air (Chen, 1990)).

The predicted velocity vector distributions and contaminant concentration contours for the five different pollutant locations can be seen in Figures 7.10-7.19. The first case, corresponding to a pollutant source located on the ceiling surface at z = 4.0 m and y = 3.0 m, can be seen in Figures 7.10

and 7.11. Figure 7.10 shows the velocity distribution, in which contour lines showing the pollutant concentration (in decipols) have been drawn. The pollutant is located inside the boundary layer zone where low velocities (less than 0.2 m/s) are found. The pollutant dispersion is strongly affected and the contaminant remains close to the ceiling surface. A large proportion of the pollutant must flow towards the outlet as only a small amount is mixed in the recirculation flow. Due to this, the concentration of the pollutant increases to 0.72 decipols close to the ceiling, particularly around the source point. In the rest of the cavity the concentration remains low. Figure 7.11 shows the contours of pollutant concentration which shows very clearly the pollutant remaining concentrated along the ceiling.

The pollutant source was then moved to the second position, located inside the incoming air jet zone, where the largest velocities are found (0.35 m/s, at z = 4.0 m and y = 2.84 m), as can be seen in Figures 7.12 and 7.13. The pollutant is entrained by the air jet as it flows toward the outlet. The pollutant concentration at the ceiling decreases to 0.34 decipols, compared with 0.72 decipols in the previous case. The largest concentration is found around the source. In the rest of the cavity the concentration is relatively uniform, with values between 0.0 and 0.02 decipol.

Figures 7.14 and 7.15 show the pollutant source located inside the recirculation zone at z = 7.18 m and y = 1.09 m. The velocities are around 0.01 to 0.1 m/s in this zone and part of the contaminant is entrained by the recirculating flow. The contaminant mixes with the air inside the recirculation zone and disperses toward the inlet; when it has reached the main air jet stream, the contaminant moves toward the outlet and exits the chamber. Along the occupied zone, the contaminant concentration is about 0.05 to 0.12 decipols.

Figures 7.16 and 7.17 show how the contaminant disperses when it is located in the centre of the recirculation zone (z = 6.36 m, y = 1.34 m), where a stagnation point is located. The concentration of the pollutant at this stagnation point increases to 0.48 decipol. The air flow velocities in the recirculation zone have decreased to 0 - 0.01 m/s, and the contaminant does not disperse and mix with the air flow, unlike the previous case.

The contaminant source was then moved to z = 1.81 m and y = 1.34 m. Figures 7.18 and 7.19 show the corresponding predictions. The contaminant is located in the recirculation zone close to the point where the flow is reintrain to incoming jet air. The velocity in the region of the source is higher that in the previous case, around 0.1 - 0.15 m/s, and the concentration of the contaminant has decreased to 0.29 decipols. In this last case the contaminant is entrained by the air moving in the recirculation zone and then by the incoming air jet which it follows until the flow exits the cavity.

7.4.2 Discussion

The predictions presented in the previous section lead to the conclusion that the location of the contaminant source is of great importance. Zones with low mean velocities, less then 0.2 m/s (e.g. boundary layers), and stagnation points (e.g. the centre of large recirculation zone), lead to an increase in the contaminant concentration. Kurabuchi and Kusuda (1987) studied similar flows in a 1:6 scale model of a laboratory. Comparisons were made of the flows produced by different fan speeds and with the fan switched off (natural ventilation). Using different locations for the contaminant source, they found that the levels of concentration around

(upstream and downstream of) the contaminant source varied with the fan operation (on, off, different air flow rates) and the location of the source.

The recirculating flow formed inside the chamber helps to disperse the contaminant rapidly. The spread of the contaminant increased when it was located inside zones of large (greater than 2.0 m/s) velocities. According to Nielsen (1981), when the contaminant source is placed in relatively stagnant regions in the room, higher concentrations will exist. His findings (supported by experiments) showed the importance of locating contaminant sources in regions of high velocity in the room. The results shown in section 7.3 support these findings.

Nielsen (1981) found that when the contaminant source was placed on the floor a decrease on the height of the supply (i.e. a narrower inlet) slot produced a decrease in concentration in the enclosure, i.e. an increase on the air circulation increased the ventilation efficiency. The increase of air circulation can bring as a consequence the creation of a draught inside the occupied zone. Murakami et al (1983) placed a contaminant source close to the floor. They found that the larger the air change rate, the larger the area of low concentration close to the ceiling and down the far wall. Other researchers have made studies with passive ventilation. Davidson and Olson (1987) studied the net rate at which a dynamically passive contaminant (i.e. when the flow pattern is not influenced by the contaminant) is purged out of a system. They compared predicted results with measurements and found that the predicted age of the contaminant at locations close to the floor was considerably higher than the measured values. They attributed the differences to possible numerical diffusion or the inadequacy of the turbulence model used (κ–ε) as well as the small number of experimental measurements they obtained. Clearly, the findings

of the above studies and of the present work show that the location of the contaminant source affects strongly the distribution of the contaminant.

7.5 Effect of Archimedes number

7.5.1 Predicted flow pattern and turbulence structure

In this section the predictions for a non-isothermal flow in a full scale chamber are presented. The case predicted is that proposed by Nielsen (1991) as a benchmark test case. The test was set to evaluate the effects of a temperature increase of the floor surface on the air flow patterns inside the chamber. The temperature of the floor surface was set to be uniform. Rates of floor heating were simulated to produce flow Archimedes numbers of 0.02, 0.04, 0.06, 0.08, 0.10, 0.148. The process followed was to use the converged solution for the previous Ar flow case as the set of initial conditions for the next Ar case. An interesting phenomenon called the hysteresis effect (Restivo (1979)) will be present during an increase or decrease of Ar; this phenomenon causes the jet to be detached from the ceiling surface.

The results predicted in the present investigation can be seen in Figures 7.20 to 7.23, in the form of mean velocity vector distributions and temperature contours. It can be observed that although the temperature contours are modified as Ar is increased (see Figures 7.22 and 7.24, Ar = 0.02 and 0.04 respectively), the mean velocity distribution remains unchanged (Figures 7.20, 7.21 and 7.23). When Ar has reached the value of 0.148 the air jet separates from the ceiling surface, as can be seen in Figure 7.25. For this last case (Ar = 0.148) both the velocity vector distribution and the temperature contours (see Figure 7.25) have been considerably modified.

7.5.2 Discussion

It was observed that the air jet remains attached to the ceiling surface due to the combined influence of the Coanda effect and the convective flow ascending from the heated floor. A gradual increase of Ar will produce the effect known as hysteresis. The air jet flowing attached to the ceiling surface will be deflected downwards as it was observed in Figure 7.25. The temperature increase induces non-uniform buoyancy forces inside the chamber which interact with the velocity fields, modifying the air flow patterns and the turbulence levels inside the chamber. It was observed that the air flow pattern remains unchanged up to Ar = 0.148. Chen (1991) found that the Ar at which the flow in the chamber changes pattern was 0.142, while Vogl and Renz (1991) estimated it to be 0.15. However Heikkinen (1991), concluded that the change in flow pattern depended on the iteration number. He predicted different flow patterns while increasing the number of iterations. This behaviour was not observed in the predictions of the present study. Chen (1991) considered the Heikkinen (1991) results and concluded that the test case proposed by Nielsen (1990) involves a critical value of Ar in which aiding and counter aiding forces are of equal magnitude: a minor disturbance would have a significant effect on the air flow pattern. This last result was observed in Figure 7.25, when the Ar number in the chamber has reached the critical point and the flow pattern has change dramatically.

7.6 Concluding remarks

The modification of the inlet angle supply affected the predicted flow pattern in all the cases studied. An air jet discharging at a small angle to the ceiling surface from a high-wall inlet produced a more homogeneous

air velocity distribution inside the chamber, especially over the occupied zone. Higher turbulence levels were observed when the jet discharged from a ceiling outlet. An angle of 45 degrees of the supply air jet, produced large mean velocities over the occupied area, which would create an undesirable draft effect. The 10^{o} angle is considered the most appropriate of those investigated for the chamber ventilation.

The contaminant dispersion study helped to identify zones of high or low contaminant concentration and to associate these zones with the location of the contaminant source. The location of contaminant source in regions with velocities below 0.2 m/s must be avoided in order to diminish the probability of high pollutant concentration in occupied areas. Based on the results obtained from the two geometrical configurations studied here and the results of Henstad (1971, 1974) and Restivo (1979), it can be expected that different chamber geometries and jet inlet angles will influence the contaminant distribution directly, and this should be investigated more extensively in future work.

The non-isothermal cases studied, showed that a gradual increase of the floor temperature (and therefore of Ar) will eventually lead to air jet separation from the ceiling surface. This was observed when Ar = 0.148. For Ar < 0.148 no changes were observed on the mean velocity distribution.

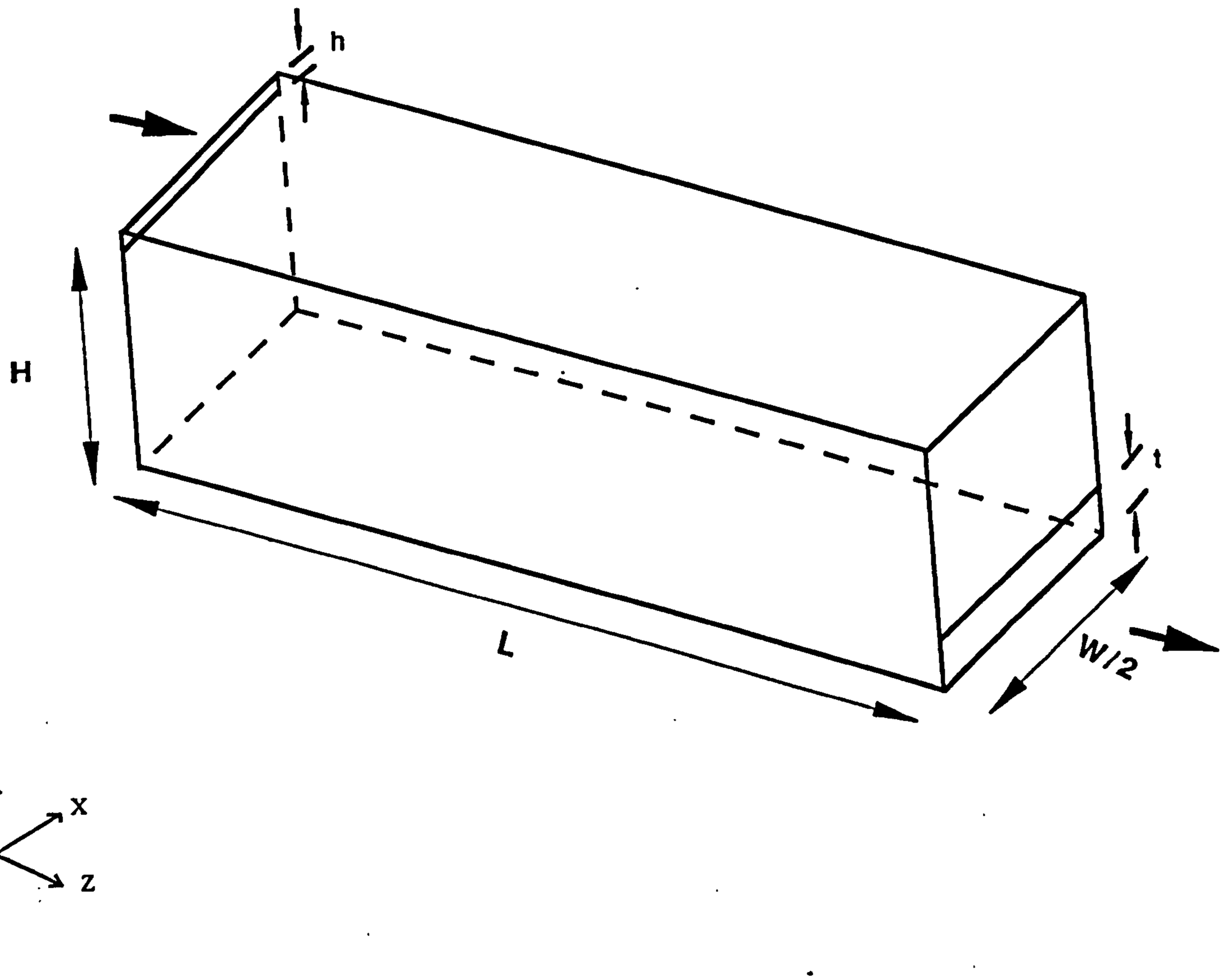

Figure 7.1 Full scale flow configuration: schematic diagram of one-half of the chamber.

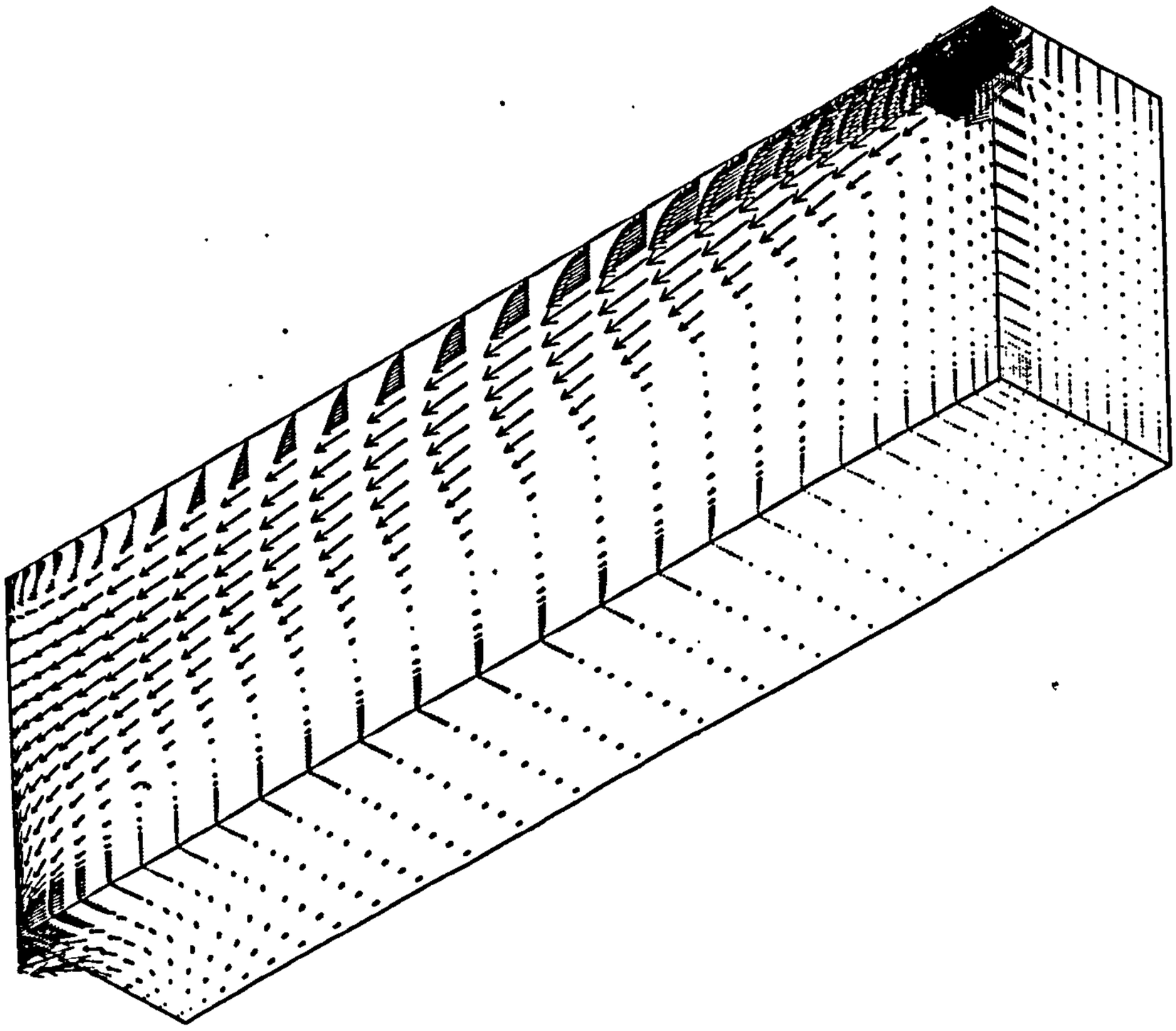

: 4.89 m/s. Min : 7.8525E-04 Max : 4.2912E+00

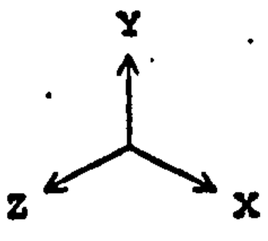

Figure 7.2 Velocity vector distribution in the planes x/W = 0.0, y/H = 0.0 and z/L = 0.0; Re = 3600, standard $\kappa-\varepsilon$ turbulence model. Inlet jet angle: 10 degrees.

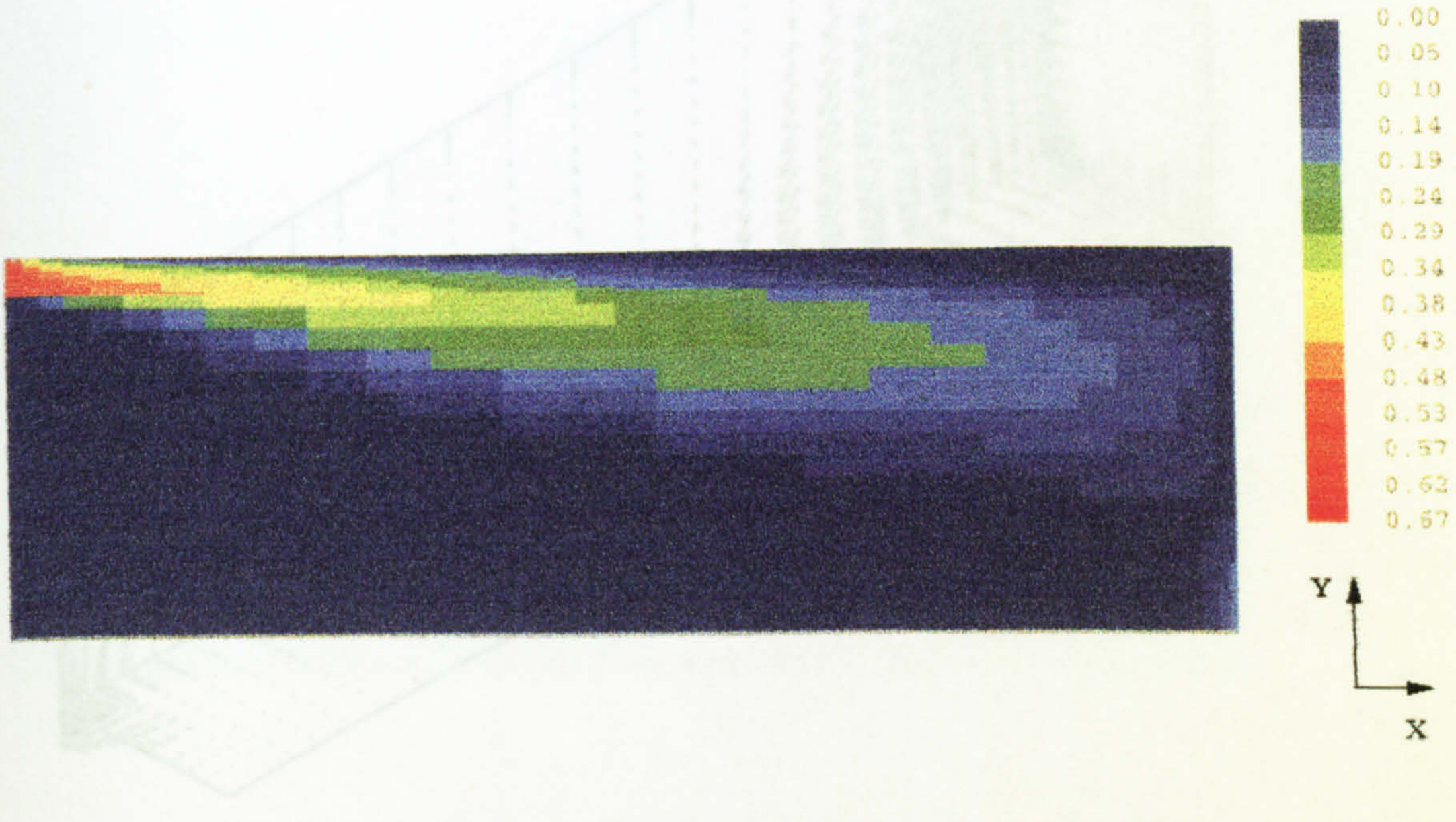

Figure 7.3 Turbulent kinetic energy contours in the plane x/W = 0.0 (symmetry plane); Re = 3600, standard $\kappa-\varepsilon$ turbulence model. Contour values in m^2/s^2. Inlet jet angle: 10 degrees.

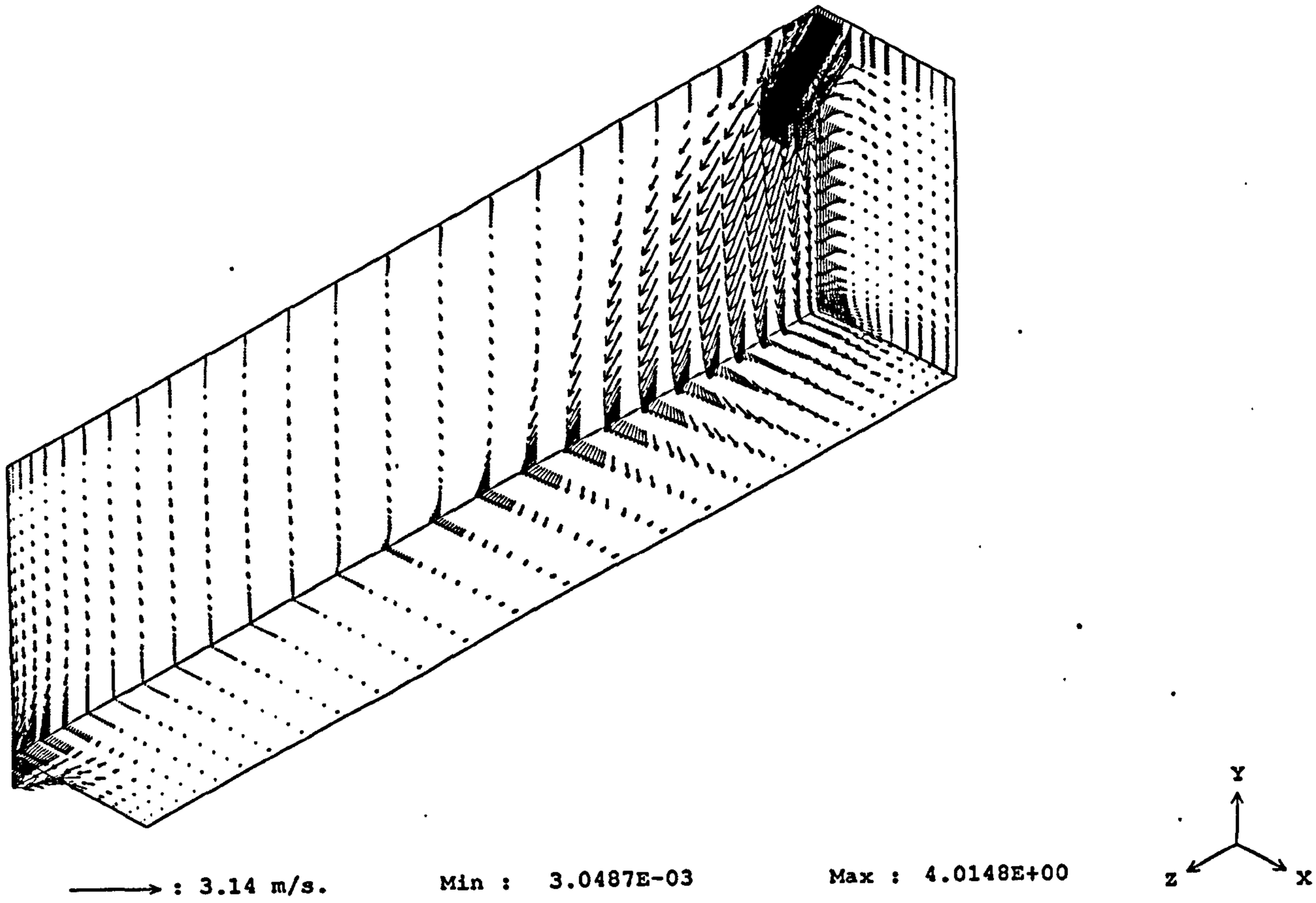

Figure 7.4 Velocity vector distribution in the planes x/W = 0.0, y/H = 0.0 and z/L = 0.0; Re = 3600, standard $\kappa-\varepsilon$ turbulence model. Inlet jet angle: 45 degrees.

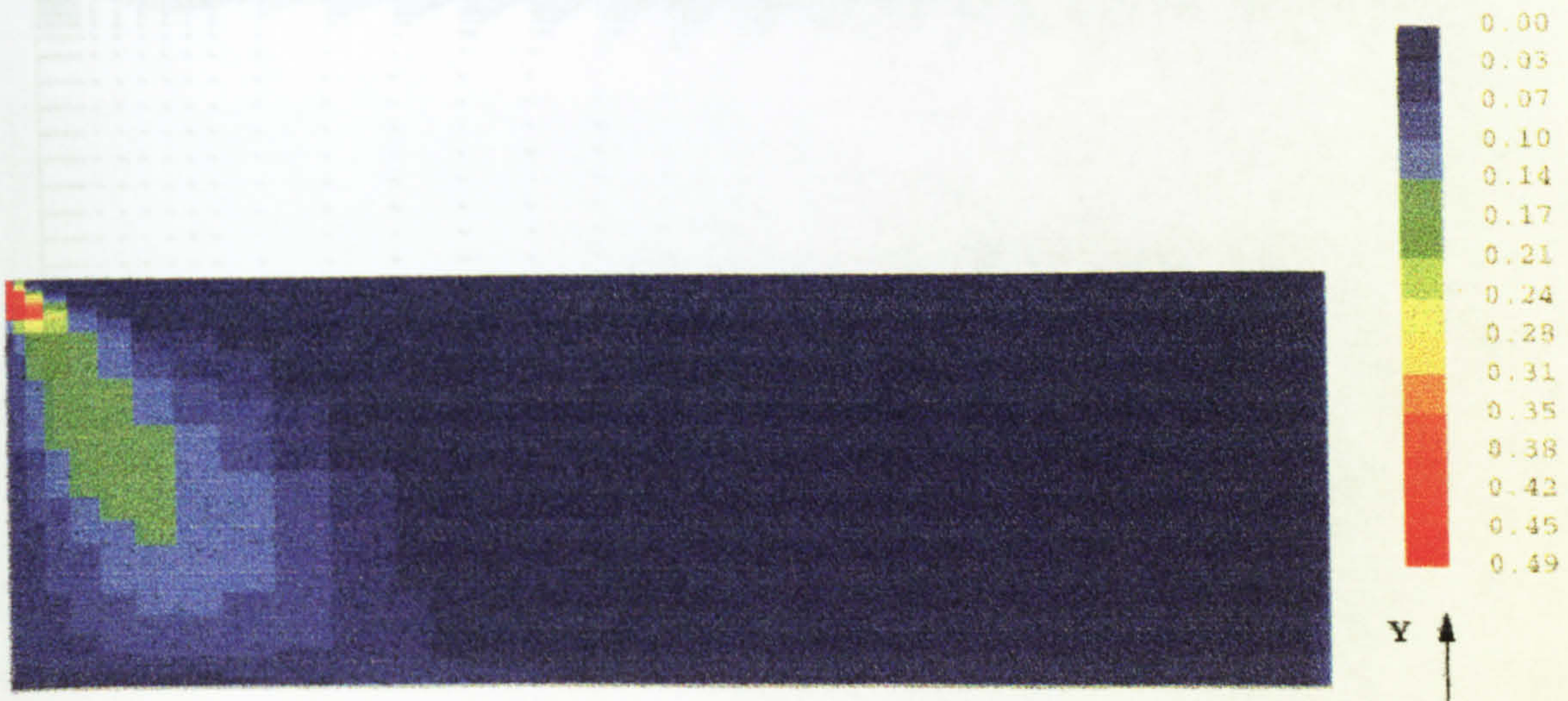

Figure 7.5 Turbulent kinetic energy contours in the plane x/W = 0.0 (symmetry plane); Re = 3600, standard $\kappa-\varepsilon$ turbulence model. Contour values in m^2/s^2. Inlet jet angle: 45 degrees.

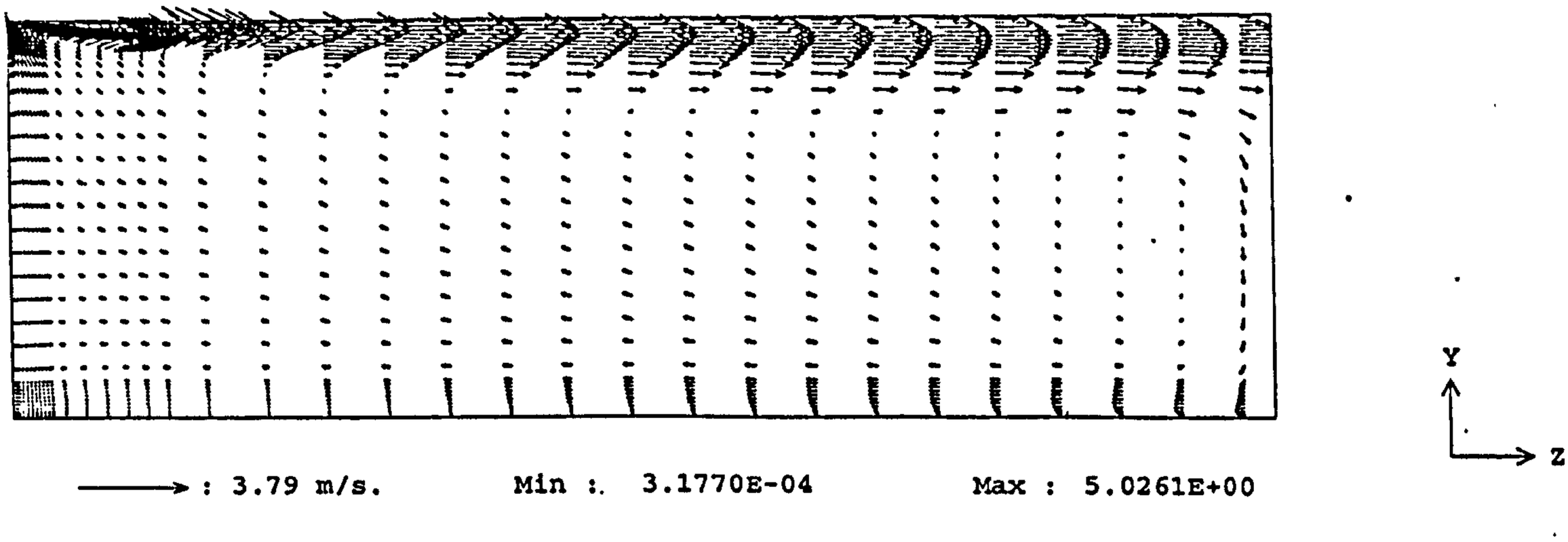

Figure 7.6 Velocity vector distribution in the plane x/W = 0.0 (symmetry plane); Re = 3600, standard $\kappa-\varepsilon$ turbulence model. Inlet jet angle: 10 degrees.

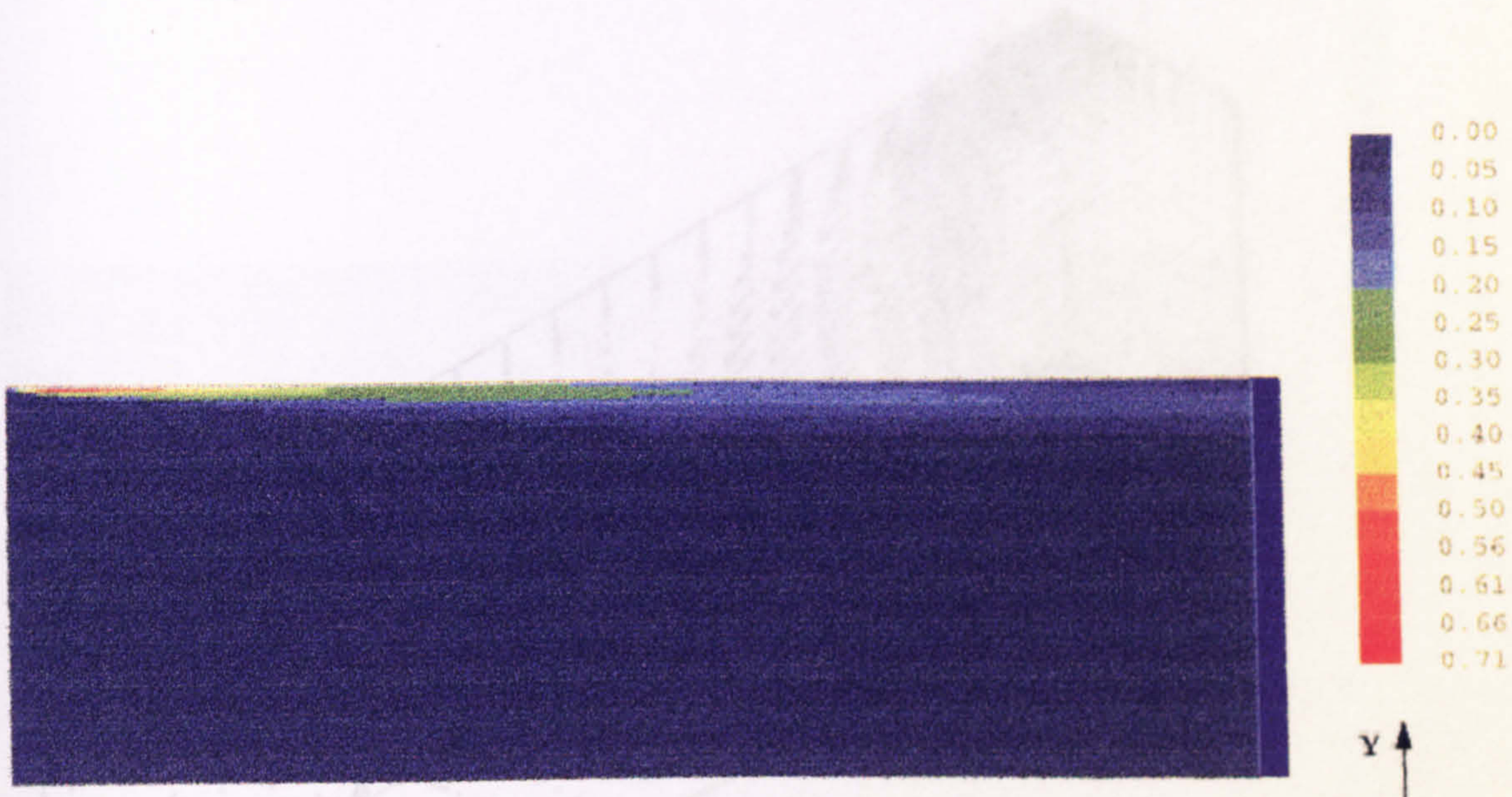

Figure 7.7 Turbulent kinetic energy contours in the plane x/W = 0.0 (symmetry plane); Re = 3600, standard κ–ε turbulence model. Contour values in m^2/s^2. Inlet jet angle: 10 degrees.

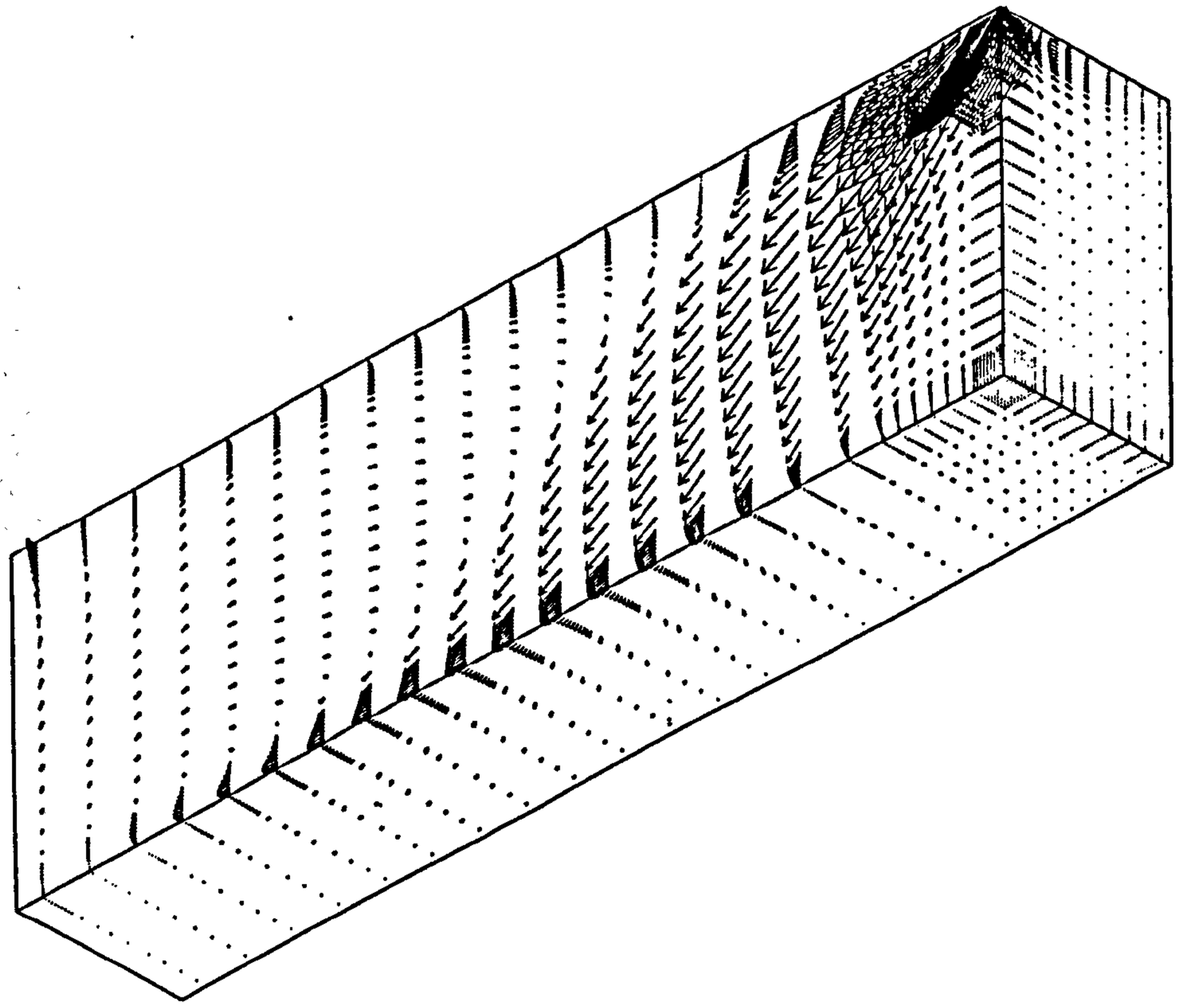

⟶ : 3.69 m/s. Min : 1.3357E-03 Max : 4.0220E+00

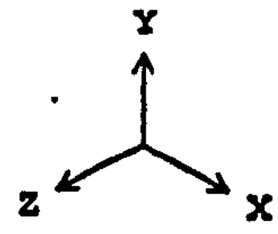

Figure 7.8 Velocity vector distribution in the planes x/W = 0.0, y/H = 0.0 and z/L = 0.0; Re = 3600, standard κ–ε turbulence model. Inlet jet angle: 45 degrees.

Figure 7.9 Turbulent kinetic energy contours in the plane x/W = 0.0 (symmetry plane); Re = 3600, standard $\kappa-\varepsilon$ turbulence model. Contour values in m^2/s^2. Inlet jet angle: 45 degrees.

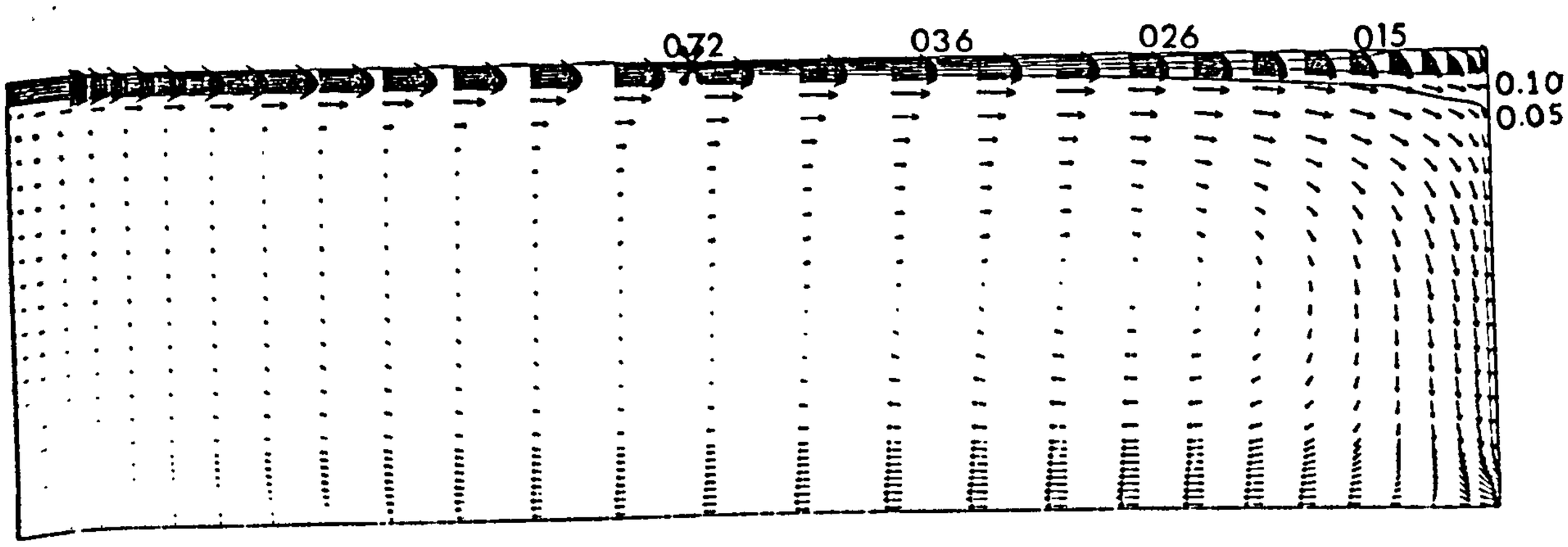

——→ : 0.94 m/s. Min : 2.9436E-04 Max : 4.5967E-01

Figure 7.10 Velocity vector distribution in the planes x/W = 0.0 (symmetry plane); Re = 5000, standard κ–ε turbulence model. Contaminant dispersion. Contour values in decipols * indicates contaminant source location.

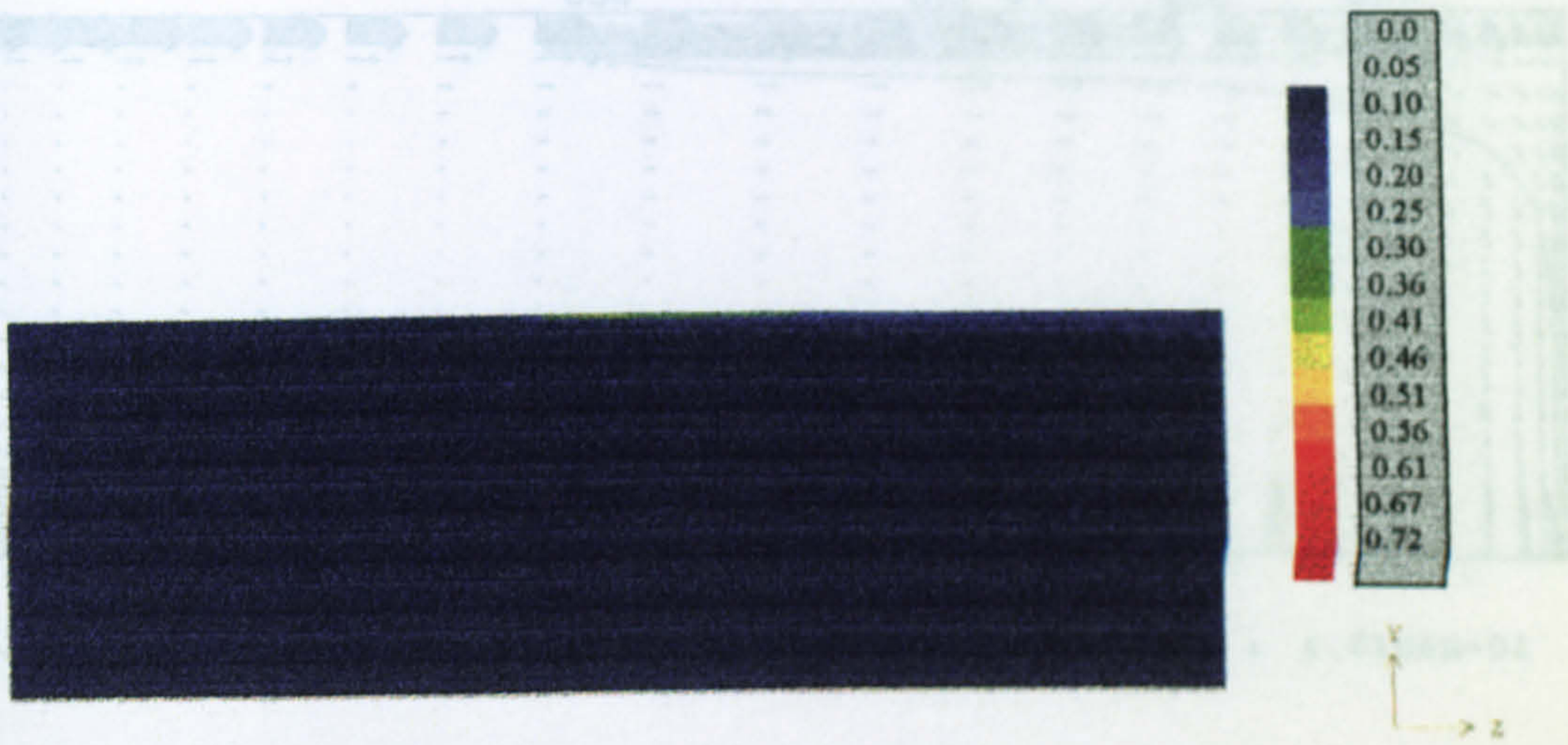

Figure 7.11 Contaminant concentration contours in the plane x/W = 0.0 (symmetry plane); Re = 5000, standard $\kappa-\varepsilon$ turbulence model. Contour values in decipols.

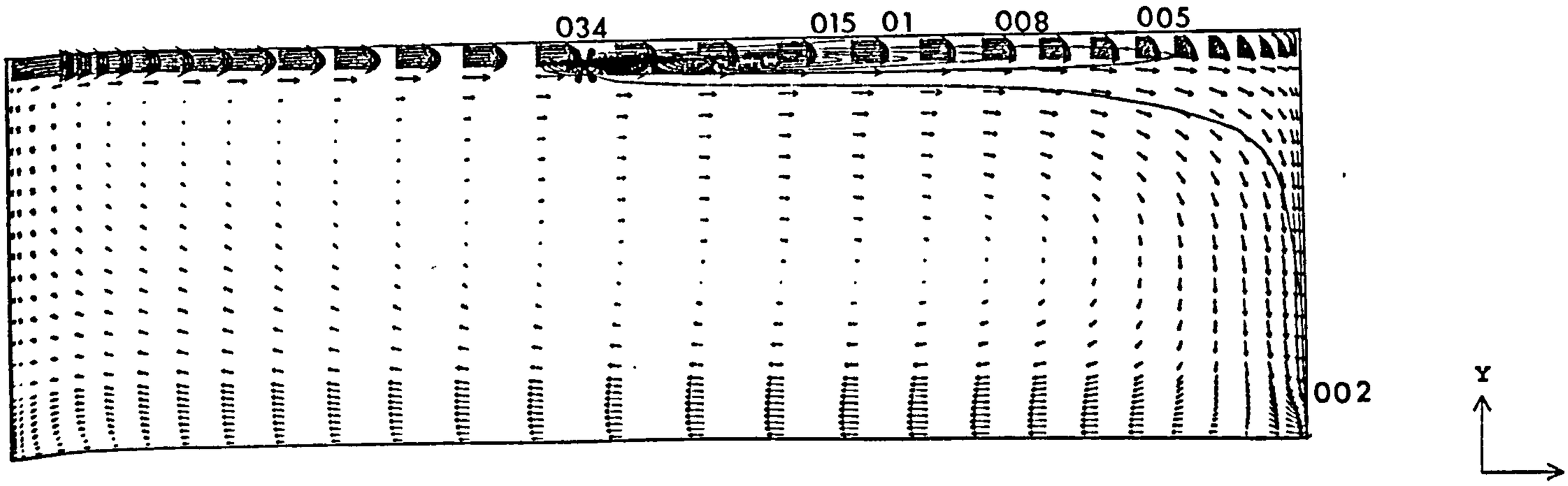

——→ : 0.97 m/s. Min : 9.7194E-03 Max : 4.6106E-01

Figure 7.12 Velocity vector distribution in the planes x/W = 0.0 (symmetry plane); Re = 5000, standard κ–ε turbulence model. Contaminant dispersion. Contour values in decipols * indicates contaminant source location.

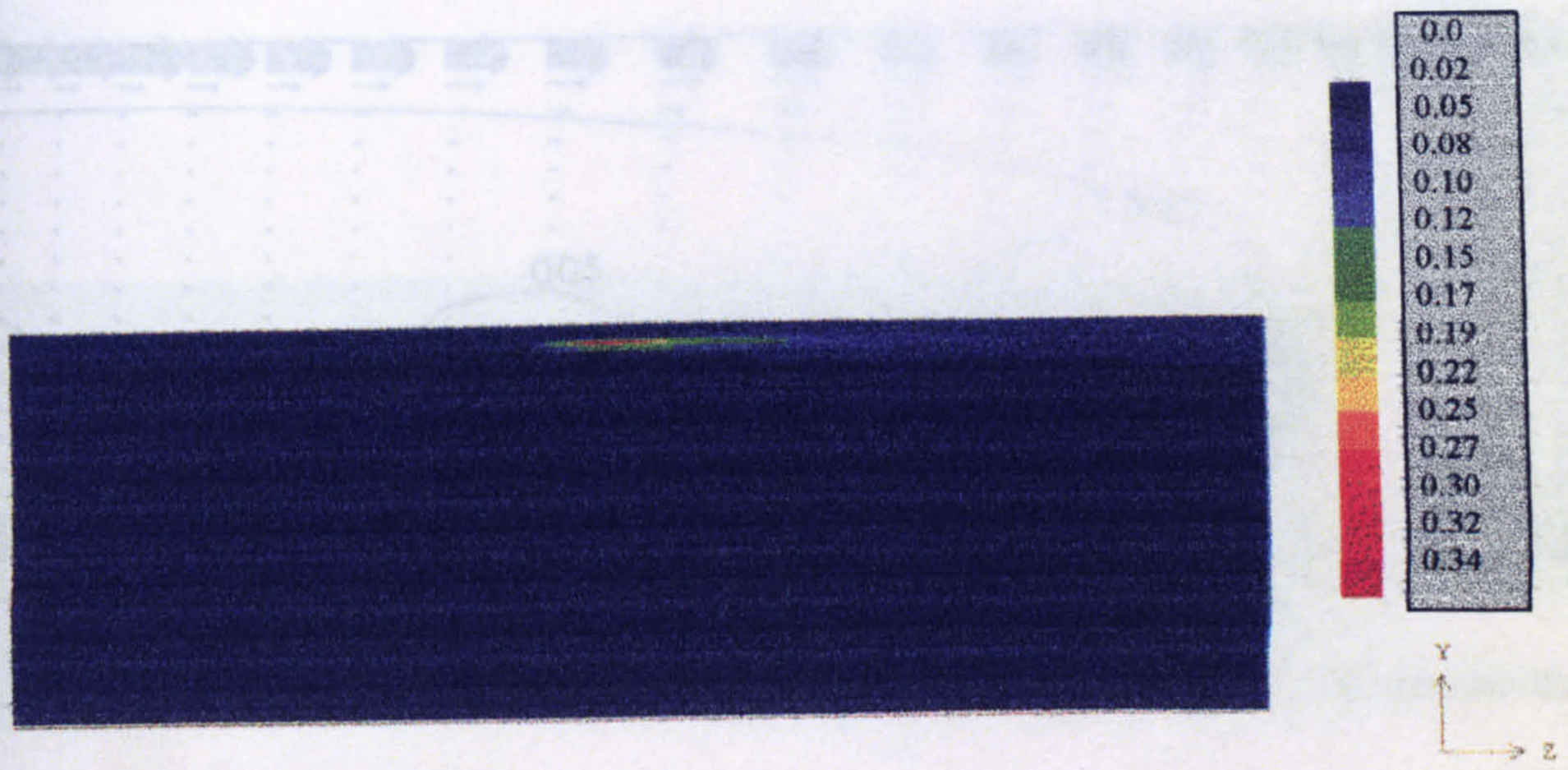

Figure 7.13 Contaminant concentration contours in the plane x/W = 0.0 (symmetry plane); Re = 5000, standard κ–ε turbulence model. Contour values in decipols.

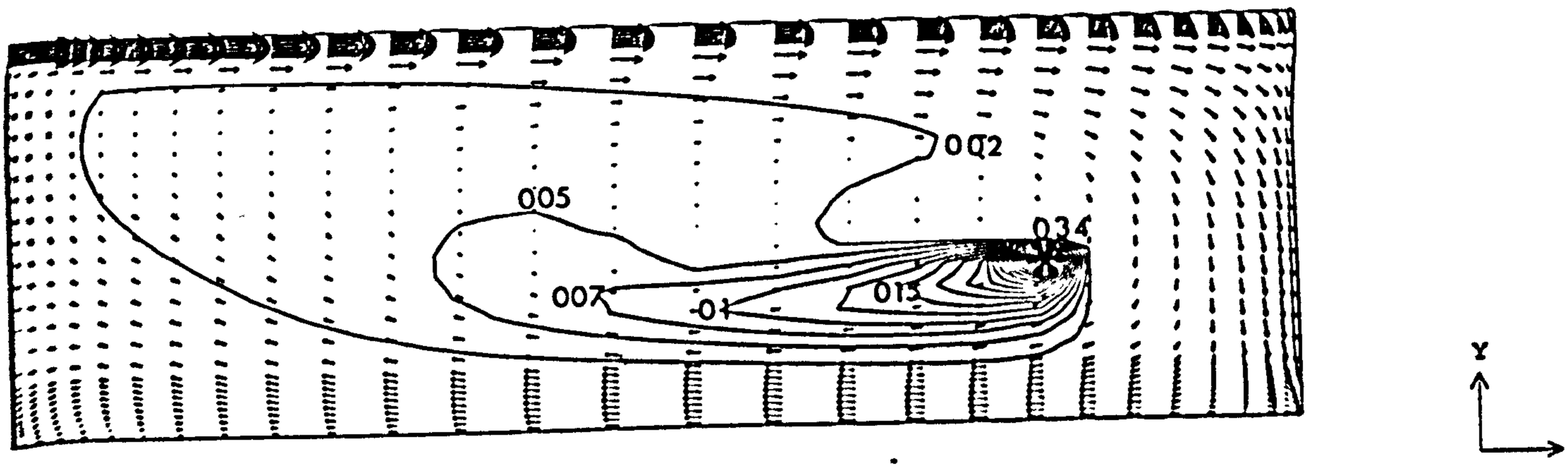

——→ : 0.96 m/s. Min : 3.5702E-03 Max : 4.6069E-01

Figure 7.14 Velocity vector distribution in the planes x/W = 0.0 (symmetry plane); Re = 5000, standard κ–ε turbulence model. Contaminant dispersion. Contour values in decipols * indicates contaminant source location.

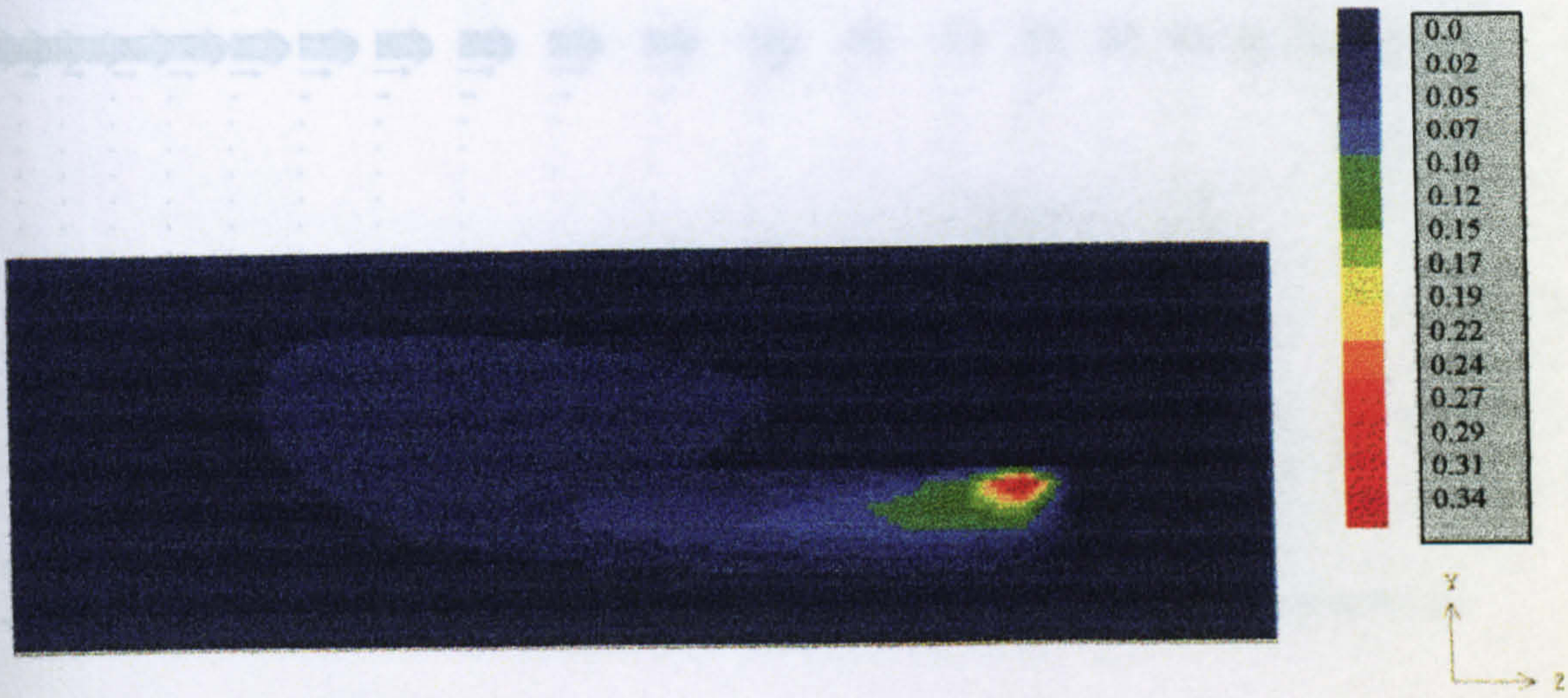

Figure 7.15 Contaminant concentration contours in the plane x/W = 0.0 (symmetry plane); Re = 5000, standard κ–ε turbulence model. Contour values in decipols.

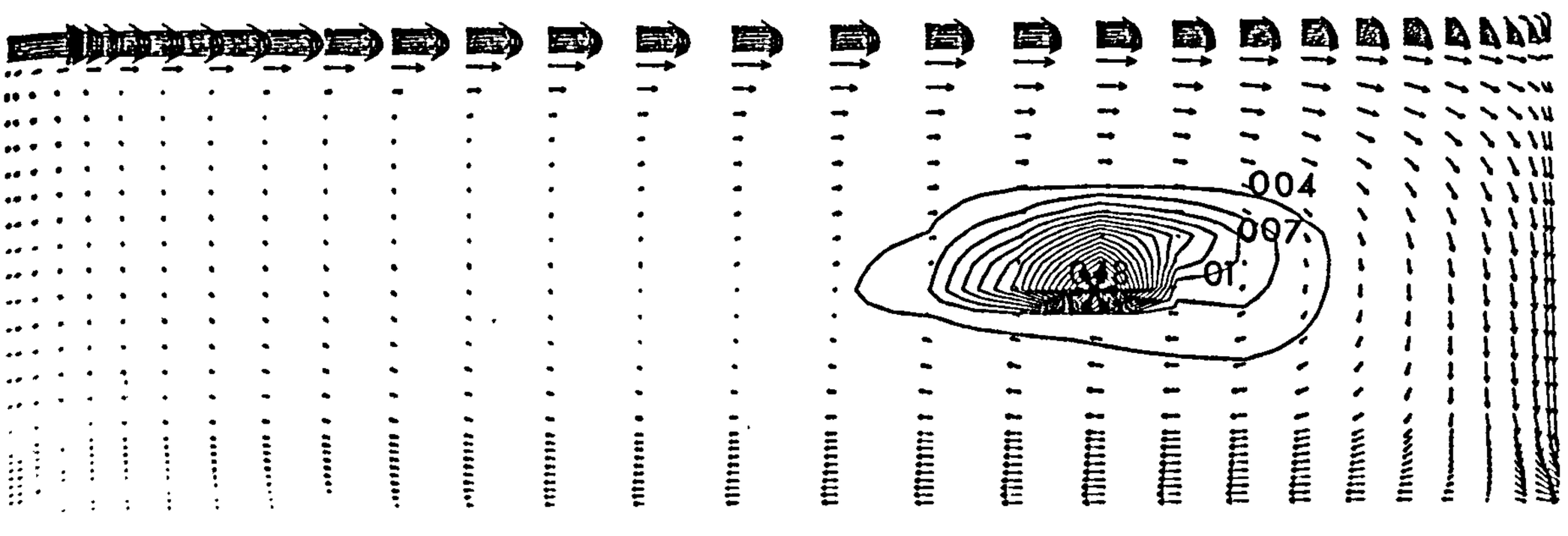

——→ : 0.94 m/s. Min : 2.9436E-04 Max : 4.5967E-01

Figure 7.16 Velocity vector distribution in the planes x/W = 0.0 (symmetry plane); Re = 5000, standard κ–ε turbulence model. Contaminant dispersion. Contour values in decipols * indicates contaminant source location.

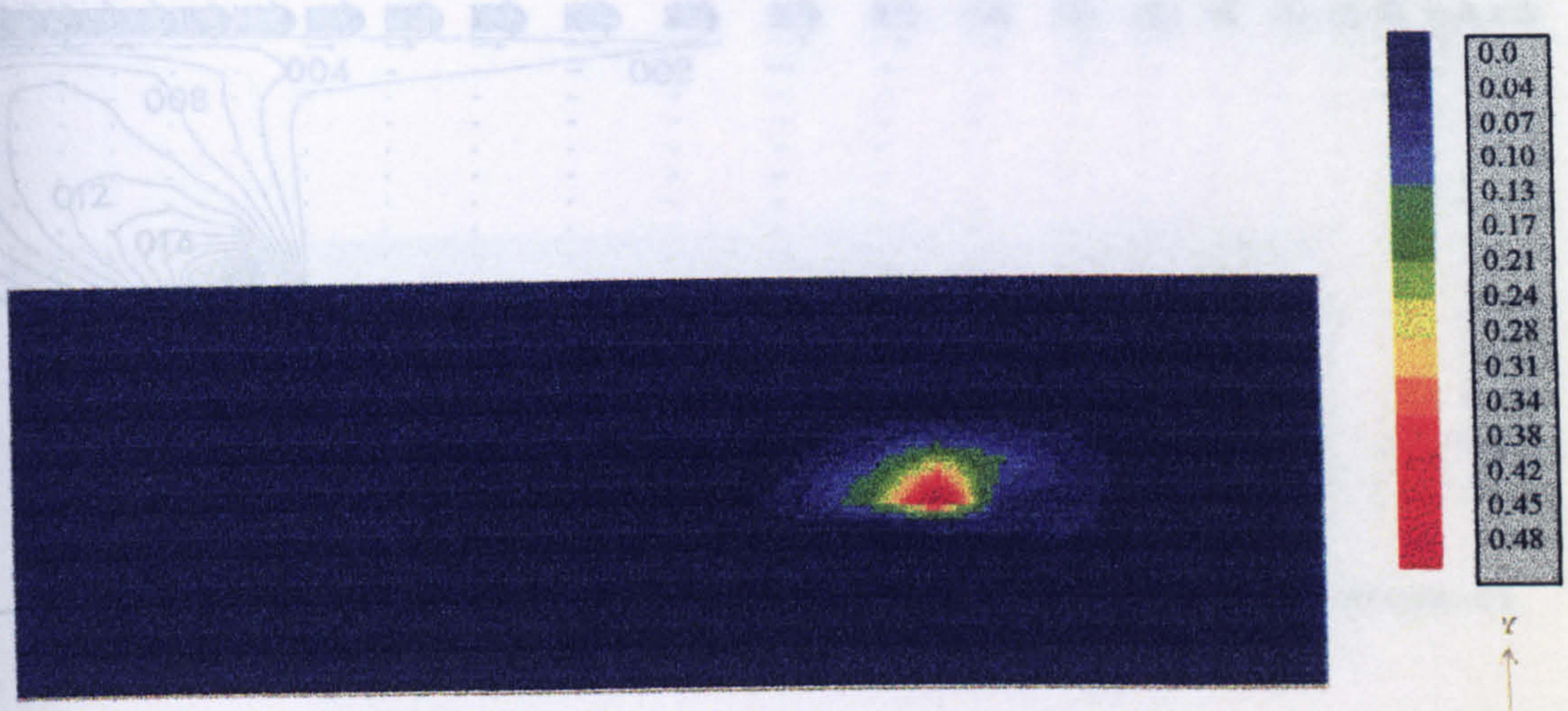

Figure 7.17 Contaminant concentration contours in the plane x/W = 0.0 (symmetry plane); Re = 5000, standard κ–ε turbulence model. Contour values in decipols.

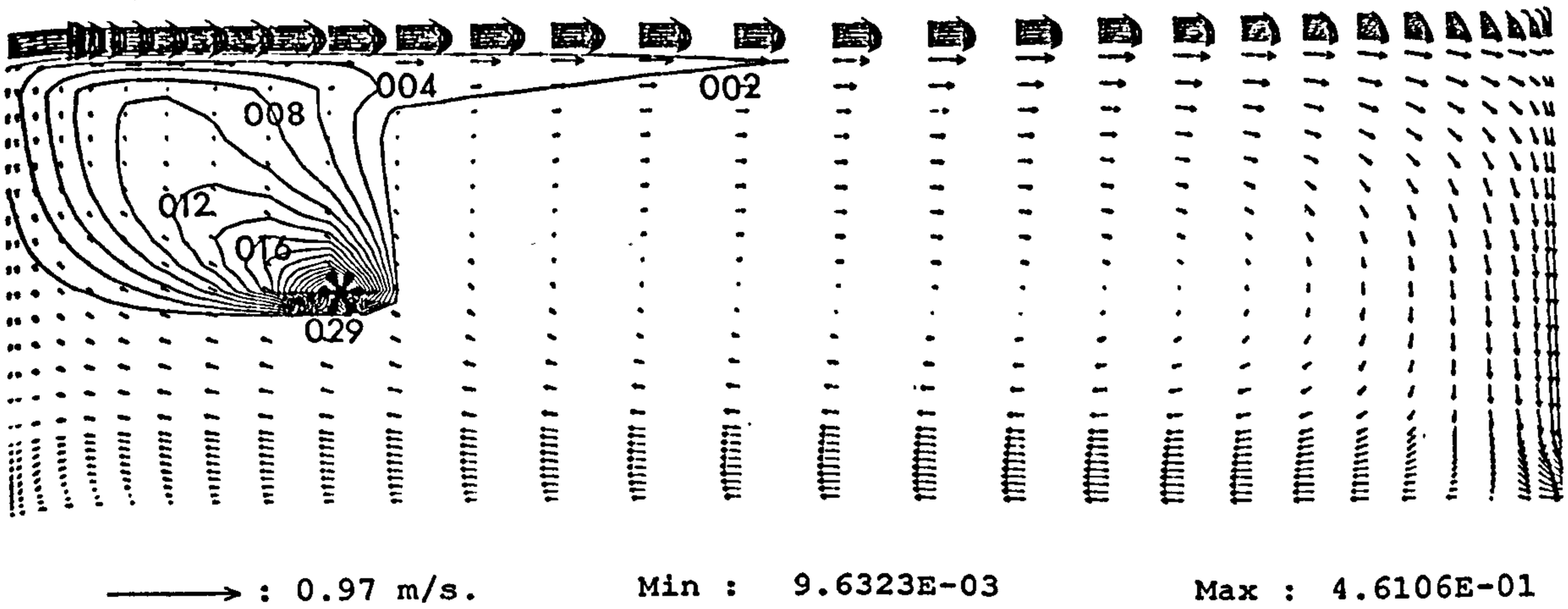

——→ : 0.97 m/s. Min : 9.6323E-03 Max : 4.6106E-01

Figure 7.18 Velocity vector distribution in the planes x/W = 0.0 (symmetry plane); Re = 5000, standard κ–ε turbulence model. Contaminant dispersion. Contour values in decipols * indicates contaminant source location.

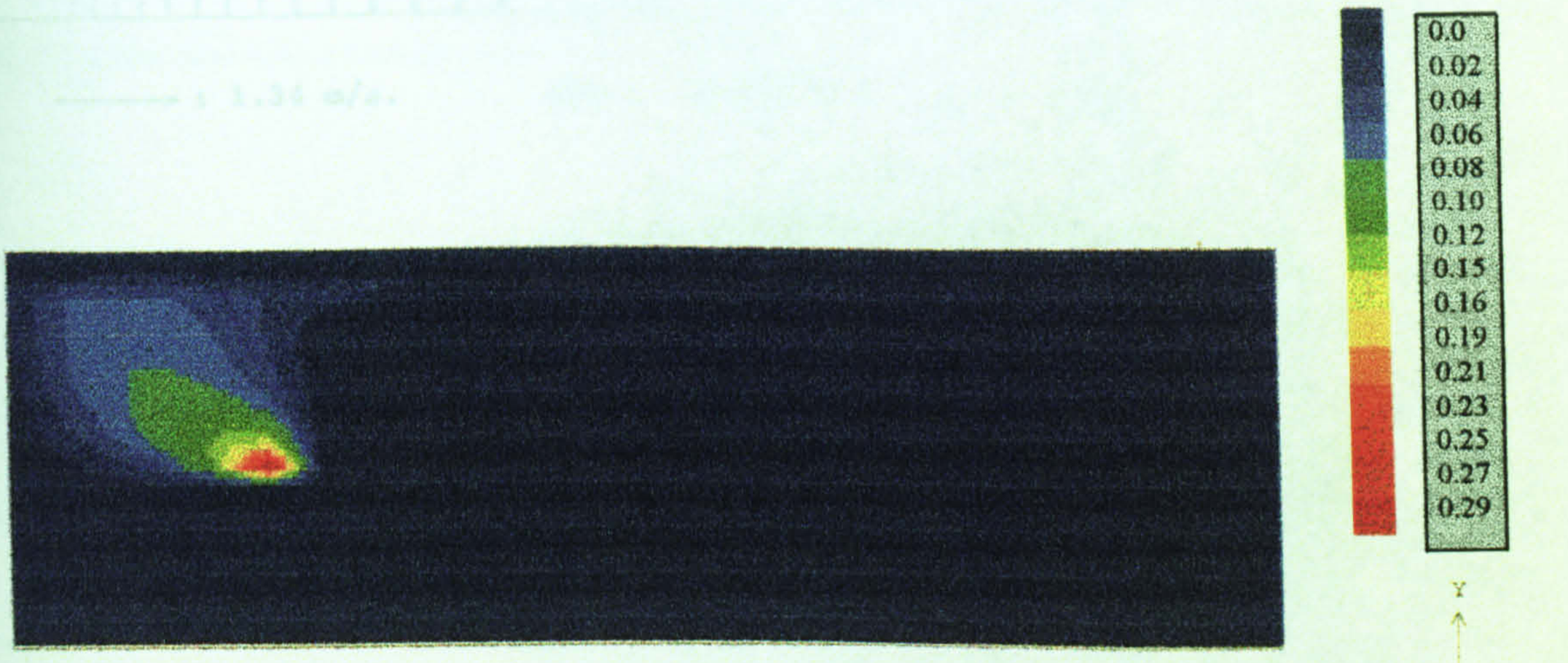

Figure 7.19 Contaminant concentration contours in the plane x/W = 0.0 (symmetry plane); Re = 5000, standard κ–ε turbulence model. Contour values in decipols.

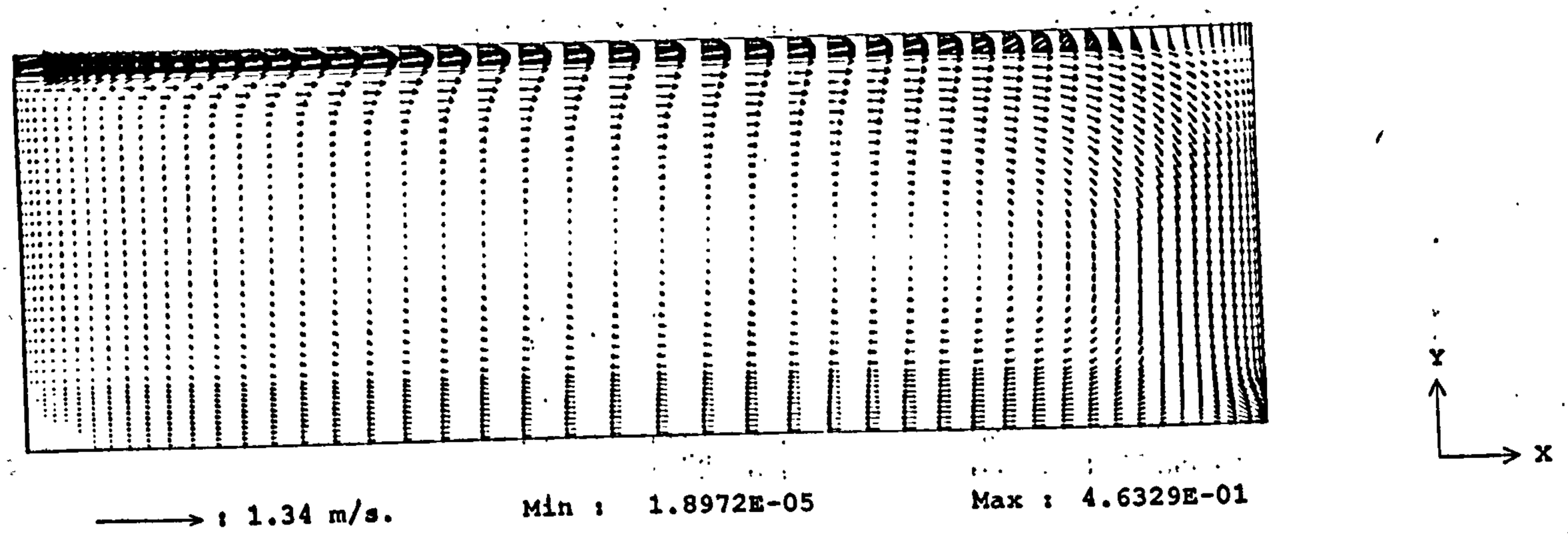

Figure 7.20 Velocity vector distribution in the plane x/W = 0.0 (symmetry plane); Re = 5000, Ar = 0.0 standard κ–ε turbulence model.

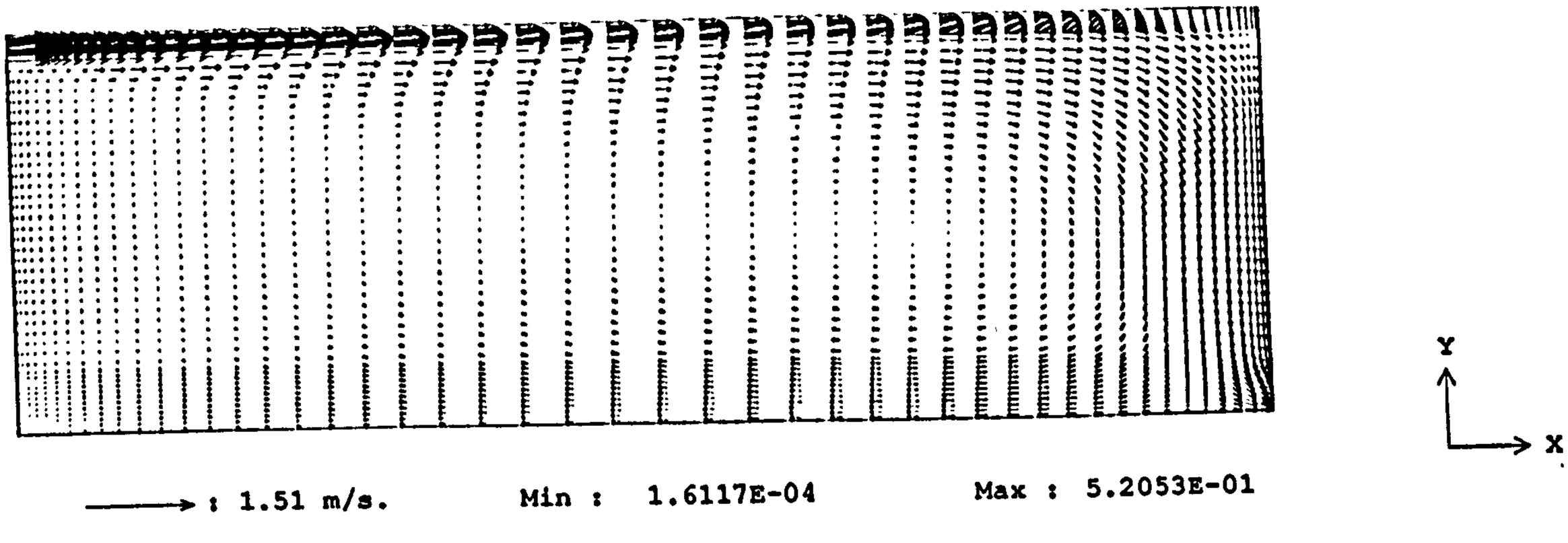

Figure 7.21 Velocity vector distribution in the plane x/W = 0.0 (symmetry plane); Re = 5000, Ar = 0.02 standard κ–ε turbulence model.

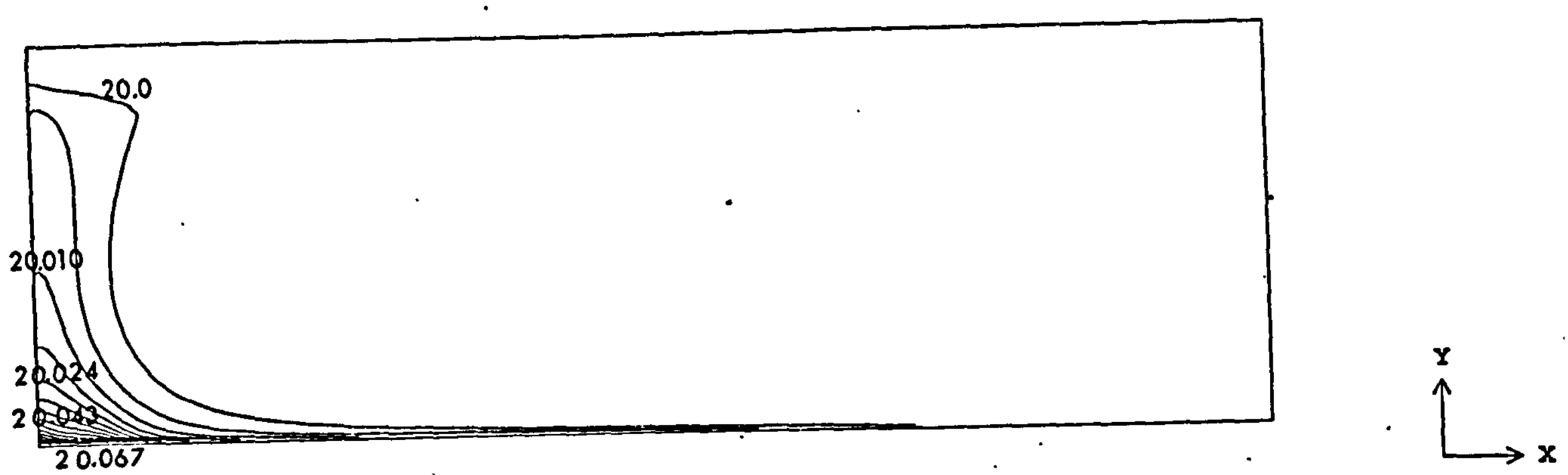

Figure 7.22 Temperature contours in the plane x/W = 0.0 (symmetry plane); Re = 5000, Ar = 0.02 standard κ–ε turbulence model. Contour values in °C.

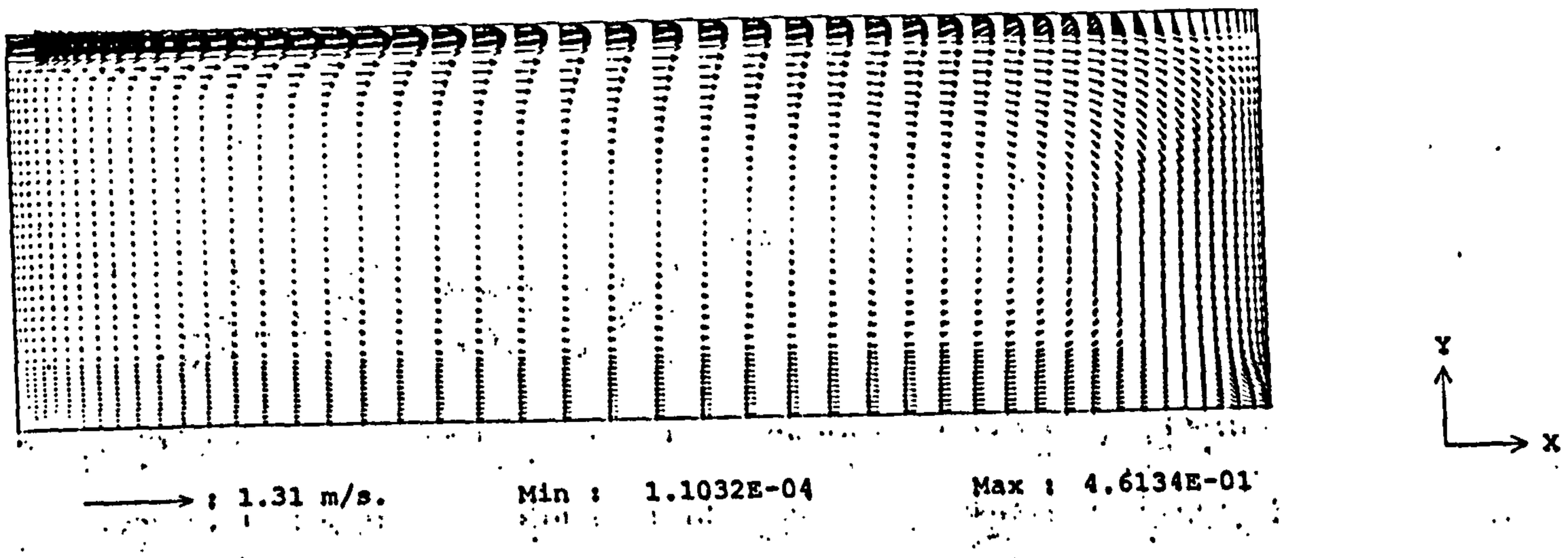

Figure 7.23 Velocity vector distribution in the plane x/W = 0.0 (symmetry plane); Re = 5000, Ar = 0.04, standard κ–ε turbulence model.

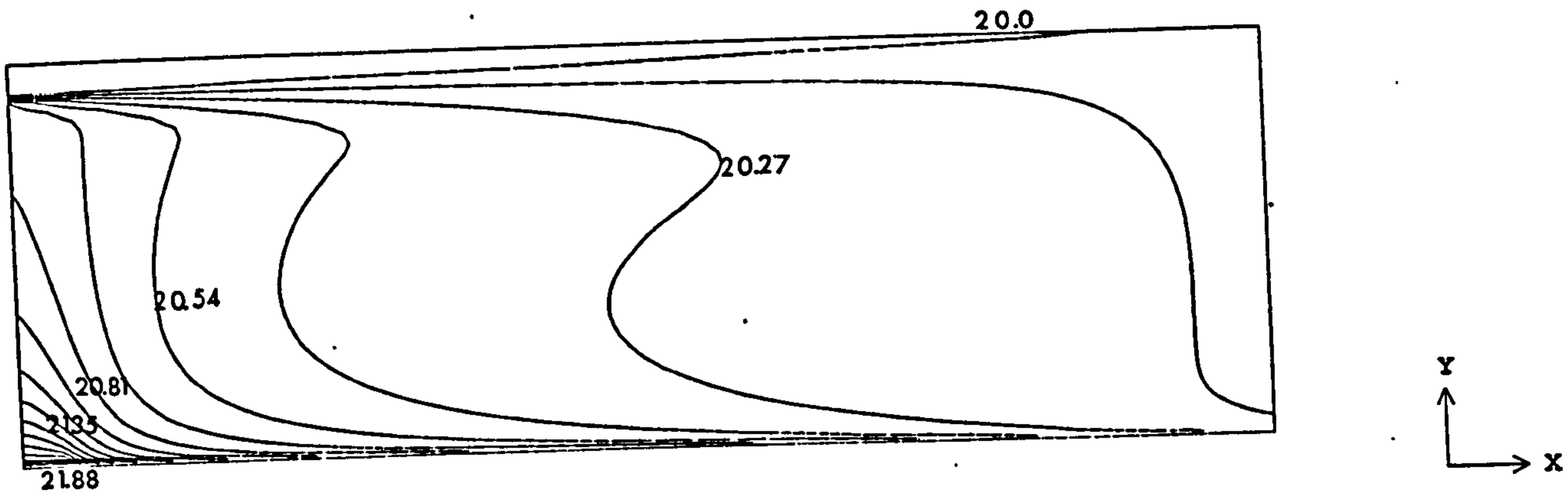

Figure 7.24 Temperature contours in the plane x/W = 0.0 (symmetry plane); Re = 5000, Ar = 0.04, standard κ–ε turbulence model. Contour values in °C.

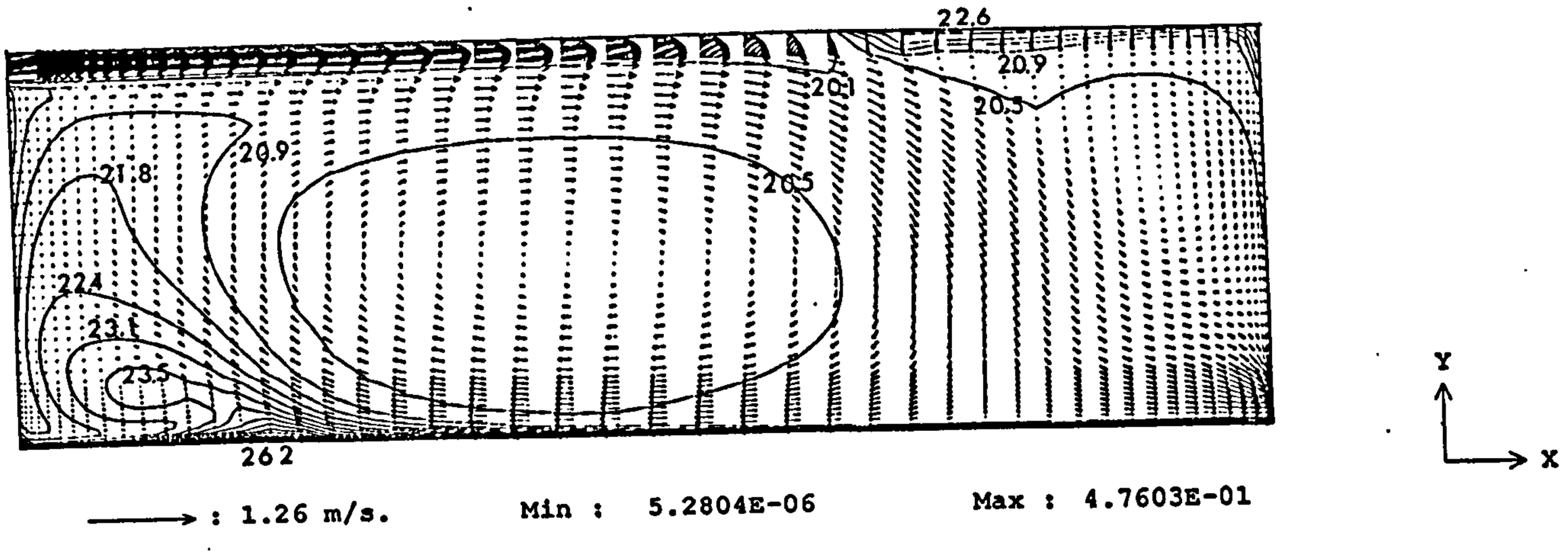

Figure 7.25 Velocity vector distribution and temperature contours in the plane x/W = 0.0 (symmetry plane); Re = 5000, Ar = 0.148, standard κ–ε turbulence model.

CHAPTER 8

CONCLUSIONS AND RECOMMENDATIONS FOR FUTURE WORK

8.1 Conclusions

The air flow pattern distributions inside four different small-scale ventilated chambers have been studied experimentally and numerically. The chambers were ventilated by a three-dimensional wall-type jet that produces a mixing-type flow, with different air supply locations.

Flow visualisation of the flow patterns inside the chambers for Reynolds numbers up to 2000, showed the presence of a highly three-dimensional jet. By utilising a water droplet aerosol it was possible to visualise the flow at Re's considerably higher than those achieved in earlier investigations (Restivo (1979)). These flow visualisation tests showed a large zone of recirculation occupying 25% to 30% of both the first (high wall inlet) and second (low wall inlet) chambers. A smaller recirculation zone was observed on the upper end wall corner. A strong mixing zone was observed over the second half of chambers 3 (ceiling inlet) and 4 (floor inlet).

The distributions of the three mean and r.m.s. velocity components were measured accurately using the LDA technique in all chambers and all regions of the flow. A CFD code was used to investigate the air flow produced by a three-dimensional wall-type jet for all the geometrical configurations studied by the LDA technique. The CFD predictions of the air flow inside the chambers were assessed against the experiments, both qualitatively against flow visualisation recordings and quantitatively against the LDA measured data. For the CFD predictions two different

turbulent models were used, the standard κ–ε and the low Reynolds κ–ε model. For the former, wall functions were used in the near wall region. Very good agreement was achieved between experimental and predicted results for all four chambers studied over many parts of the flow with both models. Both sets of results were compared when possible with sets of experimental data from previous investigations of similar three-dimensional wall-jets. The agreement is satisfactory, showing similar trends in experiments and calculations.

For Chambers 1 and 2 the maximum velocities were found in the jet core zone. In the recirculation zone the highest velocities are located 3/4 of the cavity length from the inlet. It was found that the numerical method used predicted the velocity accurately in the air jet core, but underpredicted it in some parts of the recirculating zone. The type of decay observed is related to the geometrical configuration and the type of jet formed. When the Re number is increased the velocity and the κ values also increase by a similar amount.

The kinetic energy of turbulence was highest in the vicinity of the incoming jet. Elsewhere, the κ values decreased in the recirculation zone, and remained at a constant low value over the remainder of the cavity. The kinetic energy of turbulence was underpredicted by both turbulence models.

Differences between the two turbulence models used are not significant, apart from the CPU time used for each method to obtain a converged solution. Values of the kinetic energy of turbulence predicted by the low Re model were lower than those obtained using the standard κ–ε model. The standard κ–ε model seems to be appropriate for the purposes of this calculation, using less computational time and predicting more accurately

the recirculation zones found near the upper end wall corner and the lower rear wall corner. The use of the low Re $\kappa-\varepsilon$ model would be useful in situations where the buoyancy is the main driving force, such is the case of Displacement ventilation systems.

The differences found between predicted and experimental results, can be attributed to the limitations of the turbulence models used and the uncertainties associated to experimental data. The air flow inside the jet in the four chambers studied, was found to be non-isotropic, and the implicit assumption of isotropy made in the turbulence model formulation may be one of the reasons for the discrepancies observed between experiment and calculation

The use of a fine mesh in zones where steeper gradients are located was found to be useful in predicting features of the air flow (e.g. the small recirculation zone in the upper far corner) that had not been predicted by previous studies in rooms ventilated by a mixing type flow like those in chambers 1 and 2.

The experimental and numerical results presented confirmed the assumption that the air flow patterns for this particular geometry are essentially independent of the Reynolds number. The four inlet configurations studied permitted the evaluation of several aspects of the air flow such as jet spread, within the different chambers.

Once the capability of the CFD code to accurately predict the velocity and turbulence fields was established, the effect of different parameters such as temperature, incoming air jet inlet angle and/or contaminant dispersion was investigated.

The first parametric study included the modification of the inlet angle supply. When the inlet jet angle was changed the flow pattern was modified, for all the cases studied. The air jet discharging close to the ceiling surface at angles of 10°, a more uniform air velocity distribution is produced over the occupied zone, but higher turbulence levels were observed close to the ceiling surface. It was found that a supply air jet with an angle of 45 degrees, produced large mean velocities over the occupied areas, which would produce an undesirable draft effect.

A second study investigated the contaminant dispersal. The contaminant study helped to identify zones of high or low contaminant concentration and how to associate these concentrations to the contaminant source location. Location of the source in with velocities below 0.2 m/s must be avoided in order to diminish the probability of high concentration zones in occupied areas. Although the study did not include different geometrical configurations, it can be expected that different chamber geometries, and inlet angle positions will influence the contaminant distribution directly.

The inclusion of the buoyancy force was part of the third and last parametric study. The non-isothermal case studied, showed the prevailing effect of Ar number on the air flow pattern. It was observed that a gradual increase of the floor temperature leads to air jet separation from the ceiling surface. This was observed when $Ar = 0.148$. For $Ar < 0.148$, no changes were observed on the mean velocity distribution.

The results clearly showed promise that the CFD of isothermal flow validated in this thesis against LDA data could be extended to resolve the air flow distribution in occupied rooms with different geometrical configurations to the ones used here, but clearly, further validation for the non-isothermal cases will be required.

8.2 Recommendations for future work

Further LDA data in the second half of the chambers studied, would help assess the differences between measurements and numerical predictions. The inclusion of time-resolved measurements to find the true levels of turbulence using Fast Fourier Transform (FFT) and filtering techniques.

Versions of the κ–ε model including a modification to account for non-isotropic flow should also be tested to establish whether improved agreement with the measurements can be obtained. The low Re κ–ε model could be tested on Displacement ventilation systems to assess its performance in such situations.

Predictions of the flows employing a Reynolds stress model could offer improved agreement with the measured κ values. Future predictions could be enhanced by accounting for the streamline curvature in the vicinity of the reattachment and separation points using refined discretisation method. Further numerical tests should also be performed by replacing the upwind hybrid scheme by others such as the QUICK and power law formulations to assess their performance.

Another useful line of research is to include the effect of radiation. The inclusion of heat transfer equations may be added to account for the radiation exchange processes present between occupants and the internal surfaces of a room.

A further investigation into the effects of jet inlet angles on the contaminant distribution should also be considered.

REFERENCES

Alamdari, F., Hammond, G.P. and Melo, C. (1984). Appropriate calculations methods for convective heat transfer from buildings surface. ICHEME Symposium Series, Vol. 86, Part 2, pp. 1201-1211.

Alexander, D.K., Jones, P.J., Jenkins, H. and Harries, N. (1994). Tracking air movement in rooms. The role of ventilation. 15th AIVC Conference Proceedings, Buxton, Great Britain 27-30 September 1994, pp. 484-492.

Anderson, R. and Mehos, M. (1988). Evaluation of indoor air pollutant control techniques using scale experiments. ASHRAE IAQ 88, pp. 193-208. Atlanta, GA.

Andrade, J.A. and Restivo, A. (1982). The velocity characteristics of ventilated rooms with sill mounted air supply grilles. LDA conference 1982, Lisbon, Portugal. pp. 1-12.

ASHRAE, (1981). Fundamentals Handbook, Atlanta, U.S.A.

Awbi, H.B. (1991). Ventilation of buildings. Chapman & Hall, London.

Balabani, S. and Yianneskis, M., (1996). An Experimental study of the mean flow and turbulence structure of cross-flow over tube bundles. Proc. IMech, Part C, Vol 2(10). pp. 317-331.

Baturi, V.V. (1972). Fundamentals of industrial ventilation, Pergamon Press, Oxford.

Bauman, F., Gadgil, A., Kammerud, R., Altmayer, E. and Nansteel, M. (1983). Convective heat transfer in buildings: Recent research results, Lawrence Berkeley Laboratory Report, LBL-13883, p. 15.

Bluyssen, M.P. and Lemair, T. (1992). The distribution of the perceived air quality in an office space. Roomvent '92, Denmark. pp. 1-15.

Boussinesq, J. (1877). Essai sur la theorie des eaux courantes, Mem Presentes Acad. Sci., Vol. 23, p. 46.

Bradshaw, P., Launder, B.E. and Lumley, L. (1990). Collaborative testing of turbulence models. Journal of Fluids Engineering, ASME, Vol. 113, pp. 3-4.

CIBSE Guide (1986). Chartered Institution of Building Services Engineering, London.

Chen, C.J. and Rodi, W. (1980). Vertical turbulent buoyant jets-A review of experimental data. Pergamon Press, London.

Chen, M.S.K., Fan, L.T. Hwang, C.L. and Lee, F.S. (1969). Air flow models in a confined space: a study in age distribution. Build. Sci. Vol. 4: pp. 133-144.

Chen, Q. and Jiang, Z. (1992). Significant questions in predicting room air motion. ASHRAE Trans., Vol. 98, Part 1. pp.

Chen, Q. (1991). Simulation of simple test cases. International energy Agency, Annex 2: Air flow patterns within Buildings, Research Item 1.46. AN20.1-CH-90-ETHZ15, pp. 1-10.

Chen, Q., Suter, P., and Moser, A. (1991). A data base for assessing indoor air flow, air quality and draft risk, ASHRAE Transactions, Vol. 9, Part 2, pp. 150-163.

Chen, Q., Moser, A. and Huber, A. (1991). Prediction of buoyant, turbulent flow by a low-Reynolds-number κ–ε model. ASHRAE Trans. Vol. Part 2, pp. 1-10.

Chen, Q. (1990). Application of the PHOENICS-84 code to predict low-Reynolds-number and buoyant affected flows, thermal comfort, and indoor air quality. IEA Annex 20, subtask 1, Annex report AN20-1-CH-90-ETHZ11, pp. 1-15.

Chen, Q., Vander Kooi, J. and Meyers, A. (1988). Measurements and computations of ventilation efficiency and temperature efficiency in a ventilated room, Energy and Buildings, Vol. 126, pp. 85-99.

Chen,Q. (1988). Indoor Air flow, air quality and energy consumption of building, *PhD Thesis*, Delft University, Holland.

Chen, Q. and Vander Kooi, J. (1987). Experiments and 2D approximated computations of 3D air movement heat and concentration transfer in a room. Proc. of the Int. Conference on air distribution in ventilated spaces, Roomvent '87, Vol. 40, p. 144.

Cheesewritght, R. and King K.J. (1985). "Laser Doppler Measurements in natural convection flows. Int. Conf. on laser anemometry advances and applications, Manchester, U.K., pp. 165-174.

Cheung, R., (1989). Investigation of flow patterns inside inlet ports PhD thesis, King's College London, University of London.

Chien, K.Y. (1982). Predictions of channel Boundary-layer with a low-Reynolds number model, AIAAJ., Vol. 20, p. 320

Choi, H.L. (1987). Predicting air velocities and contaminant distributions in a ventilated space using the Teach program and the standard $\kappa-\varepsilon$ model. PhD. Thesis, Cornell University, Ithaca, N.Y.

Christianson, L.L., Zhang, J.S. and Wu, G.J. (1992). Experimental evaluation of room air Contaminant movement. Int. Symposium on room air convection and ventilation effectiveness, Tokyo, Japan, pp. 265-279.

Christianson, L.L., Zhang, J.S. and Riskowski, G.L. (1990). Similitude modelling of non-isothermal air flows in rooms with internal obstructions. Roomvent '90, Oslo, Norway. pp. 1-18.

Christianson, L.L., Riskowski, G.L. and Zhang, J.S. (1988). Predicting air velocity at the pig levels. In Proc. 3d Int. Livestock Environment Symp. ASAE, Vol. 1, p. 88.

Computational Fluid Dynamics for the Building Services Engineer - tool or toy?. (1991) Institution of Mechanical Engineers Seminar, London, pp. 1-100.

Cooper, P. and Kulkarni, R. (1995). Experimental investigation of natural convection in a cubicle enclosure with colliding boundary layers. Report No. NC1/95. University of Wollongong, Australia, p. 42.

Davidson, L. and Olsson, E. (1987). Calculations of age and local purging flow rate in rooms. Build. and Environ., Vol. 22, pp. 11-127.

Deurloo, J.A., Feddes, J.J.R., Leonard, J.J. and Darby, D.E. (1988). Recirculation duct design parameters. Research Bulletin 88-1. Dept. of Agric. Eng., University of Alberta, Edmonton.

Drain, L.E. (1980). The laser Doppler technique, John Wiley and Sons, Chichester.

Durao, D.F.G. and Whitelaw, J.H. (1974). Performance characteristics of two frequency-tracking demodulators and a counting system: measurements in an air jet. Proc. 2nd Int. Workshop on Laser Velocimetry, Purdue University, Vol. 1, p. 170.

Durst, F., Melling, A. and Whitelaw, J.H. (1976). Principles and practice of laser-Doppler anemometry, Academic Press, London.

Etheridge, D.W. and Nolan, J.A., (1979). Ventilation measurements at model scale in turbulent flow, Building and Environment, Vol. 14, pp. 53-64.

Fanger, P.O., Melikov, A.K., Hanzawa, H. and Ring, J. (1988). Air turbulence and sensation of draught. Energ. Build., Vol. 12, pp. 21-39.

Freymuth, P. (1993). Flow visualisation in fluid mechanics. Rev. Sci. Instrum. Vol. 64, pp. 1-18.

Gadgil, A.J., (1980). On convective heat transfer in building energy analysis, Ph.D. Thesis and Report LBL- 10900, University of California, U.S.A.

Givoni, (1969). Cited by Bauman et al (1983).

Glicksman, L.R., Nordford, L.K., Okutan, G.M. and Holden, K.J. (1996). Scale model studies of displacement ventilation. 5th International Conference on Air Distribution in Rooms, Roomvent '96, Japan, pp. 17-19.

Gomiciaga, R., (1990). Estudio hidrodinamico tridimensional de la conveccion natural en una cavidad con razon de aspecto pequena, Msc Thesis, Solar Energy Master degree, IIM-UNAM-LES UACPyP del CCH, Temixco, Morelos, Mexico.

Gosman, A.D. and Ideriah, F.J. (1983). TEACH-2E: A general computer program for two-dimensional turbulent recirculating flows, Imperial College, London.

Gosman, A.D., Nielsen, P.V., Restivo, A. and Whitelaw, J.H. (1980). The flow properties in rooms with small ventilation openings. Trans. ASME J. Fluid. Eng., Vol. 102, pp. 316-323.

Gosman, A.D., Pun, W.M., Runchal, A.K. Spalding, D.B. and Wolfshtein, M. (1969). Heat and mass transfer in recirculating flows, Academic Press, London.

Gray, D.D. and Giorgini, A., (1980). The validity of the Boussinesq approximation for liquids and gases, Int., J. Heat Mass Transfer, Vol. 19, pp. 545-551.

Gunton, M.C., Rosten, H.I. Spalding, D.B. and Tatchell, D.B. (1983). PHOENICS: An instruction manual, TR/75/, CHAM Ltd., London.

Hammond, G.P. (1982). Complete velocity profile and "optimum" skin friction formulas for the plane wall-jet. J. Fluids Eng., ASME Trans., Vol. 104. pp. 59-66.

Hanzawa, H. Melikov, A. and Fanger, P.O. (1987). Air flow characteristics in the occupied zone of ventilated spaces. ASHRAE Trans., Vol. 93, pp. 524-539.

Hardalupas, and Laker, (1993). Thermofluids section "Model 3" Phase Doppler counter.

Heikkinen, J. and Pira, K. (1991). Simulation of simple (two-dimensional) test cases. . International energy Agency, Annex 2: Air flow patterns within Buildings, Research Item 1.46 SF. AN20.1-SF-91-VTT07. pp. 1-15.

Heikkinen, J. (1991). Modelling of a supply air terminal for room air flow simulation 12th AIVC Conference, Ottawa, Canada.

Hellickson, G.L., Young, H.G. and Witmer, W.B. (1973). Baffled centre ceiling ventilation inlet. Trans. ASME, Vol. 16, No. 4, pp. 758-760.

Hertager, B.M. and Magnussen, B.F., (1977). Numerical prediction of three-dimensional turbulent buoyant flow in a ventilated room, Heat Transfer and Turbulent Buoyant Convection, II, pp. 429-440.

Hestad, T. (1971, 1974). Cited by Restivo (1979).

Hoesel, W. and Rodi, W. (1977). New biasing elimination method for laser-Doppler velocimeter counter processing. Rev. Sci. Instrum, Vol. 48, p. 7.

Hoffman, N.A. and Galea, E. R. (1993). An extension of the fire-field modelling technique to include fire-sprinkler iteration - II, The Simulations, Int. J. Heat Mass Transfer, Vol. 36, Part 6, pp. 1445-1457.

Jackman, P.J. (1973). Air movement in rooms with the ceiling mounted diffusers (including supplements A and B). BSRIA Rep. no 81, Building Services Research and Information Association, Bracknell, UK.

Jones, P.J., Alexander, D.K., Jenkis, H. (1994). Visualising air Movement. BEPAC Seminar: New Horizons Seminar, U.K. pp. 1-6.

Jones, P.J. and Whittle, G.E. (1992). Computational fluid dynamics for building air flow prediction - current status and capabilities. Building and Environment, Vol. 27, pp. 321-328.

Jones, P.J. and O'Sullivan, P. (1985). Modelling of air flow patterns in large single volume spaces, SERC Workshop: Developments in building simulation programs, Loughborough University.

Kennedy, D. A. (1987). Water fog as a medium for visualisation of airflows. Ann. Occup. Hyg. Vol. 31, No. 2, pp. 255-259.

Koestel, A. and Tuve, G.L. (1955). Performance and evaluation of room air distribution systems. ASHVE Trans., Vol. 61 p. 533.

Kovasznay, L.S.G. (1970). Turbulent shear flows. Covengo Sulla Teoria Della Turbulenza, Rome.

Kuhen, T.H. (1990). Heat and mass transfer in occupied buildings. Proc. Ninth, International Heat Transfer Conference, Jerusalem, Vol. 1, pp. 435-444.

Kurabuchi, T. and Kusuda, T. (1987). Numerical prediction for indoor air movement. ASHRAE J., Vol. 93, pp. 26-30.

Lam, C.K.G. and Bermhorst, K. (1981). A modified form of the k-e model for predicting wall turbulence. Trans. ASME, J. Fluids Eng., Vol. 103, pp. 456-460.

Launder, B.E. and Sharma, B.I. (1978). Letters in heat and mass transfer, Vol. 1, p. 129.

Launder, B.E. and Spalding, D.B. (1974). The numerical computation of turbulent flows, Comput. Meth. Appl. Mech. Eng., Vol. 3, pp. 269-289.

Launder, B.E. and Spalding, D.B. (1972). Mathematical models of turbulence, Academic Press, London.

Lemaire, A.D. (1992). Room air and contaminant flow,- evaluation of computational methods. IEA Annex 20, Subtask 1, Annex report, TNO Delft, Netherlands.

Linke, W. (1966). Aspects of jet ventilation., BSRIA Trans. 103.

Linden, P.F., Lane-Serff, G.F. and Smeed, D.A. (1990). Emptying filling boxes: the fluid mechanics of natural ventilation. J. Fluid Mech. Vol. 212, pp. 309-335.

Markatos, N.C. and Pericleous, K.A. (1984). Laminar and turbulent natural convection in an enclosed cavity, Int. J. Heat and Mass Transfer, Vol. 27, pp. 755-772.

Markatos, N.C. Maling, M.R. and Cox, G. (1982). Mathematical modelling of buoyancy-induce smoke flow in enclosures, Int. J. Heat and Mass Transfer, Vol. 25, pp. 63-75.

Markatos, N.C. and Cox, G. (1984). Hydrodynamics and heat transfer in enclosures containing a fire source, Physicochemical Hydrodynamics, Vol. 5, pp. 53-66.

McGuirk, J.J., and Whittle, G.E., (1991). Calculation of buoyant air movement in buildings-proposals for a numerical bench-mark test case, Proceedings, Computational fluid dynamics-tool or toy?, IMechE, London, pp. 13-32.

McGuirk, J.J., and Rodi, W., (1977). The calculation of three-dimensional turbulent shear flows. 1st Symp. on Turbulent Shear Flows, Pennsylvania State University.

Melikov, A.K. and Nielsen, J.B., (1989). Local thermal discomfort due to draught and vertical temperature difference in rooms with displacement ventilation. ASHRAE Trans., Vol 96, Part 1, pp. 1050-1057.

Melling, A. (1977). Axisymmetric, turbulent flow in a motored reciprocating engine. Imperial College Mech. Eng. Dept. Report CHT/77/4.

Merzkirch, W. (1989). Flow Visualisation, Academic Press Orlando.

Mohammad, W.S. (1986). Space air conditioning of mechanically-ventilated rooms: Computation of flow and heat transfer. PhD. Thesis, Cranfield Institute of Technology.

Moog, W. (1981). Room flow test in a reduced-scale. Trans. of ASHRAE Vol. 87, Part 4, pp. 1162-1181.

Mullejans, H. (1966). The similarity between non-isothermal flow and heat transfer in mechanical ventilated rooms (BSRIA translation).

Murakami, S. and Kato, S. (1989). Numerical and experimental study on room air flow: 3-D predictions using the κ–ε turbulence model. Building and Envirommment, Vol. 24, Part 1, pp. 85-97.

Murakami, S., Kato, S. and Suyama, Y. (1987). Three-dimensional numerical simulation of turbulent air flow in a ventilated room by means of a two-equation model. ASHRAE Trans., Vol. 93 Part 2, pp. 621-42.

Murakami, S., Kato, S., and Akabayashi, S. (1985). Visualization with laser light sheet applied to internal and external air flows in buildings environmental engineering. In Fluid Control and Measurement, pp. 681-686, Pergamon Press, Oxford.

Murakami, S., Tanaka, T. and Kato, S. (1983). Numerical simulation of air flow and gas diffusion in room model- Correspondence between numerical

simulation and model experiment, Proc. 4th CIB Int. Symp. on the Use of Computers for Environmental Engineering Related to Buildings, Tokyo, pp. 90-95.

Nagasawa Y., Nitadori, M. and Matsui, S. (1990). Characteristics of spiral vortex flow and its application to control indoor air quality. Roomvent '90, pp. 1-16.

Naradajah, S. (1992). An experimental investigation of flows through inlet ports and valves. PhD thesis, King's College London, University of London.

Nielsen, P.V. (1992). Air distribution systems-Room air movement and ventilation effectiveness. Int. Symposium on room air convection and ventilation effectiveness, Tokyo, Japan, pp. 43-52.

Nielsen, P.V. (1991). Models for the prediction of room air distribution, IEA Annex 20, Research Item 1.5. 12th AIVC Conference, Ottawa, Canada.

Nielsen, P.V. (1990). Specification of a two-dimensional test case. International energy Agency, Annex 2: Air flow patterns within Buildings, Research Item 1.45. ISSN 0902-7513 R9040. pp. 1-15.

Nielsen, P.V. (1989). Numerical predictions of air distribution in rooms - status and potentials. In Building systems: Room air and air contaminants distribution. ASHRAE, Atlanta.

Nielsen, P.V. (1981). Contamination distribution in industrial areas with forced ventilation and two dimensional flow, Inst. of Refrigeration, Joint meeting E1, Essen, West Germany, pp. 223-230.

Nielsen, P.V., Restivo, A. and Whitelaw, J.H. (1979). Buoyancy affected flows in ventilated rooms. Numer. Heat Transfer, Vol. 2, pp. 115-27

Nielsen, P.V., Restivo, A. and Whitelaw, J.H. (1978). The velocity characteristics of ventilated rooms. Trans. ASME, J. Fluids. Eng., Vol. 100, pp. 291-298.

Nielsen, P.V. (1974). Flow in a air conditioned rooms, PhD Thesis, Technical University of Denmark.

Nickel, J. (1990). Air quality in a conference room with tobacco smoking ventilated with a mixed or displacement ventilation. Roomvent '90, Oslo, Norway. pp. 1-14

Nouri, J.M., Whitelaw, J.H. and Yianneskis, M. (1987). The scaling of the flow field with impeller size and rotational speed in a stirred reactor. Proc. 2nd Int. Conf. on laser anemometry-Advances and applications, Strathclyde, Scotland, September, pp. 489-500.

Ogilvie, J.R. Barber, E.M. Clarke, N. and Pavlicik, (1988). Design of recirculation air ducts for swine barn ventilation systems. In Proc. of the third Int. Livestock Environment Symposium, Pub. I-88, ASAE.

Ozoe, H. Mouri, A., Ohmuro, M., Churchil, S.W. and Lior, N (1985). Numerical calculations of laminar and turbulent natural convection in water in rectangular channels heated and cooled isothermally on the opposing vertical walls, Int. J. Heat Mass Transfer, Vol. 28, Part 1, pp. 125-138.

Patankar, S.V. (1980). Numerical heat transfer and fluid flow, Hemisphere, New York.

Polushkin, V.I. (1977). Main features of inlet jets development. Refrigeration Science and Technology. Belgrade (Yugoslavia). pp. 271-276.

Patel, V.C., Rodi, W. and Scheuerer, G. (1985). Turbulence models for near-wall and low Reynolds number flows: a Review. AIAA J., Vol. 23, pp. 1308-1319.

Poz, M.Y. (1994). Experimental investigation of planar turbulent jet in enclosures. ASHRAE Trans. No 94-16-4, p. 12.

Pozin, G.M. (1993). Determination of the ventilation effectiveness in mechanically ventilated spaces. Proc. of Indoor Air '93, Vol. 5, pp. 337-341.

Rajaratnam, S.V. (1976). Turbulent jets. Elsievier, Amsterdam.

Rajaratnan, N. and Pani, B.S. (1974). Three dimensional turbulent wall jets. ASCE Trans., J. Hydraul. Div., Vol. 100, pp. 69-83.

Reinartz, A. and Renz, U. (1984). Calculations of the temperature and flow field in a room ventilated by a radial air distributor. Int. J. Refrig. Vol. 7, pp. 308-312.

Renz, U. and Terhaag, U., (1990). Prediction of air flow patterns in a room vetnilated by an air jet -The effect of turbulence model and wall function formulation. Roomvent'90, Norway, paper 18.

Restivo, A. (1979). Turbulent flow in ventilated rooms. PhD. Thesis Imp. Coll. of Science and Technology, University of London.

Rodi, W. (1980). Turbulence models and their applications in hydraulics state of the art review. Inst. Für Hydromechanik, University of Karlsruhe, Germany.

Rolloos, M. (1977). Possibilities and limitations for the prediction of air flow patterns, temperature and velocities in large halls using scale models. Meet. of Commission E1 of the International Institute of Refrigeration, Yugoslavia, pp. 245-256.

Rosten, H.I. and Spalding, D.B. (1987). The PHOENICS equations. CHAM Ltd, Rep. No. TR/99, London.

Roulet, C-A. and Cretton, P. (1992). Field comparison of age air measurements techniques. Roomvent 92, Denmark. p. 15

Said, M.N. Jouini, D.B. and Plett, E.G. (1993). Influence of turbulence parameters at supply inlet on room air diffusion. ASME Winter Annual Meeting, New Orleans, Louisiana- November 28, paper 93-WA/HI-67, pp. 1-16.

Said,. M.N. (1991). Simulation of a two-dimensional benchmark test case. International Energy Agency, Annex 2: Air flow patterns within buildings, Research Item 1.46. AN20.1-CND-90-IRCO4. pp. 1-21.

Sandberg, M. (1989). Velocity characteristics in mechanically ventilated office rooms. In Room Vent 87, Proc. 1st International conference of air distribution in ventilated spaces, Session 2A, Stockholm, Sweden, 10-12 June.

Sandberg, M. and Sjoberg, M. (1983). The use of moments for assessing air quality in ventilated rooms. Building and Environment, Vol. 18 No. 4, pp. 181-197.

Schwartz, W.H. and Corsat, W.P. (1961). The two dimensional turbulent wall-jet. J. Fluid Mech., Vol. 10, pp. 481-495.

Setrakian, A.A. (1988). The effect of rectangular obstacles on the diffusion of a wall-jet, PhD. Thesis, Napier Polytechnic.

Sforza, P.M. and Herbst, G. (1967). A study of three-dimensional incompressible turbulent wall-jets Rep. 1022, Dept. Aerospace Engineering, Polytechnic Inst. of Brooklyn, N.Y.

Siren, K. (1993). The protection ability of the building shell against sudden outdoor air contamination. Building and Environment, Vol. 28, No. 3, pp. 255-269.

Skaret. E. and Mathisen, H.M. (1983). Ventilation efficiency- A guide to efficient ventilation. Trans. of the ASHRAE, Vol. 9, Part 2, pp. 480-495.

Skovgaard, M. (1991). Turbulent flow in rooms ventilated by the mixing principle. PhD. Thesis, The University of Aalborg, Denmark.

Spalding, D.B. (1980). Mathematical modelling of fluids mechanics heat transfer and chemical reaction processes. CFDU Rep. No. HTS/80/1, Imperial College, London.

Steventon, R.D. and Wilson, R.S.E. (1979). Nebulizer units. British J. of Clinical Equipment. July, pp. 153-155.

Subrata, R., Baker, A.J. and Kelso, R.M. (1993). Airborne contaminant CFD modeling studies for two practical 3-D room air flow fields. Proc. of Indoor Air '93, Vol. 5, pp. 349-354.

Suen, K.O. (1992). Investigation of gas flow in a motored high speed diesel engine by laser-Doppler anemometry. PhD Thesis, King's College London, University of London.

Sutcliffe, H. (1990). A guide to air change efficiency. IEA Annex V. Rep. AIC-TN-28-90. pp. 1-32.

Timmons, M.B. (1984a). Internal air velocities as affected by the size and location of continuos diffuser slots. Trans. ASAE, Vol. 27 Part 5, pp. 1514-1517.

Timmons, M.B. (1984b). Use of physical models to predict the fluid motion in slot ventilated livestock structures. Trans. ASAE Vol. 27, Part 2, pp. 502-507.

Timmons, M.B., Albright, D., Furry, B. and Torrance, E., (1980). Experimental and numerical study of air movement in slot-ventilated enclosures, ASHRAE Transactions Semi-annual Meeting, L.A. California, Vol. 86, Part 11, pp. 221-240.

Vazquez, B., and Yianneskis, M. (1993). A study of natural and forced convection in an auditorium. Trans. CIBSE, Building Services Engineering Research and Design, Vol. 14, pp. 169-179.

Vazquez, B., Samano, D. and Yianneskis, M. (1991). The effect of air inlet location on the ventilation of an auditorium. Proceedings of the Seminar "Computational Fluid Dynamics for the Building Services Engineer", Institution of Mechanical Engineers, London, pp. 57-66.

Vazquez, B., (1990). Estudio numerico bidimensional de la conveccion Natural y forzada en estado permanente en un auditorio, Msc Thesis, Solar Energy Master degree, IIM-UNAM-LES UACPyP del CCH, UNAM, Mexico.

Vazquez, B., (1986). Modelo para establecer el comportamiento termico de un auditorio, BSc Thesis, Facultad de Quimica UNAM, Mexico.

Verhoff, A. (1963). Report N626, Dept. of Aeronautical Engineering, Princenton University, USA.

Viets, H. and Sforza, M. (1966). An experimental investigation of a turbulent incompressible three-dimensional wall-jet. Rep. 968, Dept. of Aerospace Engineering, Polytechnic Inst. of Brooklyn, N. Y., USA.

Vogl, N. and Renz, U. (1991). Simulation of simple test cases. International Energy Agency, Annex 2: Air flow patterns within buildings, Research Item 1.46. pp. 1-9.

Whittle, G.E. and Clancy, E.M. (1991). Evaluation of cases B, D, E, Presentation of results from measurements and simulations. IEA Annex 20 Research Report No 1.22.

Whittle, G.E. (1986). Computation of air movement and convective heat transfer within buildings, Int. J. Ambient Energy, Vol. 3, pp. 151-164.

Wilcox, D.C. and Rubesin, W.M. (1980). Progress in turbulence modelling for complex flow fields including effects of compressibility, NASA. Tech. Paper 1517.

Yamanaka, T. and Narasaki, M. (1992). Ventilation effectiveness in the room with a single opening. Int. Symposium on room air convection and ventilation effectiveness, Tokyo, Japan, pp. 251-256.

Yang, W.J. (1989). Handbook of flow visualisation. Hemisphere, Washington D.C.

Yanta, W.J. (1973). Turbulence measurements with laser-Doppler velocimeter. Naval ordinance labs, White Oak, Silver Spring, Report NOLTR 73-94.

Zhang, J. (1991). A fundamental study of two-dimensional room ventilation flows under isothermal and non-isothermal conditions. PhD. Thesis, University of Illinois at Urbana -Champaign.